Communication 58

Sediment transport and flow conditions in steep rivers with large immobile boulders

Tamara Ghilardi

N° 31   2007   P. Heller
Analyse qualitative des systèmes complexes à l'aide de la méthode de Gomez & Probst

N° 32   2007   J. García Hernández, F. Jordan, J. Dubois, J.-L. Boillat
Routing System II - Modélisation d'écoulements dans des systèmes hydrauliques

N° 33   2007   Symposium - Flussbauliche Massnahmen im Dienste des Hochwasserschutzes, der Umwelt, Gesellschaft und Wirtschaft / Mesures d'aménagement des cours d'eau pour la protection contre les crues, l'environnement, la société et l'économie

N° 34   2007   B. Rosier
Interaction of side weir overflow with bed-load transport and bed morphology in a channel

N° 35   2007   A. Amini
Contractile floating barriers for confinement and recuperation of oil slicks

N° 36   2008   T. Meile
Influence of macro-roughness of walls on steady and unsteady flow in a channel

N° 37   2008   S. A. Kantoush
Experimental study on the influence of the geometry of shallow reservoirs on flow patterns and sedimentation by suspended sediments

N° 38   2008   F. Jordan, J. García Hernández, J. Dubois, J.-L. Boillat
Minerve - Modélisation des intempéries de nature extrême du Rhône valaisan et de leurs effets

N° 39   2009   A. Duarte
An experimental study on main flow, secondary flow and turbulence in open-channel bends with emphasis on their interaction with the outer-bank geometry

N° 40   2009   11. JUWI
Treffen junger Wissenschafterinnen und Wissenschafter an Wasserbauinstituten

N° 41   2010   Master of Advanced Studies (MAS) in Water Resources Management and Engineering, édition 2005-2007 - Collection des articles des travaux de diplôme

N° 42   2010   M. Studer
Analyse von Fliessgeschwindigkeiten und Wassertiefen auf verschiedenen Typen von Blockrampen

N° 43   2010   Master of Advanced Studies (MAS) in Hydraulic Engineering, édition 2007-2009 - Collection des articles des travaux de diplôme

N° 44   2010   J.-L. Boillat, M. Bieri, P. Sirvent, J. Dubois
TURBEAU – Turbinage des eaux potables

Preface

In steep mountain rivers, morphological features such as large mostly immobile boulders, strongly influence flow behavior and bedload transport. Without taking into account these large immobile boulders, which are acting as macro-roughness elements, classical bedload transport formula largely overestimate the sediment volume transported. The effect of randomly distributed boulders creating a cascade morphology on the sediment transport capacity and bedload fluctuations in steep mountain channels was studied for the first time by Dr. Tamara Ghilardi with systematic laboratory experiments. A wide grain size distribution was used in the experiments for the movable bedload material present between the large boulders, as it can be found in typical alpine torrents. Boulder size and density was varied in the experiments using shapes of boulders like the ones found in nature. Special attention was also given for the first time on the evolution of the sediment transport characterized by bedload pulses. This allows a new insight on the sediment transport processes in steep channels having large immobile boulders. Finally a new sediment transport formula is suggested which takes into account the presence of such large boulders.

Prof. Dr. Anton Schleiss   Dr. Mário J. Franca

Abstract

Sediment transport and flow conditions in steep rivers with large immobile boulders

Recent flood events in Switzerland and across Europe pointed out several deficiencies in hazard assessment, planning, and prediction methods for flood risk mitigation. A good understanding of the dynamics of mountain rivers, grounded on a sound physical-based theoretical framework, is primordial both from an environmental and a safety point of view. Although mountain rivers control sediment supply to lowland rivers, relatively few studies have been carried out on steep mountain channels, mainly during the last two decades. While these studies provide a multitude of sediment transport equations, generally with similar forms, most of them does not take into account the extreme conditions characterizing alpine torrents. For these latter, the presence of macro-roughness elements, such as large relatively immobile boulders, disrupts the flow and alters channel roughness. Moreover, bedload fluctuations have been observed over time in steep rivers and flumes with wide grain size distributions, even under constant sediment feeding and water discharge.

This research project investigates the impact of randomly distributed boulders (cascade morphology) on the sediment transport capacity and bedload fluctuations in steep channels. This is done by means of 41 laboratory experiments, carried out on a tilting flume at the Laboratory of Hydraulic Constructions (LCH) at Ecole Polytechnique Fédérale de Lausanne (EPFL). The influence of several boulder sizes and distance between roughness elements is investigated for three flume slopes (S=6.7%, 9.9% and 13%). Sediment transport, bulk mean flow velocities and variables describing the morphology were assessed regularly during the experiments.

Firstly, the detailed analysis of a 13 hours laboratory experiment is presented. Periodical bedload pulses are clearly visible on this long duration experiment, along with correlated flow velocity and bed morphology fluctuations. The relation among bulk velocity, morphology variables time evolution and bedload transport is investigated by correlation

analysis, showing that fluctuations are strongly linked. Visual observations indicate that the detected periodical fluctuations correspond to different bed states. Furthermore, the grain size distribution through the channel, varying in time and space, clearly influences these bedload pulses.

For all the experiments, bedload pulses were then characterized by their amplitude and period. It is shown that for higher stream power the fluctuations decrease, both in duration of a cycle and in amplitude. The presence of boulders increases the stream power needed to transport a given amount of sediments, thus decreasing the fluctuations.

The impact of increasing channel slopes on sediment transport is well known. The present research shows that it is also indispensable to take into account the presence of boulders in the estimation of the sediment transport capacity, since it is strongly decreasing with dimensionless boulder distance. Sediment transport capacity is better estimated when taking the liquid discharge as basis parameter instead of bed shear stress. The critical discharge for incipient motion is shown to be dependent not only on the channel slope but also on the dimensionless distance between boulders. A sediment transport formula based on excess discharge and taking into the presence of boulders is herein developed.

Keywords : steep rivers, flume experiments, boulders, macro-roughness elements, wide grain size distribution, bedload fluctuations, fluctuations amplitude and period, sediment transport formulae.

Résumé

Transport solide et conditions d'écoulement dans des rivières de montagne avec des gros blocs immobiles

Les récentes inondations survenues en Suisse et à travers l'Europe ont souligné l'existence de plusieurs lacunes dans l'estimation du risque, la planification ainsi que dans les méthodes de prévision utilisées dans l'atténuation des risques liés aux crues. Une bonne compréhension de la dynamique des rivières de montagne est primordiale du point de vue environnemental et sécuritaire. Bien que les rivières de montagne contrôlent l'apport de sédiments aux rivières de plaine, peu d'études ont été menées dans ce domaine, notamment pendant les dernières décennies. Ces études ont fourni plusieurs d'équations de transport solide, mais dans la plupart des cas les conditions extrêmes caractérisant les rivières de montagne ne sont pas prises en compte. La présence d'éléments de macro-rugosité, tels que les gros blocs relativement immobiles, perturbe l'écoulement et altère la rugosité du canal. De surcroît, des fluctuations de charriage dans le temps ont été observées dans les rivières et canaux à forte pentes avec granulométrie étendue, même lors d'une alimentation liquide et solide constante. Ces fluctuations sont périodiques et sont une conséquence du tri granulométrique.

Dans ce contexte, ce projet de recherche étudie l'impact de blocs aléatoirement distribués (morphologie en cascade, *cascade morphology*) sur la capacité de transport et les fluctuations de charriage dans des canaux à forte pente. Ceci est fait à travers une série de 41 essais en laboratoire, effectués dans un canal à pente variable au Laboratoire de Constructions Hydrauliques (LCH) à l'Ecole Polytechnique Fédérale de Lausanne (EPFL). L'influence de plusieurs diamètres de blocs et de la distance entre ces derniers est examinée sur trois pentes (S=6.7%, 9.9% et 13%). Le transport solide, la vitesse moyenne de l'écoulement et les variables décrivant la morphologie ont été mesurés régulièrement pendant les essais.

Dans une première étape, une analyse détaillée d'un essai de 13 heures est présentée. Des oscillations périodiques de charriage sont clairement visibles tout au long de l'essai. Des

fluctuations de la vitesse de l'écoulement ainsi que de la morphologie du lit sont également observées. Le lien entre l'évolution temporelle de la vitesse d'écoulement, des variables morphologiques et du charriage est étudié par analyse corrélationnelle. Il est démontré que ces fluctuations sont étroitement liées entre elles. Les observations visuelles montrent que ces fluctuations périodiques de charriage correspondent à différents états de lit. La granulométrie de surface dans le canal, qui varie dans le temps et dans l'espace, influence clairement les fluctuations de charriage.

Pour tous les essais, les fluctuations de charriage ont été caractérisées par leur amplitude et leur période. Il est démontré que pour des grandes puissances d'écoulement (*stream power*) les fluctuations diminuent tant en durée qu'en amplitude. La présence de blocs augmente la puissance d'écoulement nécessaire pour le transport d'une certaine quantité de sédiments, en diminuant donc les fluctuations.

L'effet de l'augmentation de la pente du canal est bien connu. Avec le présent travail de recherche il est démontré qu'il est également indispensable de prendre en compte la présence des blocs, puisque la capacité de transport solide diminue fortement avec la distance adimensionnelle entre les blocs. La capacité de charriage est mieux estimée en termes de débit qu'en termes de tension de cisaillement sur le lit du canal. Il est montré que le débit critique de mise en mouvement ne dépend pas uniquement de la pente du canal, mais également de la distance adimensionnelle entre les blocs. Une formule de charriage basée sur l'excès de débit et considérant la présence des blocs est développée dans la présente étude.

Mots-clés : rivières à forte pente, essais en canal, blocs, macro-rugosités, granulométrie étendue, fluctuations de charriage, amplitude et période des fluctuations, formules de transport solide.

Riassunto

Trasporto solido e condizioni di flusso nei fiumi di montagna in presenza di grossi blocchi immobili

Le recenti inondazioni avvenute in Svizzera e nel resto d'Europa hanno sottolineato le mancanze nei metodi utilizzati per la valutazione del rischio e per la pianificazione, così come quelle nei sistemi impiegati per l'attenuazione dei pericoli associati ai fenomeni di piena. A tale proposito, è quindi fondamentale conoscere e comprendere il comportamento dinamico dei fiumi di montagna, sia per ciò che riguarda l'aspetto ambientale sia in riferimento alla sicurezza. Nonostante l'inequivocabile funzione di controllo che gli alvei a forte pendenza esercitano sull'apporto di sedimenti verso valle, solamente negli ultimi decenni è aumentato l'interesse nell'approfondire tale tematica. Gli studi finora condotti hanno fornito una moltitudine di formule sul trasporto solido, spesso aventi espressioni simili tra di loro, ma nella maggior parte dei casi carenti nel considerare le condizioni estreme caratteristiche dei torrenti. Non si è infatti tenuto conto della presenza di macro-scabrezze, quali ad esempio i grandi massi relativamente immobili, che perturbano il flusso e alterano la rugosità dell'alveo. Inoltre nei fiumi e nei canali a forte pendenza sono state osservate delle fluttuazioni nel trasporto solido, in presenza di una granulometria estesa e con alimentazione solida e liquida costanti, che possono essere considerate periodiche e conseguenti all'assortimento granulometrico.

È in questo contesto che il presente progetto di ricerca mira a studiare l'effetto che hanno i grandi massi disposti in maniera aleatoria (*cascade morphology*) lungo l'alveo sulla capacità di trasporto solido e sulle fluttuazioni ad esso associate. Per raggiungere tale proposito, presso il Laboratorio di Costruzioni Idrauliche (LCH) dell'Ecole Polytechnique Fédérale de Lausanne (EPFL), hanno preso luogo 41 test. La distanza fra i massi e la dimensione di quest'ultimi sono i parametri discriminanti oggetto di studio: si sono ricercate eventuali correlazioni fra le variabili, considerando anche il contributo della pendenza (test applicati a tre diverse pendenze).

Nel corso delle esperienze di laboratorio, il trasporto solido, la velocità media e le caratteristiche morfologiche del canale sono state misurate ad intervalli di tempo regolari. Nella prima parte di questo studio è presentata l'analisi dettagliata di un test di 13 ore, il quale ha fornito un'ulteriore dimostrazione riguardo la presenza periodica di fluttuazioni nel trasporto solido (estese a tutta la durata). Altresì nel corso del medesimo test sono state osservate oscillazioni concomitanti con cambiamenti nel profilo di velocità e nella morfologia d'alveo. Attraverso un'analisi correlazionale è stato possibile validare tale legame temporale esistente fra le variabili sopra citate. Dall'analisi visiva è stato inoltre possibile associare a differenti stati dell'alveo, definiti dalla granulometria superficiale, il comparire di tali fluttuazioni periodiche associate al trasporto solido.

In tutti i test analizzati, a tale comportamento oscillatorio sono state correlate una determinata ampiezza ed un periodo; ed è rispetto a tali grandezze caratteristiche che si è potuta registrare una diminuzione all'aumentare della potenza di flusso (*stream power*). La presenza dei blocchi impone una potenza di flusso maggiore al fine trasportare una data quantità di sedimenti, contribuendo quindi a diminuire l'entità delle fluttuazioni.

Altro parametro caratterizzante la morfologia e la dinamica nell'alveo è la pendenza, la cui crescita ha un effetto già ben conosciuto sul trasporto solido. Nel presente studio però è dimostrato che è ugualmente indispensabile considerare allo stesso tempo anche la presenza delle macro-scabrezze. Oltre ad aver verificato la diminuzione della capacità di trasporto solido con la distanza adimensionale fra i blocchi, rispetto a quest'ultima si è dimostrata dipendente anche la portata critica di incipiente movimento. Infine, tra le ultime deduzioni tratte dalle esperienze svolte, la capacità di trasporto solido è stimata in modo migliore in termini di portata piuttosto che in quelli di sforzo tangenziale. Il presente progetto di ricerca fornisce dunque una formula di trasporto solido tenente in considerazione anche la presenza delle macro-scabrezze.

Parole chiave : fiumi a forte pendenza, esperimenti in canale, blocchi, macro-scabrezze, granulometria estesa, fluttuazioni di trasporto solido, ampiezza e periodo delle fluttuazioni, formule di trasporto solido.

Acknowledgments

A big *Merci!* also to the secretaries Scarlett and Caroline for helping me through all the administrative problems. I also thank Dr. Jean-Louis Boillat, Giovanni De Cesare and Michael Pfister for their useful answers to sometimes silly questions. I received a lot of help on my thesis topic from Elowyn Yager, who spent almost two month at LCH as invited professor and whom I met in several other occasions, and for that I am thankful.

Carrying out a stressful and physical intensive thesis would not have been possible without the colleagues and dear friends at LCH, and I mean it! They almost all helped me doing measurements on my thesis and SNCF model or putting sediments in the Avançon model at one moment or the other. There are those who left before me: Markus, Juliano, Olivier, Mathias, Jolanda, Marcel, Javier, Fadi, Matteo, Erica, Jean-Marc, Walter, Martin, Michael, Violaine, Emilie, Milad; those who will leave with me: Théodora, Ana Margarida and Raphaël; and those who will leave after me: José Pedro, Rafael, Mona, Sebastián, Mohammad Javad, Stéphane, Félix, David , Alexandre, Fränz, Sebastian, Sabine, Nicolas and Ramona. And… mmh… did I forget someone? I hope not! The hellCHteam is really big and wonderfull! I will never forget the LCH trips, Christmass dinners, *les bières à Sat et les grillades au bord du lac*!

I also thank all the trainees and students (i.e. slaves…) who intensively helped me during my experiments: Gottfried, Janina, Carole, Sabine and Sebastian. Apparently it was not a too bad slave master, since two out of five started a thesis here at LCH.

I don't know why, but I have the feeling that I forgot some small details…

Ahah! Elena! The best slave ever! I would never have finished the experiments without her, working day and night to help me and listening to my complains about the world and not only. It has been really funny exchanging really nice (…) comments on everything and everyone. I am really truly grateful for your presence at LCH. With whom will I complain about everything once I'm gone?! *Un grazie di cuore veramente!!! Forza e coraggio! Se ce l'ho fatta io ce la puoi fare pure tu! Non siamo molto diverse… e quelli che ci circondano, ci supportano e soprattutto ci sopportano sono tutti santi!*

Finally, family. Always family. This PhD research is just one phase of my life. But they loved me before it started and they will continue to love me long after I put the "Dr." in front of my name. I just don't understand how they managed to do it During my PhD! They taught me what is important in life and gave me a big support in all my decisions. *Grazie mille a Mamma, Papà, Pamela e Flavio. Santi tutti!*

And finally, the most important *GRAZIE* goes to my *finalmente* husband Enea. Without him I would never have had the courage I needed to arrive where I am and I probably would have stopped everything at the first problem. He was of huge help during my first years at the University. He taught me math, physics, informatics, databases, and so on! And for the video analysis of my thesis: impossible without his hints on image analysis! He stood by my side during the past eleven years and especially through the PhD. He is so crazy that he anyway decided to marry me just a few month before the end of the thesis… and all those who did a PhD and especially their beloved ones know how much love one needs for that! *Ti ringrazio per avermi dato amore, forza e coraggio durante tutti questi anni. Non so come farei senza di te! Enea santo subito!*

Acknowledgments

Contents

List of figures

List of tables

Notation

Symbol	Unit	Description
A_{bed}	m^2	Total bed area
A_{Bs}	m^2	Basal cross-sectional area of a boulder obtained by video analysis
A_{Bs}^{*}	-	Dimensionless basal cross-sectional area of a boulder obtained by video analysis
A_i	m^2	Basal cross-sectional area of a boulder, calculated
A_{if}	m^2	Wetted frontal cross-sectional area of a boulder, calculated
A_m	m^2	Bed area occupied by mobile sediments
A_t	m^2	Total unit bed area
b	-	Hiding factor parameter according to *Ferguson* (2005)
C	-	Chézy coefficient
C_D	-	A drag coefficient
C_G	-	Chézy coefficient associated to the bed material according to *Canovaro et al.* (2007)
C_I	-	A drag coefficient associated to the boulders according to *Yager et al.* (2007)
C_m	-	A drag coefficient associated to mobile sediments according to *Yager et al.* (2007)
C_P	-	Chézy coefficient associated to the boulder according to *Canovaro et al.* (2007)
D	m	Boulder diameter
d	m	Hydraulic parameter in the relative submergence (d/k_s)
D_f	N	Drag force of an individual object in the flow
D_s	m	Short boulder diameter according to *Canovaro et al.* (2007)
d_x	m	Characteristic grain diameter
D_x	m	Reduced boulder diameter
F	-	Darcy-Weisbach friction factor
f_x	-	Varying components of the Darcy-Weisbach friction factor
g	ms^{-2}	Gravity acceleration, equal to 9.81 ms^{-2}
h	m	Average water depth
h^{*}	m	Corrected water depth according to *Dubois* (1998)
h_a	m	Average flow depth between boulders according to *Yager et al.* (2007)
HJ	-	Number of hydraulic jumps in the flume
HJ^{*}	-	Portion of boulders presenting hydraulic jumps
i_b	Wm^{-2}	Bedload transport rate for immersed weight per unit area
j_l, j_2	-	Geometry factors according to *Bathurst* (1978)
k_s	mm-	Nikuradse's equivalent grain roughness

Symbol	Unit	Description
M	-	Equimobility parameter according to *Papanicolaou et al.* (2004)
m_b	kg	Mass of bedload
N_{Bs}	m^{-2}	Number of boulders per square meter
N_{Bst}	-	Number of boulders in the flume
N_u	m^{-2}	Number of boulders per unit bed area according to *Canovaro et al.* (2007)
N_u^{max}	m^{-2}	Maximum number of boulders per unit bed area according to *Canovaro et al.* (2007)
O	-	Grain sorting parameter according to *Ferguson* (2005)
P	m	Average protrusion of one boulder during the experiment
P^*	-	Dimensionless average protrusion of several boulder during the experiment
P_{av}	m	Average protrusion of several boulder during the experiment
$\overline{P_{av}}$	m	Average protrusion of several boulder for the whole test
P_{ds}	m	Average downstream boulder protrusion at the end of the experiment
P_{end}	m	Average boulder protrusion at the end of the experiment
P_{us}	m	Average upstream boulder protrusion at the end of the experiment
Q	l/s	Total liquid discharge
Q	m^{3}s^{-1}m^{-1}	Liquid discharge per unit width
q_b	varying	Bedload transport
q_{cr}	m^{3}s^{-1}m^{-1}	Critical discharge per unit width
q_{cr}^*	-	Dimensionless critical discharge per unit width
q_s	m^{3}s^{-1}m^{-1}	Volumetric bedload transport per unit width
q_s^*	-	Dimensionless bedload transport
$q_{s,in}$	m^{3}s^{-1}m^{-1}	Sediment supply
$q_{s,out,end}$	m^{3}s^{-1}m^{-1}	Sediment outlet averaged over the whole test
$q_{s,out,X}$	m^{3}s^{-1}m^{-1}	Sediment outlet averaged over an x minutes window
Re	-	Reynolds number
R_h	m	Hydraulic radius
S	-	Channel slope
t^*	-	Normalized time for cycle duration
T_{qs}	min	Period of bedload fluctuations
U	ms^{-1}	Flow velocity
$\bar{U}$	ms^{-1}	Flow velocity average for the whole test
u^*	ms^{-1}	Shear velocity
U_b	ms^{-1}	Mean transport velocity
U_{cr}	ms^{-1}	Flow velocity associated to the critical shear stress according to *Ferguson* (2005)
V_u	ms^{-1}	Flow velocity in the upper layer according to *Canovaro et al.* (2007)

Symbol	Unit	Description
w	m	Channel width
z_m	m	Height of the mobile sediments according to *Yager et al.* (2007)
Γ	-	Spatial density of macro-roughness according to *Canovaro et al.* (2007)
κ	-	von Kármán coefficient
λ	m	Distance between boulders
λ/D	-	Dimensionless distance between boulders, spatial density of boulders according to *Yager et al.* (2007)
ρ	kgm^{-3}	Water density, assumed to be equal to 1000 kgm^{-3}
ρ_s	kgm^{-3}	Solid density, assumed to be equal to 2650 kgm^{-3} for both, mobile sediments and boulders
$\sigma_{qs}/q_{s,end}$	-	Amplitude of bedload fluctuations
τ_0	Nm^{-2}	Total bed shear stress
τ_0^*	-	Dimensionless total bed shear stress
τ_{cr}	Nm^{-2}	Critical shear stress
τ_{cr}^*	-	Dimensionless critical shear stress
τ_{crX}^*	-	Dimensionless critical shear stress for a characteristic grain size
τ_d	Nm^{-2}	Bed drag shear stress
τ_I	Nm^{-2}	Drag bed shear stress endured by boulders according to *Yager et al.* (2007)
τ_m	Nm^{-2}	Drag bed shear stress acting on mobile sediments according to *Yager et al.* (2007)
τ_m^*	-	Dimensionless drag bed shear stress acting on mobile sediments according to *Yager et al.* (2007)
τ_s	Nm^{-2}	Skin friction shear stress according to *Canovaro et al.* (2007)
ω	Wm^{-2}	Stream power per unit width
ω_{cr}	Wm^{-2}	Critical stream power per unit width

Chapter 1

Introduction

This chapter introduces the topic of this research project, gives its objectives, and presents the structure of the dissertation.

1.1 Foreword

Recent flood events in Switzerland and across Europe pointed out several deficiencies in hazard assessment, planning, and prediction methods used for flood risk mitigation. A good understanding of the dynamic of these reaches, grounded on a sound physical-based theoretical framework, is primordial both from an environmental and a safety point of view. Intense sediment transport, coupled with erosion and deposition patterns along the streams, increase the hazard in mountainous regions (*Badoux et al.* 2013). Among all the investigations required to understand the alpine watersheds, there is a particular need to improve the knowledge on the physics of sediment transport in steep mountain streams to better predict it. These predictions are essential to assess the hazard related to flows heavily charged with sediments and more specifically to route sediments through river networks, model river incision into bedrock, restore river functionality and habitat, and mitigate debris flows initiated from channel-beds (*Lamb et al.* 2008).

Figure 1.1: Example of mountain river with boulders.

Although mountain rivers (Figure 1.1 and Figure 1.2) control sediment supply to lowland rivers, relatively few studies have been carried out on steep mountain channels, mainly during the last two decades. While these studies provided a multitude of sediment transport equations, generally with similar forms (*Fernandez Luque and van Beek* 1976; *Smart and Jäggi* 1983; *Rickenmann* 1991a; *Recking et al.* 2008a), most of them did not take into account the extreme conditions characterizing alpine torrents. It is known that the wide grain size distribution typical of these streams induces bedload pulses (*Iseya and Ikeda* 1987; *Frey et al.* 2003) and that the presence of large roughness elements has an impact both on flow conditions and sediment transport capacity (*Canovaro et al.* 2007; *Yager et al.* 2007; *Yager et al.* 2012a; *Yager et al.* 2012b).

In this context, this research project investigates the impact of randomly distributed boulders on the sediment transport capacity and bedload fluctuations in steep channels. This is done by means of laboratory experiments, carried out at the Laboratory of Hydraulic Constructions (LCH) at Ecole Polytechnique Fédérale de Lausanne (EPFL).

Further, this chapter contextualizes the research project, formulates the main objectives and describes the structure of the dissertation.

Figure 1.2: Example of mountain river with boulders.

1.2 Context

The 2000 and 2005 flood events in Switzerland and across Europe evidenced the needs for advanced process understanding and prediction of hydrological extremes and complex hazards. The rainfall space-time distribution is often not properly accounted for and its relation to the onset, magnitude and intensity of the triggered hazards is poorly understood. Strong coupling, interaction and feedback mechanisms among the chain of processes that lead a raindrop from the atmosphere to the floodplain are yet to be fully described. Accounting for space and time variability of the physical processes at the appropriate scale and representing the interactions among processes, becomes a key issue for accurate predictions in simulation models. The study of this chain of processes is the goal of the APUNCH (Advanced Process UNderstanding and prediction of hydrological extremes and Complex Hazards) project, financed by the Swiss Competence Center for Environmental Sustainability (CCES) of the Swiss Federal Institutes of Technology Domain (ETH domain). The APUNCH project included five different modules for a total 13 subtasks under the collaboration of 9 research groups of the ETH domain (Figure 1.3; http://www.cces.ethz.ch/projects/hazri/apunch). The present research project is part of the sediment transport task of the APUNCH project.
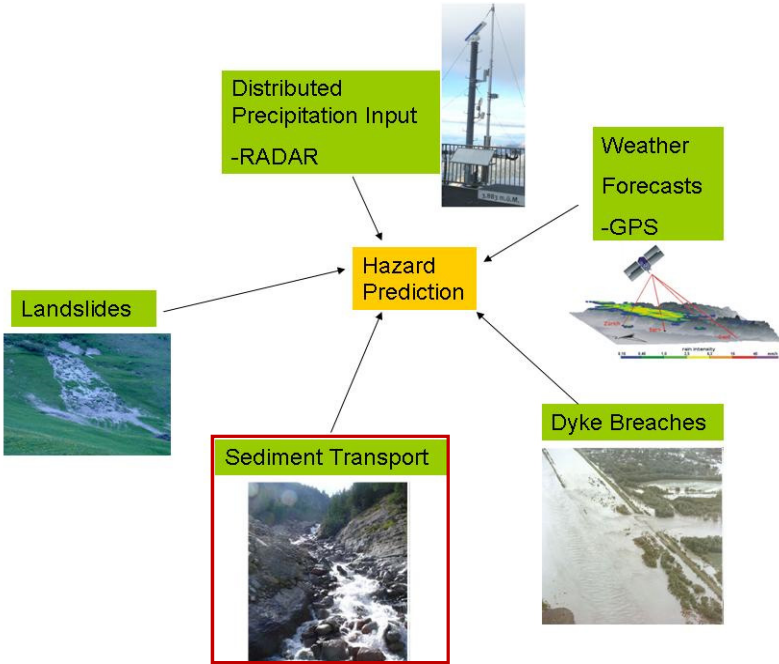
Figure 1.3: Topics of the APUNCH (Advanced Process UNderstanding and prediction of hydrological extremes and Complex Hazards) project of the CCES of the ETH domain, where the present research is highlighted in red.

Furthermore, this research project is jointly financed by the Swiss Federal Office of Energy (SFOE). The goal is to analyze the impact of a small dam break in alpine watersheds. The study is carried out in collaboration with the Environmental Hydraulic Laboratory (LHE) of EPFL. The LHE team studies the wave propagation in the upper reach, just downstream of the dam, and this research applies to the floods occurring downstream sections, with a stationary discharge (Figure 1.4).
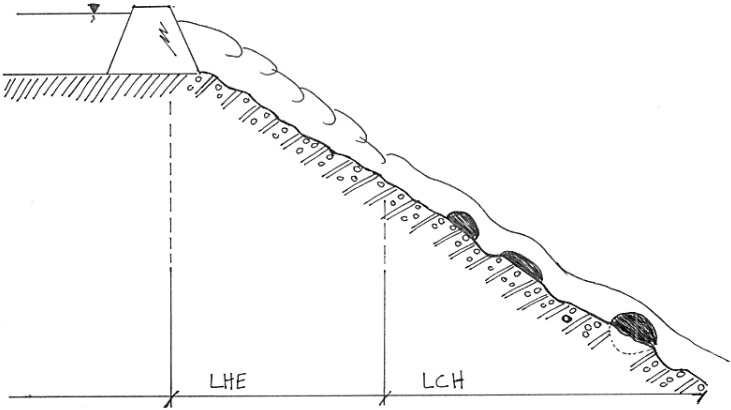
Figure 1.4: Study reaches as defined in the SFOEN project.

1.3 Objectives and methods

A large number of research projects concerning sediment transport were carried out in the past century. However, sediment transport in mountain streams is poorly understood compared to the knowledge existing on lowland rivers. In particular, the presence of large relatively immobile boulders, often encountered in mountain streams and their effect on sediment transport capacity has been studied only by *Yager et al.* (2007; 2012a), by means of an artificial reproduction of a riverbed composed of regularly spaced spheres on a mobile bed of uniform sand.

The present study aims at understanding the influence of macro-roughness elements on the sediment transport. The research was carried out by means of mobile bed laboratory experiments on a flume at the Laboratory of Hydraulic Constructions (LCH) of the Ecole Polytechnique Fédérale de Lausanne (EPFL). A riverbed was reproduced at a geometric scale roughly of 1:15 to 1:30, representing typical alpine rivers, composed of mobile sediments and immobile large scale boulders. The slope was steep and at the upstream section water and solid discharge were introduced continuously.

The influence of boulders is studied as a function of several relevant parameters:

1. Water and sediment discharges (several combinations)

2. Flume slope (three slopes)

3. Size of boulders (three sizes)

4. Spatial density of boulders, defined as the ratio of the average distance between these and their diameter (four densities)

Continuous assessment of sediment transport leaving the channel and variables describing the flow and the bed morphology, allows the investigation of the interaction and mechanisms of feedback among these, namely in what concerns time-varying bedload and average transport capacity.

The object of the present research may be synthesized in three main questions:

1. Is there a link among bedload fluctuations observed in steep channels, flow velocity and morphological parameters?

2. How do boulders influence bedload pulses observed in steep channels?

3. How do boulders influence the sediment transport capacity and the initiation of motion?

1.4 Structure of the report

The present document is divided into 9 chapters (Figure 1.5). Chapters 4, 5, 6, and 7, which contain the main novel theoretical developments of the present research, are written in the form of scientific publications. Those chapters are thus self-contained and are framed by this *Introduction* (Chapter 1), the *Literature review* (Chapter 2), the *Experimental methods* (Chapter 3), some *Further observations on morphology and sediment transport* (Chapter 8) and the *Conclusions and further developments* (Chapter 9).

In this *Introduction* (Chapter 1), details about the framework and

Figure 1.5: Structure of the report.

objectives of the research project are given. The second chapter (Chapter 2) consists in a *Literature review* of several relevant topics needed for the understanding of the observed phenomena, such as the hydraulics of mountain rivers (2.2) and the bedload transport (2.3), which are not covered in such detail in Chapters 5 to 8.

The *Experimental methods* are presented in Chapter 3, where the experimental setup and measurement details are given in section 3.1 and the test parameters and experimental procedure described in section 3.2. Complementary, the details on the velocity measurement system, developed during the present research project, are given independently in Chapter 4: *Bulk velocity measurements by video analysis of dye tracer in a macro-rough channel.*

Chapter 5 analyses in detail the *Bedload fluctuations in a steep channel* observed during one long duration experiment. Fluctuations are analyzed by means of correlation functions and phase analysis, characterizing the cycles of bedload and the link and feedback mechanism between this and flow velocity and bed morphology. Visual observations show that bed states are linked to different sediment transport stages. Several sediment transport capacity formulae were applied to the time varying data and compared with measured sediment transport fluctuations as well.

Chapter 6 investigates *Period and amplitude of bedload pulses in a macro-rough channel* as a function of various measured variables by analyzing a total of 38 tests. A clear link between fluctuation characteristics and the stream power is identified: when the latter increases, the period and amplitude of pulses decrease. The link between bedload fluctuations and morphology is also investigated.

In Chapter 7 the *Sediment transport in steep channels with boulders* is analyzed. The effect of boulder configuration is shown and is taken into account to develop a sediment transport formula. It is clearly shown that the sediment transport capacity decreases with increasing spatial density of boulders.

In Chapter 8 *Further observations on morphology and sediment transport*, not investigated in previous chapters, are given. In particular, this chapter presents a preliminary analysis of the flow hydrograph experiments. Moreover, the influence of the variation of the discharge is analyzed based on two experiments having all other parameters constants. Finally, complementary observations on the bedload pulses phenomena, grain size distributions, and bed morphology are presented.

Chapter 9 gives general *Conclusions and further developments*, answering the questions previously formulated in the objectives of this research, and giving an outlook on further research.

The appendixes provide detailed information about the used boulder configuration (Appendix A) and on each experiment carried out during this research (Appendix B).

In Chapters 4, 5, 6, and 7, the necessary theoretical and experimental framework is given, since they have been submitted in the present form to peer reviewed journals. Therefore, information about methods and laboratory measurements may be repeated along the document. A cover page gives a summary of the contents of each chapter.

References are all given at the end of the manuscript. Tables and figures are numbered incrementally in each chapter and contain the reference to the chapter (i.e. Table 1.9, Figure 3.9). Equations are numbered continuously through the document.

Chapter 2

Literature review

This chapter offers an overview about the main characteristics of mountain rivers and about the main previous developments on the mechanisms of sediment transport in these torrents. First, mountain rivers are described (2.1). Then, hydraulic characterization of these is given (2.2) and finally, fundaments on sediment transport phenomena in steep rivers are presented (2.3).

2.1 Mountain rivers

Although mountain rivers control sediment supply to lowland rivers, only relatively few studies have been carried out on steep mountain channels, and this mainly during the last two decades. These rivers are typically characterized by a stepped longitudinal profile (*Chin and Wohl* 2005; *Comiti et al.* 2009) and channel slopes larger than 4-5% (*Comiti and Mao* 2012). The channel bed is composed of coarse mobile sediments, found generally in the pools or scouring holes downstream of steps, and by large relatively immobile boulders (*Rickenmann* 2001; *Papanicolaou et al.* 2004; *Yager et al.* 2007), that can arrange is steps spanning through the whole channel width (step-pool morphology) or in a more irregular manner (cascade morphology) (*Montgomery and Buffington* 1997).

Steep reaches constitute an important part of the total channel length in mountainous regions, since most sediments reaching the floodplains are mobilized on hillslopes and transit trough high-gradient torrents. Thus, mountain rivers exert significant control on the size, quantity and timing of sediment delivered to lower gradient regions of the watershed (*Yager et al.* 2007). Bedload is the main form of sediment transport in these rivers, since there the mean diameter of grains is relatively large. In this kind of transport, particles are never exclusively carried by the fluid, but slide, roll, and move downstream by small jumps (saltation) (*Yalin* 1977; *Heyman et al.* 2013).

Gravel bed and boulder bed streams (e.g. mountain rivers) are characterized by a wide grain size distribution that is composed of finer, more mobile sediments and large, relatively immobile grains or boulders (*Jäggi* 1995; *Rickenmann* 1997, 2001; *Papanicolaou et al.* 2004; *Yager et al.* 2007). Due to the presence of coarse clasts, the channel-boundary resistance is high (*Wohl* 2000; *Wilcox et al.* 2006). Sediment sources are temporally and spatially variable (*Jäggi* 1995; *Rickenmann* 2001; *Papanicolaou et al.* 2004; *Yager et al.* 2007).

Montgomery and Buffington (1997) identified seven types of reaches in mountainous regions: colluvial, bedrock, and five alluvial channel types. The latter are classified for generally decreasing channel slopes: cascade, step-pool, plane bed, pool riffle, and dune ripple. Cascade and step-pool morphologies (cf. Table 2.1), which occur on the steepest

alluvial channels, are resilient to changes and have high ratios of transport capacity to sediment supply.

Table 2.1: Diagnostic features of step-pool and cascade morphologies (adapted from *Montgomery and Buffington* (1997)).

	Step-pool	Cascade
Typical bed material	Cobble-boulder	Boulder
Bedform pattern	Vertically oscillatory	Random
Dominant roughness elements	Bedforms (steps, pools), grains, banks	Grains, banks
Dominant sediment sources	Fluvial, hillslope, debris flows	Fluvial, hillslope, debris flows
Sediment storage elements	Bedforms	Lee and stoss sides of flow obstructions
Typical confinement	Confined	Confined
Typical pool spacing (channel widths)	1 to 4	< 1

In cascade channels (Figure 2.1a and Figure 2.2a), much of the flow energy is dissipated by tumbling and jet-and-wake interactions around and over individual large clasts (*Montgomery and Buffington* 1997). These types of channels are characterized by longitudinally and laterally disorganized bed materials, generally consisting of boulders (diameter >250 mm, (*D'Agostino et al.* 1994)) and cobbles (diameter ranging between 60 and 250 mm, (*D'Agostino et al.* 1994)). Due to the large particle size, these bed materials are immobile during low return period flows (*Montgomery and Buffington* 1997; *Lenzi et al.* 1999).

In step-pool channels (Figure 2.1b and Figure 2.2b), the large clasts are organized into channel-spanning steps and are separated from pools spacing roughly one to four times the channel width and containing finer material (*Montgomery and Buffington* 1997).
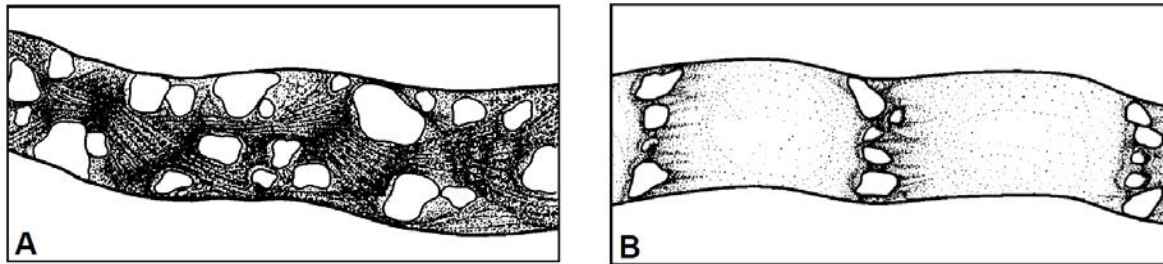
Figure 2.1: Schematic planform illustration of alluvial channel morphologies at low flow: (A) Cascade channel; (B) step-pool channel. From *Montgomery and Buffington* (1997).
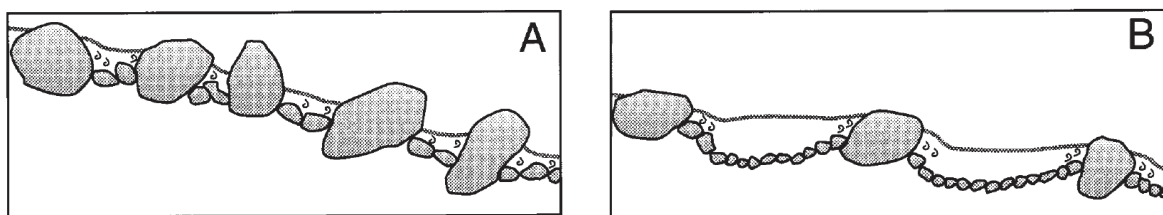
Figure 2.2: Schematic longitudinal profiles of alluvial channel morphologies at low flow: (A) Cascade channel; (B) step-pool channel. From *Montgomery and Buffington* (1997).

As mentioned by *Wohl* (2000) in her book *Mountain rivers*, "*standard hydraulic equations developed for low gradient sand-bed channels do not apply well to mountain channels along which steep gradients and large grain and form roughness promote non-logarithmic velocity profiles, localized critical and supercritical flow, and strongly three-dimensional flow*". The resistance equations commonly used do not estimate accurately the flow velocity and shear stress in torrents, mainly because of the presence of macro-roughness elements such as boulders, large woody debris, and step-pool morphology. The bedload transport equations, generally based on bed shear stress predictions, magnify this error since they assume that sediment transport increases non-linearly with the excess shear stress (*Yager et al.* 2012a).

The channel morphology has high spatial variability, but relatively low temporal variability because only infrequent floods exceed channel-boundary resistance (*Wohl* 2000). It has been shown that in coarse gravel bed torrents, the grain size distribution of the transported bedload approaches that of the bed material only for high flow intensities (*Lenzi et al.* 1999; *Rickenmann* 2001). *Lenzi et al.* (1999) found that in the Rio Cordon, a steep Italian torrent with an average bed slope of 15%, the transported mean grain size approaches that

of the bed material only at about three times the critical discharge of beginning of motion. *Ferro* (1999) pointed out that many Sicilian and Calabrian gravel-bed streams have a bimodal bed particle size distribution, characterized by a fine and a coarse component. In these torrents, the water depth is small compared to the roughness elements. Even during floods, the flow depth can be in the same range as the roughness size (*Bathurst* 1978; *Wiberg and Smith* 1991; *Ferro* 1999; *Bezzola* 2002; *Canovaro et al.* 2007).

For these reasons there is a need to differentiate between highly and rarely mobile grains when analyzing the sediment transport in mountain streams. Many studies investigating the influence of macro-roughness elements, such as boulders (isolated or arranged in steps) and large woody debris, on flow conditions (without sediment supply) have been carried out (*Bathurst* 1978; *Ferro* 1999; *Wilcox et al.* 2006; *Canovaro et al.* 2007), but, to the author knowledge, only a single research work analyses the influence of immobile boulders on bedload in steep flumes (*Yager* 2006; *Yager et al.* 2007). However, in the latter study, sphere size (representing immobile boulders), bed slope and water discharge were kept constant, thus the influence and the sensibility to other numerous parameters still need to be assessed.

2.2 Hydraulics of mountain rivers

2.2.1   Energy dissipation

The energy loss over a given channel reach is caused by the interactions between stream flow and the channel boundaries which dissipate energy as water moves around and over bed and bank irregularities resulting in resistance to the flow (*Wohl* 2000; *David et al.* 2011). This energy dissipation is due to skin friction, to form drag caused by differential pressure around objects (*Ferguson* 2007; *David et al.* 2011), to form induced stresses (*Nikora et al.* 2001) due to the spatial and time intermittency of the turbulent velocity field with the heterogeneous river bed, and to spill resistance. The latter is the energy dissipation from flow acceleration and deceleration, usually over or downstream of steps (*Curran and Wohl* 2003; *David et al.* 2011).

Large roughness elements, such as isolated boulders, clusters of boulders (steps), and woody debris, found in many steep torrents, act as obstacles to the flow. A drag force is exerted on these obstacles when the flow is forced around them. The momentum of the flow is reduced locally and the velocity distribution is modified (*Wiberg and Smith* 1991).

In step-pool rivers, the presence of hydraulic jumps downstream of steps was described by several authors (*Comiti and Lenzi* 2006; *Wilcox and Wohl* 2007; *Endreny et al.* 2011). Hydraulic jumps with breaking waves, as observed downstream of boulders, dissipate a high amount of flow energy, which is proportional to the drop height (*Comiti and Lenzi* 2006). *Curran and Wohl* (2003) state that spill resistance accounts for 90% or more of the total resistance in step-pool channels. The latter resistance is the resistance associated with flow accelerations and decelerations generated at steps in the step-pool streams, where the flow plunges from step to pool.

2.2.2 Flow resistance

All the above mentioned forms of energy dissipation (2.2.1) are generally incorporated into a single resistance coefficient, such as the Darcy-Weisbach f (*Ferguson* 2007):

$$\frac{U}{u^*} = \frac{U}{\sqrt{gR_hS}} = \left(\frac{8}{f}\right)^{1/2} \tag{1}$$

where U is the flow velocity, u^* the shear (or frictional) velocity, a kinematic scale that characterizes shear at the bed and the turbulence levels of the flow and computed as $u^* = (gR_hS)^{1/2}$, g the gravity acceleration, R_h the hydraulic radius, and S the river slope, which is equal to the energy slope when considering uniform flow conditions. A widely used formula for expressing f in rough turbulent flow is:

$$\left(\frac{8}{f}\right)^{1/2} = \frac{U}{u^*} = \frac{2.3}{\kappa}\log\left(\frac{12.2R_h}{k_s}\right) \tag{2}$$

where $\kappa = 0.4$ is the von Kármán coefficient in open channel flows and k_s the Nikuradse's equivalent grain roughness (*Keulegan* 1938; *Wohl* 2000).

A major difficulty in replicating the interaction of flow and sediment in mountain streams is the lack of accurate methods for predicting flow resistance (*Papanicolaou et al.* 2004), which is assertively stated in *Bathurst* (1978): "*The problem of resistance to flow in rivers concerns the prediction of velocity of flow knowing the resistive properties of river channels*". Without reliable estimates of velocity and flow depth, the forces that mobilize sediments are difficult to obtain (*Yager et al.* 2007). Most investigations of the subject concentrated on flows with small-scale roughness, in which the size of the sediment is small compared to the flow depth (*Bathurst* 1978). In this case, conventional methods for predicting flow resistance, which focus on grain (skin) resistance neglecting the effect of form drag and dispersive character of turbulence in the lower layer of the flow, may be applied (*Papanicolaou et al.* 2004). *Bathurst* (1978) states that at relative roughness $k_s/h > 0.3$, the roughness cannot be considered as small scale (skin) roughness anymore. When the relative roughness exceeds this value, the resistance to flow is higher than that estimated by the logarithmic resistance equation for small-scale roughness. *Dubois* (1998) confirms that for the relative submergence of $h/d_{84} \leq 4$ (where d_{84} is a grain size characterizing the bed sediments, for which 84% in weight of the amount of sediments have smaller diameters, and h the flow depth) macro-roughness effects disrupt the free surface and can no longer be neglected. In other words, self similarity of the flow within the trough and crests of the riverbed and scale separation through the vertical does not exist anymore (*Ferreira et al.* 2012). Drag resistance, one of the form-induced moment sinks existing in rough flows, which is created by the localized flow separation and the resulting pressure gradient around the obstacle (high pressure upstream and low pressure downstream), needs to be taken into account when looking at rivers with high relative roughness produced, for example, by large boulders (*Bathurst* 1978; *Canovaro et al.* 2007; *Yager et al.* 2007). *Bathurst* (1978) states that roughness elements can be considered large scale only when the relative roughness exceeds the unit value. For relative roughness ranging from 0.3 to 1, there seems to be a transitional flow regime.

Roughness elements protruding from the channel bed interfere with the flow, causing drag forces that create a local reduction of the flow momentum, modifying the velocity distribution. If the number of macro-roughness elements is sufficiently elevated, the

assumption of a logarithmic velocity profile is no longer valid (*Wiberg and Smith* 1991; *Canovaro et al.* 2007) and the classical expression of flow resistance formulae cannot be applied because that approach requires that the roughness elements on the bed act collectively as one surface, applying a frictional shear on the flow (*Bathurst* 1978).

Dubois (1998) states that, when the depth of water is smaller than the height of the roughness elements, the mean flow velocity remains practically constant. But when water flows over the top of the elements, a small increase of the water height induces a large raise in velocity.

According to *Canovaro et al.* (2007), two regions can be identified in the flow field in presence of macro-roughness elements. A near bed region where the flow velocity is relatively low and constant, and an upper region, in proximity to the water surface, where the flow is characterized by higher velocities, distributed according to a profile which deviates from a logarithmic law (Figure 2.3a) (*Wiberg and Smith* 1991; *Canovaro et al.* 2007). Such observations are not taken into account in most flow resistance formulae, because they are of the logarithmic type (Figure 2.3b), using a single representative roughness scale and admitting that conditions for the existence of a logarithmic layer are verified (*Barenblatt* 1996).

(a)   (b)
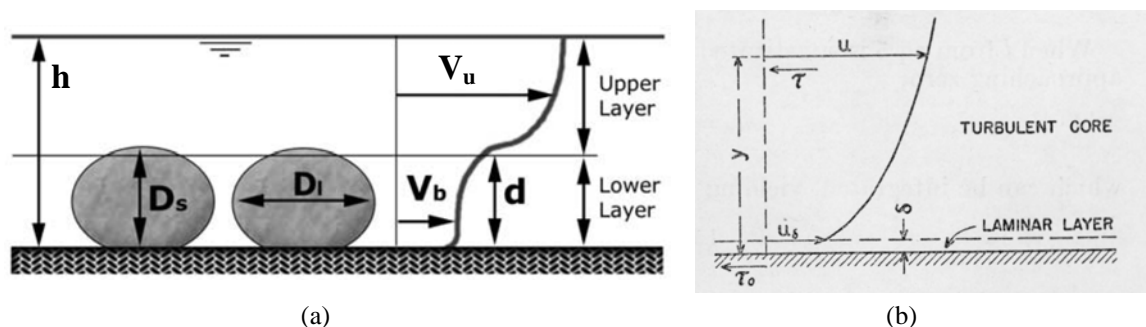
Figure 2.3: (a) Sketch of the flow field in presence of boulders (D_s: short diameter; D_l: long diameter; V_b: lower layer flow velocity; V_u: upper layer flow velocity; d: lower layer thickness) (adapted from *Canovaro et al.* 2007). (b) Velocity profile in presence of small scale roughness elements (from *Keulegan* 1938).

Many authors argued that resistance equations should include the additional effects of channel slope, Froude number, Reynolds number, sediment mobility, channel geometry, and aeration (*Yager et al.* 2007). Some authors (*Bathurst* 1978; *Wiberg and Smith* 1991;

Canovaro et al. 2007; *Yager et al.* 2007) have suggested that in case of macro-scale roughness, the flow velocity profile and therefore the flow resistance are not merely a function of relative submergence, but they also depend on other parameters characterizing roughness geometry, such as spatial density and arrangement of macro-roughness elements.

For example, based on field measurements, *Bathurst* (1978) developed resistance equations depending on relative submergence (defined as R_h/d_{84}), roughness shape, size distribution and spacing, and channel geometry as follows:

$$\begin{cases} \left(\dfrac{8}{f}\right)^{1/2} = \dfrac{U}{\left(gR_hS\right)^{1/2}} = \left(\dfrac{R_h}{0.365d_{84}}\right)^{2.34}\left(\dfrac{w}{h}\right)^{7(j_1-0.08)} \\[4mm] \left(\dfrac{8}{f}\right)^{1/2} = \dfrac{U}{\left(gR_hS\right)^{1/2}} = \left(\dfrac{R_h}{0.748d_{84}}\right)^{5.83}\left(\dfrac{w}{h}\right)^{7(j_2-0.08)} \end{cases} \tag{3}$$

where w is the channel width. $j_1 = \dfrac{\sum_1^n A_{if}}{A_{bed}}$ and $j_2 = \dfrac{\sum_1^n A_i}{A_{bed}}$ are geometry factors depending on the roughness spacing, where A_i is the basal cross-sectional area of large-scale roughness, A_{if} the wetted frontal cross-sectional area of an element, and A_{bed} the total bed area. Field measurements showed that j_1 and j_2 are directly linked.

Field and flume data suggest that flow resistance is inversely related to the spacing between large grains and the degree of particle submergence in the flow (*Bathurst* 1978; *Ferro* 1999; *Yager et al.* 2007).

Dubois (1998) studied the flow on spheres with different spatial densities and found the following resistance equation:

$$\left(\frac{8}{f}\right)^{1/2} = 5.62\log\frac{h^*}{D} + 3.13\,j_2^{-0.613} \tag{4}$$

where D is the sphere diameter and $h^*=h-0.8D$ the corrected water depth for a turbulent flow.

The wall resistance is generally neglected in mountain rivers since, although the channel may be narrow, the resistance contribution is small compared to that caused by plunging flows, steps (clusters of boulders) or isolated roughness (boulders) (*Yager et al.* 2012a).

According to *Einstein and Barbarossa* (1952), the flow resistance can be partitioned into several distinct additive components, such as for example (*Wilcox et al.* 2006):

$$f_{total} = f_{grain} + f_{spill} + f_{debris} \tag{5}$$

where f_{total} is the total flow resistance calculated according to eq. (1), f_{spill} and f_{debris} the components of Darcy-Weisbach friction factor associated with spill over steps (energy dissipation due to acceleration and deceleration) and large woody debris, respectively, and f_{grain} the bed roughness caused by skin friction and form drag on individual grains in the absence of bedforms, calculated according to eq. (2). Other resistance factors could also be introduced in equation (5), such as a form drag around bedforms f_{form}, a form drag acting on boulders f_{drag}.

Wilcox et al. (2006) and *David et al.* (2011) showed that in mountain rivers, the grain resistance is only a small component of the total resistance. It is suggested that interaction effects between different resistance factors invalidate the hypothesis that resistance components can be evaluated independently and then summed to obtain the total channel resistance. *Wilcox et al.* (2006) hypothesized that such interactive effects are grater in step-pool channels than in low-gradient channels. The challenge of quantifying relative contribution of different friction sources is further complicated by the presence of wakes, jets, and standing waves created by roughness elements in steep streams (*David et al.* 2011) and by the skirting effects of the flow around them (*Robert et al.* 1992; *Nelson et al.* 1993; *Baiamonte et al.* 1995; *Buffin-Bélanger and Roy* 1998).

2.2.3   Bed shear stress

The conditions under which sediment movement occurs are commonly defined in terms of bed shear stress, which represents the contact forces per unit area acting on the riverbed.

For turbulent flows under uniform conditions, where mass (gravity) force is balanced exclusively by bed shear force, the total bed shear stress τ_0 (Nm^{-2}) is defined as:

$$\tau_0 = \rho \left(u^*\right)^2 = \rho g R_h S \tag{6}$$

where ρ is the water density. Although barely found in natural rivers, when performing an upscaling approach to river reaches at a sufficiently large scale, the consideration of the uniform flow approximation is assumed valid. Equation (6) may thus be used to represent the actual action upon the bed (*Franca et al.* 2008). Furthermore, this approximation is widely used in field studies and practical applications.

The corresponding dimensionless form of bed shear stress, generally used in the sediment transport formulae, is calculated as follows (*Graf and Altinakar* 2008):

$$\tau_0^* = \frac{\tau_0}{\left(\rho_s - \rho\right) g d_{50}} \tag{7}$$

Bed shear stress is explicitly considered in momentum balance equations as a contact force term and the work by this has a direct repercussion in the energy loss of the flow. Thus a direct link between total bed shear stress and flow resistance exists and is given by (*Graf and Altinakar* 2008):

$$\left(\frac{8}{f}\right)^{1/2} = \frac{U}{u^*} = \frac{U}{\sqrt{\tau_0 / \rho}} \tag{8}$$

The main difficulty in determining bed shear stress ensues from the high spatial and temporal variability of the hydraulic characteristics along mountain rivers. The spatial variability of the bed, caused by grains and bedforms, create important variations of velocity and shear stress across a cross-section or along a reach (*Wohl* 2000).

Large grains or boulders present in steep rivers can endure a significant portion of the total shear stress and thereby reduce the stress available to move the finer sediments between them. Roughness elements protruding from the channel bed interfere with the flow, causing a drag resistance that create a local reduction of the flow momentum, modifying the velocity distribution (*Wiberg and Smith* 1991; *Yager et al.* 2007).

The drag force D_f (N) of an individual object in the flow is given by (*Bathurst* 1978):

$$D_f = \frac{1}{2}\rho U^2 C_D A_{if} \tag{9}$$

where C_D is a drag coefficient, depending on the object shape (*Boillat* 1980). This drag constitutes a momentum sink in the flow which is represented as the so called drag shear stress (τ_d). In the presence of several (*n*) elements within the flow, such as isolated boulders in mountain rivers, and considering them with a similar drag coefficient, drag shear stress acting upon the riverbed is given by (*Bathurst* 1978):

$$\tau_d = \frac{1}{2}\rho U^2 C_D \frac{\sum_1^n A_{if}}{A_{bed}} \tag{10}$$

In order to take into account the presence of large roughness elements, several authors suggested a bed shear stress partitioning method. This partitioning $\tau_0 = \tau' + \tau'' + \dots \tau^n$ is based on the assumption that the total channel roughness and bed shear stress (τ_0) can be decomposed into linearly additive components (τ', τ'', etc.), each characterizing a particular roughness element (*Buffington and Montgomery* 1997). This is the same principle shown in section 2.2.2 for flow resistance terms (eq. (5)), thus care should be taken as well to consider the interaction between the different roughness elements as praised by *Wilcox et al.* (2006) and *David et al.* (2011) for the partitioning of the resistance factor.

Canovaro et al. (2007) applied the same principle as *Bathurst* (1978) used to calculate the drag shear stress related to the macro-roughness elements for a unit surface area. However, they took into account as well the skin friction, caused both by the boulders and the bed material by separating the global shear stress τ_0 into a drag shear stress τ_d, related to the macro-roughness-induced drag force and a joint surface shear stress τ_s, related to the surface-induced friction force from the boulders and from the base material beneath the boulders, typically a mobile fraction.

$$\begin{cases} \tau_0 = \tau_d + \tau_s \\ \tau_0 = \rho g h S \left(1 - \dfrac{2 D_s \Gamma}{3h} \right) \\ \tau_d = \dfrac{1}{2} \rho C_D N_u A_{if} V_b^2 \\ \tau_s = \rho U^2 \left[\dfrac{1 - \Gamma}{C_G^2} + \dfrac{\Gamma}{C_P^2} \right] \\ \Gamma = \dfrac{N_u}{N_u^{max}} \end{cases} \tag{11}$$

where Γ is the spatial density of macro-roughness, defined as the ratio between the number of macro-roughness elements per unit bed area (N_u) to the maximum number of elements that is possible to arrange in the same area (N_u^{max}), D_s is the short boulder diameter (cf. Figure 2.3a). The drag coefficient C_D is assumed to be constant and equal to 1.5. C_G is the Chézy coefficient associated to the bed material beneath the boulders (estimated for $\Gamma=0$) and C_P the Chézy coefficient associated to the boulder skin friction (estimated for $\Gamma=1$). For τ_0, the term inside brackets acts as a reduction factor, in order to exclude the volume fraction occupied by boulders from calculations.

A similar approach for stress partitioning was adopted by *Yager et al.* (2007). The authors analyzed the influence of boulder spatial density on bedload transport for regularly spaced macro-roughness elements. For the stress partitioning, *Yager et al.* (2007) proposed to split the total boundary shear force $\tau_0 A_t$ into a drag force related to the large immobile grains $\tau_I A_i$ and a drag force related to the finer, mobile bed $\tau_m A_m$ (equations (12) and (13)). The skin friction is not taken into account in this stress partitioning.

$$\tau_0 A_t = \tau_I A_i + \tau_m A_m \tag{12}$$

$$\text{with} \begin{cases} \tau_0 = \rho g h S \\ \tau_m = \dfrac{1}{2} \rho C_m U^2 \\ \tau_I = \dfrac{1}{2} \rho C_I U^2 \dfrac{A_{if}}{A_i} \end{cases} \tag{13}$$

where C_m the drag coefficient for mobile sediment, C_I the drag coefficient for immobile grains.

The values of C_I and C_m are assumed to be constant by *Yager et al.* (2007) and *Yager et al.* (2012a), although they may vary with flow conditions and sphere protrusion, spacing, and submergence. Several researchers analyzed the value of C_m in gravel-bed rivers. *Yager et al.* (2012a) proposed a constant value of C_m=0.44, based on data collected by *Marcus et al.* (1992). Working with the same data set, *Scheingross et al.* (2013) proposed a power law to represent the coefficient C_m:

$$C_m = 0.57 \left(R_h / d_{84,mobile} \right)^{-0.96}$$

(14)

C_m may also be calculated using the Variable Power Equation of *Ferguson* (2007), as explained by *Scheingross et al.* (2013):

$$\frac{U}{u^*} = \left(\frac{8}{f} \right)^{1/2} = \frac{a_1 a_2 \left(d / k_s \right)}{\left[a_1^2 + a_2^2 \left(d / k_s \right)^{5/3} \right]^{1/2}}$$

(15)

where a_1=6.5, a_2=2.5, and d/k_s the relative submergence. d is generally the water depth or the hydraulic radius and k_s is generally a grain size representative of the roughness. The above mentioned friction factor is then introduced in the C_m calculation as proposed by *Scheingross et al.* (2013):

$$C_m = 2 \left(\frac{u^*}{U} \right)^2$$

(16)

In the latter approach, later in this text (cf. Chapter 5), it is found that the relative submergence defined as R_h/d_{50}, estimates C_m values closer to those expected, allowing a good estimation of sediment transport. *David et al.* (2011) underlined that the determination of the drag coefficient is one of the major source of errors when calculating drag around objects.

All the mentioned shear stress partitioning studies (*Bathurst* 1978; *Yager* 2006; *Canovaro et al.* 2007; *Yager et al.* 2007), agreed that a partitioning between the surface occupied by

the large-scale roughness and the surface occupied by mobile sediments (small-scale roughness) is necessary. Nevertheless, the authors used different definitions for the surface. For instance, *Bathurst* (1978) and *Canovaro et al.* (2007), used the ratio of cross-sectional area occupied by macro-roughness by total bed area (unit total bed area in Canovaro's study), whereas *Yager et al.* (2007; 2012a) used the ratio of cross-sectional area occupied by macro-roughness by the bed area occupied by immobile grains. Only *Canovaro et al.* (2007) partitioned the stress between drag and skin friction shear stress. *Bathurst* (1978) just took into account the drag shear stress related to large-scale roughness, whereas *Yager et al.* (2007) also used the drag shear stress linked to mobile grains.

As *Lenzi et al.* (2006) underlined, if the roughness increases due to the number of boulders, the form drag will also increase. This implies lower shear stresses available at the bed for sediment entrainment. It is suggested (*Petit et al.* 2005; *Lenzi et al.* 2006; *Yager et al.* 2007; 2012a) that only the part of the total bed shear stress not acting on boulders will induce sediment transport. Hence, the presence of boulders decreases the sediment transport capacity (*Yager et al.* 2007; *Ghilardi and Schleiss* 2011, 2012; *Yager et al.* 2012a). Boulder dimensionless distance λ/D (-) and protrusion P_{av} (m) are proven to be good proxies for sediment transport in mountain streams (*Yager et al.* 2012b).

Figure 2.4: Macro-roughness arrangements: (a) random pattern; (b) transversal stripe pattern; (c) longitudinal stripe pattern (from *Canovaro et al.* 2007).

Canovaro et al. (2007) analyzed the influence of macro-roughness arrangement and spatial density on the flow resistance and velocity profile. Three types of arrangements were used: random pattern, transversal stripe pattern and longitudinal stripe pattern (Figure 2.4). The random pattern refers to an irregular arrangement of macro-roughness elements, which intended to be a representation of the macro-roughness occurring in a steep mountain stream with a cascade morphology.

Transversal stripe pattern represent a step-pool like morphology. Finally the longitudinal stripe pattern do not have any apparent natural counterpart, but was chosen by *Canovaro et al.* (2007) in order to have a more complete understanding of the influence of the arrangement of the obstacles on the flow resistance.

On Figure 2.5a and Figure 2.6a an abrupt increase in total water depth h with Γ at lower spatial densities can be seen for both random and transversal stripes patterns. It becomes asymptotically constant when Γ is approaching 1. Figure 2.5b and Figure 2.6b show a non monotonic trend for the upper layer flow velocity V_u, which changes as a function of Γ: it decreases when Γ is small and then increases when Γ is larger than 0.3 approximately.
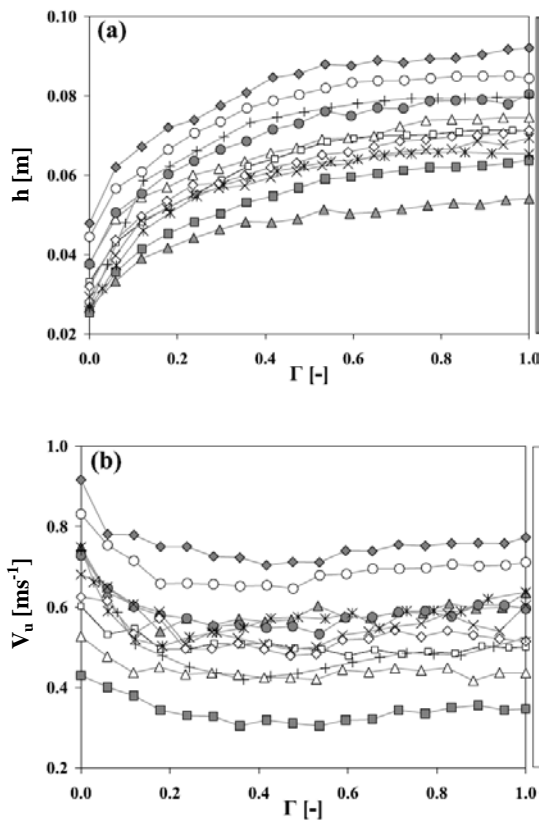
Figure 2.5: Total water depth h (a) and upper layer flow velocity V_u (b) as functions of spatial density (Γ) in case of random pattern (adapted from *Canovaro et al.* 2007).
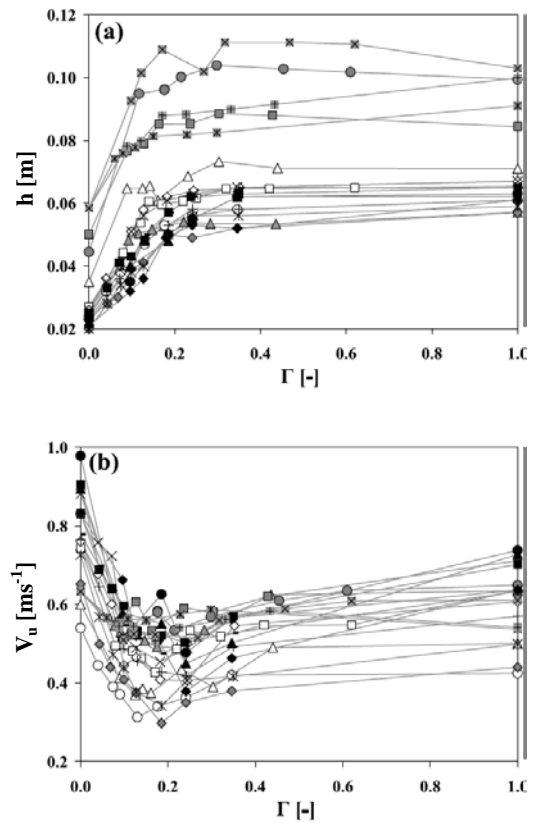
Figure 2.6: Total water depth h (a) and upper layer flow velocity V_u (b) as functions of spatial density (Γ) in case of transversal stripe pattern (adapted from *Canovaro et al.* 2007).

Figure 2.7 shows a comparison among the three patterns studied by *Canovaro et al.* (2007), in terms of shear stress partitioning (eq. (11), Figure 2.7a) and Chezy coefficients (Figure 2.7b). The behavior of random pattern is intermediate between transversal stripe and longitudinal stripe patterns, both in terms of τ_d/τ_0 and *C*. The influence of the different patterns seems to be negligible when the spatial density is low ($\Gamma<0.08$). This may be related to the fact that there is no interference between wakes forming around the individual boulders. Results suggest that transversal stripe pattern, which simulates a step-pool morphology, is the most dissipative arrangement.
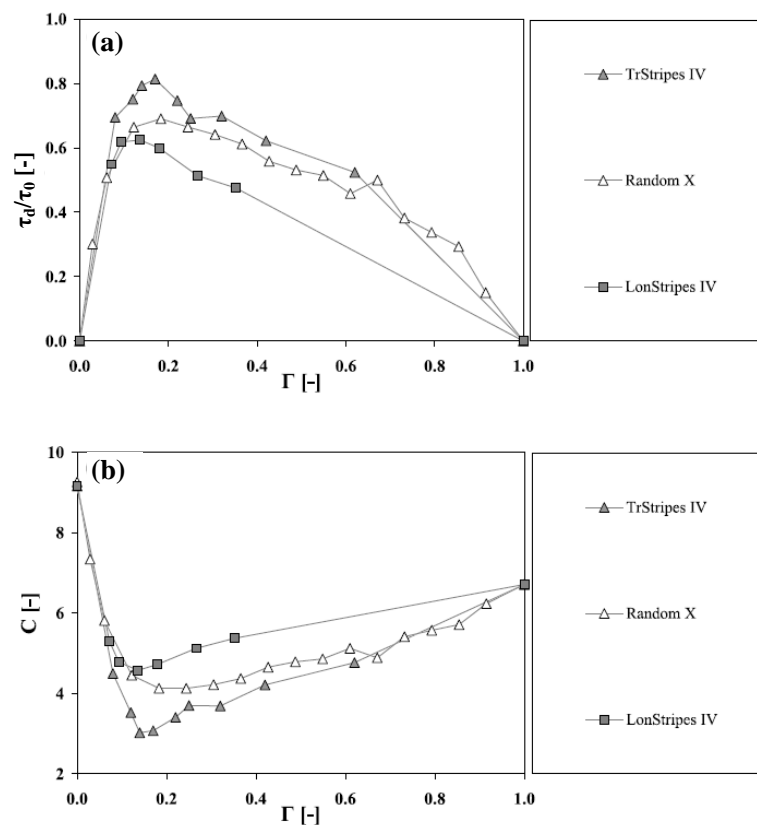
Figure 2.7: Comparison of (a) drag shear stress to total shear stress ratio (τ_d/τ_0), and (b) dimensionless Chézy coefficient (*C*) as a function of spatial density Γ developed by the three pattern employed (adapted form *Canovaro et al.* 2007).

Figure 2.7a shows the ratio between drag shear stress τ_d and total shear stress τ_0 in function of spatial density Γ. The ratio value increases with Γ and reaches a maximum when Γ is in the range of 0.2 to 0.4. The maximum ratio τ_d/τ_0 is higher for transversal stripe (0.9) than

for random pattern (0.7). This indicates that in these spatial density conditions, the drag around the roughness plays a primary role in the development of the flow resistance. With a further increase of Γ the values of τ_d/τ_0 declines until it reaches 0 when $\Gamma=1$: at this point, total shear stress is entirely associated to the skin friction developed on the surface of the macro-roughness. The results suggest that, in the range of $\Gamma=0.2$ to 0.4, step-pool morphology have a higher impact on drag flow resistance than randomly distributed boulders (*Canovaro et al.* 2007). Not surprisingly, Figure 2.7b shows that the average dimensionless Chézy coefficient C presents a minimum value in the same Γ range (0.2 to 0.4) in which the maximum τ_d/τ_0 is found.

Canovaro et al. (2007) pointed out that three different flow conditions occur depending on the spatial density (Γ):

Isolated roughness: for low Γ values (high distance between elements), no wake interaction occurs. Flow resistance is thus proportional to the number of elements. Most authors (*Bathurst* 1978; *Canovaro et al.* 2007; *Yager et al.* 2007) consider solely this type of flow condition in the development of their models, even if this simplification rarely corresponds to reality.

Wake interference: wakes overlap behind each element when they are sufficiently close together. In this case, flow resistance is no longer given by the sum of single effects, because flow separation and recirculation causing vortex shedding and dissipation phenomena of each wake interfere with those of adjacent elements.

Skimming: roughness elements form a more or less smooth continuous bed composed of the element crests and enclosed pockets of dead fluid when elements are closely packed. *Ferro* (1999) suggest that this phenomenon applies for values of spatial density Γ greater than 0.5.

Canovaro et al. (2007) suggest that the minimum of C value depends on the transition from an isolated roughness to a wake interference flow. They also suggest that the channel slope and the flow discharge play a second order role on the relationship between d/D_s, τ_d/τ_0, C and Γ.

In their flume tests, *Yager et al.* (2007) analyzed the effect of isolated macro-roughness spacing and protrusion on bedload (Figure 2.8). The influence of the following parameters was studied: sphere spacing λ, sphere protrusion P^* (adimensionalized as $P^*=((D-z_m)/D)$, where z_m is the height of the mobile sediment deposit). The spheres were placed with a regular distribution in the bed, as shown in Figure 2.8b, and bed slope, discharge, channel width and sphere diameter were kept constant.
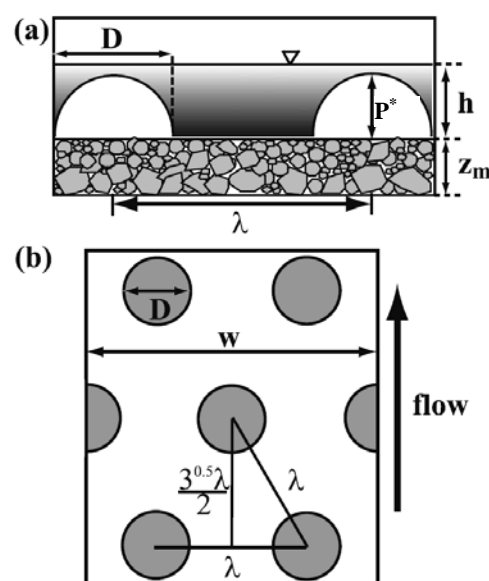
Figure 2.8: Idealized channel with protruding boulders: (a) cross-section, (b) plan view. Modified from *Yager et al.* (2007).

According to *Yager et al.* (2007), for a given λ/D the roughness increases with protrusion. Therefore, for higher protrusions, the mean flow velocities are lower (Figure 2.9a), whereas average flow depth h (Figure 2.9b) and flow depth between the immobile grains h_a (Figure 2.9c) are higher. When protrusion is relatively large or immobile grains dense ($\lambda/D<3$), the stress on mobile sediments is significantly reduced (Figure 2.9e and Figure 2.9f). *Yager et al.* (2007) confirmed that the stress on mobile sediments is more efficiently reduced in the range of $1<\lambda/D<3$. This corresponds well with *Canovaro et al.* (2007) results, for which the most effective range of spatial density Γ is about 0.2 (assuming that for a unity surface the following relationship applies: $\lambda\approx1/N_u^{1/2}$ and for $\lambda/D\approx2$:

$$\Gamma = \frac{N_u}{N_u^{\max}} = \frac{\pi D^2 N_u}{4} = \frac{\pi}{4(\lambda/D)^2} = 0.2$$). According to *Yager et al.* (2007) this range

corresponds to the one naturally observed in steep channels. If the spacing is wider or the immobile grains are more buried, the stress will not be effectively reduced (*Yager et al.* 2007). These general trends were not confirmed with laboratory tests, however, because as for *Smart and Jäggi* (1983), no changes in velocity and flow depth were detectable, probably because of the measurement precision, according to the authors.
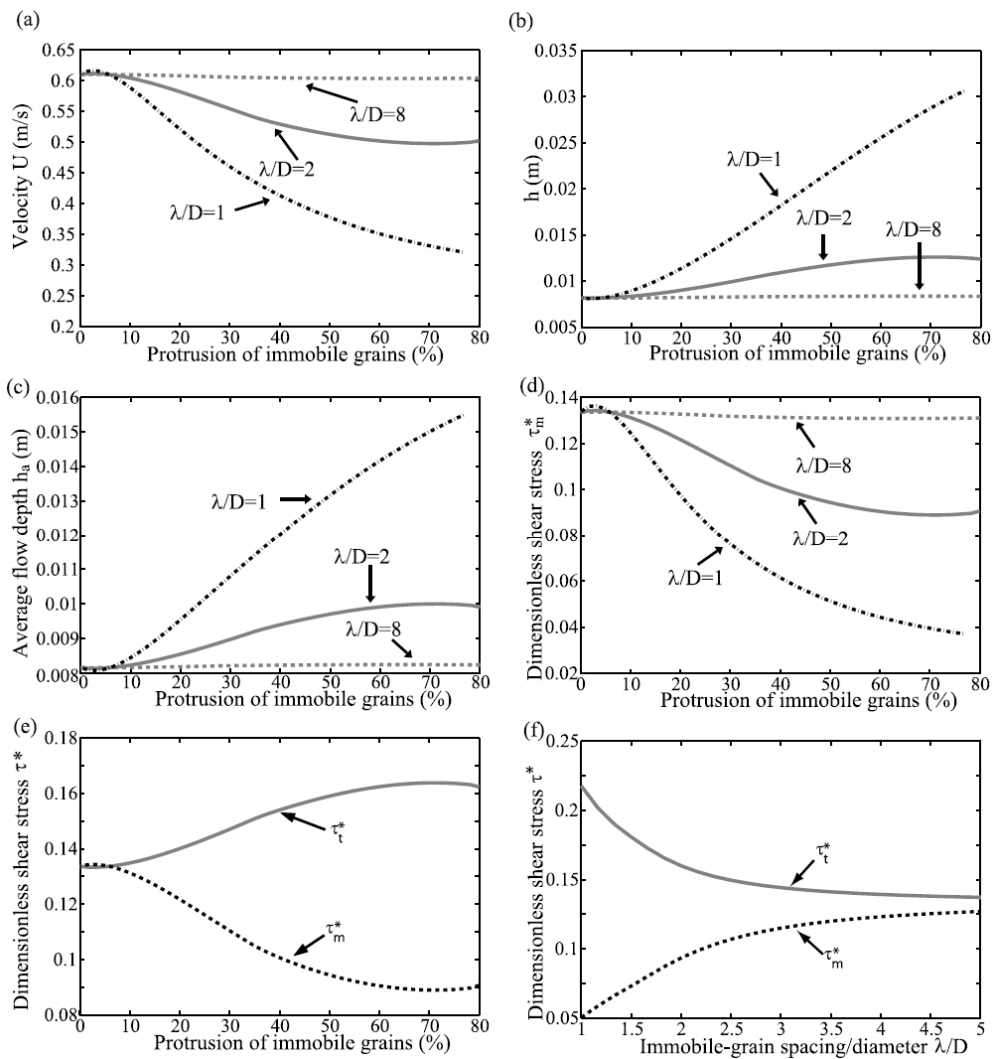
Figure 2.9: Stress-partitioning predictions as a function of the immobile grain protrusion: (a) flow velocity, (b) flow depth between immobile grains, (c) average flow depth, (d) dimensionless drag shear stress on the mobile sediments, and (e) dimensionless total shear stress and drag shear stress on the mobile sediments for

λ/D=2. (f) Variation of the dimensionless stresses (for 50% protrusion) with λ/D. All other parameters are held constant (q=0.0049 m^{3}s^{-1}m^{-1}, S=0.10 (-), C_m=0.047 (-), and C_l=0.4 (-)). In *Yager et al.* (2007).

2.2.4 Stream power

One of the main problems of shear stress calculations is the need of a precise knowledge of the channel hydraulics, which typically has a high local variability in mountain rivers (cf. section 2.1). On the other hand, *Bagnold* (1966) stream power per unit width (17) can be approximated from bulk channel properties, such as width and slope, combined with the discharge of the river, as follows:

$$\omega = \rho g q S = \tau_0 U \qquad (17)$$

where q is the discharge per unit width. This approach is particularly interesting since it avoids the problem of selecting representative cross-sections for hydraulic measurements, which is particularly challenging in steep mountain rivers, presenting a high spatial variability (cf. section 2.1).

The stream power quantifies the rate of loss of energy as water flows downstream, or in other words the power available for performing geomorphic work (*Bagnold* 1966; *Ferguson* 2005; *Petit et al.* 2005; *Parker, C et al.* 2011). *Bagnold* (1966) proposed to quantify bedload as a function of the stream power and suggested that bedload transport rate increases nonlinearly with stream power above a threshold or critical value.

Bagnold (1966) argues that, since the stream power per unit width has the same unit as the bedload transport rate for immersed weight (i_b), there can be no reasonable doubt that the transport rate is related primarily to the available power.

$$i_b = \frac{\rho_s - \rho}{\rho} m_b g U_b \qquad (18)$$

where m_b is the mass of bedload and U_b is the mean transport velocity. i_b is thus expressed in units of work rate per unit bed area, the same unit as the available power identified by means of stream power ω (*Bagnold* 1966; *Parker, C et al.* 2011). *Parker, C et al.* (2011) show that the stream power per unit bed area is most closely correlated with bedload than mean bed shear stress. *Gomez and Church* (1989) underline that, when limited hydraulic

information is available, sediment transport formulae based on stream power should be used.

2.3 Sediment transport in mountain rivers

2.3.1 Characteristics of bedload

The bedload is the part of the total sediment load that is traveling just above the bed level and is transported by intergranular collision rather than by fluid turbulence. The particles roll, slide, and move downstream by saltation (small jumps) (*Yalin* 1977; *Gomez and Church* 1989; *Camenen and Larson* 2005; *Heyman et al.* 2013). Bedload is the main form of sediment transport in mountain rivers, since the grain size distribution is generally coarse. Despite being a key process in mountainous landscape evolution, sediment transport in steep rivers is still poorly understood and largely unpredictable. Most bedload transport formulae overestimate sediment transport up to several orders of magnitude, even when developed on steep flume experiments (*Yager et al.* 2007; *Yager et al.* 2012b; *Heyman et al.* 2013).

Several reasons explain the failure of traditional formulae. For instance, the complexity of the flow in such rivers is generally not taken into account. Large protruding boulders reduce the bedload transport capacity and lead to over-prediction of solid discharge (*Lenzi et al.* 2006; *Yager et al.* 2007; *Yager et al.* 2012b; *Heyman et al.* 2013). Additionally, the presence of graded sediments induces bedload fluctuations, even under constant water and sediment feed. This phenomenon has been observed by several researchers (*Iseya and Ikeda* 1987; *Frey et al.* 2003; *Recking et al.* 2008b; *Recking et al.* 2009; *Heyman et al.* 2013) and seems to be caused by longitudinal and vertical grain sorting, along with bedforms migration and formation/destruction.

When dealing with the wide grain size distribution of mountain rivers, many problems arise as a consequence of relative particle size interaction, as hiding and protrusion effects influencing the initiation of motion (*Lenzi et al.* 2006). Several research were carried out in order to establish whether the grains of the bed show size-selective transport or

equimobility. In the first case, the grains are entrained for the same dimensional value of shear stress that they would have in a well-sorted bed (no hiding/protrusion effects). This means that the dimensionless critical shear stress is the same for all the particles. On the other hand, in case of equimobility, the relative size effects are so extreme that they lead to the same value of dimensional shear stress for all particle sizes, which means that the dimensionless critical shear stress is higher in finer particles because of hiding effects and higher in coarser sediments due to protrusion (*Lenzi et al.* 2006). Situations of bedload transport in between these two extremes (size-selective transport and equimobility) generally exist. Several authors observed that on steep streams a partial transport occurs, during which a portion of the grain size distribution remains immobile (*Lenzi* 2001; *Yager* 2006; *Mao et al.* 2008; *Yager et al.* 2012a).

2.3.2 Bedload transport formulae

In 1966 Bagnold said: "*During the present century innumerable flume experiments have been done, and a multitude of theories have been published in attempts to relate the rate of sediment transport by a stream of water to the strength of the water flow. Nevertheless, as is clear from the literature, no agreement has yet been reached upon the flow quantity (discharge, mean velocity, tractive force, or rate of energy dissipation) to which the sediment transport rate should be related*" (*Bagnold* 1966). This statement is still valid almost 50 years later, and it is particularly true for mountain rivers. As described by *Gomez and Church* (1989), four principal approaches have emerged to design bedload transport formulae, based on bed shear stress (*Fernandez Luque and van Beek* 1976; *Smart* 1984; *Recking et al.* 2008a), stream discharge (*Schoklitsch* 1962; *Rickenmann* 1991b), stream power (*Bagnold* 1966, 1980; *Parker, C et al.* 2011), and stochastic functions for sediment movement (*Einstein* 1950; *Parker, G* 1990).

Most bedload transport formulae have the following form (*Rickenmann* 1997):

$$q_b = \alpha \left(X - X_{cr} \right)^{\beta} S^{\gamma} \tag{19}$$

Where q_b is the bedload transport, which may be expressed in different units depending on the equation ($\mathrm{m^3 s^{-1} m^{-1}}$, $\mathrm{kg s^{-1} m^{-1}}$, or dimensionless, most generally either the first or the latter unit are used), α, β, and γ are generally empirical constants, S is the bed slope, X may be the liquid discharge q per unit width, stream power ω per unit width, or more generally the dimensionless shear stress τ^*, being X_{cr} the corresponding critical value, at which the bedload transport begins. The coefficient α often depends on some grain size diameters and on water ($\rho = 1000\ \mathrm{kg m^{-3}}$) and solid ($\rho_s = 2650\ \mathrm{kg m^{-3}}$) density. The exponent β is often set to 1 (*Schoklitsch* 1962; *Rickenmann* 1990), but can range up to 2-3 (*Fernandez Luque and van Beek* 1976; *Bagnold* 1980; *Wong and Parker* 2006), and γ has been found to vary between 1.5 and 2 (*Meyer-Peter and Müller* 1948; *Schoklitsch* 1962; *Rickenmann* 1990), but could also be nil (*Fernandez Luque and van Beek* 1976; *Wong and Parker* 2006). Other more complex forms of sediment transport formulae exist (*Smart and Jäggi* 1983), but they can often be reduced to the afore-mentioned form.

In Switzerland, one of the most often used bedload formula for steep mountain streams is the Smart-Jäggi formula (*Smart and Jäggi* 1983; *Smart* 1984), which applies to slopes ranging from 0.2 to 20%:

$$q_s = \frac{4}{(\rho_s / \rho - 1)} \left(\frac{d_{90}}{d_{30}} \right)^{0.2} q S^{1.6} \left(1 - \frac{\tau_{cr}^{\ *} \left(\rho_s / \rho - 1 \right) d_m}{hS} \right) \tag{20}$$

where q_s is the volumetric bedload transport per unit width in $\mathrm{m^3 s^{-1} m^{-1}}$, d_{90}, d_{30} and d_m are three characteristic grain size values (where d_x is the grain size diameter for which $x\%$ in weight of the amount of sediments have smaller diameters), $\tau_{cr}^{\ *}$ the dimensionless critical shear stress, assumed to be 0.05. Nevertheless, all the aforementioned formulae do not take into account the presence of large immobile boulders often found in mountain rivers.

The volumetric sediment transport per unit width q_s ($\mathrm{m^3 s^{-1} m^{-1}}$) is then often represented by the following non-dimensional parameter (*Einstein* 1950):

$$q_s^* = \frac{q_s}{\sqrt{(\rho_s / \rho - 1) g d_{50}{}^3}} \tag{21}$$

2.3.3 Critical bed shear stress

Accurate prediction of sediment transport requires the establishment of rigorous criteria to evaluate when the initiation of sediment motion takes place. This concept is based on the experimental work of *Shields* (1936), who showed that the dimensionless shear stress at incipient motion (dimensionless critical shear stress τ_{cr50}^*) varies with particle Reynolds number *Re*, but is roughly constant at a value of $\tau_{cr50}^*=0.045$ for $Re>10^2$, corresponding to a particle diameter of about 3 mm (*Shields* 1936; *Lamb et al.* 2008). Once the dimensionless shear stress acting upon the channel bed sediments exceeds the critical value, initiation of motion happens. The traditional Shields criterion was shown to be inappropriate for mountain stream because of the poorly sorted sediments (hiding effect existing between particles) and the macro-roughness elements. Herein an overview of the wide range of hypothesis concerning the values of critical shear stress in mountain rivers is given, being the dependence on grain sizes (hiding effects) and slope widely recognized (*Buffington and Montgomery* 1997; *Ferro* 1999; *Papanicolaou et al.* 2004; *Lenzi et al.* 2006; *Lamb et al.* 2008; *Recking et al.* 2008a).

Buffington and Montgomery (1997) underlined an apparent lack of a universal τ_{cr50}^* for gravel-bedded rivers. *Ferreira et al.* (2007) developed the concept of competent velocity related to distinct gravel grains. *Buffington and Montgomery* (1997) pointed out that, since gravel-bedded rivers are often armored (surface and subsurface grain size distributions can differ significantly), analysis of incipient motion of gravel-bedded rivers should use surface values of critical shear stress, no matter how well the subsurface grain size distribution correlates with the bedload transport size distribution. The fact that subsurface and bedload transport grain size distribution are often similar indicates that subsurface-based mobility values are appropriate for describing bedload transport beyond incipient motion (*Buffington and Montgomery* 1997). Traditional formulae for the calculation of the critical shear stress often do not consider roughness effects, causing an overestimation of τ_{cr50}^* and introducing a range of scatter that varies with the magnitude of neglected roughness. *Buffington and Montgomery* (1997) state that variation in particle packing and protrusion can result in an order of magnitude range in τ_{cr50}^*, while bed form drag in

natural rivers can comprise 10-75% of the total channel roughness, indicating a similar range of $\tau_{cr50}{}^*$ variation if bed form resistance is not accounted for.

Papanicolaou et al. (2004) suggested the following formulae for determining the critical shear stress:

- $$\tau_{cr50}^* = 0.0851\left(\frac{h}{d_{50}}\right)^{-0.266} \tag{22}$$

    for a uniform grain size distribution and

$$\tau_{cr_{pr}}^* = \tau_{cr50}^* \left(\frac{\overline{d}_{pr}}{d_{50}}\right)^{-m} \tag{23}$$

    for a wide grain size distribution, where h/d_{50} is the relative submergence, $\overline{d}_{pr}$ is the median particle diameter of a fraction with size p and density r, $\tau_{cr50}{}^*$ the dimensionless critical shear stress for the d_{50} sized particles, $\tau_{cr_{pr}}^*$ the dimensionless critical shear stress for the $\overline{d}_{pr}$ fraction. Values of $m<1$ indicate that the finer particles are mobilized at critical shear stresses smaller than those for coarser particles, and vice versa for $m>1$. Papanicolaou recommend to use $m=0.65$. This formula is applicable to streams with a slope range of 0.2% to 9% and a d_{50} of 3 to 44mm.

- $$\tau_{cr50}^* = 0.042\left(10^{2.2S}\right) \tag{24}$$

    for slopes S ranging from 2% to 20%. This equation can be fractionalized as showed in equation (23) and applies for the same range of d_{50}.

Lamb et al. (2008) proposed an empirical equation expressed as a function of channel slope to best fit their field and flume data:

$$\tau_{cr50}^* = 0.15S^{0.25} \tag{25}$$

The authors underline that a reasonable explanation for increasing critical shear stress with slope is the enhanced stream aeration. *Recking et al.* (2008a) advocate a similar form for the critical shear stress, as a function of $S^{0.275}$. *Lamb et al.* (2008) also show that critical shear stress abruptly increases as particles emerge from the flow for channel slopes higher

than 5%. Lamb's model also indicates that turbulent fluctuations highly affect incipient motion. Fluctuations increase the drag and lift forces on the particles, so that mobility is increased (i.e τ_{cr}^* is decreased) for all channel slopes. On the other hand, the magnitude of the turbulent fluctuations are much larger for lower slopes (deeper flows), which results in a significant increase in τ_{cr}^* with increasing channel slopes (*Lamb et al.* 2008).

Ferro (1999) proposes to use the following relationship:

$$\tau_{cr}^* = 0.056 \left[\frac{0.4}{\left(\frac{d_{max}}{1.8 d_{50}} \right)} + 0.6 \right]^2 \tag{26}$$

where d_{max} and d_{50} are the maximum and median diameter. According to this formula, the threshold of particle movement of a non-uniform sediment bed depends on the stability of coarser particles and on their concentration, which affects the values of the characteristic diameters d_{max} and d_{50} of the mixture.

According to *Lenzi et al.* (2006), the critical shear stress for a given grain size fraction of diameter d_i in a wide grain size distribution is influenced by the hiding and protrusion of the particles. There can be a size-selective mobility or an equimobility. They suggest that the mobility of particles sizes, i.e. their Shields parameter τ_{ci}^*, within a non-uniform mixture is largely controlled by relative size d_i with respect to a reference diameter d_x of the bed grain size distribution (mostly d_{50}), following a power law:

$$\tau_{ci}^* = a \left(\frac{d_i}{d_x} \right)^b \tag{27}$$

where the coefficient a corresponds to the dimensionless shear stress for the reference grain size d_x and the exponent b varies from 0 (fully size-selective entrainment) to -1 (complete equimobility conditions).

Lenzi et al. (2006) argue that an intermediate condition between the two extremes is possible. They fitted the following power law to data from Rio Cordon, Italy:

$$\tau_{ci}^* = 0.143\left(\frac{d_i}{d_{50}}\right)^{-0.737} \tag{28}$$

In this river, the authors found dimensionless critical shear stresses of >0.1 and up to 0.3 for finer particles (<0.2 m). For larger clasts the dimensionless critical shear stress drops between 0.07 and 0.03.

2.3.4 Critical stream power

Some sediment transport formulae are based on differences between stream power and critical stream power. Firsts developments, done by Bagnold in the late 1970s (*Bagnold* 1977, 1980), where recently revisited by other authors (*Ferguson* 2005; *Petit et al.* 2005 ; *Parker, C et al.* 2011). *Gomez and Church* (1989) show that the stream power has a clearer correlation with sediment transport than bed shear stress or discharge. Nevertheless, most formula do not predict sediment transport consistently well.

Bagnold (1980) proposed the following formula for ω_{cr} critical stream power estimation:

$$\omega_{cr} = 290 d_x^{3/2} \log\left(\frac{12h}{d_x}\right) \tag{29}$$

where d_x denotes a characteristic diameter of the mobilized particles. This equation gives ω_{cr} values in $\mathrm{kgm^{-1}s^{-1}}$, thus not the same unit as stream power defined earlier in this document (cf. section 2.2.4). As specified by *Ferguson* (2005), this is due to the fact that *Bagnold* (1980) omitted the gravity g in the stream power formula used in this paper. It must also be noted that in order to define the critical stream power according to equation (29), knowledge of flow conditions (water depth) are needed, thus counteracting the ease of use of the stream power where only information about reach averaged gross values (q, S) is needed.

Several following studies analyzed the critical stream power values. According to *Petit et al.* (2005), the critical stream power depends on bedform resistance. They showed that on steep streams, with high bedform resistance, critical specific stream power is high.

On the other hand, *Ferguson* (2005) argues against Petit suggestion, by showing that stream power is unaffected by bedform resistance because $\omega_{cr}=\tau_{cr}U_{cr}$, where τ_{cr} is the critical shear stress and U_{cr} an associated flow velocity, is invariant. *Ferguson* (2005) states that, even in presence of form resistance, both actual stream power and critical stream power depend only on gross channel properties and not on the within-channel flow details.

Ferguson (2005) indicates that hiding effects should be taken into account in critical stream power estimation. The author proposes two formulae, based on a logarithmic flow resistance equation and on the Manning-Strickler relation, respectively:

$$\begin{cases} \omega_{cr,i} = \dfrac{2.30}{\kappa} \rho \left(\tau_{cr}^{*} \dfrac{\rho_s - \rho}{\rho} g d_b \right)^{3/2} \log \left(\dfrac{30\tau_{cr}^{*} \dfrac{\rho_s - \rho}{\rho}}{eoS} \left(\dfrac{d_i}{d_b} \right)^{1-b} \right) \left(\dfrac{d_i}{d_b} \right)^{3(1-b)/2} \\ \\ \omega_{cr,i} = a\rho \left(\tau_{cr}^{*} \dfrac{\rho_s - \rho}{\rho} g d_b \right)^{3/2} \left(\dfrac{\tau_{cr}^{*} \dfrac{\rho_s - \rho}{\rho}}{S} \right)^{1/6} \left(\dfrac{d_i}{d_b} \right)^{5(1-b)/3} \end{cases} \tag{30}$$

where d_b is a representative bed diameter and d_i a given absolute grain diameter. o is a grain sorting parameter (for $o=1$ grains are well sorted, for $o>10$ grains are poorly sorted). b is a hiding factor which takes values between 0 and 1 (for $b=0$ no hiding and protrusion effects are observed, for $b=1$ the equal mobility of different grain sizes is reached (*Parker, G et al.* 1982). b is assumed equal to 0.6 by *Ferguson* (2005). a is a constant, found to correspond to a value either of 6.7 or 8.2 (*Ferguson* 2005). An assumption regarding the τ_{cr}^{*} is needed. Ferguson's approach implies the calculation of a critical stream power for every grain size. Furthermore, these equations predict lower critical stream power at higher slopes, going in the opposite direction of what is foreseen by *Petit et al.* (2005).

Parker, C et al. (2011) argued that the critical stream power is less variable with slope than the critical mean bed shear stress. Additionally, they showed that, as suggested by *Petit et al.* (2005) and contrary to *Ferguson* (2005) theory, the critical stream power indeed increases with bed slope.

2.3.5 Critical discharge

Several sediment transport formulae are based on excess unit discharge (q-q_{cr}, where q_{cr} is the critical discharge per unit width) calculations (*Meyer-Peter and Müller* 1948; *Schoklitsch* 1962; *Rickenmann* 1990). The dimensional critical discharge has widely been found to be inversely correlated to the channel slope (*Schoklitsch* 1962; *Bathurst* 1987; *Rickenmann* 1990; *Ferguson* 1994) and dependent on the grain size distribution.

Rickenmann (1991b) proposes the following equation for critical discharge per unit width, in units of ($m^3s^{-1}m^{-1}$):

$$q_{cr} = 0.065 \left(\frac{\rho_s}{\rho} - 1 \right)^{1.67} g^{0.5} d_{50}{}^{1.5} S^{-1.12} \tag{31}$$

Ferguson (1994) and *Schoklitsch* (1962) give similar formulae, with slightly different coefficients, for critical discharge at incipient motion.

2.3.6 Bedload formulae considering boulders

As for the flow conditions (section 2.2), sediment transport formulae require adaptation to take into account the stress borne by relatively immobile grains (*Yager et al.* 2007). Moreover, in mountain rivers it seems necessary to distinguish between highly and rarely mobile grains (two grain size distributions) and to account for the limited availability of sediments, since the area occupied by the relatively immobile grains does not contribute to sediment supply.

Bed coverage and immobile-grain protrusion may influence the sediment availability in steep rough streams. When the sediment supply increases, the proportion of bed covered by gravel increases too and the sphere protrusion decreases, for a given sphere spacing. In fact, the immobile-grain diameter and spacing are relatively static on an annual basis, while the protrusion should vary in time, depending on the supply of mobile sediments (*Yager et al.* 2007).

After calculating shear stress as shown in section 2.2.3, equation (13), *Yager et al.* (2007) suggest to adimensionalize the shear stress on mobile grains using the median grain size of

the mobile fraction (d_{50m}) instead of the median grain size of the whole grain size distribution, which would include the immobile grains as well. The dimensionless critical shear stress is also calculated separately for the mobile grains, being the formulae as follows (*Yager et al.* 2007):

$$\begin{cases} \tau_{m,cr}^* = \dfrac{\tau_{m,cr}}{(\rho_s - \rho) g d_{50m}} \\[2mm] \tau_m^* = \dfrac{\tau_m}{(\rho_s - \rho) g d_{50m}} \end{cases} \tag{32}$$

where $\tau_{m,cr}^*$ and $\tau_{m,cr}$ are the dimensionless critical and critical shear stresses of mobile sediments, and τ_m^* is the dimensionless stress acting upon the mobile sediment.

The dimensionless critical shear stress is assumed to be equal to 0.045 according Shields, even though it has been demonstrated that this value is not appropriated for steep rough channels with a wide grain size distribution (*Buffington and Montgomery* 1997; *Lenzi et al.* 2006). These dimensionless parameters are used in the bedload formulae adapted by *Yager et al.* (2007) to take into account the stress borne by rarely mobile grains. According to several authors (*Petit et al.* 2005; *Lenzi et al.* 2006; *Yager et al.* 2007; 2012a) only the shear stress acting on mobile sediments (τ_m^* in *Yager et al.* (2007)) contributes to sediment transport.

Considering the limited availability of mobile sediment, *Yager et al.* (2007) suggests to scale the predicted transport rate by the proportion of the bed area that is occupied by the mobile fraction: A_m/A_t, where A_m in the bed area occupied by the mobile fraction and A_t is the total bed area, which is a function of immobile grains spacing (λ).

For example, the transport equation from *Fernandez Luque and van Beek* (1976) (FLvB), is modified as follow by *Yager et al.* (2007):

$$q_s^* = 5.7 \left(\tau^* - \tau_{cr}^* \right)^{1.5} \qquad \text{(FLvB original form)} \tag{33}$$

$$q_{sm}^* = 5.7 \left(\tau_m^* - \tau_{m,cr}^* \right)^{1.5} \frac{A_m}{A_t} \qquad \text{(FLvB modified by *Yager et al.* (2007))} \tag{34}$$

where q_s^* is the dimensionless sediment transport and q_{sm}^* is the dimensionless sediment transport rate of the mobile sediments, accounting for the limited area of the bed occupied by the mobile fraction.

Figure 2.10a shows that the protrusion effect is not significant when grains are widely spaced, but it becomes important when $\lambda/D>2$. Figure 2.10b illustrates the effect of boulder spacing on sediment transport when using the equations modified by *Yager et al.* (2007). When $\lambda/D<2$ the sediment transport rates predicted by the modified equation is at least one order of magnitude lower than when boulders are not present.
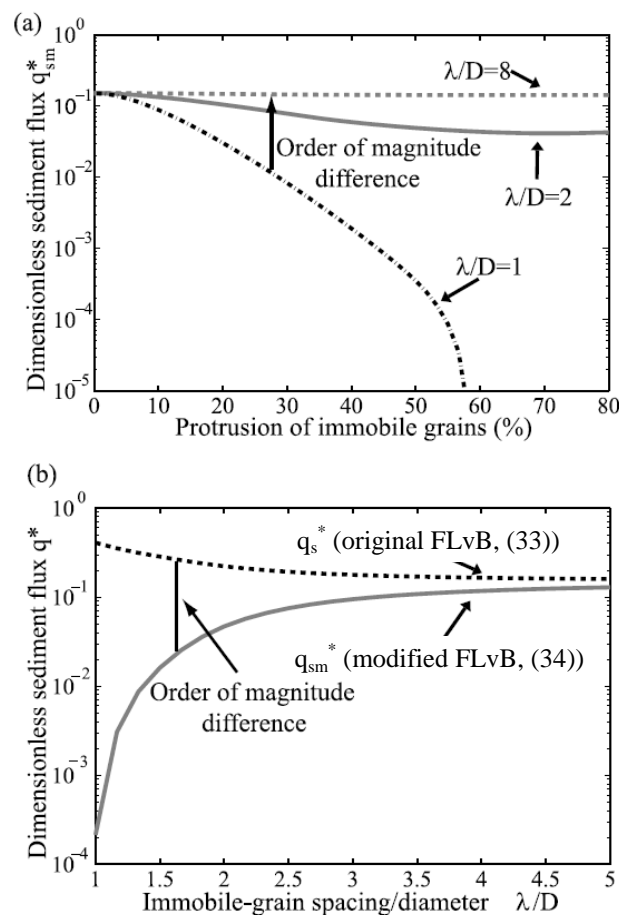
Figure 2.10: (a) Calculated dimensionless transport rates with the modified *Fernandez Luque and van Beek* (1976) (FLvB) equation as a function of immobile grain protrusion for a range of λ/D. (b) Dimensionless sediment fluxes as a function of λ/D, for a 50% protrusion. In *Yager et al.* (2007).

Yager et al. (2007) showed that most sediment transport equations perform better in steep channels when modified to account for the effects of the large, relatively immobile grains,

and the limited availability of the mobile sediments. They showed that a modified transport equation predicts sediment fluxes generally within an order of magnitude, with a persisting general overestimation of bedload. They suggested that sediment transport equations that use flow velocity may predict sediment flux better than sediment transport equations that use the flow depth or hydraulic radius. This statement needs to be used carefully since *Canovaro et al.* (2007) showed that near-bed flow velocity, which is the more relevant for sediment entrainment, may be considerably different from the mean flow velocity in rivers with boulders (cf. section 2.2.2).

The above presented method to take into account the presence of boulders (*Yager et al.* 2007) in applicable to a bed with isolated roughness elements. However, the hiding effect and selective transport caused by the graded mobile sediment is not taken into account, since the equation assumes that all of the mobile grain sizes move at the same critical bed shear stress.

Several authors (*Parker, G* 1990; *Lenzi et al.* 2006; *Yager* 2006) argued that in steep streams with large grain size distribution, a size-selective transport may happen. Finer grains may move at lower bed shear stresses than coarser grains. Sediment transport equations can predict the sediment flux quite precisely in steep channels only when all grain sizes mobilize during large floods, but they perform rather poorly under typical and more frequent transport conditions, when larger grains are immobile (*Lenzi et al.* 1999; *Yager* 2006). Thus, further developments are needed in order to take into account the size-selective transport and the hiding effect linked to the large grain size distribution existing in mountain streams. *Yager* (2006) and later *Yager et al.* (2012a) attempted to include a selective transport over clusters of boulders (steps) in bedload transport formulae.

The selective transport is taken into account in the *Parker, G* (1990) formula. *Yager et al.* (2012a) modified this formula to account for clusters of boulders. In *Parker, G* (1990), a hiding function is calculated for each sediment fraction. The volumetric transport rate per unit width for each grain size in the relatively mobile sediments can be calculated. The total transport rate of all grain sizes is given by the sum of each fraction. A similar approach was already proposed by *Einstein* (1950). *Yager et al.* (2012a) proposed to apply

Parker's formula only for the mobile fraction and to scale the total transport rate to take into account the fraction of the surface occupied by mobile sediments.

Yager (2006) and *Yager et al.* (2012a) applied the modified *Fernandez Luque and van Beek* (1976) (FLvB) and the modified *Parker, G* (1990) formulae to field data obtained from the Erlenbach river (Switzerland). The original hiding functions used by Parker are replaced with those calibrated on this river. The original FLvB formula systematically over-predicted sediment volumes of several orders of magnitude (Figure 2.11a), while the original Parker equation over-predicted sediment volumes for 98% of the measurements. Nevertheless predictions were within an order of magnitude for 42% of the measurements (Figure 2.11b). This better performance results from the fact that Parker equation takes into account the size-selective transport of sediments. The modified FLvB equation predicted sediment volume within an order of magnitude for 51% of the data (Figure 2.11c). This equation, which takes into account the limited sediment availability and the stress borne by immobile grains, performed better than the original Parker equation. Thus, in steep streams, the size-selective transport could be equally important as the effects of limited availability of sediment and the stress borne by the immobile grains. The modified Parker equation, that accounts for all of these aspects, predicted the sediment volume to within an order of magnitude (higher and lower values) of the measured values for 69% of the measurements (Figure 2.11d).
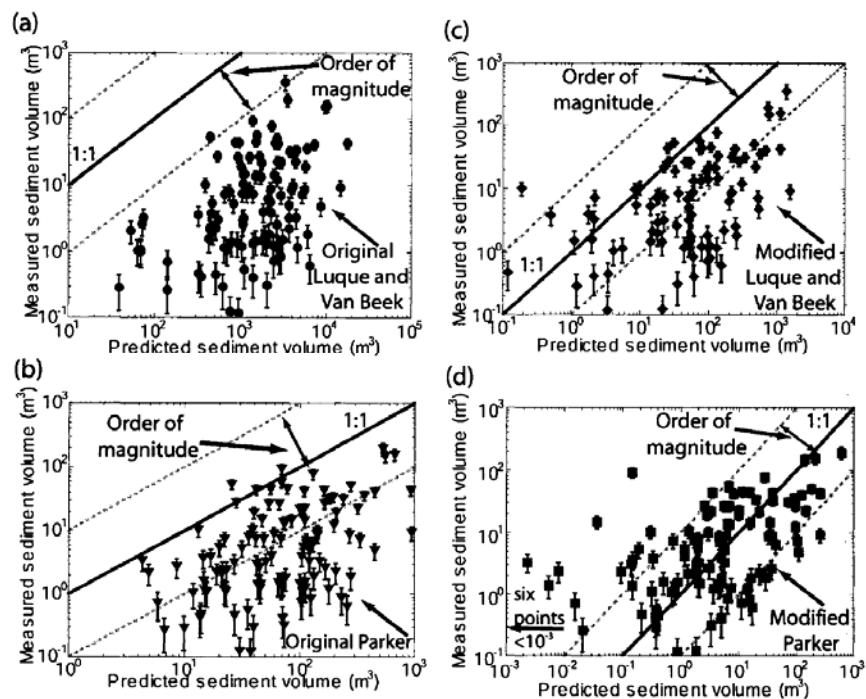
Figure 2.11: Measured and predicted sediment volumes for 117 sediment transport events in the Erlenbach river (Switzerland) for: a) the original *Fernandez Luque and van Beek* (1976) equation; b) the original *Parker, G* (1990) equation; c) the modified FLvB equation; d) the modified Parker equation (d). In *Yager* (2006).

2.3.7 Bedload fluctuations

Field measurements of sediment transport in mountain rivers have shown that this is not a direct function of hydraulic parameters and hysteretic behaviors were observed (*Rickenmann* 1994; *Gintz et al.* 1996; *Heyman et al.* 2013). Furthermore, the presence of a wide grain size distribution in mountain rivers has an impact on bedload. In the last decades, several researchers studied this phenomenon in experimental flumes (*Iseya and Ikeda* 1987; *Frey et al.* 2003; *Recking* 2006; *Bacchi et al.* 2009). According to *Iseya and Ikeda* (1987), two main factors cause sediment transport to fluctuate, namely migration of bedforms and segregation of the surface grain size, often expressed through the development of an armor layer. They showed that a longitudinal sediment sorting occurs when a wide grain size distribution is constantly fed into a flume, this segregation producing rhythmic fluctuations in the bedload transport rate. Sediment particles

availability in sand and gravel mixtures, induced by longitudinal sediment sorting, determines the magnitude of sediment transport rate and its pulses. According to *Iseya and Ikeda* (1987), fluctuations in sediment transport rates are immediately visible when the gravel represents the majority of the gravel-sand mixture.

Iseya and Ikeda (1987) identified two main bed states (smooth and congested), and a transitional state between these two (Figure 2.12). These three types of bed states were observed in sequences (longitudinal sediment sorting) when the bed materials were sufficiently graded (between almost all gravel and almost all sand).
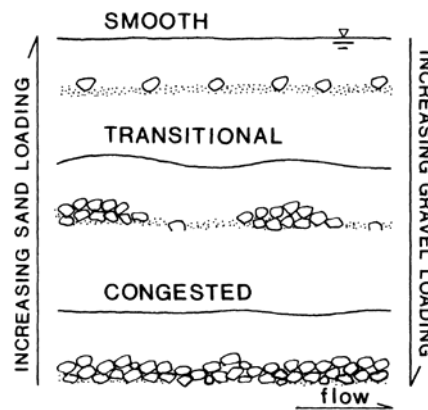
Figure 2.12: Schematic illustration of the bed states identified by *Iseya and Ikeda* (1987) (from *Iseya and Ikeda* 1987).

The length of each bed state section was observed to vary with the ratio representing the mixing of sand and gravel materials. They observed a varying grain size distribution at the outlet, depending on the bed state at the downstream end of the flume. When the bed was congested, a minimum amount of gravel was moving, and almost no sand was transported, implying a minimum value of sediment transport. On the contrary, for smooth beds, the amount of moved gravel increased and the sand discharge was large only in this bed state, implying a maximum value of sediment transport. The slope of the congested bed was observed to be steeper than that of the smooth bed (*Iseya and Ikeda* 1987; *Bacchi et al.* 2009; *Recking et al.* 2009). This is due to the fact that steeper slopes are needed in order to move coarser particles (*Iseya and Ikeda* 1987). *Iseya and Ikeda* (1987) also identified a vertical grain sorting in their experiments, with a surface layer that may be at most twice or three as thick as a gravel diameter.

Frey et al. (2003) confirmed that fluctuating sediment discharge and grain size distribution are highly dependent. At the outlet of an experimental flume they observed that high solid discharges carried mainly fine grains, whereas the sediments were coarser during low solid discharge events. They also visually observed that a bed-armoring process was associated with transient antidune-like structures. These bedforms increased bed resistance and thus decreased solid discharge. The armoring layer was eventually destroyed, leaving a finer bed in place with practically no bedforms, the largest outgoing sediment discharges being observed at this moment. The cyclic change in bedforms and thus grain size distribution starts once again with the formation of the armoring layer.

Recking et al. (2008b; 2009) carried out tests with a uniform and a wide grain size distribution, on the same laboratory setup, and noticed that bedload fluctuations were not observed in setups with uniform grain size distributions, confirming that fluctuations are a consequence of grain sorting in graded sediments. *Recking et al.* (2009) and *Kuhnle and Southard* (1988) suggested that peak solid discharges are caused by the formation and migration of bedload sheets, which are highly mobile (fine sediments) and low-relief bed forms. This phenomenon is accentuated in low flow conditions (small discharge) and is associated with fluctuations on bed slopes, bed load and bed state (*Recking et al.* 2009). *Recking et al.* (2009) observed that bed aggradation is associated with reduced mobility for all the diameters and with a longitudinal and vertical grain sorting, resulting in a coarsening of the bed surface and fining of the subsurface. Fluctuations in bed slope occurred and were shown to be linked to bed states changing (fining and paving). The local slope downstream of regions of aggradation was observed to increase to a maximum value, followed by an abrupt increase of gravel mobility. Coarse sediments are mobilized, and fine sediments previously hidden under surface layer are transported, generating bedload sheets. This increased mobility of all grain sizes destroys the pavement downstream, causing a peak in sediment transport. The erosion of the bed stops when aggradation starts again from the flume upstream section. *Recking et al.* (2009) observed that the bedload sheets are ephemeral and progressively disappearing by interacting with the coarse bed during their migration. The aggradation phenomenon occurs over a longer period than the degradation phenomenon (*Kuhnle and Southard* 1988; *Recking et al.* 2009). *Recking et al.*

(2009) give the following description of the different bed states and phenomena causing bedload pulses in steep rivers with a wide grain size distribution (Figure 2.13).
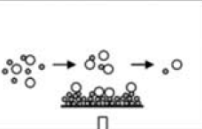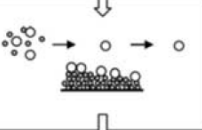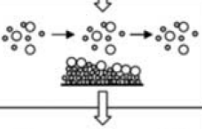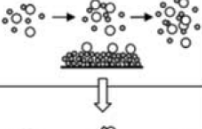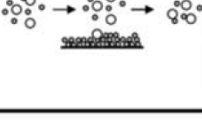
Observed periodical bed state		Consequences on transport	Energy conservation
	Aggradation with reduced gravel mobility. Longitudinal and vertical grain sorting produce progressive bed subsurface fining.	Injected sediments are stored in the bed and the outlet solid discharge is low.	Low efficiency e. Slope increase until $S=S_M$ verifying $eS_M=\varphi(q_s, q)$
	Congested bed (some runs develop a pavement): transport of coarse gravels, finer gravels being quickly stored in the bed	Outlet solid discharge is minimum and similar to expected value with transport of a uniform sediment mixture.	The gravel transport rate efficiency is minimum e_m: $e_m S < \varphi(q_s, q)$
	Aggradation is not infinite and stops when the new energy slope S_M allows transporting injected sediments	$q_{s(in)}=q_{s(out)}$, presence of fine sediments in the bedload layer increases the coarse gravel mobility.	$e_m S_M = \varphi(q_s, q)$ but abrupt transport rate efficiency increase to $e_M \gg e_m$.
	Increased gravel mobility and strong local erosion producing a **bedload sheet**.	Peak solid discharge associated with bedload sheet migration.	$e_M S_M \gg \varphi(q_s, q)$. S decreases until $e_M S = \varphi(q_s, q)$ is verified
	Gravel mobility is reduced abruptly when a minimum slope S_m is attained. In some runs antidune waves contribute to reducing this mobility.	Cells of immobile coarse gravels stop the finer gravel transport. The outlet solid discharge decreases abruptly. Aggradation starts again.	Abrupt transport rate efficiency decrease $e \ll e_M$, $eS_m \ll \varphi(q_s, q)$. New slope increase.

Figure 2.13: Sketch of periodical bedload sheet production (from *Recking et al.* (2009)).

To the author knowledge, the impact of macro-roughness elements, such as large immobile boulders, on bedload fluctuations has never been studied. These elements disrupt the flow and boulder exposure decreases the shear stress available for sediment transport (cf. *Lenzi et al.* 2006; *Yager et al.* 2007). It can however be inferred that these roughness elements do not cause bedload fluctuations, since *Yager et al.* (2007) used a uniform grain size distribution for their tests and did not observe any bedload pulses.

2.4 Summary

The influence of boulders on flow conditions has been fairly well studied in the past, compared to sediment transport studies (cf. section 2.2, *Bathurst* 1978; *Dubois* 1998; *Canovaro et al.* 2007; *Yager et al.* 2007). According to *Canovaro et al.* (2007) the bed shear stress endured by boulders is maximum and the Chézy coefficient is minimum for a

dimensionless distance between boulders of $\lambda/D=2$. The authors suggest that this distance corresponds to the transition from isolated roughness elements to a wake interference flow. The influence of large roughness elements on sediment transport capacity has been only poorly studied yet (*Yager et al.* 2007; *Yager et al.* 2012a). *Yager et al.* (2012a) suggest that boulder protrusion is a good proxy for sediment transport in mountain rivers. Moreover, several authors (*Petit et al.* 2005; *Lenzi et al.* 2006; *Yager et al.* 2007; 2012a) argue that only the bed shear stress acting on mobile sediments contributes to bedload transport. Nonetheless, no other research analyzing the effect of varying boulder diameter and distances on sediment transport capacity could be found in the literature. Other studies showed that stream power and discharge give better results of sediment transport estimates in the absence of large roughness elements (*Gomez and Church* 1989; *Rickenmann* 1991b; *Parker, C et al.* 2011). However, to the author knowledge, no study regarding the influence of roughness geometry, on the critical discharge nor on the critical stream power have yet been carried out. The presence of a wide grain size distribution in mountain rivers has been proved to be responsible for bedload fluctuations, even under constant water and sediment feed (*Iseya and Ikeda* 1987; *Recking et al.* 2009), nevertheless the influence of boulders on these fluctuations has never been analyzed.

Chapter 3

Experimental methods

To assess the impact of boulders on sediment transport capacity of mountain rivers, systematic laboratory experiments were carried out on a laboratory tilting flume.

Experiments were performed with different flume slopes S, boulder diameters D and dimensionless boulder distances λ/D, for multiple couples of liquid and solid discharges constantly fed upstream of the channel.

In chapter 3.1 the experimental setup and the instrumentation for the measurements are described. Chapter 3.2 presents the test parameters and the experimental procedure.

3.1 Experimental setup

3.1.1   Global description

The present research is based on mobile bed laboratory experiments (Figure 3.1) carried out on an 8 m long and 0.5 m wide tilting flume. Water and sediment are fed constantly at the flume inlet. The influence of varying configurations of randomly placed boulders (couples of boulder diameter and density) on sediment transport capacity is studied for three different steep channel slopes. The sediment supply ($q_{s,in}$) and the boulder configuration are defined previously to the experiment. Water discharge is adapted so that boulders are visible most of the time.
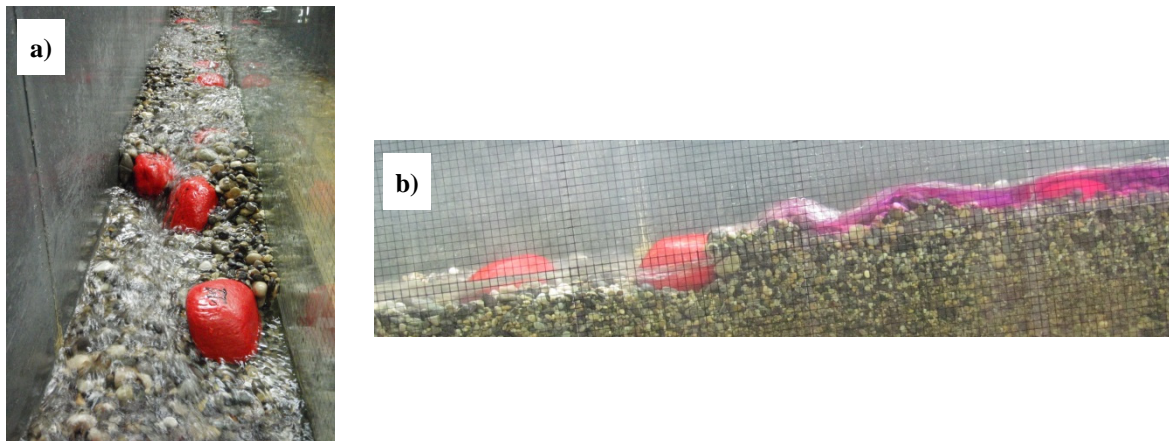
Figure 3.1: View of the flume during an experiment a) from the front and b) from the left-side wall.

The usable flume length is 7 m and the flume width was reduced to 0.25 m by introducing a PVC wall on right-side of the flume. Figure 3.2 presents a sketch with the main characteristics of the experimental set-up and Figure 3.3 displays pictures showing the experimental facility with several of its components.
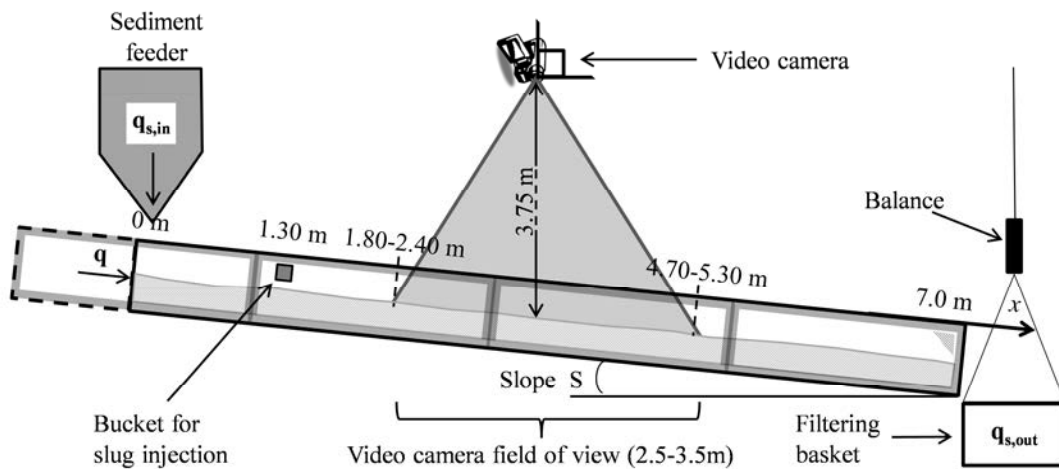
Figure 3.2: Sketch of the experimental setup.

Water discharge, fed constantly by the closed general pumping system of the laboratory, is measured by an electromagnetic flow-meter (±0.01 l/s accuracy, 5 in Figure 3.3). Bed substratum, composed by the mobile sediments (cf. 7 in Figure 3.3), was confined at both the upstream and the downstream sections by a PVC trapezoidal weir (4 in Figure 3.3) and a PVC vertical plate respectively. This way, the mobilization of the entire mobile bed was avoided and stable hydraulic conditions were assumed at the upstream section.

Sediments are constantly fed into the system by a calibrated sediment feeder (±5 %, 9 in Figure 3.3). Sediments are recirculated by a conveyor from the channel outlet to the inlet belt (8 in Figure 3.3), where they are distributed through the entire flume width by a system of nails assuming a uniform distribution across the channel section (3 in Figure 3.3). A filtering basket (14 in Figure 3.3) suspended to a balance (±1 kg, 11 in Figure 3.3) recuperates the sediments and filters the water from these at the outlet, where the weight is read manually every minute (15 in Figure 3.3). The sediment circuit is closed by the transfer of these from the downstream basket to the sediment feeder and then the conveyor belt, thus the feeding system assures continuity on the recirculation of sediments in the whole system. During the emptying of a basket, sediments are collected in a second basket. During this operation, that takes about 5 to 10 minutes, the basket weight is not measured. Details about the mobile sediments used in the experiments and their supply are given in chapter 3.1.2 and 3.1.2.

A photo camera (13 in Figure 3.3) is placed on the side of the flume, parallel to the channel in the central part of this, and takes pictures every minute for assessment in time of the flow conditions and bed morphology. The bed morphology is also measured continuously during the experiment with a point gauge (6 in Figure 3.3) and at the end of the experiment with a point laser (10 in Figure 3.3).

A camcorder (2 in Figure 3.3) is placed horizontally at about 3.9 m from the flow surface. It visualizes a longitudinal reach of the channel between 2.3 and 3.5 m long, depending on the used zoom. A bucket occupying the whole flume width is used for dye injection (12 in Figure 3.3), needed for bulk velocity measurements. Four bars are placed at the top of the flume (1 in Figure 3.3) and are used for image scaling in video analysis. This system is used for bulk flow velocity measurements as is described in detail later in section 3.1.5 and Chapter 4. Details on the measurements carried out during and after the experiments are given in section 3.1.5.
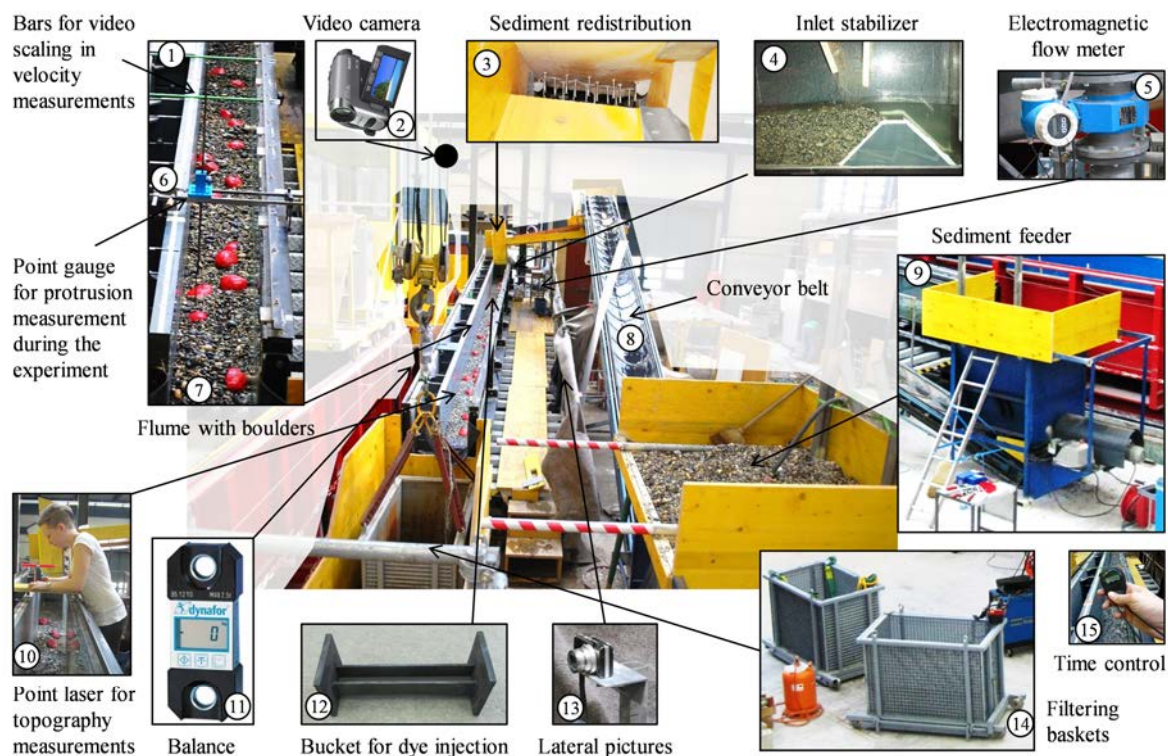
Figure 3.3: Picture of the experimental facility and details.

3.1.2 Mobile sediments

Experiments are carried out with a mobile bed, the same grain size distribution being supplied to the system during the tests. In order to represent the characteristics of mountain rivers, a wide grain size distribution was used. *Hersberger* (2002) analyzed the grain size distribution of several alpine rivers. Mobile bed material with a gradation similar to typical alpine gradation identified by *Hersberger* (2002) was herein chosen for these experiments. The comparison between the grain diameter distribution curve of the used sediments and typical alpine river curves is given in Figure 3.4.
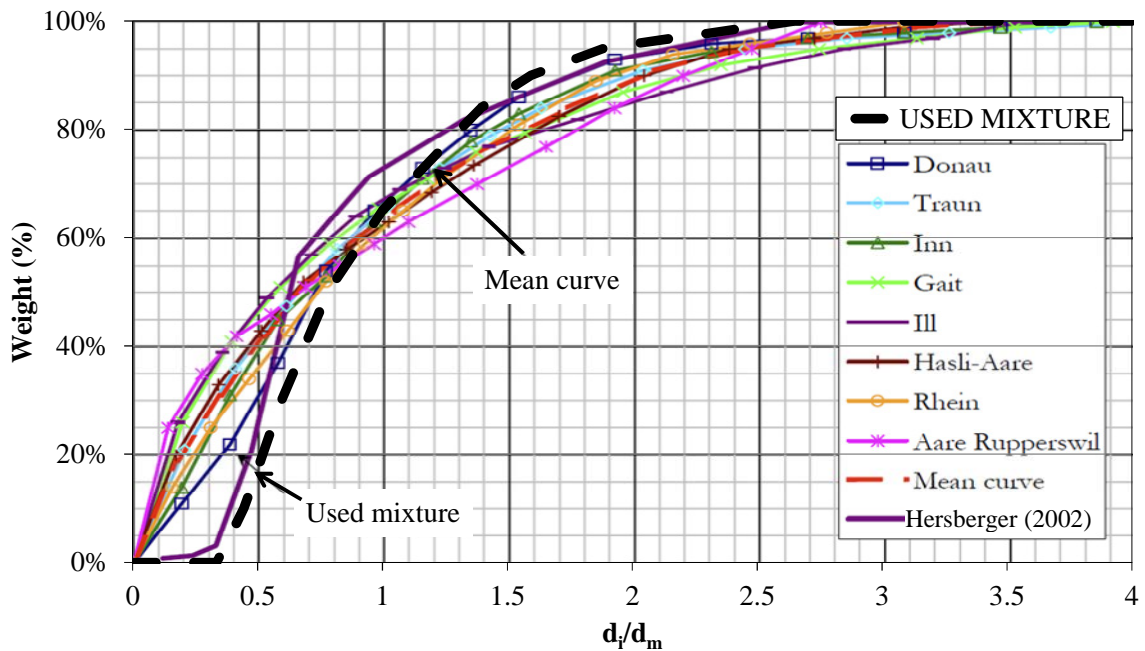
Figure 3.4: Normalized grain size distribution of bed sediments of alpine rivers and of the sediment mixture used in this research (adapted from *Hersberger* 2002). Grain sizes (d_i) are normalized by the mean diameter (d_m).

The characterization of the grain size distribution of the supplied sediments, which are shown in Figure 3.5, is given in Table 3.1, where d_m=11.9 mm is the mean diameter, corresponding to d_{65} and d_x is the grain size diameter for which $x\%$ in weight of the amount of sediments have smaller diameters. Boulders are not taken into account in this distribution and are not supplied as mobile sediments. The density of the sediment is ρ_s=2650 kgm^{-3}.

The ratio between the flume width w and the d_{50} (w/d_{50}=0.25/(9.3x10^{-3})≈27) is consistent with that encountered in mountain rivers. In the literature, values of w/d_{50} ranging between 10 and 100 are found for the range of slopes used in the present study (6.7, 9.9, and 13%). River width studied in nature range from 2.5 m to 7.5 m approximately, which means that the experiments are performed with a scale of 1:10 to 1:30 (cf. *Rickenmann* 2001; *MacFarlane and Wohl* 2003).

Table 3.1: Characterization of the grain size distribution of the supplied sediments.

$d_m = d_{65}$(mm)	d_{10} (mm)	d_{30} (mm)	d_{50} (mm)	d_{84} (mm)	d_{90} (mm)	d_{max} (mm)
11.9	5.3	7.1	9.3	16.6	19	32

Figure 3.5: Sediments used for the mobile bed substratum.

To verify the constant distribution of the supplied graded sediments through time, grain size distribution measurements were carried out at several instants during an experiment. As referred to in section 2.3.7 and discussed in detail in Chapter 5 and Chapter 6, bedload fluctuations are observed during the experiments. Samples of the supplied sediments were taken at the inlet at varying bedload transport states (average sediment transport event, low sediment transport, and peak sediment transport). As shown in Figure 3.6, the sediment supply is practically constant in time. This confirms that bedload stages are not induced by the supplied grain size distribution.
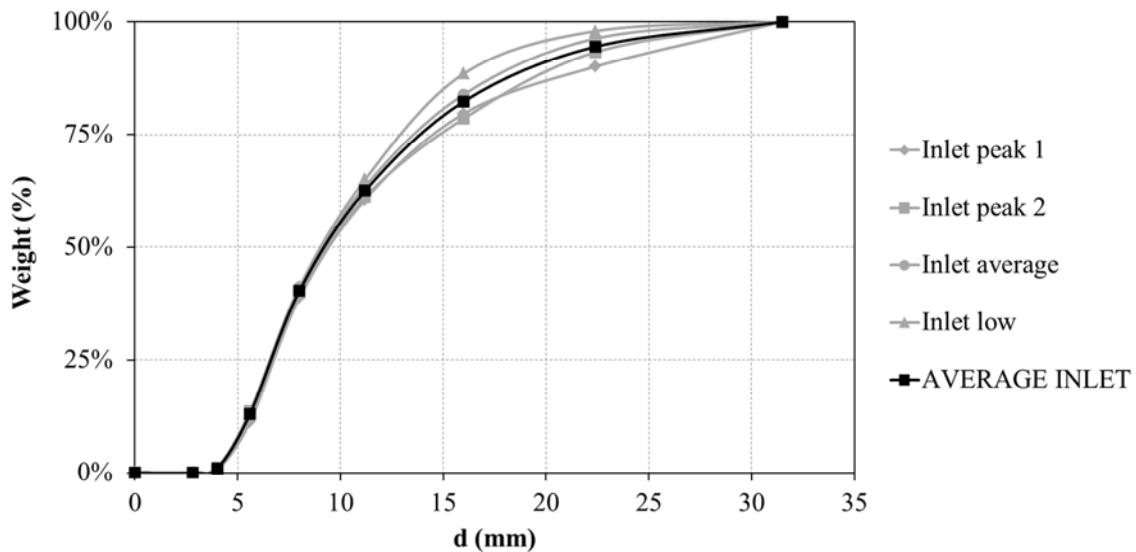
Figure 3.6: Supplied grain size distribution measured for several instants in time.

3.1.3   Sediment supply

The sediment feeder (9 in Figure 3.3) assembled by *Hersberger* (2002) is employed. It was built to supply a grain size distribution similar to the one used in the present study (cf. Table 3.1 and Figure 3.4). Challenges in conceiving a satisfactory sediment feeder include the wide grain size distribution used in the tests, where the maximum diameter is 32 mm, and the large amount of sediments to recirculate during experiments. See *Hersberger* (2002) for more details on the conception of the sediment feeding system. A detailed sketch of the apparatus is given in Figure 3.7.

Vertical walls were added on the top of the feeder in order to increase its capacity. The amount of sediments to supply is decided and calibrated ($\pm5\%$) by means of an Electronic Frequency Modulator (6 in Figure 3.7) prior to the experiment, being than kept constant throughout the entire experiment. This modulator allows regulating both the frequency of the motor and the working time intervals.

In order to have a constant sediment supply through the experiments, sediments needed to be wetted continuously during the experiments since the very beginning to these. This avoids changes in sediment supply after emptying the filtering basket full of wetted sediments into the feeder. Standard deviations on the supplied sediments were observed to

vary between 13.5% of the average inlet for low sediment supply to 2.5% at high sediment supplies. Higher deviations for low supply tests are due do the fact that the cylinder (2 in Figure 3.7) is not rotated continuously for these experiments. If a very coarse grain is blocked in the lips of the opening (7 in Figure 3.7), some sediments would eventually fall out of the feeder, thus increasing the variability of sediment supply.

Frontal view   Lateral view
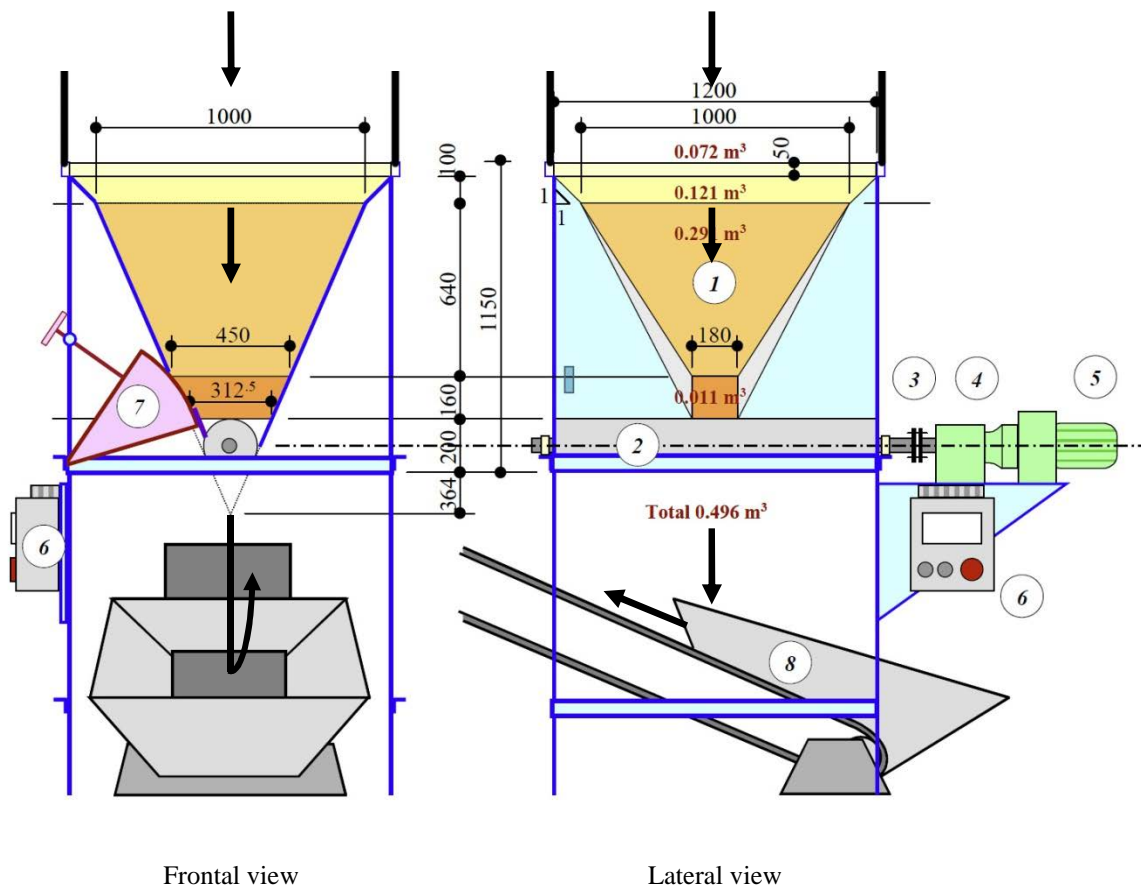
Figure 3.7: Scheme of the used sediment supply: 1) sediment reservoir; 2) rotating cylinder (with a slide opening); 3) fuse to prevent rotating cylinder from damage; 4) mechanic step-down gear; 5) motor; 6) Electronic Frequency Modulator; 7) gate to adjust the opening with thick plastic lip; 8) conveyor belt (modified from *Hersberger* 2002). Arrows indicate the direction of sediment movement.

As shown in Figure 3.3, the sediment feeder is placed adjacently to the flume outlet. The conveyor belt (8 in Figure 3.7 and Figure 3.3) transports the sediments from the feeder outlet to the inlet. The conveyor belt velocity is not limiting the sediment supply and is

constant in time. Sediments are homogeneously distributed through the entire flume width by a nail labyrinth (3 in Figure 3.3), assuming a uniform distribution across the section.

At the flume outlet, sediments are collected by a filtering basket, separating the mixture water-sediments. When the basket is full or the sediment feeder empty, the first is emptied into the latter. Sediments are thus re-used during the experiment. This system allows the use of a relatively limited amount of sediments and the supply of a constant amount of sediment into the flume. As shown in 3.1.2 and in Figure 3.6, no grain sorting is observed at the inlet of the flume.

The weight of the filtering baskets is measured manually every minute in order to obtain the sediment transport and its fluctuation through time. Further details about the measurements are given in section 3.1.5.

3.1.4 Boulders

The goal is to study the influence of varying boulder diameters D and dimensionless distances between boulders λ/D, where λ is the average distance between boulders. λ/D represents boulder density evaluated through linear dimensions. The couples D and λ/D and the corresponding characteristics, assessed in the present study, are given in Table 3.2 and presented in Appendix A.

Figure 3.9 illustrates a top and frontal view of the boulders. Boulder diameters varying between about 1/3 and 1/2 of the flume width were used (D=0.075, 0.100, and 0.125 m). Dimensionless distances of λ/D=2, 3, and 5 were used. A total of 9 boulders configuration were studied. A tenth configuration is given by λ/D=4 and D=0.075 cm. This configuration, which has the same number of boulders as λ/D=3 and D=0.100 m, was used only in one test (cf. Table 3.3), to infer the impact of boulders on the sediment transport capacity, reference tests without boulders (uniquely with mobile sediments in the channel) were also carried out.

Table 3.2: Number of boulders N_{Bst} (-) in the flume, number of boulders per square meter N_{Bs} (m^{-2}) and initial bed surface A_i/A_t (%) occupied by spheres of diameter D, as a function of boulder diameter D and dimensionless distance λ/D.

	D=0.075 m			D=0.100 m			D=0.125 m		
	N_{Bst} (-)	N_{Bs} (m^{-2})	A_i/A_t (%)	N_{Bst} (-)	N_{Bs} (m^{-2})	A_i/A_t (%)	N_{Bst} (-)	N_{Bs} (m^{-2})	A_i/A_t (%)
λ/D=2 (-)	78	44.6	19.7	44	25.1	19.7	28	16.0	19.6
λ/D=3 (-)	35	20.0	8.8	19	10.9	8.5	12	6.9	8.4
λ/D=4 (-)	19	10.9	4.8	-	-	-	-	-	-
λ/D=5 (-)	12	6.9	3.0	7	4.0	3.1	4	2.3	2.8

Water worked boulders of crystalline rock were collected at the river Moesa in Lumino, Ticino (Switzerland). Boulders, with forms visually as close to a sphere as possible, were selected on a weight basis. Only boulders with a weight corresponding to that of a sphere of diameter $D\pm5$ mm were kept (ρ_s=2650 kgm^{-3}).

The position of the boulders for every configuration (couple D and λ/D) is randomly chosen by a computational routine. This represents a cascade morphology, typical of steep mountain rivers (cf. Table 2.1, (*Montgomery and Buffington* 1997)). In the lateral axe, three positions are possible: left-center-right. In the longitudinal axe, the number of equally distributed positions is calculated as L/D, where L is the flume length. The computational routine choses in which of these positions to place the $N_{Bst} = \dfrac{1}{\lambda^2}$ boulders. Boulders are then positioned as close as possible to the calculated position. The initial position of boulders for a given configuration is always the same and is given in Appendix A. The surface grain size distribution changes considerably when compared to the situation without boulders, as shown in Figure 3.8 when taking into account the presence of boulders. The influence of boulders on surface grain size distribution increases with boulder size and surface occupied by boulders (smaller λ/D). Boulders are however not transported by the flow, thus only the grain size distribution of mobile sediments (cf. Table

3.1) is further considered in the manuscript, boulders being accounted for as obstacles to the flow.
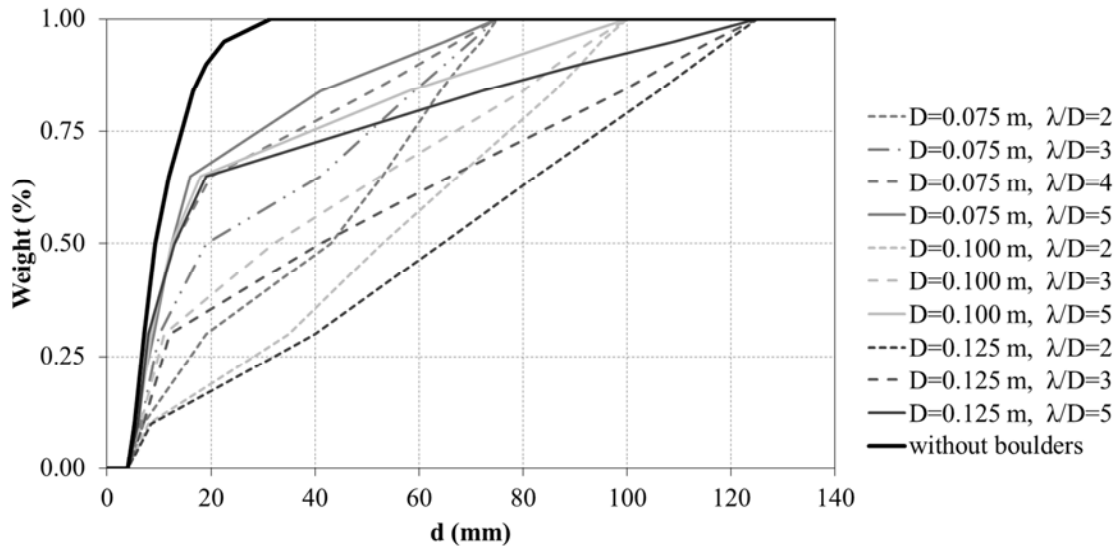
Figure 3.8: Surface grain size distribution including boulders, for all the tested configurations of boulders.

An initial plane bed of mobile sediments of 0.2 m of thickness is placed in the flume, boulders are then arranged at the chosen position half submerged by the sediments. The black line visible in Figure 3.9 indicates the half submergence line.

The position of every boulder is measured by a point laser at the beginning and at the end of the experiments. The initial central point is marked with a dot, and the maximum elevation with a cross. These points can be coincident, in this case only a dot is marked, as can be seen on boulder number 2 in Figure 3.9.
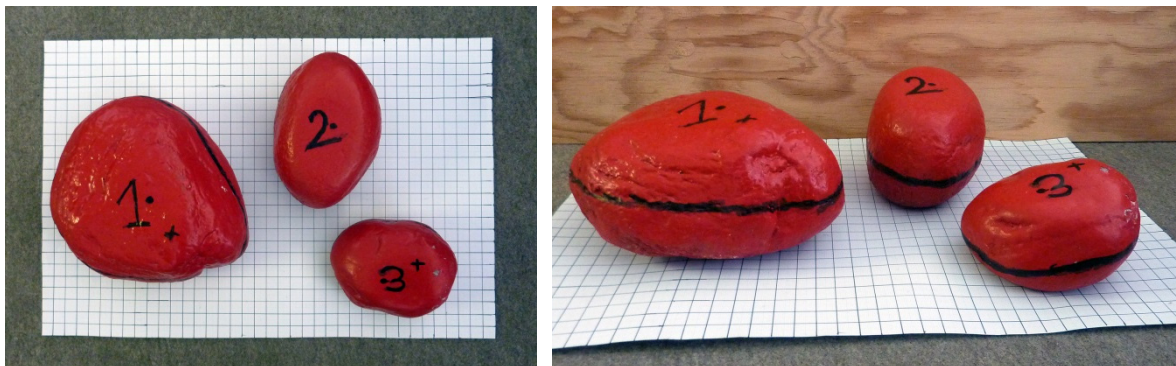
Figure 3.9: Top and front view of boulders corresponding to the three diameters used. 1) D=0.125 m, 2) D=0.100 m, 3) D=0.075 m. The graded paper is 0.25 cm wide, as the flume, and 0.38 m long, being the grid cells dimensions of 0.01x0.01 m^2.

3.1.5 Measurements

The following paragraphs describe instrumentation and procedures used for the various measurements carried out during and after the experiments. These include evaluation of sediment transport and velocity in the channel, as well as parameters related to the river bed morphology, such as the boulder protrusion, the number of hydraulic jumps, the boulder surface, and the final bed topography.

a) Flow velocity

Average flow velocity was measured every 15 minutes by means of a technique using dye-tracer and video analysis (±5 %, Figure 3.10). This technique, based on the analysis of a colorant (tracer) dilution, allows the measurement of mean bulk velocities through the channel reach. The passage of the cloud of colorant in the reach in analyzed based on the difference between images, the movement of the mass center of the cloud defining the average flow velocity (*Calkins and Dunne* 1970). Five colorant injections are done in order to obtain a velocity value. Chapter 4 describes in detail this bulk velocity measurement technique as well as its validation by comparison with other existing methods.

Figure 3.10: Flume with colorant during a bulk flow velocity measurement.

b) Sediment output

Sediment output is inferred through the weight of the filtering baskets (14 in Figure 3.3), which is registered every minute. Filtering baskets are suspended at the outlet of the flume, under the water jet formed at the outlet. Due to the wide grain size distribution used, the waters flows out of the sediments, and thus out of the basket, quickly (high amount gravitational water and small amount of capillary water). This means that the influence of the water on the basket weight is constant through time (force of the constant jet at the outlet of the flume) and does practically not change with the basket filling. A Dynafor 2t

balance, with measuring precision of ± 1 kg, is used (11 in Figure 3.3). Knowing the precise time and amount of sediments, an average value of the sediment discharge is then calculated continuously over a sliding 10 minutes window ($q_{s,out,10}$), in order to have a smoothed overview of the bedload fluctuations (cf. 3.2).

c) Boulder protrusion

The portion of boulders protruding from mobile sediments (boulder protrusion, cf. Figure 2.8) was shown to be a good proxy for sediment transport in steep rough channels (*Yager et al.* 2007; 2012b). In this study, boulder protrusion in measured during the experiment (Figure 3.11a) as well as at the beginning and end of the experiments (Figure 3.11a).
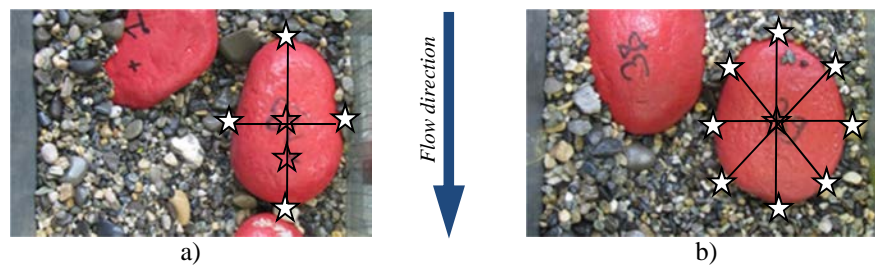
Figure 3.11: The position of the measured points is indicated by stars for measurements: a) during the experiments, measured with a point gauge; b) before and after the experiments, measured with a point laser.

During the experiments the protrusion P of 4 boulders is measured with a point gauge (± 1 mm, Figure 3.11a), with a time interval of approximately 10 minutes (2-3 minutes per boulder, in a loop). P is calculated as the averaged height differences between: top-upstream, top-downstream, top-left, and top-right, for every boulder at the edge with the gravel. A sub-sampled linear interpolation in time allows then the averaging between boulders with a regular time-step, originating the value of P_{av}, the average boulder protrusion, at every minute of the test.

Before and after the experiments, the protrusion of all the boulders in measured at the eight cardinal points, on the highest point and at the center (Figure 3.11b) with a point laser (± 1 mm). In the example given in Figure 3.11b the center corresponds to the highest point (cf. section 3.1.4).

d) Hydraulic jumps counting

Hydraulic jumps (Figure 3.12) are counted based on visual observation after velocity measurements are performed, about every 15 minutes. This parameter is an indicator of the amount of energy dissipation and is intrinsically related to channel morphology since hydraulic jumps generally appear downstream of protruding boulders. Dimensions of the hydraulic jumps are not measured. If more than 15 boulders are placed in the flume, only the jumps present in the part of the flume visualized by the video camera used for velocity measurements are counted, otherwise the total number of hydraulic jumps in the flume is counted. The number of hydraulic jumps HJ is then scaled to correspond to the total number of hydraulic jumps in the flume ($HJ=HJ.N_{Bsu}/N_{Bst}$, where N_{Bsu} corresponds to the number of boulders for which the presence of hydraulic jumps was checked) and adimensionalized by the total number of boulders in the flume N_{Bst}, giving the dimensionless number of hydraulic jumps $HJ^*=HJ/N_{Bst}$.

Figure 3.12: Example of an hydraulic jump.

e) Boulder surface

Bed parallel surface occupied by boulders A_{Bs}, called in short "boulder surface", is obtained by means of video analysis (Figure 3.13). The video recorded for velocity measurements is used for bed parallel boulder surface estimation. Individual boulders are identified in a single frame (in white in Figure 3.13b, Figure 3.13a showing the original image). The correct identification of boulders is checked on Figure 3.13c. The surface of each boulder is calculated based on the image scaling (Figure 3.13d) and the error is estimated to be approximately 2% of the estimated boulder surface. Finally, the surface of the flume occupied by boulders is then scaled by the flume surface visible in the video, giving a dimensionless boulder surface $A_{Bs}^*=A_{Bs}/A_{video}$.

For experiments 1 to 23 (cf. Table 3.3, test 23 being presented and analyzed in detail in Chapter 5), the video camera was turned on only during velocity measurements. The calculation is done before every colorant injection (about 5 times every 15 minutes). From test 24, the video camera is recording continuously and boulder surface is calculated every minute.
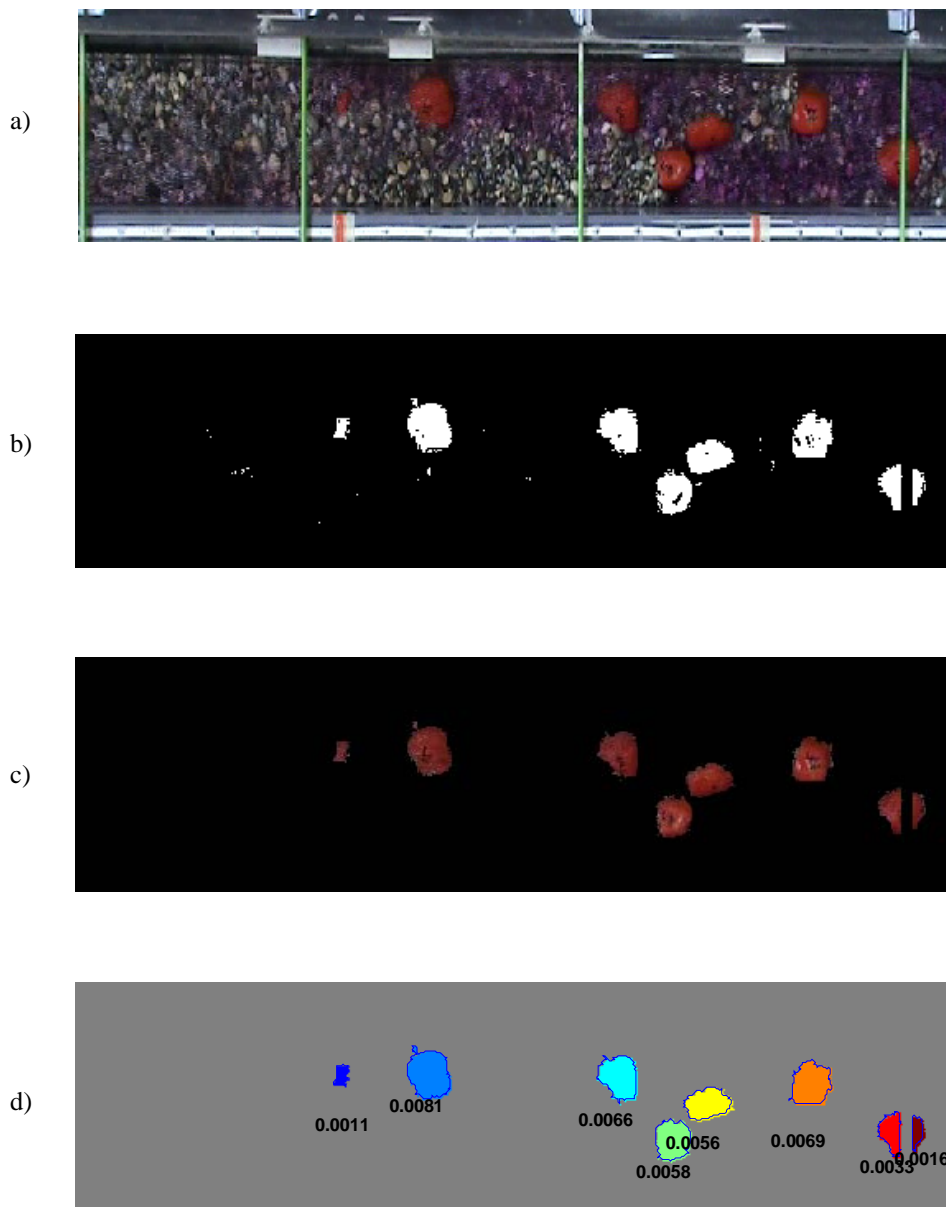
Figure 3.13: (a) True color picture, taken from the camcorder. (b) Regions where boulders are identified. Only regions with more than 25 pixels are considered to be boulders. (c) Content of the regions identified in (b), in true color. (d) Surface of every boulder, in m^2.

f) Supplementary available data

The bed morphology at the end of the experiment is measured with a point laser (±1 mm, 10 in Figure 3.3) on a regular grid of 5x5 cm^2. These measurements supply information about the bed variability at average sediment transport.

Lateral pictures (13 in Figure 3.3) were taken every minute in the central part of the flume (about 1.5 m long reach). These data give interesting information about the rapidity and amplitude of bed changes (Figure 3.14). The sediment levels in time and the grain size distribution evolution can be analyzed based on this series of pictures.
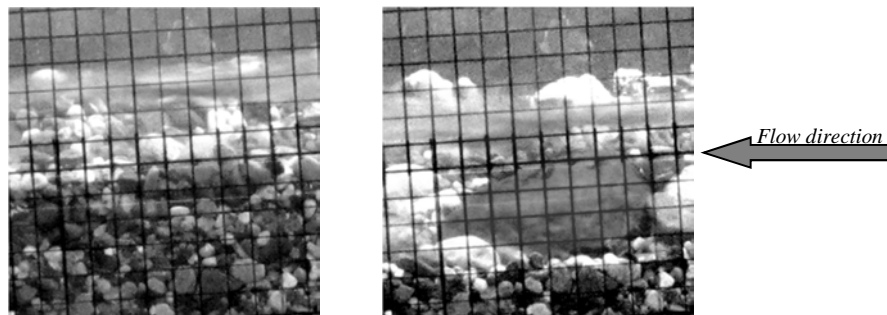
Figure 3.14: Example of fast erosion around a boulder.

3.2 Tests parameters and procedure

3.2.1 Experimental procedure

a) Preparation of the experiment

A plane bed of 0.2 m of thickness is prepared before the experiments and boulders are placed into the flume half covered by mobile sediments (the black line on the boulders visible in Figure 3.9 corresponds to the half-submerged situation), which corresponds to a protrusion equal to approximately 30% of the diameter ($P^*=P_{av}/D\approx0.3$). The protrusion of every boulder is measured with a point laser as described in section 3.1.5c and illustrated in Figure 3.11b. Pictures of the initial flume configuration are taken and bed area occupied by boulders can be calculated both form protrusion measurements and scaled pictures.

The amount of sediment to supply ($q_{s,in}$) is decided prior to the experiment and the sediment feeder is calibrated accordingly. The sediment supply remains constant during all the experiment. The initial amount of water to supply is decided based on the tested configuration (λ/D, D, S and $q_{s,in}$) and based on observations from previous experiences.

A camera taking pictures every 60 seconds in placed at the side of the central part of the flume and is started before the experiment. The evolution of sediment deposition can thus be checked in the left side of the central part of the flume.

The filtering basket is suspended at the outlet of the flume and its initial weight is noted.

b) Experimental run

Water and sediment supply are started at the same time. During the experiment flow velocity U, boulder surface A_{Bs} and number of hydraulic jumps HJ are measured about every 15 minutes; the protrusion of 4 boulders is measured in a loop (cf. section 3.1.5). The basket weight is read every minutes and the sediment transport is directly calculated, based on the weight and time differences. Since the fluctuations on a one minute basis are very high, an average of sediment transport over a ten minutes moving window ($q_{s,out,10}$) is calculated. The measuring procedure has been described in section 3.1.5.

The equilibrium condition between liquid and solid discharge has to be such that boulders are still relatively visible at the end of the experiment. The test is stopped immediately after a peak in bedload, when the average outlet sediment discharge over the last 10 minutes is equal to the sediment supply ($q_{s,out,10} \approx q_{s,in}$). The overall cumulative average of the outlet sediment transport computed for a given instant T ($q_{s,out,av}$, Eq.(35)) has to be within ±20% of the sediment supply at the end of the experiment.

$$q_{s,out,av}(T) = \left(\int_0^T q_{s,out}(t)\mathrm{d}t \right) \Big/ T \qquad (35)$$

c) After the experiment

After the experiment, the protrusion of every boulder is measured with a point laser as described in section 3.1.5. The bed morphology is also measured on a 5x5 cm^2 regular grid with a laser probe.

Top pictures of the bed are taken longitudinally every 10 cm and a reconstruction of the situation at the end of experiments can be done (cf. Appendix B for tests 9 to 41). This allows calculating the bed parallel surface of every boulder, by means of image analysis. An estimation of the surface grain size distribution is also possible.

d) Hydrograph and grain size distribution

For test number 20 and following (except test 40, Table 3.3), the effect of an increasing discharge is studied. For this, no sediment supply is used.

The water worked channel bed obtained after a sediment transport experiment is employed. An initial low water discharge is supplied to the flume. This initial discharge does not move the sediments and is about 0.003 to 0.006 $m^3s^{-1}m^{-1}$, depending on the channel slope and the boulder configuration. The discharge is then increased by small steps of 0.0008 to 0.0020 $m^3s^{-1}m^{-1}$, depending on the configuration. Once the sediments start moving, the constant discharge is kept for about 10 minutes. For every tested discharge velocity measurements are carried out (five color dye injections).

All the sediments reaching the outlet are collected (separately for each discharge) and the grain size distribution is further measured.

The discharge is increased until visual observations indicate that also grain sizes with diameters comparable to d_{90} are transported and reach the flume outlet.

These hydrograph experiment supply data of: discharge, flow velocity, and transport grain sizes. The data can be linked to bed morphology. A preliminary analysis is carried out in section 8.2.

3.2.2 General test parameters

The following paragraph gives an overview of the test parameters, summarized in Table 3.3. Further results are presented in Chapter 5 to Chapter 8. Table 3.3 also lists the measurements carried out for each test. $q_{s,av}$ indicates that only the average sediment transport was measured, while $q_{s,x}$ indicates that the bedload was measured every minute. U indicates the velocity measurements. $A_{Bs(U)}$ indicates that the boulder surface is

calculated at every velocity measurement, while A_{Bs} indicates that the boulder surface is calculated every minute. P_{av} indicates that the protrusion of several boulders has been measured during the test. HJ indicates that the number of hydraulic jumps was counted. HQ indicates that hydrograph experiments (described in section 3.2.1) where carried out at the end of the test.

Mainly three dimensionless boulder distance λ/D (2, 3, and 5) and three boulder diameters D (0.075, 0.100, and 0.125 m) were used. Reference tests without boulders where also done. Tests were carried out on three flume slopes (6.7, 9.9, and 13%). Several couples of solid and liquid discharges where tested. A single flume width of 0.25 m and grain size distribution of mobile sediments were used for all the experiments.

a) Flume slope

Three flume slopes S have been tested in order to study the influence of boulders on sediment transport capacity: 6.7%, 9.9% and 13%. All the three λ/D configurations have been tested for several couples of liquid discharge (q) and sediment supply ($q_{s,in}$) couples on a 6.7% slope. All the configurations were tested for a fixed sediment supply of $q_{s,in}$=0.1343x10^{-3} m^{3}s^{-1}m^{-1}. A similar sediment supply was used on the other two slopes for several experiments. On the 9.9% slope, only the configuration λ/D=3 and D=0.100 m is tested for three couples of solid and liquid discharges. A reference test without boulders is also carried out. This allowed analyzing the influence of the slope for one boulder configuration. On the 13% slope, the diameter D=0.100 m has been used with all the λ/D distances. All the diameters were used for λ/D=3. One reference without boulders test was carried out.

b) Boulder configuration

Boulders diameters D=0.075 m, 0.100 m and 0.125 m were used. Dimensionless boulder distance λ/D equal to 2, 3 and 5 were used, for a total of 9 boulder configurations. A total of 4 to 78 boulders was placed in the flume, depending on the configuration. A test with boulders placed in the same position as for the configuration λ/D=3 and D=0.100 m is carried out with boulders of diameter D=0.075 m, which means that λ/D=4, on the 13%

slope. Reference tests without boulders are done in order to infer the impact of boulders on sediment transport capacity.

c) Sediment supply

Sediment supply varied between 0.0287×10^{-3} m^{3}s^{-1}m^{-1} (corresponding to 19 g/s, with ρ_s=2650 kgm^{-3}) and 0.2355×10^{-3} m^{3}s^{-1}m^{-1} (corresponding to 156 g/s). All the configurations were tested with $q_{s,in}$=0.1343×10^{-3} m^{3}s^{-1}m^{-1} on the 6.7% slope. A similar amount of sediments has been used for several tests on the other slope. In particular, all diameters were tested for λ/D=3 and all λ/D were tested for D=0.100 m, with a sediment supply of $q_{s,in}$=0.1464×10^{-3} m^{3}s^{-1}m^{-1}.

d) Water discharge

The water discharge needed for suitable equilibrium conditions (boulders visible after a sediment transport peak; final bed slope corresponding to the flume slope) varied between 0.0104 m^{3}s^{-1}m^{-1} (corresponding to 2.60 l/s) and 0.0424 m^{3}s^{-1}m^{-1} (corresponding to 10.60 l/s). This corresponds to average water depth ranging from 0.027 m to 0.0531 m, with an average of 0.036 m.

Table 3.3: Experimental parameters and indication of the measurements performed for each test.

Test	S (%)	λ/D (-)	D (m)	N_{Bs} (m^{-2})	q (m^{3}s^{-1}m^{-1})	$q_{s,in}$ x10^{-3} (m^{3}s^{-1}m^{-1})	$q_{s,out}$ x10^{-3} (m^{3}s^{-1}m^{-1})	Measurements
1	6.7	0	0.000	0.0	0.0204	0.1857	0.1509	$q_{s,av}$, U
2	6.7	3	0.125	6.9	0.0240	0.1555	0.1706	$q_{s,av}$, U, $A_{Bs(U)}$
3	6.7	3	0.100	10.9	0.0240	0.1389	0.1555	$q_{s,av}$, U, $A_{Bs(U)}$
4	6.7	2	0.100	25.1	0.0228	0.0574	0.0646	$q_{s,x}$, U, $A_{Bs(U)}$, P_{av}
5	6.7	2	0.100	25.1	0.0424	0.1570	0.1736	$q_{s,x}$, U, $A_{Bs(U)}$, P_{av}
6	6.7	3	0.075	20.0	0.0212	0.0906	0.1040	$q_{s,x}$, U, $A_{Bs(U)}$, P_{av}
7	6.7	2	0.125	16.0	0.0228	0.0634	0.0746	$q_{s,x}$, U, $A_{Bs(U)}$, P_{av}
8	6.7	2	0.075	44.6	0.0209	0.0287	0.0236	$q_{s,x}$, U, $A_{Bs(U)}$, P_{av}
9	6.7	3	0.125	6.9	0.0236	0.1011	0.1122	$q_{s,x}$, U, $A_{Bs(U)}$, P_{av}, HJ
10	6.7	5	0.100	4.0	0.0223	0.1343	0.1346	$q_{s,x}$, U, $A_{Bs(U)}$, P_{av}, HJ
11	6.7	5	0.075	6.9	0.0222	0.1343	0.1307	$q_{s,x}$, U, $A_{Bs(U)}$, P_{av}, HJ
12	6.7	5	0.125	2.3	0.0208	0.1343	0.1503	$q_{s,x}$, U, $A_{Bs(U)}$, P_{av}, HJ
13	6.7	3	0.075	20.0	0.0238	0.1343	0.1401	$q_{s,x}$, U, $A_{Bs(U)}$, P_{av}, HJ
14	6.7	3	0.125	6.9	0.0235	0.1343	0.1192	$q_{s,x}$, U, $A_{Bs(U)}$, P_{av}, HJ
15	6.7	3	0.100	10.9	0.0233	0.1343	0.1244	$q_{s,x}$, U, $A_{Bs(U)}$, P_{av}, HJ
16	6.7	0	0.000	0.0	0.0162	0.1343	0.1189	$q_{s,x}$, U
17	6.7	2	0.100	25.1	0.0372	0.1343	0.1390	$q_{s,x}$, U, $A_{Bs(U)}$, P_{av}, HJ
18	6.7	2	0.125	16.0	0.0352	0.1343	0.1365	$q_{s,x}$, U, $A_{Bs(U)}$, P_{av}, HJ, HQ
19	6.7	2	0.075	44.6	0.0391	0.1343	0.1461	$q_{s,x}$, U, $A_{Bs(U)}$, P_{av}, HJ, HQ
20	6.7	3	0.100	10.9	0.0177	0.0563	0.0607	$q_{s,x}$, U, $A_{Bs(U)}$, P_{av}, HJ, HQ
21	6.7	5	0.100	4.0	0.0162	0.0563	0.0565	$q_{s,x}$, U, $A_{Bs(U)}$, P_{av}, HJ, HQ
22	6.7	0	0.000	0.0	0.0148	0.0563	0.0654	$q_{s,x}$, U, HQ
23	6.7	5	0.075	6.9	0.0168	0.0563	0.0571	$q_{s,x}$, U, $A_{Bs(U)}$, P_{av}, HJ, HQ
24	6.7	3	0.075	20.0	0.0188	0.0563	0.0528	$q_{s,x}$, U, A_{Bs}, P_{av}, HJ, HQ
25	6.7	5	0.125	2.3	0.0156	0.0563	0.0604	$q_{s,x}$, U, A_{Bs}, P_{av}, HJ, HQ
26	6.7	0	0.000	0.0	0.0159	0.0936	0.0996	$q_{s,x}$, U, HQ
27	6.7	5	0.100	4.0	0.0183	0.0936	0.0876	$q_{s,x}$, U, A_{Bs}, P_{av}, HJ, HQ
28	9.9	3	0.100	10.9	0.0131	0.0936	0.0891	$q_{s,x}$, U, A_{Bs}, P_{av}, HJ, HQ
29	9.9	0	0.000	0.0	0.0112	0.0936	0.0876	$q_{s,x}$, U, HQ
30	9.9	3	0.100	10.9	0.0146	0.1358	0.1434	$q_{s,x}$, U, A_{Bs}, P_{av}, HJ, HQ
31	9.9	3	0.100	10.9	0.0166	0.1917	0.1977	$q_{s,x}$, U, A_{Bs}, P_{av}, HJ, HQ
32	13	3	0.100	10.9	0.0114	0.1917	0.1992	$q_{s,x}$, U, A_{Bs}, P_{av}, HJ, HQ
33	13	3	0.100	10.9	0.0107	0.1464	0.1449	$q_{s,x}$, U, A_{Bs}, P_{av}, HJ, HQ
34	13	3	0.075	20.0	0.0109	0.1464	0.1721	$q_{s,x}$, U, A_{Bs}, P_{av}, HJ, HQ
35	13	2	0.100	25.1	0.0128	0.1464	0.1675	$q_{s,x}$, U, A_{Bs}, P_{av}, HJ, HQ
36	13	5	0.100	4.0	0.0104	0.1464	0.1675	$q_{s,x}$, U, A_{Bs}, P_{av}, HJ, HQ
37	13	3	0.125	6.9	0.0104	0.1464	0.1645	$q_{s,x}$, U, A_{Bs}, P_{av}, HJ, HQ
38	13	0	0.000	0.0	0.0106	0.1917	0.2158	$q_{s,x}$, U, HQ
39	13	3	0.100	10.9	0.0124	0.2355	0.2536	$q_{s,x}$, U, A_{Bs}, P_{av}, HJ, HQ
40	13	3	0.100	10.9	0.0118	0.2355	0.2611	$q_{s,x}$, U, A_{Bs}, P_{av}, HJ
41	13	4	0.075	10.9	0.0118	0.2355	0.2657	$q_{s,x}$, U, A_{Bs}, P_{av}, HJ, HQ

Chapter 4

Bulk velocity measurements by video analysis of dye tracer in a macro-rough channel

This chapter presents the bulk velocity measurement technique developed during this research project, based on dye tracer dilution and video analysis, and validates it through a comparison with other existing techniques, namely water depth measurements, ultrasonic velocity profiler and salt dilution measurements.

Abstract. Steep mountain rivers have hydraulic and morphodynamic characteristics that hinder velocity measurements. The high spatial variability of hydraulic parameters such as water depth, river width and flow velocity, makes the choice of a representative cross-section to measure the velocity in detail challenging. Additionally, sediment transport and rapidly changing bed morphology exclude the utilisation of standard and often intrusive velocity measurement techniques. The limited technical choices are further reduced in the presence of macro-roughness elements, such as large, relatively immobile boulders. Tracer tracking techniques are among the few reliable methods that can be used under these conditions to evaluate the mean flow velocity. However, most tracer tracking techniques calculate bulk flow velocities between two or more fixed cross-sections. In the presence of intense sediment transport resulting in an important temporal variability of the bed morphology, dead water zones may appear in the few selected measurement sections. Thus a technique based on the analysis of an entire channel reach is needed in this study. A dye tracer measurement technique in which a single camcorder visualises a long flume reach is described and developed. This allows to overcome the problem of the presence of dead water zones. To validate this video analysis technique, velocity measurements were carried out on a laboratory flume simulating a torrent, with a relatively gentle slope of 1.97% and without sediment transport, using several commonly used velocity measurement instruments. In the absence of boulders, salt injections, water depth and ultrasonic velocity profiler measurements were carried out, along with dye injection technique. When boulders were present, dye tracer technique was validated only by comparison with salt tracer. Several video analysis techniques used to infer velocities were developed and compared, showing that dye tracking is a valid technique for bulk velocity measurements. RGB Euclidean distance was identified as being the best to measure of the average flow velocity.

Keywords: bulk flow velocity; macro-rough channel; dye tracer tracking

4.1 Introduction

Mountain rivers occupy a significant part of world catchments. Although they control sediment supply to lowland rivers, relatively few studies have been carried out on these torrents. They are characterised by longitudinal slopes ranging from 0.1% to 20% (*Papanicolaou et al.* 2004) and by a wide grain size distribution composed of fine mobile sediments and large, relatively immobile, boulders (*Rickenmann* 2001; *Yager et al.* 2007), which can be arranged randomly or in rows (*Pagliara and Chiavaccini* 2006). In torrents, the water depth is small in comparison to the roughness elements, and the sediment transport can be intense. Bed morphology and hydraulic parameters, such as water depth and flow velocity, have high spatial variability, and in the presence of sediment transport, high temporal variability can also be observed in the above-mentioned parameters (*Recking et al.* 2009). Challenges in measuring hydraulic parameters under these conditions are found not only in the field (*Calkins and Dunne* 1970; *Church and Kellerhals* 1970) but also in laboratory experiments (*Recking* 2006; *Pagliara* 2007). High spatial variability of the channel morphology does not allow sampling on a regular grid, while the high temporal variability does not allow the installation of fixed systems. The presence of macro-roughness elements hinders the use of methods sampling a large flow surface, the small water depth excludes most intrusive techniques since these would disturb the flow, and the presence of intense sediment transport excludes to use fragile instruments. Thus most of the existing velocity measurement techniques are not appropriate, and selecting one or several representative cross-sections (i.e., average or typical cross-sections) to estimate average velocities is challenging in macro-rough mountain torrents (*Calkins and Dunne* 1970). Due to the spatiotemporal variability, hydraulic parameters such as the water depth and the average flow velocity are often not measured but estimated indirectly using empirical relationships, for example resistance equations (*Yager et al.* 2007; *Recking et al.* 2009; *Pagliara et al.* 2010; *Heyman et al.* 2013).

The present chapter focuses on bulk flow velocity measurement techniques in an experimental flume. Several difficulties to perform velocity measurements can be identified for our sediment transport flume experiments (*Ghilardi and Schleiss* 2012):

small average flow depth (between 0.027 and 0.053 m); high variability of water depth both in space and time (up to 0.1 m); mobile and rapidly changing bed; intense sediment transport; roughness elements often protruding from the water (in our particular case, due to the presence of boulders); small flume width (here, 0.25 m). One technique, based on video analysis of dye tracer over an entire flume reach, proved to be adequate for estimating channel flow velocities.

In section 4.2, a review of some existing velocity measurement techniques is presented, and their application to the hydraulic conditions of steep rough channels is described. In section 0, the experimental facility is described. Section 4.4 presents the procedure of the dye tracking technique leading to the estimation of the bulk flow velocities. Section 4.5 compares the dye tracer technique and data treatment to other velocity measurement methods for validation purposes. Salt and dye tracer tracking measurements are the only available methods that are applicable in the presence of boulders. In the absence of boulders, direct Ultrasonic Velocity Profiles (UVP) velocity measurements and mean velocities inferred from water depth (WD) measurements are also used for comparison. In section 6 the main conclusions are given.

4.2 Review of main velocity measurement techniques

Most velocity estimation techniques yield local information about the flow conditions. These methods require that one or more representative cross-sections are identified. The data obtained for the cross-sections are then averaged to estimate the average bulk flow velocity. Techniques that are commonly used to measure velocity in open-channel flows include: water depth (WD) measurements; Micro-propeller vertical profiling; Acoustic Doppler Velocimeter (ADV); Ultrasonic Velocity Profiles (UVP); Acoustic Doppler Velocity Profiles (ADVP); Acoustic Doppler Current Profiler (ADCP); hot wire; Laser Doppler Anemometry (LDA); Electromagnetic Current Meters (EMC); Pitot probes; Particle Image Velocimetry (PIV) and Particle Tracking Velocimetry (PTV); tracer tracking methods, with various types of tracers (salt and dyes).

Water depth (WD) measurements (using point-gauges, ultrasonic distance meters, and other instruments) and back-calculation of flow velocity seems to be a simple technique for determining average flow velocities when the discharge is known. However, as mentioned before, representative cross-sections are difficult to identify and other challenges need to be tackled. It is difficult to determine the base level (bed level) from which the water depth has to be measured, primarily because of the high relative roughness encountered in mountain rivers. The uncertainty of the water depth measurement is directly linked to the ratio between the water depth and the roughness height (*Rickenmann* 1990; *Recking* 2006). Thus large errors may occur in water depth measurements in torrents, since the elevation of the bed changes abruptly over short distances. The bed level is even more difficult to determine in the presence of intense bedload, because of the existence of a moving layer and rapid changes in the bed configuration. Moreover, the water surface is highly irregular, thus making its unambiguous measurement difficult.

Micro-propeller vertical profiling (full- and partial-depth, (*Church and Kellerhals* 1970)) are easy and precise ways to measure the mean velocities of flows with simple geometries in clear-water prismatic open-channels. In the flows targeted in the present research, however, several disadvantages of this method exist, including the sensitivity of the instrumentation blades to impact with sediments transported by the flow and the intrusiveness of the method, which causes local erosion when measuring velocities near a mobile bed.

Techniques based on the Doppler shift frequency of the echoes reflected by small suspended particles (seeding) comprise: Acoustic Doppler Velocimeters (ADV), Ultrasonic Velocity Profiles (UVP), 3D Acoustic Doppler Velocity Profiler (ADVP) and Acoustic Doppler Current Profiler (ADCP).

ADV, composed of one central emitter and three (or four) sound receivers, allows point measurements of the three components of the flow velocity. It has been widely used since a long time in laboratory (*Kraus et al.* 1994) and field (*Wilcox and Wohl* 2007) studies of open channel flows. ADV need to be immersed in the water, thus are intrusive, and require space to accommodate the probes and the near field needed between the emitter and the

measuring point. In shallow flows with restricted space for the measurements this techniques is limited. Furthermore, when the aim is to obtain bulk-average velocities, ADV require a large amount of measuring points.

UVP (*Amini et al.* 2009) measure instantaneous velocity 1D profiles along a beam axis. Several beams can be used to obtain velocity profiles at a single cross-section and an average cross-section velocity can then be calculated. Bathymetry uncertainties for UVP measurements are at most of the size of one measuring gate. Thus this is not relevant in the present case for the calculation of vertical averaged velocities. UVP transducers need to be partially immersed in the water; thus UVP measurement is an intrusive technique. In the present case, with widely varying water levels and bed morphology, the use of UVPs with a regular sampling grid for the cross-sections is not possible. Moreover, the size of mobile sediments is not negligible with respect to the water depth, and the signal echoed by gravel interferes with the backscattered signal.

ADVP, developed at the Ecole Polytechnique Fédérale de Lausanne (EPFL) (*Franca and Lemmin* 2006), allows full-depth quasi-instantaneous 3D velocity profiling and is suitable for use both in the field (*Franca et al.* 2008) and in the laboratory (*Blanckaert and De Vriend* 2004; *Leite Ribeiro et al.* 2012; *Dugué et al.* 2013). ADVP is intrusive, and while this influence is negligible for slow flow, at high flow velocities such as those considered in this study, ADVP changes the flow characteristics and influences flow velocities. The presence of macro-rough elements and gravel bars precludes the use of ADVP because it requires considerable free space.

ADCP, constituted typically of a central body where diverging transducers working simultaneously as emitters and receptors are installed, are commonly used for large-scale studies. They are used for estimating large features of flows in lakes (*Lorke and Wüest* 2005) and rivers (*Le Coz et al.* 2008). The dimensions of ADCP instrumentation and the weight do not allow an easy and fine displacement of the instrumentation in shallow flows with such singularities and obstacles as bed forms and large boulders.

Techniques commonly used to measure flow velocities in fluid mechanics, such as Hot Wire anemometry (cf. *Hinze* (1975) for details) and Laser Doppler Anemometry (LDA)

(cf. *Nezu and Nakagawa* (1993) for details), are not adequate in the case of intense bedload transport and spatial variability of the channel bed. Furthermore, the apparatus is not easily movable, which is important when local conditions change so abruptly in space such as the herein treated channel flows. With the presence of boulders and bed forms the installation of such equipment in a flume is not easy. Regarding LDA, hidden (shadow) areas of the flow hinder the penetration of the laser light.

Electromagnetic Current Meters (ECM) use the Faraday principle of electromagnetic induction, stating that the voltage produced by water moving in a magnetic field is proportional to the velocity of the water (*MacVicar et al.* 2007). ECM is used in laboratory and field research (*Roy et al.* 2004), for 2D velocity measurements. This instrumentation is robust, but too intrusive and thus disturbing the flow (*Voulgaris and Trowbridge* 1998).

Pitot probes (*USBR* 1980), commonly used for field measurements, are also too intrusive. Furthermore the risk of damage is high when used in shallow flow with intense sediment transport.

Particle Image Velocimetry (PIV) and Particle Tracking Velocimetry (PTV), particularly Large-Scale Particle Image Velocimetry (LSPIV), are techniques for measuring velocity fields based on image analysis, i.e., tracking light particles transported by the flow. PIV uses a laser to illuminate particles transport by a thin layer in the flow (*Raffel et al.* 1998; *Pokrajac et al.* 2007), while LSPIV uses only light particles transported on the water surface (*Fujita et al.* 1998; *van Prooijen and Uijttewaal* 2002; *Jodeau et al.* 2008; *Muste et al.* 2008; *Kantoush et al.* 2011; *Mattioli et al.* 2012). The light particles on the surface are representative of the surface flow velocity and recirculation cells with signatures at the free surface (*van Prooijen and Uijttewaal* 2002) and can be applied in shallow water, where the horizontal velocity is predominant and greatly exceeds the vertical velocity. These applications need extremely controlled light conditions and special equipment, and in the presence of intense sediment transport, they present problems in the identification of tracking particles.

If the reach average bulk velocity has to be known, as was the case in our research project, tracer tracking techniques are sufficient (*Ghilardi and Schleiss* 2011, 2012). These

techniques are applicable in both the field (*Calkins and Dunne* 1970; *Church and Kellerhals* 1970) and the laboratory (*Cao* 1985; *Rickenmann* 1990; *Weichert* 2005; *Recking et al.* 2008b). Four types of tracer exist: salt, dye, other traceable chemical compounds and radioisotopes (*Church and Kellerhals* 1970). The first two tracer types are the most widely used. The tracer travel time can be calculated either between the injection point and the measurement point (*Calkins and Dunne* 1970) or between two or more sampling positions (*Rickenmann* 1990; *Recking et al.* 2008b). The latter method is generally used for laboratory experiments.

In salt tracer velocity measurement, a slug of salt solution is injected into the water, and the water conductivity increases due to the passage of the salt cloud. This change in conductivity can be recorded at one or more measurement cross-sections by means of electrode couples, providing conductivity–time curves. These electrode couples are often formed by two vertical metal strips attached to opposite walls of the channel at a selected cross-section (*Smart and Jäggi* 1983; *Weichert* 2005). In the case of high temporal bed variability (vertical fluctuations), the electrodes need to be long enough to accommodate the changes in the bed level. The fluid velocity can be calculated as the distance between two cross-sections divided by the travel time of the tracer cloud between them. The starting point of conductivity increase is generally clearly defined. The identification of the end point is often difficult because the tail of the curve can be relatively long (*Day* 1976; *Rickenmann* 1990). This is also the case when working with dye as a tracer. Water conductivity can also be measured by conductivity-meter probes, which measure the change in conductivity between two electrodes placed only few millimetres apart from each other. Since intrusive and local, the choice of a representative point for the measurement is needed. In our study, we used vertical metal strips attached to the flume walls to carry out conductivity measurements, in order to obtain average values over the cross-section.

Video camera-based techniques are often used in hydraulics research to estimate flow velocities (*Le Coz et al.* 2010; *Mattioli et al.* 2012) and concentration fields (*Thomas and Marino* 2012; *Nogueira et al.* 2013). Dye tracer velocities can be estimated by means of video analysis. *Recking et al.* (2008b) described the introduction of a slug of colorant in a

flume and the analysis of the passage of the cloud between two positions in the flume using two video cameras (recording at 20 frames per second) placed 4 meters apart from each other at the flume surface. Only two cross-sections were thus analysed. The two camcorders must be perfectly synchronised for the travel time to be calculated correctly. *Recking* (2006) reported that for highly turbulent flow (Re>6000), no infiltration of the colorant in the bed was observed; thus, no delay in the tracer release was introduced. He emphasised that for steep slopes (9%) and small relative water depths, the signal can be quite noisy due to the rapid changes in light conditions induced by the fluctuating water surface. Nevertheless, the shape of the concentration curve remains the same. The video was analysed in grey scale, and the colorant plume was identified by a peak in grey scales (the image becomes darker). The peak velocity was used by Recking to estimate the bulk velocity.

Tracer tracking measurements over time at one fixed position provide three types of information: the initial rise in concentration, the peak concentration and the centre of mass of the tracer cloud. According to *Calkins and Dunne* (1970), the initial rise in concentration is a measure of the maximum velocity through the channel reach. The peak in concentration is commonly used to obtain the travel time and sometimes to estimate the bulk flow velocity. *Calkins and Dunne* (1970) and *Church and Kellerhals* (1970) claim that the time delay of the centroid of the concentration curve between two points represents the mean residence time of the tracer in the reach between the aforementioned points and thus can be used to estimate the mean velocity in the reach. Researchers primarily use centroid velocities to estimate bulk flow velocities (*Church and Kellerhals* 1970; *Davies and Jäggi* 1981; *Smart and Jäggi* 1983; *Rickenmann* 1990; *Weichert* 2005), although some researchers use the peak tracer concentration (*Cao* 1985; *Recking* 2006; *Recking et al.* 2008b). *Cao* (1985) compared the velocities estimated using the peak and the centre of mass of the salt solution and those estimated from WD measurement and found that velocities estimated using the peak of the conductivity travel time were closer to those estimated from WD measurement. He attributes this outcome to the presence of "dead zones", characterised by small longitudinal velocities, that result in slow release of the tracer after the passage of the main flow and the formation of long tails in the conductivity

curves (*Cao* 1985). According to *Day* (1976) and *Church and Kellerhals* (1970), gross errors in salt tracking can occur if the electrode is placed in a zone with no longitudinal velocity component (a dead zone) in the stream.

The main difficulty with the salt and dye tracer techniques is the choice of representative cross-sections for the measurements, as discussed in the introduction. For instance, if the measurement is carried out in a section where a dead zone is present, the final result could be strongly affected. A new method for analysing a whole reach at once is thus presented in this study.

Table 4.1 summarises a critical assessment stating the main advantages and drawbacks of the aforementioned techniques for conditions where channel bed morphology is quite heterogeneous, the roughness elements have low submergence and intense bedload occurs. The intrusiveness criterion is relevant for small flow depth. Intrusive methods would influence largely the flow conditions and the bed morphology. The sediment transport criterion addresses both the bedload and the suspended load. It indicates if the presence of sediment transport would be a problem for the integrity of the technique and for the field of view of this (i.e., LDA). The number of measures criterion refers to the sampling grid density necessary to obtain bulk average velocities which may be time consuming and difficult to position in shallow flows. The spatiotemporal variability, including the presence of protruding boulders, is a problem for all the techniques requiring a regular sampling grid. The presence of dead water zones complicates the choice of a representative cross-section. This is especially the case for tracer tracking between two fixed sections, since the position of dead water zones varies in space and time in a way that measurement positions are influenced. Finally, the presence of air in the flow, which may be relevant immediately downstream of boulders, would be a main drawback for some of the measurement techniques.

Table 4.1: Comparison of the advantages (√) and drawbacks (x) of the mentioned techniques to estimate bulk flow velocity in open channel flows. In section 4.5 WD, UVP, and Salt (metal strips) are compared with the technique herein developed: Dye (1 reach).

Method	Advantages (√) / Drawbacks (x)					
	Intrusiveness	Sediment transport	Number of measures	Spatiotemp. variability	Dead water zones	Aeration
Water depth	√	x	√	x	√	√
Micro-propeller	x	x	x	x	x	x
ADV	x	x	x	x	x	x
UVP	x	x	x	x	x	x
ADVP	x	x	x	x	√	x
ADCP	x	x	x	x	x	x
Hot wire	x	x	x	x	√	x
LDA	√	x	x	x	√	x
ECM	x	x	x	x	x	x
Pitot probe	x	x	x	x	x	x
PIV/LSPIV	√	√	√	√	x	√
Salt (probe)	x	√	x	x	x	√
Salt (metal strips)	√	√	√	√	x	√
Dye (2 sections)	√	√	√	√	x	√
Dye (1 reach)	√	√	√	√	√	√

4.3 Experimental details

The velocity measurement technique presented herein was developed within the framework of a research project focused on analysing the impact that randomly distributed relatively immobile boulders have on sediment transport in steep-slope rivers. This research was carried out using mobile bed laboratory experiments conducted using a tilting flume 8 m long (with a usable length of 7 m) and 0.25 m wide (Figure 4.1) at the Laboratory of Hydraulic Constructions (LCH) of the Ecole Polytechnique Fédérale de Lausanne (EPFL) (*Ghilardi and Schleiss* 2011, 2012).
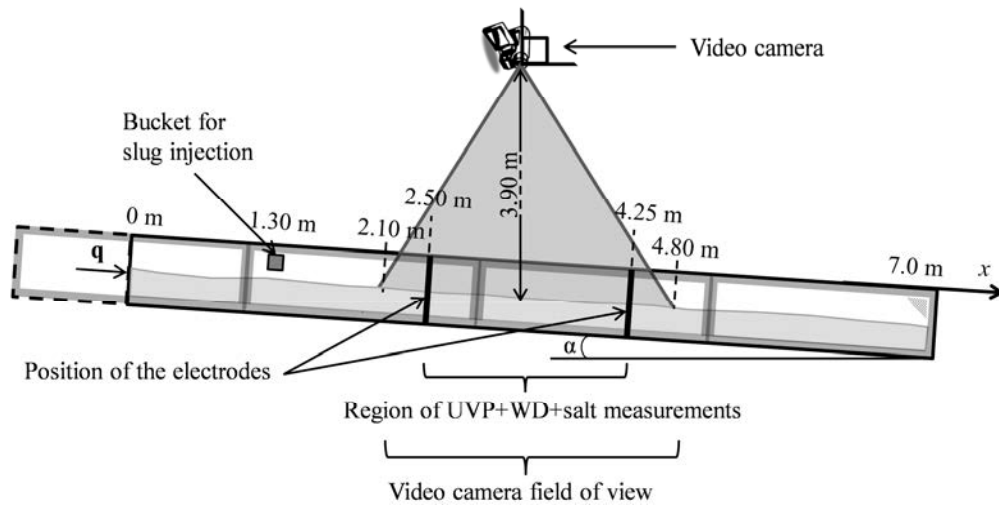
Figure 4.1: Sketch of the measurement zones.

For the comparison with the standard velocity measurement techniques, the flume slope was set to α=1.97% to produce a high water depth but no sediment transport. Water discharge, fed constantly by a closed pumping system, was measured using an electromagnetic flow meter ($\pm$0.01 l/s). A plane bed was prepared with sediments with the following grain size distribution characteristics: d_m=d_{65}=11.9 mm, d_{30}=7.1 mm, and d_{90}=19 mm, where d_m is the mean grain size, corresponding to d_{65}, and d_x is the grain size diameter at which x% by weight of the sediments are smaller. During the experiments, no sediment transport occurred; thus, no bed forms were observed.

In the case of a plane bed test without boulders, flow velocities were measured by four techniques for three different discharge rates: 5.0 l/s, 7.25 l/s and 9.5 l/s. This range was chosen to yield a sufficiently high water depth for UVP measurement (37 mm on average for Q=5.0 l/s) on the one hand and avoid local scouring downstream of boulders and sediment transport (limiting the discharge to Q=9.5 l/s) on the other hand. UVP and WD measurements yielded estimates of the flow velocity for a given cross-section. For both methods, 17 cross-sections, spaced 0.1 m apart longitudinally, were gauged at distances between 2.55 and 4.25 meters from the flume inlet (see Figure 4.1). The water and bed levels were measured at 12 equally spaced locations — thus, every 0.02 m— across every section using a point gauge. Three 4-MHz UVP probes were placed in the cross-section, at the middle, first quarter and third quarter of the flume width (0.25 m), at an angle of 20°

with the vertical. The depth-averaged velocity profiles were used to calculate the bulk average cross-sectional velocity.

For the salt velocity measurements, two couples of electrodes were placed on the flume wall, 1.75 m apart from each other in the streamwise direction (at 2.50 m and 4.25 m from the flume inlet), as shown in Figure 4.1, to measure the conductivity of the water.

For the fourth velocity measurement technique, developed in the present research, a single video camera was used (see Figure 4.1). The camera was positioned horizontally above the flume, approximately 3.9 m above the water surface. The area within the camera field of view was slightly larger than the flume domain measured by the other systems, between 2.10 m and 4.80 m from the inlet of the flume. Spotlights on the laboratory ceiling were systematically lightened during the experiments, but ambient light from outside the laboratory was also present. More details on this technique are given in section 4.4.

Slug injections of dye (potassium permanganate, which has a dark violet colour) and salt were conducted at the same time. A mixture of water, salt and dye was injected in the flume instantaneously through the whole flume width, using a tilting bucket with a volume of approximately 200 ml, located 1.3 m from the inlet. The amount of dye and salt added is not relevant to the velocity measurements because the only requirements are that the salt peak is well defined and that the dye contrast is sufficient to be visible in the videotapes. For each tested discharge rate, the procedure was repeated five times, and the average velocity value was calculated. Visual observations of the colorant injection confirmed good and rapid vertical mixing. The problem of slow transverse mixing was solved by injecting the tracer simultaneously across the whole width of the flume. In the longitudinal direction, the velocity of the colorant is equivalent to the velocity of the flow after the advective zone (where an equilibrium is established between the effects of velocity shear and turbulent diffusion (*Rutherford* 1994). Thus the colorant injection point should be selected carefully relatively to the field of measurements. In our case, the field of view of the camera was downstream of the advective zone. This is confirmed by the validation of the velocity measurement made with other techniques further in this text. Since a large flume reach (0.25x2.70 m^2) is globally assessed by our technique, dead zones do not present a concern.

When channel velocity measurements were carried out with boulders present, only tracer techniques (salt and dye) were used. WD measurements were not feasible because of the presence of hydraulic jumps and rapid local variations in the water surface. UVP could not be used for the same reasons and because of the difficulty of sampling with a regular grid in the presence of boulders. Tests were conducted for two dimensionless distances between boulders, $\lambda/D=2$ and $\lambda/D=3$, where λ is the average distance between boulders and D is the boulder diameter. Boulders with $D=0.1$ m were used in these tests. Bed sediments covered approximately half of the boulders' height.

4.4 Dye tracking velocity measurement technique

4.4.1   Video camera setup

A tracer-based velocity measuring technique using one video camera (a SONY DCR-HC48E, 24 frames per second, 576x720 pixels) covering a wide domain of the channel (0.675 m^2, as described in section 0) is herein described and compared with other velocimetry methods. This technique differs from other dye-tracer based methods described in the literature in which two cameras are used and the velocity is estimated by analysing correlated concentration time signals acquired simultaneously at the two camera positions (*Recking et al.* 2008b). That is, the measurement technique developed in this study takes into account a whole channel reach, rather than only what happens on average between two cross-sections, as do standard salt tracking methods and the dye method presented by *Recking et al.* (2008b). This allows avoiding the problem of dead water zones, which can develop during mobile bed experiments at the position where the measurement equipment (video camera or electrodes, according to the method) is initially placed.

Reference bars (see Figure 4.2a) placed transversally on top of the flume permit adequate longitudinal image scaling, which compensates for the distortion due to the inclination and the position of the flume with respect to the camera. The lenses distortion has not been considered, because a longitudinal correction is already done based on the position of the

reference bars with respect to the centre of the image. The latter has a known position along the flume. The camera is aligned with the flume axis and the flow occurs from left to right in the video, thus every vertical column of pixels in a frame corresponds to a cross-section in the flume. This means that approximately 720 cross-sections are measured in a stretch of approximately 2.7 m, yielding a cross-section every 4 mm.

4.4.2   Video analysis and velocity estimation

Recorded video images can be treated in various colour spaces to identify the colorant and calculate an intensity curve with respect to time: greyscale (as used by (*Recking et al.* 2008b), RGB (Red/Green/Blue), CYMK (Cyan/Yellow/Magenta/blacK), HSL levels (Hue/Saturation/Luminosity), single colours, or a combination of these options.

Greyscale and RGB-scale images (obtained through analysis of the RGB Euclidean distance, ED_{RGB}, as described below) were applied and compared in the present study. Two types of greyscale analysis were used: Grey Levels (GL) method and Cross-section Grey Levels (CSGL) method.

To determine the dye concentration over time, using the Grey Levels (GL) method, the image is converted into grey scale, and then only the value of every pixel where colorant is found is taken into account. An average concentration is calculated over time (frames) for every cross-section (column).

In the Cross-Section Grey Level (CSGL) method, the image is also converted into a greyscale image. However, unlike in the GL method, the whole flume width, including the area where colorant is not present, is taken into account in calculating the average grey-level value, according to the procedure used by *Recking et al.* (2008b). This approach was adopted for all of the frames and was applied to approximately 720 cross-sections. In this respect, the approach taken differed from the two-section analysis approach used by *Recking et al.* (2008b). A data analysis is needed in order to identify the part of the dye intensity curve indicating the presence of colorant (greyscale levels 10% darker than the base image), especially to identify the end of the cloud, given the long tail of the curve (cf. section 4.1).

For the RGB analysis, a base RGB image that serves as reference is obtained by averaging 10 frames before the colorant arrival. Every pixel thus has an average base RGB value. In the subsequent frames, when colorant is identified in a pixel, the RGB Euclidean distance (ED_{RGB}, eq. (36)) is calculated as follows:

$$ED_{RGB}(t) = \sqrt{(R(t)-R_b)^2 + (G(t)-G_b)^2 + (B(t)-B_b)^2} \qquad (36)$$

where the index b indicates the RGB value of the base image and t denotes the time. Only pixels where the dye tracer has been identified are used.

In order to detect the presence of colorant, several colour maps, such as the RGB colours, the grey level values, and the HSV values, were analysed and compared visually with the video images. Then, a criteria based on a combination of minimum and maximum values of these colour scales was established to indicate the presence of colorant. This thorough procedure is made for each experimental configuration (same light conditions and hydraulic conditions, for the same camera position), and assumed valid through the entire duration of the experiment.

For the calculation of the colorant concentration in the images, a base image without colorant and the image with colorant were compared. In turbulent flows, the velocity distribution is almost uniform within the flow depth, thus detection of the dye intensity may be considered representative of the total colorant concentration in the vertical layer and not only of the flow surface.

Table 4.2 summarises the characteristics and the differences between the aforementioned video analysis methods.

Table 4.2: Comparison of the video analysis techniques used.

Video analysis method	Colour scale	Colour intensity	Pixels used
ED_{RGB}	RGB	Eq. 1	only those with dye
GL	grey scale	grey level	only those with dye
CSGL	grey scale	grey level	entire flume width

Figure 4.2a shows a frame with colorant in the presence of boulders, and Figure 4.2c illustrates the coloured flow with a side view of the flume. Figure 4.2b shows in white the pixels where colorant has been detected during the video analysis. In some regions, the colorant could not be identified because of the reflection of light on the water surface. However, this corresponds to an average error in colorant concentration below 10% on a cross-section.
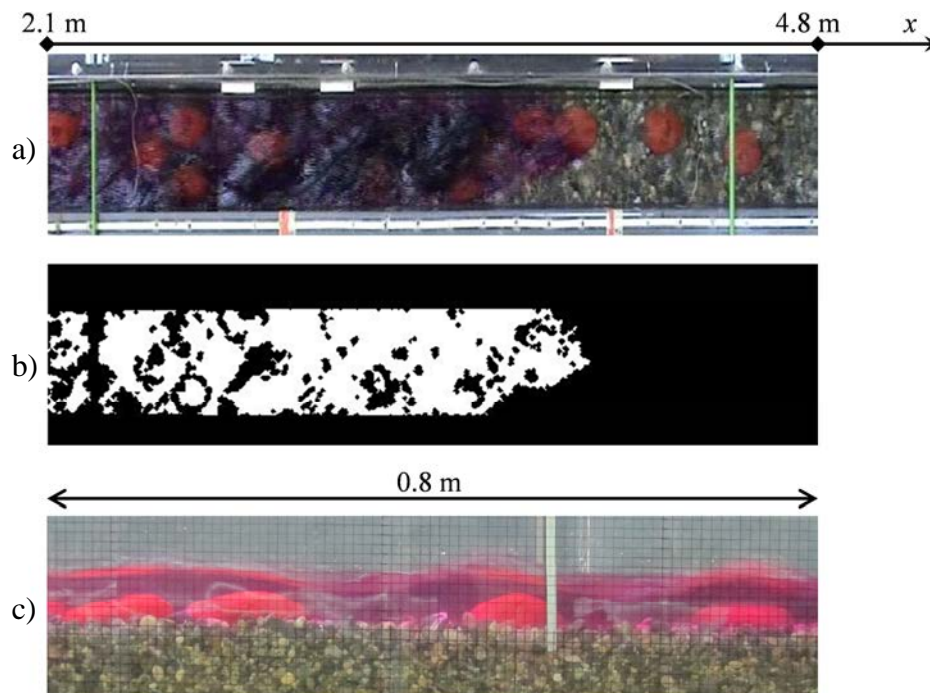
Figure 4.2: (a) An example of a video frame with colorant. (b) The white pixels are those where colorant was detected in the video analysis, for the same frame shown in part (a). (c) Image of a side view of the flume (0.8 m reach) with colorant. Boulders are coloured in red and the dye is purple.

For every cross-section, the average colorant concentration is calculated as a function of time. Time series were obtained for all of the video analysis techniques mentioned, namely, ED_{RGB}, GL and CSGL. As mentioned previously, methods for estimating flow velocity from concentration time series use as a reference either the peak value (estimating the time between peaks measured at two different positions) or the time corresponding to the centroid of the curve (estimating the time between centroids measured at two different positions) (*Calkins and Dunne* 1970). Both methods are applicable to our technique and are demonstrated and discussed herein.

The position of the centroid of the curve over time is calculated at every cross-section, and the time corresponding to the peak is registered. Figure 4.3a presents a typical colorant concentration evolution over time, exemplified for ED_{RGB}, for three different longitudinal positions along the channel. The concentration curve is also sketched in Figure 4.3a. From one position in the flume to another, there is a shift in time and a decrease in the maximum concentration (the maximum ED_{RGB} value). For every curve, a T_{peak} can be identified. Examining the curve corresponding to the cross-section at 3.59 m, one can see that defining T_{peak} may be challenging due to the scatter of the points. For every concentration curve, a centroid is calculated, producing a corresponding time T_{CDM}. These two characteristic times are obtained for every cross-section. The centroid is clearly delayed with respect to the peak. Although in the front of the cloud the colorant may not be fully distributed across the section (cf. Figure 4.2a), potentially biasing the results towards the cross-section maximum velocities, this does not seem relevant to concentration distribution, as seen in the first points captured in Figure 4.3a.

Figure 4.3b shows the time for the centroid for every position in the flume assessed longitudinally by the camera for the five slug injections conducted at a discharge rate of Q=5.0 l/s without boulders present. The data are clearly aligned, and the results of the five colorant injections collapse well. The slope of the graphic corresponds to the centroid velocity, which corresponds to the mean flow velocity. For T_{peak}, the same procedure described for Figure 4.3b is applied. The technique employed for greyscale values (GL and CSGL) follows the same steps as those for ED_{RGB} video analysis.

4.5 Results and discussion

To validate the velocity measurement techniques described in this study, the techniques are compared with three methods widely used to estimate open-channel flow velocities: salt tracer (using the centroid S_{CDM} and peak S_{peak} methods), Ultrasonic Velocity Profiler (UVP) and Water Depth based (WD) measurement. In the presence of macro-roughness elements, the techniques described in section 4.4 can be compared only to the salt tracer method, due to difficulties associated with using the two other methods (cf. section 4.1 and

Table 4.1). Table 4.3 shows the results of velocity measurements obtained for flows in the flume with and without boulders, along with those obtained with the other techniques and with the colorant-based methods.
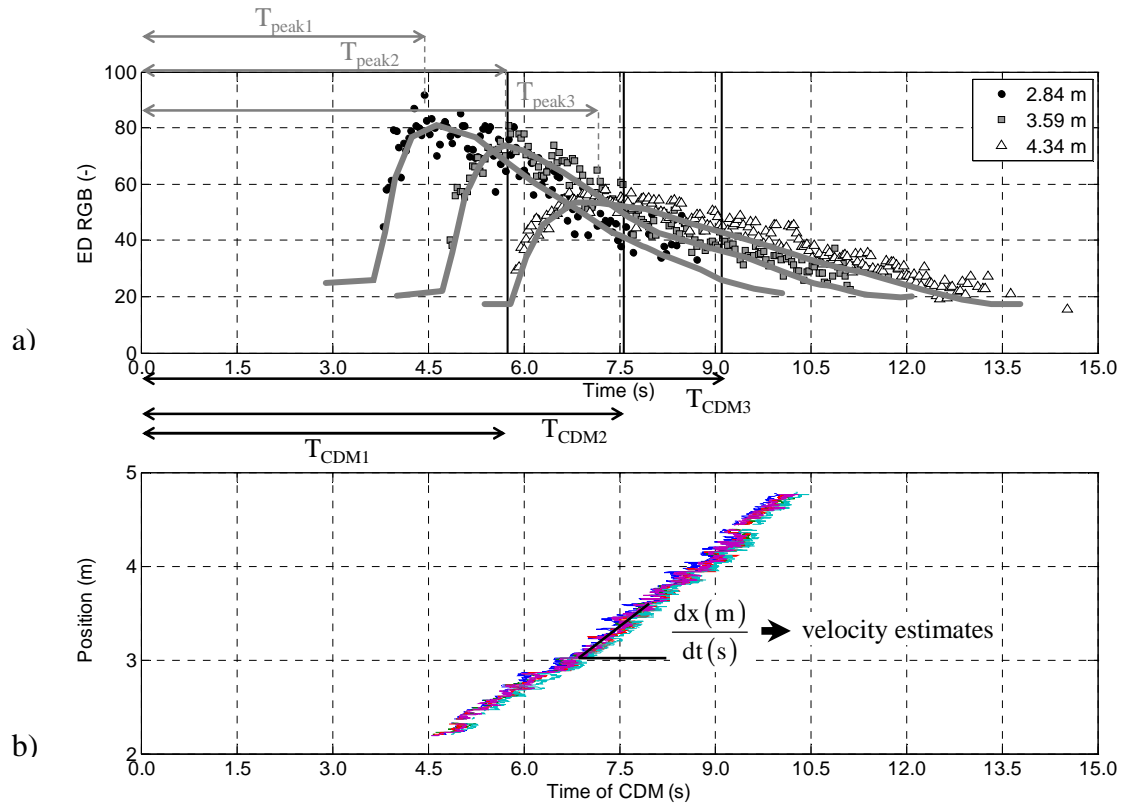
Figure 4.3: (a) An example of RGB Euclidean distance (ED_{RGB}) time evolution for cross-sections at 2.84 m, 3.59 m and 4.34 m (for colorant injection without boulders at a discharge rate of 5.0 l/s). The time of centroids (T_{CDM}) and of peaks (T_{peak}) are identified on the graph. A sketch of the concentration curve is given for each cross-section. (b) Position of the centroid CDM over time, estimated for each longitudinal position for the five colorant injections.

For measurements carried out without boulders, flow velocities calculated with WD are slightly higher than those obtained with UVP. Table 4.3 clearly shows that in the absence of boulders, the peak velocity is closer to the WD velocity, while the centroid velocity is closer to the UVP velocity for all tracer analysis methods. The relative channel roughness is high (the d_m/h is between 0.18 to 0.50, where h is the water depth); thus, large errors in the WD measurements and consequently in the velocity calculations are expected.

In general, the peak velocity results obtained with the salt injection method and the three video analysis techniques are similar. The same can be said for the centroid velocity estimates.

In the presence of boulders, the salt tracking method is considered to yield adequate velocity estimates. In this case, the peak and centroid velocities also correspond well for both tracers.

The differences between the peak and centroid velocities are smaller for the measurements obtained without boulders present. The increase in the differences in the velocities measured in the presence of boulders is most likely due to the impact of dead zones with low longitudinal velocities that are present downstream from boulders. This phenomenon is even more visible in the presence of sediment transport because of the scouring holes and recirculation zones that form downstream from boulders.

Table 4.3: Results of mean velocity (m/s) measurements for the three techniques WD, UVP and salt (peak S_{peak} and centroid S_{CDM}) and the centroid and peak velocity for the colorant-based video analysis technique: ED_{RGB} (RGB Euclidean Distance), GL (Grey Levels) and CSGL (Cross-Section Grey Levels).

		Q (l/s)		
		5.00	7.25	9.50
Without boulders	WD	0.53	0.62	0.72
	UVP	0.47	0.61	0.69
	S_{CDM}	0.48	0.55	0.66
	S_{peak}	0.52	0.66	0.74
	$ED_{RGB,\ CDM}$	0.46	0.57	0.65
	$ED_{RGB,\ peak}$	0.51	0.67	0.76
	GL_{CDM}	0.41	0.51	0.56
	GL_{peak}	0.51	0.67	0.76
	$CSGL_{CDM}$	0.48	0.55	0.61
	$CSGL_{peak}$	0.52	0.65	0.74

		Q (l/s)		
		5.00	7.25	9.50
With boulders	S_{CDM}	0.37	0.50	0.62
	S_{peak}	0.45	0.63	0.66
$\lambda/D=2$	$ED_{RGB,\ CDM}$	0.34	0.46	0.59
	$ED_{RGB,\ peak}$	0.45	0.61	0.73
	GL_{CDM}	0.28	0.40	0.52
	GL_{peak}	0.44	0.61	0.72
	$CSGL_{CDM}$	0.36	0.43	0.51
	$CSGL_{peak}$	0.45	0.61	0.74
	S_{CDM}	0.32	0.44	0.53
	S_{peak}	0.34	0.65	0.72
$\lambda/D=3$	$ED_{RGB,\ CDM}$	0.32	0.43	0.56
	$ED_{RGB,\ peak}$	0.47	0.64	0.72
	GL_{CDM}	0.27	0.37	0.49
	GL_{peak}	0.42	0.62	0.72
	$CSGL_{CDM}$	0.38	0.43	0.54
	$CSGL_{peak}$	0.39	0.60	0.72

Table 4.4 compares the video analysis methods developed (ED_{RGB}, GL and CSGL) with the other techniques. A variable Δ is introduced to express the deviation between the colorant-based velocity estimates ($v_{i,C}$) and the estimates obtained with the other methods ($v_{i,M}$). This parameter Δ takes into account the ensemble of the three discharges tested by means of a dimensionless averaged difference and is calculated as follows (eq. (37)):

$$\Delta = \frac{1}{3}\sum_{i=1}^{3}\left|\frac{v_{i,C} - v_{i,M}}{v_{i,M}}\right| \tag{37}$$

where M indicates one of the measurement techniques (S_{peak}, S_{CDM}, UVP or WD) used for comparison with the colorant technique C and i indicates the discharge (from one to three). The absolute difference in the velocity values is normalised with respect to the result of the comparison technique. The average of the differences for every discharge is then used to validate the colorant techniques.

Table 4.4: Velocity differences Δ (eq. (37)) between the colorant-based velocity measurements (ED_{RGB}, GL and CSGL) and the other techniques (S_{peak}, S_{CDM}, UVP and WD). Velocity values are given in Table 4.3. In the vertical the grey cells correspond to the best result between ED_{RGB}, GL and CSGL and the other techniques.

| | | Δ without boulders | | | | Δ with boulders | | | |
| | | | | | | $\lambda/D=2$ | | $\lambda/D=3$ | |
		S_{CDM}	S_{peak}	UVP	WD	S_{CDM}	S_{peak}	S_{CDM}	S_{peak}
ED_{RGB}	CDM	0.030	0.121	0.051	0.105	0.069	0.205	0.017	0.202
	Peak	0.143	0.022	0.096	0.053	0.213	0.049	0.423	0.133
GL	CDM	0.129	0.225	0.164	0.212	0.202	0.318	0.129	0.316
	Peak	0.139	0.021	0.092	0.051	0.193	0.050	0.349	0.088
CSGL	CDM	0.031	0.137	0.074	0.123	0.107	0.241	0.077	0.234
	Peak	0.125	0.006	0.079	0.028	0.210	0.054	0.314	0.070

The results presented in Table 4.4 show that the ED_{RGB} estimates for the centroid velocity are closer to the results obtained by salt tracking (and to UVP in the absence of boulders, in grey in Table 4.4) than the estimates obtained by GL and CSGL analysis for the same characteristic time. For peak velocities, the CSGL video analysis method results are generally closer to the salt tracking peak (S_{peak}) velocity and to the WD results (in the absence of boulders).

As mentioned in section 4.1, most researchers agree on the use of the centroid velocity to evaluate average flow velocities. Thus, the RGB Euclidean distance (ED_{RGB}), seems to be the best video analysis method, if the salt tracking centroid is taken as a reference.

With the technique developed in this study, using a single camera visualising a 2.70-m-long reach, local changes in velocity caused by the presence of boulders may be analysed. Furthermore, this measurement setup avoids the problems associated with selecting suitable cross-sections for measurements. With both salt tracer and dye tracer methods (using two video cameras), depending on the cross-sections selected, the presence of dead zones at the electrodes or the camera location can have an impact on the velocity estimation, as explained by *Day* (1976). Lastly, during sediment transport experiments, gravel bars are generally present in similar experiments and can occupy up to half of the flume width (*Ghilardi and Schleiss* 2012). Conductivity signals during measurements with the salt injection method are attenuated by the presence of such gravel bars. The same applies to the video analysis technique described by *Recking et al.* (2008b), applied in this study using the CSGL method (see section 4.4) because it takes into account the whole flume width in the video analysis. The GL and ED_{RGB} techniques (see section 4.4) only analyse the part of the video where colorant has previously been detected, thus avoiding the weakening of the signal due to the flume's average cross-section, instead of the actual flow's average cross-section.

As can be seen in Figure 4.3b, there is a certain scatter in the time of arrival of the centre of mass at a given position. However, the error on dx/dt seems to be smaller than 5% for the $ED_{RGB, CDM}$. Our results are confirmed by other measurement techniques, confirming that the average velocity is tracked. However, the video should be captured downstream of the advective zone, as discussed above.

4.6 Conclusions

In steep channels, water depth and morphology vary rapidly. It is therefore difficult to select representative cross-sections for measurements. The use of classical tracer techniques to estimate velocities between two (or more) cross-sections partially avoids the

problem of cross-section selection. Nevertheless, it is necessary to avoid tracer measurements in dead water zones, which are often present in channels of this type. Measurements in dead zones produce long tails in tracer intensity measurements. The main advantage (cf. Table 4.1) of the method presented in this study is that it completely avoids this problem of cross-section selection. The position of the video camera allows the visualisation and analysis of an entire reach ($0.25 \times 2.70 \ m^2$) at one time. A global analysis of tracer transport can thus be conducted.

Three flow velocity estimation techniques based on video analysis of dye concentration were examined and validated. In the absence of macro-roughness elements, the results proved to be similar to those obtained with standard techniques such as Water Depth (WD) and ultrasonic velocity profile (UVP) measurements. Only the salt tracking method, which is widely used in steep flumes and mountain rivers, is also applicable in the presence of macro-roughness elements and was compared with the dye tracer technique for validation purposes. The method presented here proved to be valid, and the results were comparable.

Several video analysis methods were compared. The method developed in this study, which involves calculating the velocity of the centroid based on the RGB Euclidean distance ED_{RGB}, using only pixels with colorant, yielded the smallest differences with respect to the centroid velocity determined from salt injection. The latter is the most widely used technique for measuring water velocity in mountain rivers and steep channels.

Cross-Section Grey Level CSGL analysis using the whole image was found to yield results that are similar to peak velocities determined from salt injection. Because the whole cross-section is analysed in this data analysis method, the calculation is faster. However, gravel bars occupying more than half the cross-section are often present when working with a mobile bed and sediment supply on steep slopes. In this case, the amplitude of the signal is reduced. The presence of gravel bars covering the electrodes has the same impact on conductivity measurements when working with a saline tracer. This problem can be avoided using the measurement system and data analysis described in this study, which involves using the whole reach and analysing only the part of the cross-section where colorant is identified.

Other advantages of this innovative velocity measurement system are its simplicity and versatility. A simple video camera is used. The camera is positioned with the flow visualised in the horizontal video axis at a height of approximately 3.9 m above the water surface. The videotapes obtained are analysed by means of a computational procedure. No special light conditions are needed. Direct light on the flow must, however, be avoided and the image must not be too dark; otherwise, the dark colorant (violet ink) might not be identified. The applicability of this velocity measurement technique to field measurements in small shallow mountain rivers could also be explored. However, depending on the local conditions (vegetation, light conditions, surface pattern, etc.) it may be difficult to place the camera in order to visualise a long river reach. Finally, adequate vertical and transversal mixing of the colorant and assuring that the video is taken out of the advective zone are important issues in field measurements.

Chapter 5

Bedload fluctuations in a steep channel

This chapter analyses in detail the cyclic fluctuations of hydraulic and morphologic characteristics throughout one long duration experiment. The analysis of the pulses is carried out from several points of view: time series observation, correlation functions, phase analysis and visual observations of bed states corresponding to various bedload stages. Finally, sediment transport equations are applied to the data and compared to measured bedload fluctuations. Appendixes to this chapter are given at the end of the latter.

Abstract: Bedload fluctuations have been observed over time in steep rivers and flumes with wide grain size distributions even under constant sediment feeding and water discharge. Observed bedload pulses are periodical and a consequence of grain sorting. Moreover, the presence of large relatively immobile boulders often present in mountain streams, such as erratic stones, has an impact on flow conditions. The detailed analysis of a 13 hours laboratory experiment is presented in this chapter. Boulders were randomly placed in a flume with steep slope (6.7%) and water and sediment were constantly supplied to the flume. Along with sediment transport and bulk mean flow velocities, boulder protrusion, boulder surface, and number of hydraulic jumps, indicators of the channel morphology, were measured regularly during the experiment. Periodical bedload pulses are clearly visible on this long duration experiment, along with correlated flow velocity and bed morphology fluctuations. The link between bulk velocity, morphology variables time evolution and bedload transport are analyzed by correlational analysis, showing that fluctuations are strongly related. A phase analysis for all the observed variables is performed where the average shape of time cycles of fluctuations are shown. Observations indicate that the detected periodical fluctuations correspond to different bed states. Furthermore, the grain size distribution through the channel, varying in time and space, is clearly influencing these bedload pulses. Finally, known bedload formulae are tested showing that only the use of a drag shear stress allows a correct estimation of the time fluctuations.

Key words: bedload fluctuations, boulders, steep rivers.

5.1 Introduction

Flow conditions and sediment transport are well studied for lowland mild slope rivers. On the contrary, only relatively few studies were made on steep mountain channels, mainly during the last two decades. Steep channels are a subset of mountain rivers and are typically characterized by longitudinal slopes larger than 4-5% (*Comiti and Mao* 2012) and by channel beds composed of coarse mobile sediments and large, relatively immobile, blocks or boulders (*Rickenmann* 2001; *Papanicolaou et al.* 2004; *Yager et al.* 2007). Boulders can be found in steps crossing the whole channel width (step-pool morphology) or in a more irregular manner (cascade morphology) (*Montgomery and Buffington* 1997). In these streams, the water depth is typically shallow in comparison to the roughness of elements such as the large isolated boulders. The latter are considered macro-roughness elements when the relative roughness, defined as the ratio between the roughness scale and the water depth, exceeds the unit value (*Bathurst* 1978). In coarse gravel bed streams, the grain size distribution of the transported bedload is similar to that of the bed material only for high flow intensities (*Wilcock and McArdell* 1993, 1997; *Lenzi et al.* 1999; *Rickenmann* 2001). Moreover, in these streams, water depth is small when compared to the roughness elements and large relatively immobile boulders, considered macro-roughness elements. These rivers, often called gravel or boulder bed streams, constitute an important part of the total water course in mountainous regions, since sediments mobilized on hillslopes transit through these high-gradient streams before reaching floodplains (*Yager et al.* 2007).

The presence of a wide grain size distribution in mountain rivers has an impact on bedload transport, inducing bedload fluctuations. In the last decades, several researchers studied bedload pulses in experimental flumes (*Iseya and Ikeda* 1987; *Frey et al.* 2003; *Bacchi et al.* 2009; *Recking et al.* 2009). *Iseya and Ikeda* (1987) showed that longitudinal sediment sorting occurs when a wide grain size distribution is constantly fed into a flume, and this segregation producing rhythmic fluctuations in the bedload transport rate. Sediment particle availability, modulated by longitudinal sediment sorting, determines the magnitude of sediment transport rate and how it pulses. According to *Iseya and Ikeda* (1987), two main factors cause sediment transport to fluctuate, namely migration of bedforms and

segregation of the surface grain size. *Recking et al.* (2008b) and *Recking et al.* (2009) carried out tests with uniform and wide grain size distribution and noticed that bedload fluctuations were not observed in setups with uniform grain size distributions, confirming that fluctuations are a consequence of grain sorting in graded sediments.

Frey et al. (2003) showed that fluctuating sediment discharge and grain size distribution are highly dependent. At the outlet of an experimental flume they observed that high solid discharges carried mainly fine grains, whereas the sediments were coarser during low solid discharge events. They also visually observed that a bed-armoring process was associated with transient antidune-like structures. These bedforms increased bed resistance and thus decreased solid discharge. The armoring layer was eventually destroyed, leaving a finer bed in place with practically no bedforms, the largest outgoing sediment discharges being observed at this moment. The cyclic change in bedforms and thus grain size distribution starts once again with the formation of the armoring layer.

Recking et al. (2009) suggested that peak solid discharges are caused by the formation and migration of bedload sheets. This phenomenon is accentuated in low flow conditions (small discharge) and is associated with fluctuations on bed slopes, bed load and bed state. They observed that bed aggradation is associated with reduced mobility for all the diameters and with a longitudinal and vertical grain sorting, resulting in a coarsening of the bed surface and fining of the subsurface. The local slope downstream of regions of aggradation was observed to increase to a maximum value, followed by an abrupt increase of gravel mobility. Coarse sediments are mobilized, and fine sediment previously hidden under the surface layer are transported. This increased mobility destroys the pavement downstream. The erosion of the bed stops when aggradation starts again from the flume upstream section.

The presence of boulders, acting as macro-roughness elements, disrupts the flow by altering the channel roughness. The boulders bear a significant amount of the total shear stress, thus reducing the stress available to move finer sediments (*Yager et al.* 2007). As underlined by *Lenzi et al.* (2006), when the roughness increases also the form drag increases, implying lower effective shear stress at the bed for sediment entrainment. A

shear stress partitioning method is pursued in the literature when the presence of macro-roughness elements is accounted for. Parameters needed for shear stress partitioning and bed resistance equations generally resume to the number of boulders, their cross-section, the bed area occupied by them, the distance between boulders and a drag coefficient (*Bathurst* 1978; *Canovaro et al.* 2007; *Yager et al.* 2007). *Yager et al.* (2007) suggested that only the part of the shear stress not acting on boulders will induce sediment transport, hence the presence of boulders decreases the sediment transport capacity (see also (*Ghilardi and Schleiss* 2011, 2012)). Boulder dimensionless distance λ/D (-), where λ (m) is the average distance between boulders of diameter D (m), and protrusion P_{av} (m) are thus good proxies for sediment transport in mountain streams (*Yager et al.* 2012b).

In step-pool rivers, the presence of hydraulic jumps downstream of steps was described by several authors (*Comiti and Lenzi* 2006; *Wilcox and Wohl* 2007; *Endreny et al.* 2011). Hydraulic jumps with breaking waves, as observed downstream of boulders, dissipate a high amount of flow energy, which is proportional to the drop height (*Comiti and Lenzi* 2006). *Curran and Wohl* (2003) state that spill resistance accounts for 90% or more of the total resistance in step-pool channels. The latter resistance is the resistance associated with flow accelerations and decelerations generated at steps in the step-pool streams where flow plunges from step to pool.

Boulders have rarely been taken into account in bedload transport experimental studies. To the authors' knowledge, before *Ghilardi and Schleiss* (2011, 2012), only *Yager et al.* (2007) carried out experiments on steep slopes in the presence of boulders protruding from the channel bed. Regularly spaced spheres and a uniform grain size distribution were used by these authors. Additionally, flow velocities are generally not measured in studies analyzing bedload pulses (as for example in (*Recking et al.* 2009; *Heyman et al.* 2013)).

The main general goal of the research project framing this chapter is to analyze the impact that randomly distributed boulders have on sediment transport capacity in steep slope rivers, being the specific objective of the present chapter the analysis of bedload pulses in one long duration experience. For that purpose, flume experiments were performed with constant water and sediment supply in the presence of boulders. Data presented herein are

based on the results of one long duration experiment performed on a steep channel (S=6.7%). Fluctuations in boulder protrusion, bed surface occupied by boulders, number of hydraulic jumps, and average flow velocity are observed. The relation between these variables is studied in detail in terms of time series, correlation functions, and phase analysis. Mechanisms of bedload fluctuations are described in detail and finally several sediment transport equations are applied to the data and compared with our results. Following the present introduction, the experimental methods are presented. Then results are analyzed and finally main conclusions are drawn.

5.2 Research methods

Bedload fluctuations are investigated by means of laboratory experiments, carried out on a steep (6.7%) 8 m long (7 m usable) and 0.25 m wide tilting flume (Figure 5.1a) at the Laboratory of Hydraulic Constructions (LCH) of the Ecole Polytechnique Fédérale de Lausanne (EPFL). Some boulders, with a mean diameter of 1/3 of the flume width (D=0.075 m) and herein defined as elements that are not transported by the flow, are placed in in the flume partially covered by mobile sediments. Water and sediments were supplied at the flume inlet. Measurements of bedload, flow velocity and several morphological parameters were performed as explained next.
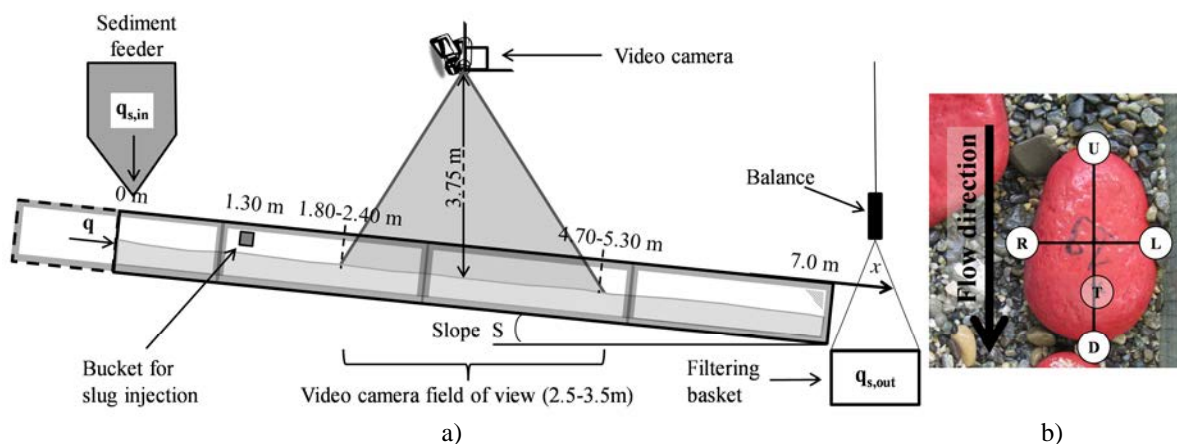
Figure 5.1: a) Sketch of the experimental setup. b) Points for measurement of boulder protrusion during the experiment. T indicates the position of the highest (top) point of the boulder. Upstream (U), downstream (D), right(R), and left (L) indicate, respectively, the points where the vertical distance with the top is calculated (TU, TD, TR, TL). The average vertical distance is the protrusion P.

Water discharge, fed constantly by the closed general pumping system of the laboratory, is measured by an electromagnetic flow-meter (± 0.01 l/s). Sediments are constantly fed into the system by a calibrated sediment feeder situated upstream. A filtering basket suspended to a balance recuperates the sediments at the outlet where the weight (± 1 kg) is measured every minute. The one minute interval sediment discharge measurement was then averaged over a 10 minute sliding window ($q_{s,out,10}$), to provide a smoothed overview of the bedload time evolution. Sediments are recirculated between the sediment feeder and the downstream basket. No sediment sorting was observed at the outlet of the feeder.

The protrusion P of four chosen boulders is measured with a point gauge during experiments, with a time interval of approximately 10 minutes (2-3 minutes per boulder, in a loop). P is calculated as the averaged vertical distances between: top and upstream (TU), top and downstream (TD), top and left (TL), and top and right (TR) (cf. Figure 5.1b), for every boulder at the edge with the gravel. For every measured boulder, protrusion P is sub-sampled by linear interpolation to have a value every minute. An average protrusion value between the boulders P_{av} is then calculated for every minute of the experiment. The protrusion is finally normalized with respect to the boulder diameter: $P^*=P_{av}/D$.

Flow average velocity U was measured every 15 minutes by means of a technique using dye-tracer and video analysis. For a detailed description of the technique herein used read Chapter 4. This technique, based on the analysis of a colorant (tracer) dilution, allows the measurement of mean bulk velocities through the channel reach. The passage of the cloud of colorant in the reach is analyzed based on the difference between images, the movement of mass center of the cloud defining the average flow velocity (cf. *Calkins and Dunne* (1970)). The average of five independent measures, based on five different colorant injections, is done in order to obtain a velocity value.

Hydraulic jumps HJ are counted manually based on visual observation after flow velocities measurements, i.e. about every 15 minutes. This parameter is an indicator of the amount of energy dissipation and of the morphological variety, since they generally appear downstream of protruding boulders. The number of hydraulic jumps HJ is scaled and normalized by the number of boulders in the flume N_{Bst}: $HJ^*=HJ/N_{Bst}$.

Surface occupied by boulders A_{Bs}, parallel to the river bed (top view), called in short "boulder surface", is obtained by means of video analysis. The calculation is done on a single frame about 5 times every 15 minutes, for the first part of the experiment. From minute 488, the video camera is recording continuously and boulder surface is calculated every minute. Boulders surface is scaled by the flume surface visible in the video, giving a dimensionless boulder surface A_{Bs}^{*}, representing areal fraction covered by boulders.

The grain size distribution of the supplied sediments is: d_{50}=9.3 mm, d_m=d_{65}=11.9 mm, d_{30}=7.1 mm, d_{84}=16.6 mm, d_{90}=19.0 mm, where d_m is the mean grain size, corresponding to d_{65} and d_x is the grain size diameter for which x% in weight of the amount of sediments have smaller diameters. Boulders are not taken into account in this calculation and are not supplied as mobile sediments; they were instead placed in the channel bed before the experiment. Boulders are relatively immobile, which means that they are not transported by the flow, although they may move even several times their diameter during experiments, due mainly to the scour hole formed around these.

A plane bed is prepared before the experiments and boulders are placed randomly into the flume (cascade morphology) half covered by mobile sediments, which corresponds to a protrusion equal to approximately 30% of the diameter (P^{*}≈0.3). The boulders were placed with an average dimensionless distance between boulders of λ/D=5, where λ is the average distance between boulders of diameter D=0.075 m. Water and sediment supply are started at the same time. During the experiment, flow velocity, boulder surface, and number of hydraulic jumps are measured about every 15 minutes. A_{Bs}^{*}, HJ^{*} and U are then linearly interpolated, in order to have a regular interval of 1 minute, the same measuring period used for sediment transport $q_{s,out,10}$.

A criterion to establish the relation between liquid and solid discharge was set, assuming the relative immobility of the boulders and imposing that the boulders always protrude after a burst in sediment transport. To ensure equilibrium conditions, we verified that the cumulative average of the outlet sediment transport was within ±15% of the sediment supply at the end of the experiment. The cumulative average of the outlet sediment

transport ($q_{s,out,av}$) is computed for a given instant T as shown in eq. (38), based on the one minute interval sediment transport.

$$q_{s,out,av}\left(T\right) = \frac{\int_0^T q_{s,out}(t)\mathrm{d}t}{T} \tag{38}$$

The present paper analyzes the fluctuations in sediment flux, bulk velocities and boulder protrusion observed throughout a long duration experiment (774 minutes, roughly 13 hours) on a steep flume (6.7%). The water discharge was set to q=1.68x10^{-2} m^{3}s^{-1}m^{-1} and the sediment supply to $q_{s,in}$=0.0563x10^{-3} m^{3}s^{-1}m^{-1}, both kept constant. The sediment density is ρ_s=2650 kgm^{-3}. Twelve boulders (N_{Bst}=12) of diameters D=0.075 m have been randomly placed in the flume, with an initial protrusion of 40%, this configuration corresponding to a dimensionless distance of λ/D=5 and to an occupation of 3% of the bed surface by the boulders.

5.3 Results

5.3.1 Time series analysis

During the experiment, cyclic fluctuations of bedload transport were observed. Both phenomena mentioned by *Iseya and Ikeda* (1987 and *Frey et al.* (2003), bedform migration and grain sorting, have been visually observed. Figure 5.2 shows the values measured for the long duration experiment, for sediment transport $q_{s,out,10}$, bulk velocities U, average boulder protrusion P^*, boulder surface A_{Bs}^*, and number of hydraulic jumps HJ^*. The range of values, mean and standard deviation of the fluctuating variables are given in Table 5.1.

Cyclic pulses in sediment transport $q_{s,out,10}$ observed throughout the experiment (Figure 5.2) are clearly coupled with the other measured variables. Table 5.1 shows that the measured sediment flux ranges from 0 to 0.2400x10^{-3} m^{3}s^{-1}m^{-1}, with an average value of $q_{s,in} \approx q_{s,out,av}$=0.0570x10^{-3} m^{3}s^{-1}m^{-1} and a standard deviation of 0.0517x10^{-3} m^{3}s^{-1}m^{-1}, which corresponds to a considerable value of 90% of the average. Four bedload bursts, corresponding to well defined peaks in the sediment transport rate, are clearly identified in

Figure 5.2. Low sediment transport periods ($q_{s,out,10} \leq q_{s,in}$) are longer than high transport periods, characterized by intense transport ($q_{s,out,10} \geq q_{s,in}$), being the sediment output $q_{s,out,10}$ smaller than the inlet during 63% of the time. For all the measured parameters, the increase from the lower value to the peak is faster than the decrease after the peak. This is especially visible in the sediment transport curve, which increases from close to zero to a maximum in 10 to 30 minutes, decreasing in a period of 50 to 70 minutes.

Table 5.1: Minimum, maximum and average values, standard deviation (σ) and ratio between standard deviation and mean values of sediment transport $q_{s,out,10}$, velocity U, boulder protrusion P^*, dimensionless boulder surface A_{Bs}^*, and the dimensionless number of hydraulic jumps HJ^*.

	range (min ÷ max)	mean	σ	σ/mean
$q_{s,out,10}$	$0 \div 0.2400 \times 10^{-3}$ m³s⁻¹m⁻¹	0.0570×10^{-3} m³s⁻¹m⁻¹	0.0517×10^{-3} m³s⁻¹m⁻¹	0.90
U	$0.39 \div 0.69$ ms⁻¹	0.53 ms⁻¹	0.06 ms⁻¹	0.11
P^*	$0 \div 0.51$	0.22	0.15	0.69
A_{Bs}^*	$0 \div 0.047$	0.016	0.012	0.75
HJ^*	$0 \div 0.58$	0.30	0.20	0.66

Figure 5.2: Time series of sediment supply ($q_{s,in}$), bedload at the outlet averaged over a 10 minutes window ($q_{s,out,10}$), and global bedload outlet ($q_{s,out,av}$) on the left-hand side axis. Time series of mean velocity (U), dimensionless average protrusion (P^*), dimensionless boulder surface (A_{Bs}^*), and dimensionless number of hydraulic jumps (HJ^*) on the right-hand side axis. Results for a long duration test (774 minutes), with boulders of diameter $D=0.075$ m, $\lambda/D=5$ (-), $q_{s,in}=0.0563 \times 10^{-3}$ m³s⁻¹m⁻¹, $q=1.68 \times 10^{-2}$ m³s⁻¹m⁻¹, $S=6.7\%$.

Fluctuations can be seen also for the other measured parameters. Boulder protrusion P^* ranges from 0 (boulders completely covered by the mobile sediments) to 0.51 (boulders largely exposed), with an average value of 0.22 and standard deviation of 0.15. As visible in Figure 5.2, peaks in protrusion take place clearly after peaks in sediment transport. During the experiment, rapid changes in bed morphology, and especially erosion and deposition around boulders, was observed (cf. Figure 5.3). Boulders were sometimes moved by falling into the scouring whole downstream of them, but they were never transported by the flow. The two pictures in Figure 5.3 are taken with one minute of interval, at instants 693 and 694 minutes from the beginning of the experiment. This period corresponds to a small peak in sediment transport, as seen in Figure 5.2.

Flow direction
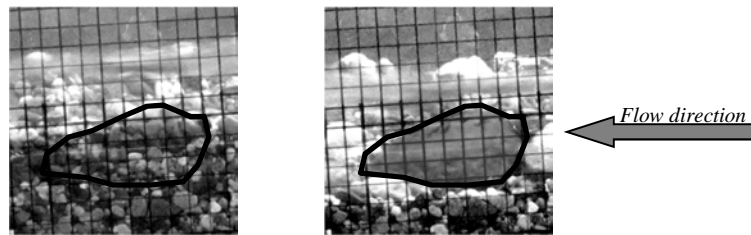
Figure 5.3: Example of erosion around a boulder after a small bedload peak ($q_{s,out,10} \approx q_{s,in}$): pictures correspond to instants 693 and 694 minutes. The black shape indicates the position of the boulder, as visible in the right hand side pictures.

Dimensionless boulder surface A_{Bs}^* fluctuates in phase with protrusion, as expected (cf. Figure 5.2). The link between P^* and A_{Bs}^* can be easily seen using a partially covered sphere as example: the projected surface increases as a function of diameter and protrusion when the latter is smaller than 0.5, as shown by _Yager et al._ (2007), remaining constant for higher protrusions. Since experiments are carried out with water-shaped boulders, the link between the surface and protrusion is less direct and cannot be expressed by a simple equation, but the principle remains the same. The boulder normalized surface ranges from 0 to 0.047, with an average of 0.016 and a standard deviation of 0.012.

The temporal evolution of the number of hydraulic jumps HJ^* is also clearly related to the average boulder protrusion, fluctuating in phase with it. The protrusion downstream boulders is 1.5 times bigger than the protrusion upstream, as shown in _Ghilardi and Schleiss_ (2012). As the average protrusion increases, we visually observed that the size of

scouring holes does, too, causing the formation of hydraulic jumps downstream of macro-roughness elements. Rarely hydraulic jumps are present in other places. Between 0 and 58% of the boulders can have hydraulic jumps downstream of them, depending on the average protrusion of the boulder. On average, hydraulic jumps are present downstream of 30% of the boulders. The presence of hydraulic jumps dissipates energy, which is then not available anymore for sediment transport. This energy dissipation may be one cause of the global decrease in sediment transport capacity induced by boulders observed in the experiments, compared to experiments without boulders (*Ghilardi and Schleiss* 2012).

Variations in mean flow velocities U are less pronounced, ranging from 0.39 ms^{-1} to 0.69 ms^{-1}, with an average of 0.53 ms^{-1}. Nevertheless, velocities also vary concomitantly with bedload and the peak in velocity seems to take place shortly before the peak in sediment transport.

5.3.2   Correlational analysis

Figure 5.4 shows the normalized auto-correlation function of time varying variables presented in Figure 5.2. The first meaningful peak in the auto-correlation functions, at roughly 155 minutes for all the variables. This corresponds to the duration of one periodic oscillation which is the same for all variables: bedload, flow velocity, boulder protrusion, boulder surface, and number of hydraulic jumps. Two statistically significant peaks (correlation values of about 0.20) are seen namely at lags of about 155 minutes and 310 minutes. The time lag between the first and the second peak (155 minutes) corresponds to the time lag of the first peak in auto-correlation functions, thus apparently the duration of the fluctuation cycles remains constant in time. Significant negative peaks happen at about one third of the time lag cycle indicating that the increase before a peak is faster than the decrease after the peak as stated earlier and can be confirmed by direct observation of Figure 5.2.

Figure 5.5 presents the normalized cross-correlation functions between sediment transport and other variables presented in Figure 5.2. Cross-correlation functions contain several statistically significant positive peaks (above and about 0.20), separated by lags of about

155 minutes. Well-behaved cyclic oscillations in auto-correlation (Figure 5.4) and cross-correlation functions (Figure 5.5) confirm the periodicity observed earlier in Figure 5.2. First peaks of cross-correlation functions do not occur for zero time lags, indicating that the cycles in measured variables although correlated are not fluctuating in phase.
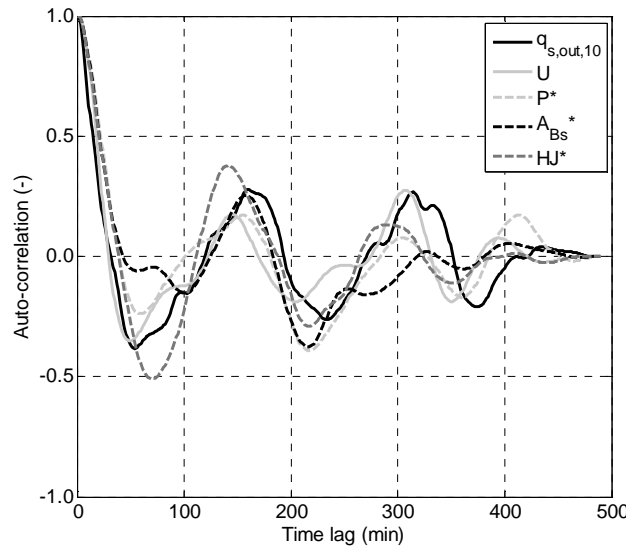
Figure 5.4: Normalized auto-correlation function for: bedload ($q_{s,out,10}$); mean velocity (U); dimensionless average protrusion (P^*); dimensionless boulder surface (A_{Bs}^*); and dimensionless number of hydraulic jumps (HJ^*).

The cross-correlation function between sediment transport and bulk velocities ($q_{s,out,10}$-U) peaks for a time lag of three minutes (cf. Figure 5.2). On the other hand, cross-correlation between sediment transport ($q_{s,out,10}$) and the remaining variables (P^*, A_{Bs}^*, and HJ^*), which are all linked to the presence of boulders, has its maxima for a time lag around -27 minutes.

The fact that the time lag of each of the three morphological indicator variables with sediment transport is the same indicates that these fluctuate in phase (cf. section 5.2). Cross-correlation functions between these variables (P^*-A_{Bs}^*, P^*-HJ^*, A_{Bs}^*-HJ^*, not shown here) show a peak at zero time lag, with values of about 0.7-0.8.
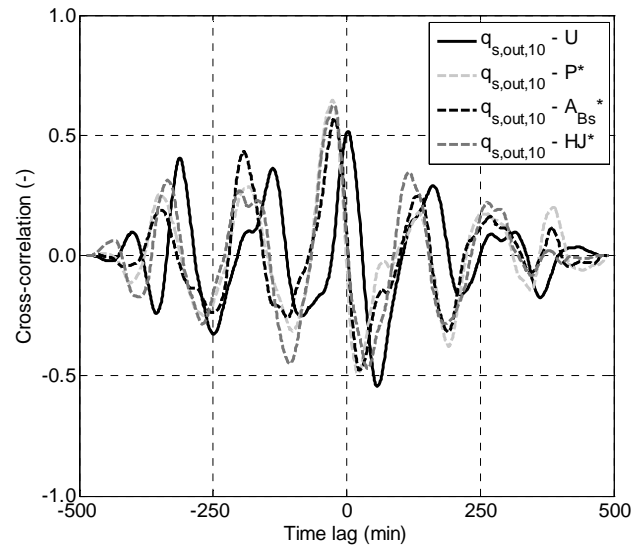
Figure 5.5: Normalized cross-correlation between bedload ($q_{s,out,10}$) and the other variables, namely: mean flow velocity (U); dimensionless average protrusion (P^*); dimensionless boulder surface (A_{Bs}^*); and dimensionless number of hydraulic jumps (HJ^*).

5.3.3 Phase analysis

A phase analysis based on the identification of bedload cycles in the instantaneous signal is here presented. A cycle is herein identified as going from a small peak in bedload, where the maximum sediment outlet is similar to the inlet, to the first small peak in bedload after an intense peak ($q_{s,out,10} >> q_{s,in}$). This definition allows identifying three complete cycles for most of the variables, in the period in which all the variables were measured (about 488 minutes, cf. Figure 5.2). For bedload and boulder surface four cycles were detected during the total experience period. The original data for all remaining variables are conditionally sampled by the bedload phase. For every variable, data are normalized between 0 (minimum) and 1 (maximum) by the range difference between the maximum and the minimum values measured within one cycle. The time is normalized by the duration of every cycle, resulting in t^*. The identified cycles occur between 0 and 187 minutes, 187 and 340 minutes, 340 and 468 minutes and finally between 468 and 680 minutes (cf. Figure 5.2), and are herein identified as cycle 1, 2, 3, and 4 respectively.

In Figure 5.6 phase sampled variables are presented with respective phase-averages, having as basis sediment transport unit cycles. Remarkably, all variables have a consistent evolution within one bedload cycle, and a similar behavior is observed between all. An event characterized by a burst in the sediment transport is clearly observed. Furthermore, the increasing period of the burst is steep whereas the decrease presents a lower slope as observed earlier.

Although the duration slightly varies from one cycle to the other (187, 153, 128, and 212 minutes for cycles 1, 2, 3, and 4 respectively), the shape remains the same. This is confirmed by Figure 5.6f, where the normalized phase averages for all variables are shown within one sediment transport variable.

Bedload starts to increase, at about $t^*=0.2$, when the morphological variables are at a minimum. These parameters influence energy dissipation, and thus the minimal value of normalized phase average of morphological variables suggests that energy dissipation is also at a minimum.

Sediment transport reaches the peak and starts decreasing again at $t^*=0.43$, when morphological parameters are at about half of their maximum value. The increasing period before bedload maxima takes about $\Delta t^*=0.22$ and the decreasing period takes about $\Delta t^*=0.32$, confirming again the observations of Figure 5.2 and Figure 5.4. Local maxima in the variables describing flumebed morphology happen about at a normalized lag of 0.17 after sediment transport and velocity maxima, converging with the findings made with the earlier correlational-based analysis. When morphological parameters reach their maximum value, the bedload transport has decreased until the average transport ($\approx q_{s,in}$) and will soon reach the minimum value. Morphological parameters values continue to decrease until a minimum, when bedload starts increasing again for a new cycle.

The phase analysis thus confirms a strong relation between the bedload fluctuation observed in the flume and flow velocity, and of these with the bed morphology evolution in time. A feedback system thus exists between channel morphology, flow kinematics and sediment transport.
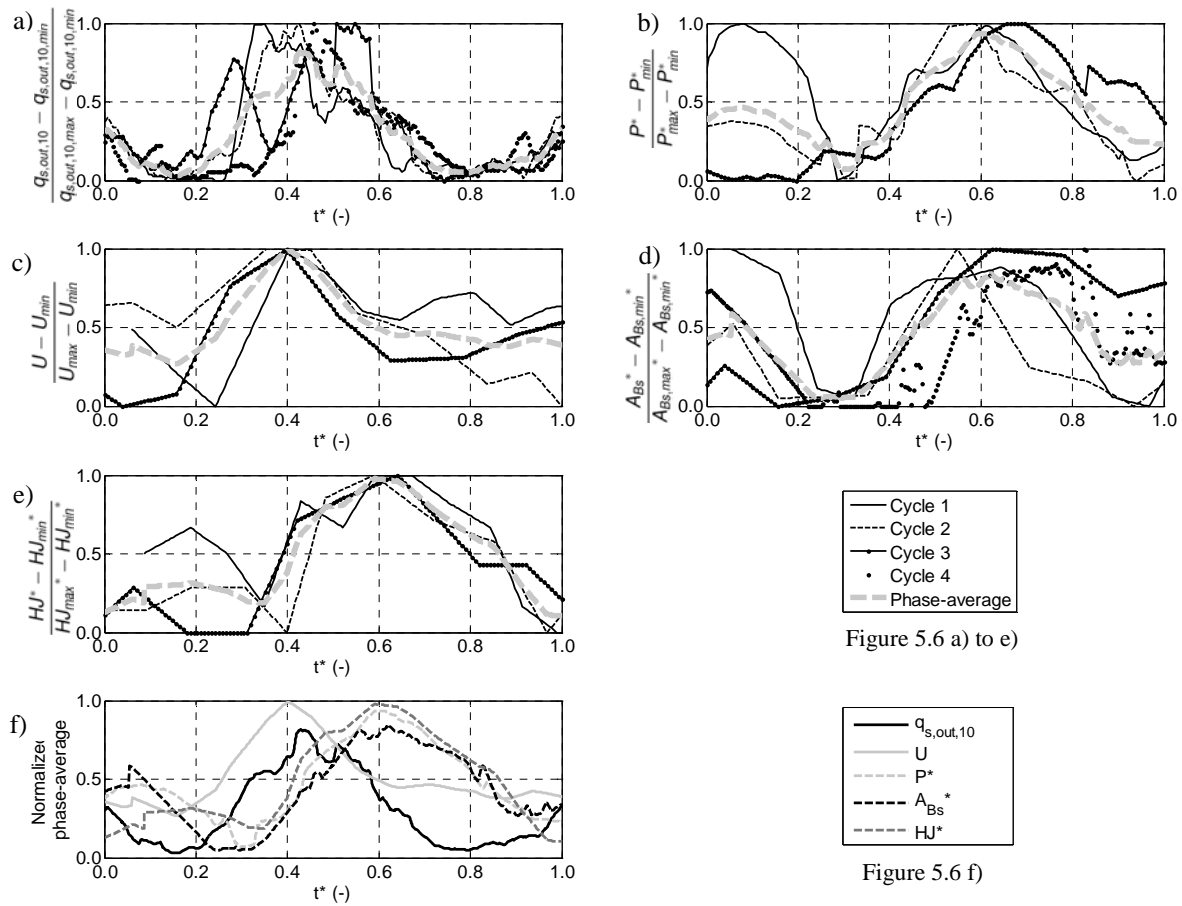
Figure 5.6: Phase analysis for the measured variables normalized with local extreme values (results for cycles 1 to 4 and phase-averages): a) bedload $q_{s,out,10}$; b) dimensionless average protrusion P^*; c) mean flow velocity U; d) dimensionless boulder surface A_{Bs}^*; e) dimensionless number of hydraulic jumps HJ^*. f) Normalized phase-average for each of the variables. Normalized time t^* corresponds to one cycle duration.

5.3.4 Mechanisms of bedload fluctuations

The observed sediment transport fluctuations correspond to different bed states, as shown in Figure 5.7 and argued earlier by *Recking et al.* (2009), *Iseya and Ikeda* (1987), and *Frey et al.* (2003). Figure 5.7 illustrates different bed states observed in the experiment at four different moments. The test was stopped four times, in order to take measurements of the bed and to take the pictures of the bed surface. These cover an approximately 1.50 m long reach.

(a) Low bedload transport, at a normalized time of about t^*=0.15 (cf. Figure 5.6f).
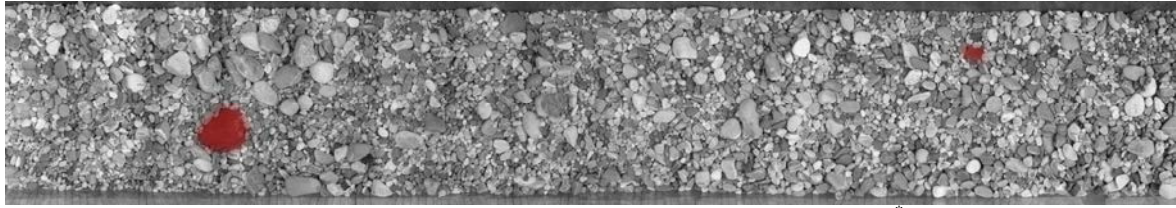
(b) $q_{s,out,10} \approx q_{s,in}$ before a peak in sediment transport, at a normalized time of about t^*=0.28(cf. Figure 5.6f).
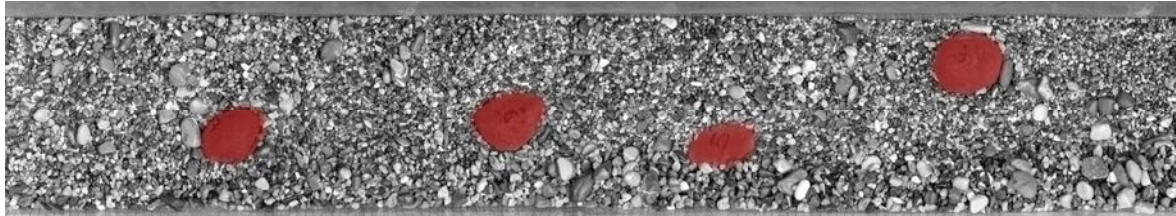
(c) Peak in sediment transport, at a normalized time of about t^*=0.43 (cf. Figure 5.6f).

(d) $q_{s,out,10} \approx q_{s,in}$ after a peak in sediment transport, at a normalized time of about t^*=0.64 (cf. Figure 5.6f).

Figure 5.7: Flume view from the top of a reach about 1.50 m long, at several key instants during the experiment: (a) at low bedload transport, at a normalized time of about t^*=0.15; (b) at $q_{s,out,10} \approx q_{s,in}$ before a peak in sediment transport, at a normalized time of about t^*=0.28; (c) at the peak in sediment transport, at a normalized time of about t^*=0.43; (d) at $q_{s,out,10} \approx q_{s,in}$ after a peak in sediment transport, at a normalized time of about t^*=0.64.

Figure 5.7a shows the bed during a low bedload period (at a normalized time t^*=0.15, cf. Figure 5.6). Due to vertical grain sorting, a layer of 1 to 2 very coarse grains covers the surface, leaving the fine sediments hidden under it, as can be seen in the laterally taken picture in Figure 5.8. The diameter of the surface grains is close to or larger than d_{90} (19 mm in this case). At this stage of sediment transport (Figure 5.7a), coarse riffles can be seen. These bedforms present an upstream long reach which is almost horizontal followed by a steep and shorter slope downstream of it (cf. Figure 5.8 for a similar experiment).

When few boulders are present, like in the present long duration experiment, or even in experiments without boulders (not shown here), riffles easily develop during low sediment transport period. As observed in other experiments, fluctuation cycles are longer and with larger amplitudes when fewer boulders are present (*Ghilardi* 2013), due to the creation of riffle structures (cf. Figure 5.8). The slope of the downstream part of the riffles slowly increases with time, as more gravel is deposited upstream. Downstream, a rapid is formed where flow accelerates and, eventually, the steep slope fails and the structure disintegration propagates in the upstream direction. Fine sediments trapped under the armor-layer are then mobilized and washed away, enhancing the bedload and provoking the breaking of downstream bed structures in their passage. This phenomenon can happen partially in the downstream and central part of the flume and produce small peaks on the sediment transport measured downstream. It also starts from the upper part of the flume and, in this case, an important peak in sediment transport is observed, due to the washing of the bed structures in the entire channel.
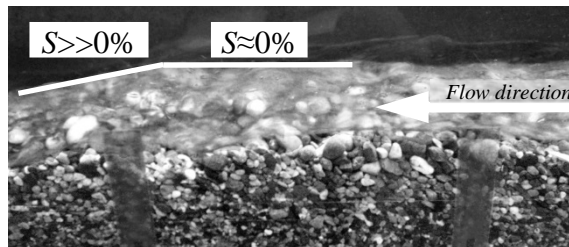
Figure 5.8: Coarse riffle formation in an experiment carried out without boulders.

The grain size distribution at the surface changes when the sediment transport starts to increase. Figure 5.7b shows the bed state before a peak in sediment transport, when $q_{s,out,10} \approx q_{s,in}$ (here at a normalized time of $t^* = 0.28$, cf. Figure 5.6). The surface grain size distribution corresponds to the sediments supplied upstream. Boulders are still mostly covered by sediments.

At the peak of bedload transport (Figure 5.7c, at a normalized time of $t^* = 0.43$, cf. Figure 5.6) the sediments visible on the bed surface are very fine, the grain size being close to d_{30} (7.1 mm in this case), or slightly larger. All grain sizes are transported and neither longitudinal nor vertical segregation is visible. Practically no bedforms are visible at this stage. The bed is often plane and water occupies the whole width, which is not the case in

most parts of the flume during low bedload periods. During bedload bursts, boulders start to get visible again but are not yet at the maximum of protrusion.

At the end of the burst in bedload transport, when $q_{s,out,10} \approx q_{s,in}$ (Figure 5.7d, at a normalized time of $t^*=0.64$, cf. Figure 5.6), the grain size distribution of the surface layer is again close to the supplied mobile grain size distribution, where both fine and coarse gravels are present. At this moment boulders have the highest protrusion. They may even be totally exposed, and it is often at this moment that they may move, due to the scouring holes that may form downstream or laterally by local erosion processes.

Due to the presence of boulders, the drag near the bed is increased. Moreover, macro-roughness elements disrupt the flow and boulder exposure decreases the shear stress available for sediment transport (cf. (*Lenzi et al.* 2006; *Yager et al.* 2007)). Boulders do however not cause the fluctuations, since pulses seem to be less frequent and with larger amplitude without them. On the contrary, sediment transport pulses are more frequent and with lower amplitude with the increase of the spatial density of boulders (*Ghilardi* 2013). *Yager et al.* (2007) used a uniform grain size distribution for their tests, and did not observe any bedload pulses, indicating that the pulses are not caused by the presence of immobile boulders.

5.3.5 Sediment transport formulae

The following sediment transport formulae, developed for relatively steep rivers, are applied to the measured data in order to estimate the bedload transport rate through time, using time varying parameterization (e.g. (*Recking et al.* 2009)): *Fernandez Luque and van Beek* (1976) formula (FLvB), *Rickenmann* (1991b), and *Recking et al.* (2008a) formula for discontinuous bedload. Both *Fernandez Luque and van Beek* (1976) and *Rickenmann* (1991b) avoid formulating hypothesis on the critical shear stress for incipient motion, thus the value of $\tau_{cr}^*=0.045$ is used. *Recking et al.* (2008a) suggest that $\tau_{cr}^* = 0.15 S^{0.275} = 0.071$, this value is thus used for Reckings formula. Details on these formulae are given in Appendix at the end of this chapter. The wall resistance herein neglected, as it generally is in mountain rivers since, although the channel may be narrow, the resistance contribution

is small compared to that caused by plunging flows, steps (clusters of boulders) or isolated roughness (boulders) (*Yager et al.* 2012a).

Figure 5.9 shows the sediment transport measured and calculated according to the three aforementioned formulae with all of them overestimating the measured sediment transport. Although the *Recking et al.* (2008a) formula estimates the average sediment transport to be almost double that of the measured bedload (cf. Table 5.2 later in the text), this formula gives in average the smallest difference in the estimates. The Rickenmann formula gives an almost constant overestimation of bedload (4x), whereas FLvB prediction fluctuates in time and overestimates bedload by six times. Sediment transport calculated with Recking and FLvB formulae show peaks shifted in time with respect to the measured transport. This is due to the use of the total bed shear stress ($\tau_t = \rho g R_h S$, where ρ is the water density, g the gravity, R_h the hydraulic radius, and S the slope), deduced for flow under uniform conditions, and applied in most of existing sediment transport formulae. When the flow velocities increase, the water depth (calculated as $h = Q/(UB)$, where h is the water depth and B the flume width) decreases, and thus bed shear stress decreases. Recking and FLvB formulae are similar in the structure of $q_s = a(\tau^* - \tau_{cr}^*)^b$ and depend only on τ^*. Keeping the bed slope (S) constant, fluctuations in τ^*, fully determined by variations of water depth, are thus directly linked to the calculated bedload transport. This problem is partially avoided by Rickenmann formula, due to the use of the Froude number to the power 1.1. This number is linked to the velocity U to the power 3/2 and thus to the use of the Froude number to the power 1.1 counteracts the impact of the total shear stress (proportional to $U^{3/2}$) in the peak shifting. Nevertheless, peaks are smoothed by this formula.
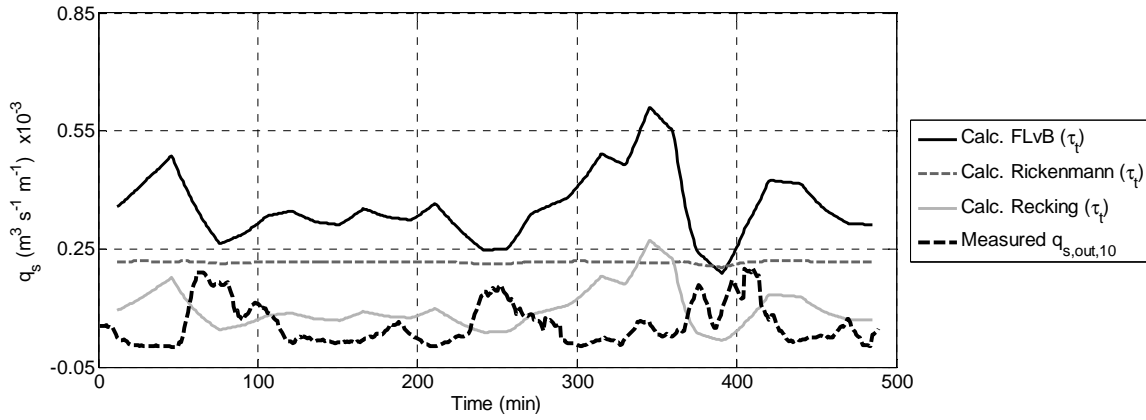
Figure 5.9: Measured bedload ($q_{s,out,10}$) and sediment transport estimated with formulae proposed by *Fernandez Luque and van Beek* (1976), *Rickenmann* (1991b), and *Recking et al.* (2008a).

The above-mentioned formulae were modified according *Yager et al.* (2007) and *Yager et al.* (2012a) in order to take into account the presence of boulders. Several modifications are proposed in *Yager et al.* (2007) to account for the limited sediment supply and the presence of rarely mobile macro-roughness elements, taking into account the scale A_m/A_t, where A_t is the total bed surface and $A_m=A_t-A_{Bs}$ is the surface of the mobile bed. *Yager et al.* (2007) suggests a shear stress partitioning method and argue that only part of the total bed shear stress available by the flow acts on the mobile sediments contributing to sediment transport, the so-called drag shear stress acting on mobile sediments, herein parameterized by the square of the measured bulk velocity U in time, $\tau_m=\rho C_m U^2/2$, where C_m is a drag coefficient.

Several researchers analyzed the value of C_m in gravel-bed rivers. *Yager et al.* (2012a) proposed a constant value of $C_m=0.44$, based on data collected by *Marcus et al.* (1992). Working with this same data set, *Scheingross et al.* (2013) proposed a power law to represent the coefficient C_m: $C_m = 0.57 \left(R_h / d_{84,mobile} \right)^{-0.96}$, giving an average value of $C_m=0.38$. C_m may also be calculated using the Variable Power Equation (VPE) proposed by *Ferguson* (2007), as explained in *Scheingross et al.* (2013). In this approach, after several trials, the relative submergence is defined as R_h/d_{50}, since it estimates C_m values closer to those expected (average $C_m=0.08$), allowing a good estimation of sediment transport. Details are given in Appendix at the end of this chapter.

Figure 5.10 presents the total exerted forces on the channel bed, computed as $A_t\tau_t = A_t\rho g R_h S$, where R_h is time variable and corresponds to a channel-averaged value, and the drag forces on mobile sediments $A_m\tau_m = A_m\rho C_m U^2/2$, where C_m is estimated according to the three different mentioned authors. Measured sediment transport is also represented in Figure 5.10.

Drag forces fluctuate jointly with sediment transport, independently of the formula used for the calculation of C_m. Total forces present only small fluctuations and peaks are in discordance with sediment transport peaks as discussed earlier.

The use of the drag shear stress, as proposed by *Yager et al.* (2007), reproduces the fluctuations in sediment transport (measured and predicted values are in phase). Since the use of bed shear stress is already overestimating the sediment transport (cf. Figure 5.9), the drag coefficient function proposed by *Ferguson* (2007), corresponding to the only drag shear stress smaller than the total shear stress, is selected hereinafter to be tested in the modified formulae. The overestimation of drag forces by *Yager et al.* (2012a) and *Scheingross et al.* (2013 is due to the high drag coefficient C_m values.
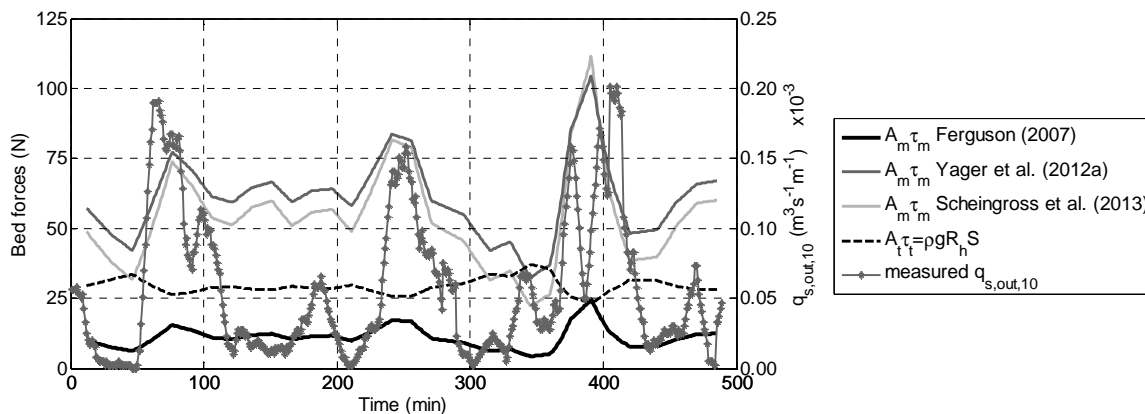
Figure 5.10: Total bed forces $A_t\tau_t$ applied on the total channel bed area and drag forces $A_m\tau_m$ applied on the bed area occupied by mobile sediments, calculated according several authors proposition for C_m estimates (left-hand side axis), and measured bedload ($q_{s,out,10}$) (right-hand side axis).

Figure 5.11 presents the bedload calculated with the very same formulae as in Figure 5.9 but where the shear stress is modified according to *Yager et al.* (2007), using the drag coefficient C_m calculated according to *Ferguson* (2007). Measured transport is presented as

well in Figure 5.11. This time, peaks of the predicted sediment transport adequately follows the measured bedload for all the applied formulae and no shifting in time is present anymore. A good correspondence between the shape of the measured bedload curve and the shape of the curves estimated with transport formulae modified according to *Yager et al.* (2007) is observed. This indicates that even if the fluctuations in bulk flow velocities are smaller (σ/mean=0.11) than those observed for bedload transport (σ/mean=0.90, cf. Table 5.1), they are enough to explain the amplitude in bedload pulses. Some parts of the measured bedload curve are not well explained by velocity measurements indicating that further investigation is needed to account for the presence of boulders. The bedload transport estimations improve for all formulae when modified according to *Yager et al.* (2007) using a drag coefficient calculated with the VPE of *Ferguson* (2007), as visible in Table 5.2. However, Recking's formulae now underestimates bedload transport, mainly because of the high dimensionless critical shear stress value (0.071) which is assumed to be a function of the slope. For this formula, there is often no excessive shear stress (τ^*-τ_{cr}^*<0), where bedload was considered to be nil. Both FLvB and Rickenmann formulae overestimate bedload by approximately 100%.
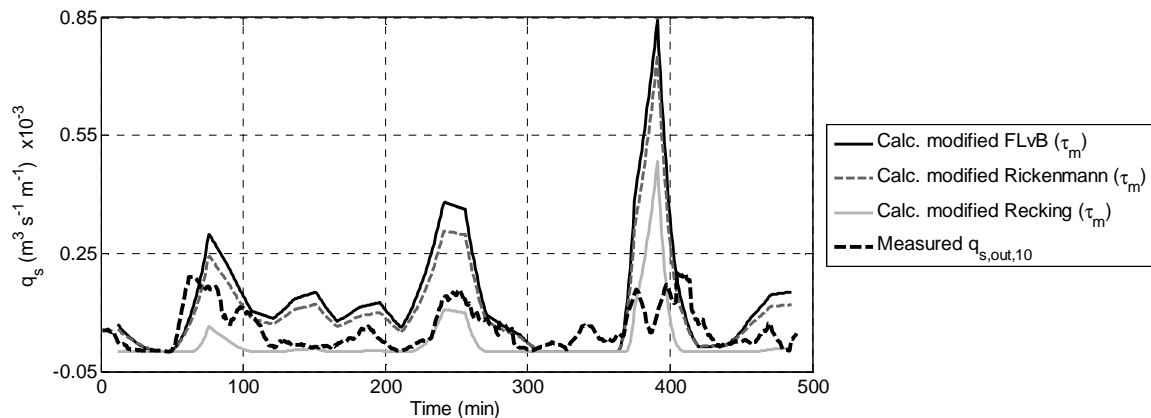
Figure 5.11: Measured bedload ($q_{s,out,10}$) and sediment transport formulae modified according *Yager et al.* (2007) and using *Ferguson* (2007) for the C_m calculation in τ_m: *Fernandez Luque and van Beek* (1976), *Rickenmann* (1991b), and *Recking et al.* (2008a).

All the modified sediment transport formulae have similar shapes with the difference between them being small. Table 5.2 shows that, on average, *Rickenmann* (1991b formula

is the one with the smallest difference, if *Recking et al.* (2008a) is excluded given the reasons mentioned above.

The use of the drag shear stress on mobile sediments allows reproducing the bedload bursts quite accurately. Nevertheless, a correct estimation of the drag coefficient C_m is critical. In the VPE of *Ferguson* (2007), the use of d_{84} as grain size representative of the roughness instead of d_{50}, induces an overestimation of bedload transport of about 15 times the measured values.

Table 5.2: Deviation between the calculated and measured averaged sediment defined as $(q_{s,calc}\text{-}q_{s,out,av})/q_{s,out,av}$ for each formulae, original and modified according to *Yager et al.* (2007), using *Ferguson* (2007) for the calculation of the drag coefficient (C_m) in the latter.

Shear stress approach	*Recking et al.* (2008a)	*Rickenmann* (1991b)	*Fernandez Luque and van Beek* (1976)
τ_t (original formulae)	0.7	2.8	5.3
τ_m (modified formulae)	-0.6	0.9	1.3

5.4 Conclusions

A long duration steep flume experiment, carried out with a wide grain size distribution and in presence of relatively immobile boulders, revealed an interaction between bedload and flow velocity fluctuations and variations in morphological parameters, such as boulder protrusion, bed surface occupied by boulders and number of hydraulic jumps. This could be demonstrated by the analysis of time-series and confirmed by correlational and phase analyses.

The duration of the cycles is the same for all the measured variables, however a delay between the variables exist, i.e. morphological parameters, influencing energy dissipation, fluctuate with a time lag with bedload transport pulses. Bedload and flow velocities fluctuate almost in phase, with the peak in velocities occurring just minutes before the peak in bedload.

Phase analysis shows that, when sediment transport starts increasing, values of morphological parameters are at a minimum, suggesting that energy dissipation is also at a minimum value. Bedload starts decreasing again when morphological variable values are at about 50% of their maximum value. When morphological parameters reach their maximum value, the bedload transport has decreased until the average transport and soon reaches a minimum value. Morphological parameters values continue to decrease until a minimum, when bedload starts increasing again for a new cycle.

The observation of the experiment shows that, before a burst in sediment transport, the channel bed is paved and boulders are not visible. Local deposition creates an almost horizontal bed reach followed by steeper slopes downstream. On these, just before the burst in sediment transport, the local slope can be very high with local flow velocity increasing drastically. Eventually, some grains are eroded downstream of these riffles. The whole structure is then rapidly washed out and sediment discharge increases drastically, causing the peak in sediment transport. The velocity is smaller when the protrusion is close to its maximum, seemingly due to the additional flow drag induced by the boulders. Their presence disrupts the flow and dissipates energy through the presence of hydraulic jumps downstream of the boulders. After the peak in boulder protrusion, the latter slowly decreases. During this time sediment transport measured at the outlet is very low. Once the protrusion reaches a minimum, sediment transport starts to increase again. This is a clear indication of the impact of boulders on sediment transport capacity, possibly due to decrease in shear stress available for sediment transport.

Finally, the present paper shows that the total bed shear stress values fluctuate out of phase to bedload pluses. On the contrary, the use of the drag shear stress, directly dependent on flow velocity, gives bedload estimates fluctuating in phase with measured sediment transport and with better bedload estimates. The choice of the drag coefficient is however critical in order to obtain correct sediment transport estimates.

APPENDIX TO CHAPTER 5

Sediment transport formulae

- *Recking et al.* (2008a) formula for discontinuous sediment transport is

$$q_s^* = 15.6\left(\tau^* - 0.15S^{0.275}\right)^2 \tag{39}$$

where q_s^* is the dimensionless sediment transport according to *Einstein* (1950) and τ^* the dimensionless shear stress, usually calculated as:

$$\tau^* = \frac{\tau}{(\rho_s - \rho)g\,d_{50}} = \frac{\rho\,g\,R_h\,S}{(\rho_s - \rho)g\,d_{50}} \tag{40}$$

where R_h is the hydraulic radius, d_{50} the median grain diameter, ρ_s=2650 kgm^{-3} the density of sediments, and ρ=1000 kgm^{-3} the density of water.

Recking assumes the shear stress to be proportional to the slope as $0.15S^{0.275} = 0.071$.

- *Rickenmann* (1991b) formula is

$$q_s^* = \frac{3.1}{\sqrt{s-1}}\left(\frac{d_{90}}{d_{30}}\right)^{0.2} \tau^{*1/2}\left(\tau^* - \tau_{cr}^*\right)Fr^{1.1} \tag{41}$$

where $Fr = \dfrac{U}{\sqrt{g\,Q/(UB)}}$ is the Froude number and τ_{cr}^* is the critical dimensionless shear stress, assumed to be equal to 0.045.

- *Fernandez Luque and van Beek* (1976) formula is

$$q_s^* = 5.7\left(\tau^* - \tau_{cr}^*\right)^{3/2} \tag{42}$$

where τ_{cr}^* is the critical dimensionless shear stress, assumed to be equal to 0.045.

Drag coefficient C_m

- According to *Yager et al.* (2012a), based on *Marcus et al.* (1992) data set, the drag coefficient has a constant value of C_m=0.44

- According to *Scheingross et al.* (2013), the drag coefficient follows a power law:

$$C_m = 0.57 \left(R_h \, / \, d_{84,mobile} \right)^{-0.96} \tag{43}$$

This expression is also based on *Marcus et al.* (1992) data set.

- *Scheingross et al.* (2013) propose to use the Variable Power Equation (VPE) of *Ferguson* (2007) in order to calculate the drag coefficient. *Ferguson* (2007) states that:

$$\frac{U}{u^*} = \left(\frac{8}{f} \right)^{1/2} = \frac{a_1 a_2 \left(d \, / \, D \right)}{\left[a_1^2 + a_2^2 \left(d \, / \, D \right)^{5/3} \right]^{1/2}} \tag{44}$$

where a_1=6.5 and a_2=2.5. f is the Darcy-Weisbach friction factor and u^* the shear velocity. d/D is the relative submergence, here assumed to be equal to R_h/d_{50}. The above mentioned friction factor is then introduced in the C_m formula as proposed by *Scheingross et al.* (2013):

$$C_m = 2 \left(\frac{u^*}{U} \right)^2 \tag{45}$$

Chapter 6

Period and amplitude of bedload pulses in a macro-rough channel

This chapter analyses in detail the duration and amplitude of cyclic bedload fluctuations as a function of several variables. Amplitude and duration of bedload pulses are determined based on correlation analysis and it is shown that these clearly decrease when the stream power increases. The boulder configuration influences sediment transport capacity and thus the stream power needed to transport a given amount of sediments.

Abstract: It is known that bedload fluctuates over time in steep rivers with wide grain size distributions, even under conditions of constant sediment feed and water discharge. Bedload fluctuations, which are a consequence of grain sorting, are periodic and are related to fluctuations in the flow velocity and bed morphology. The presence of large relatively immobile boulders, such as erratic blocks which are often present in mountain streams, has a strong impact on flow conditions and sediment transport. However, their influence on bedload fluctuations has not been studied. Sediment transport fluctuations were investigated in this study in a set of 38 laboratory experiments carried out on a steep tilting flume under several conditions of constant sediment and water discharge, for three different slopes (S=6.7%, 9.9%, and 13%). Sediment transport, bulk mean flow velocities and variables describing the morphology were measured regularly during the experiments. Periodic bedload pulses were clearly visible in all of the experiments, along with flow velocity and bed morphology fluctuations. Correlation analysis showed that the durations of these cycles were similar, although they were not necessarily in phase. The pulses were characterized by their amplitude and period as a function of various boulder spatial densities and diameters. This chapter shows that for higher stream power, the fluctuations decrease, both in cycle duration and in amplitude. The presence of boulders increases the stream power needed to transport a given amount of sediment, thus decreasing fluctuations.

Key words: Bedload fluctuations; Sediment transport; Boulders; Steep channel.

6.1 Introduction

Despite the importance of mountain rivers in the control of the sediment supply to lowland mild-slope rivers (*Wohl* 2000; *Yager et al.* 2007), only a few studies were conducted on steep channels, and these were primarily performed in the last two decades. Steep channels are a subset of mountain rivers and are typically characterized by longitudinal slopes larger than 4-5% (*Comiti and Mao* 2012) and by channel beds composed of coarse mobile sediments and large and relatively immobile blocks or boulders (*Rickenmann* 2001; *Papanicolaou et al.* 2004; *Yager et al.* 2007). Boulders can be found in steps spanning the whole channel width (step-pool morphology) or in a more irregular manner (cascade morphology) (*Montgomery and Buffington* 1997). In these streams, the water depth is typically shallow in comparison to the roughness of elements such as the large boulders. The latter are considered macro-roughness elements when the relative roughness, defined as the ratio between the roughness scale and the water depth, exceeds the unit value (*Bathurst* 1978).

The wide grain size distribution present on steep slopes has a noticeable impact on bedload, causing its fluctuation even under constant water and sediment feed (*Iseya and Ikeda* 1987; *Frey et al.* 2003). According to *Iseya and Ikeda* (1987), two main factors cause sediment transport to fluctuate, namely, migration of bedforms and segregation of the surface grain size distribution, which results in the formation of an armor layer. *Iseya and Ikeda* (1987) showed that longitudinal sediment sorting occurs when graded sediments are constantly fed into a flume, producing rhythmic fluctuations in the bedload transport rate. Longitudinal sediment sorting influences sediment particle availability and determines the magnitude of the sediment transport rate and its pulses. *Recking et al.* (2009) indicated that this phenomenon is accentuated in low-flow conditions (small discharge) and is associated with fluctuations of bed slopes, bed load and bed state. *Recking et al.* (2008b) and *Recking et al.* (2009) carried out tests with uniform and wide grain size distribution on similar installations and noticed that bedload fluctuations were not observed in setups with uniform grain size distributions. This confirms that fluctuations are a consequence of grain sorting in mixed sediment compositions.

To the authors' knowledge, before the present study the impact of isolated boulders on bedload transport was analyzed only by *Yager et al.* (2007). They carried out experiments on steep slopes, in the presence of boulders represented by regularly spaced spheres, and with uniform bed material. The isolated boulders present a morphology similar to what can be found in nature in a reach characterized by a cascade morphology. Most sediment transport equations estimate bedload transport rates based on the difference between the critical and the total shear stress. Macro-roughness elements endure a significant part of the total stress and disrupt the flow by altering the channel roughness (*Wohl* 2000; *Yager et al.* 2007; *David et al.* 2011). The form drag caused by boulders increases with the number of boulders. Increased form drag results in lower shear stresses available at the bed for sediment entrainment (*Bathurst* 1978; *Lenzi et al.* 2006; *Yager et al.* 2007; *Yager et al.* 2012a). Hence, the presence of boulders decreases the sediment transport capacity (*Yager et al.* 2007; *Ghilardi and Schleiss* 2012; *Yager et al.* 2012a). The dimensionless boulder distance λ/D (-), representing the boulder density, where λ (m) is the average distance between boulders of diameter D (m), and the protrusion of the boulders are directly linked to the sediment transport capacity (*Yager et al.* 2007). Several parameters may be used to account for the presence of boulders in bed shear stress and bed resistance equations. These parameters generally pertain to the number of boulders, their cross section, the bed area occupied by them, the distance between boulders and a drag coefficient (*Bathurst* 1978; *Canovaro et al.* 2007; *Yager et al.* 2007; *Pagliara et al.* 2008; *Yager et al.* 2012a).

Along with the form drag resistance caused by boulders, energy can be dissipated by spill resistance due to flow acceleration and deceleration, which usually occur over or downstream of steps in rivers (*Curran and Wohl* 2003; *David et al.* 2011). Energy losses due to spill resistance are linked to the presence of hydraulic jumps downstream of steps or boulders and are proportional to the drop height (*Curran and Wohl* 2003; *Comiti and Lenzi* 2006).

Several authors noted the possible dependence of critical bed shear stress on the channel gradient (*Papanicolaou et al.* 2004; *Lamb et al.* 2008; *Recking et al.* 2008a) and morphology (*Church et al.* 1998), along with the channel roughness and hiding effects associated with a wide grain size distribution (*Buffington and Montgomery* 1997; *Lenzi et*

al. 2006). Bed shear stress calculations require a precise knowledge of the channel hydraulics, which present high local variability in mountain rivers. On the other hand, according to *Bagnold* (1966), the stream power per unit width ω depends on such bulk channel properties as the river width and slope, combined with the discharge of the river, as expressed in the following equation:

$$\omega = \rho g q S = \tau U \tag{46}$$

where ρ (1000 kgm^{-3}) is the fluid density, g (9.81 ms^{-2}) is the acceleration due to gravity, q (m^{3}s^{-1}m^{-1}) is the specific discharge, S (-) is the slope, τ (Nm^{-2}) is the total bed shear stress, and U (ms^{-1}) is the average flow velocity.

The stream power quantifies the rate of loss of energy as water flows downstream and thus the power available for performing geomorphic work (*Bagnold* 1966; *Ferguson* 2005; *Petit et al.* 2005; *Parker, C et al.* 2011). Bagnold proposed that the bedload transport rate increases nonlinearly with stream power above a threshold or critical value. *Petit et al.* (2005) suggested that the critical specific stream power increases with the bedform scale due to the significant loss of energy available for sediment transport.

The objective of this paper is to show the relationship between sediment transport pulses and the time-varying flow velocity and parameters representing the channel morphology (boulder protrusion, boulder surface, and number of hydraulic jumps). This objective was achieved by means of experimental tests conducted using a laboratory flume, for which the bedload, bed morphology and flow velocity were continuously assessed. The results presented and discussed in this paper are based on 33 experiments with boulders and 5 experiments without boulders, carried out for several different combinations of conditions of time-constant water and sediment supply. A preliminary and partial analysis of these experiments is given in *Ghilardi* (2013). A correlation analysis between the observed bedload fluctuations, velocity, and bed morphology is here shown for one of the tests indicating that these factors fluctuate concomitantly in time, although not necessarily in phase (cf. Chapter 5). The period and amplitude of the pulses in the sediment transport were determined and their relation with the water discharge, bed shear stress, stream power, and density of the boulders was analyzed.

Following this introduction, the experimental methods are described, the results of the analysis of the experiments are presented and discussed, and lastly, main conclusions are drawn. The analysis of the results of one experiment is presented in detail. The same analysis approach was applied to the remaining experiments, and the combined results are discussed.

6.2 Research methods

The effect of randomly distributed relatively immobile boulders, reproducing a cascade morphology as described by *Montgomery and Buffington* (1997), on bedload fluctuations was investigated by means of laboratory experiments carried out on a steep (S=6.7%, 9.9%, and 13%), 8 m long (7 m usable), 0.25 m wide, tilting flume at the Laboratory of Hydraulic Constructions (LCH) of the Ecole Polytechnique Fédérale de Lausanne (EPFL) (Figure 6.1). The boulders, with mean diameters ranging between 1/3 and 1/2 of the flume width, are herein defined as elements that are not transported by the flow. Water and sediments were supplied at the flume inlet. Measurements of bedload, flow velocity and several morphological parameters were performed as explained next.
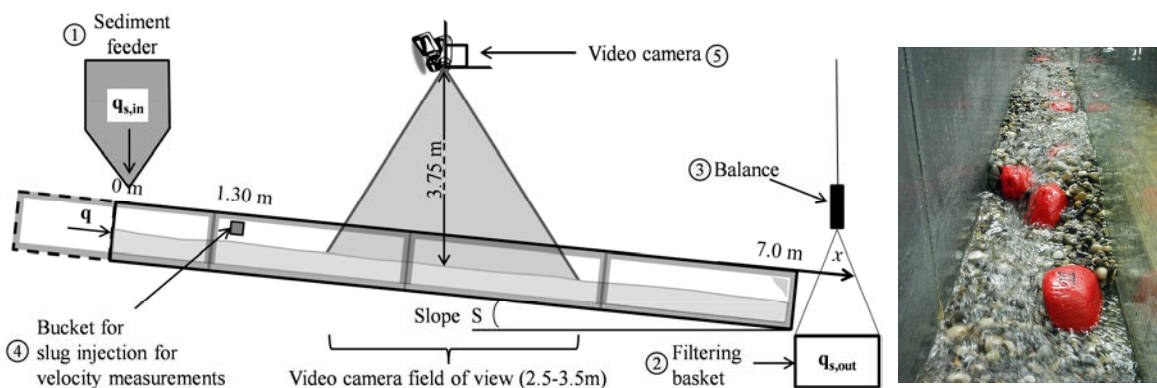
Figure 6.1: Sketch of the experimental setup (left-hand side) and example of the channel morphology during an experiment (right-hand side).

Water discharge, fed constantly by the closed general pumping system of the laboratory, was controlled by an electromagnetic flow-meter (±0.01 l/s). Sediments were constantly fed into the system by a calibrated sediment feeder situated upstream (1 in Figure 6.1). A filtering basket (2 in Figure 6.1) suspended from a balance (3 in Figure 6.1) recovered the sediments at the outlet, where the weight (±1 kg) was measured every minute. The one minute interval sediment discharge measurement was then averaged over a sliding window ($q_{s,out,X}$, where X represents the size of the window), to provide a smoothed overview of the bedload time evolution. The size of the sliding window (X) is visually defined in order to reproduce all peaks in sediment transport; for the several experiments, it ranged between 3 and 10 minutes. Sediments were recirculated between the sediment feeder and the downstream basket. No sediment sorting occurred in the sediments introduced by the feeder.

The average flow velocity U was measured every 15 minutes using a technique involving a tracer dye and video analysis. A detailed description of the technique is given in Chapter 4. This technique, based on the analysis of dilution of a colorant (tracer dye), permits the measurement of mean bulk velocities through the channel reach. The passage of the cloud of colorant inserted upstream in the reach (4 in Figure 6.1) was analyzed based on the differences between images captured by a video camera (5 in Figure 6.1), with the movement of the mass center of the cloud defining the average flow velocity (cf. *Calkins and Dunne* 1970). The average of five independent velocity measurements, based on five different colorant injections, was calculated.

The protrusion P of four boulders was measured with a point gauge (± 1 mm) during the experiments at time intervals of approximately 10 minutes (2 to 3 minutes per boulder, in a loop). P was calculated as the average vertical distance between the highest point of the boulder and the four corners of this boulder (upstream, downstream, left and right) at the gravel interface. For every measured boulder, the protrusion P was sub-sampled by linear interpolation to have a value every minute (the same sampling rate for bedload measurements). An average protrusion value between the boulders P_{av} was then calculated for every minute of the experiment. The protrusion was then normalized with respect to the boulder diameter: $P^{*}=P_{av}/D$.

Hydraulic jumps HJ were counted manually based on visual observation after the flow velocity measurements were taken, i.e., about every 15 minutes. This parameter is an indicator of the amount of energy dissipation and of the morphological variety of the channel because hydraulic jumps generally appear downstream of protruding boulders. The number of hydraulic jumps was scaled and normalized by the number of boulders in the flume using the following relation: $HJ^*=HJ/(N_{Bs}A_t)$, where A_t is the total flume surface and N_{Bs} the number of boulders per square meter.

The surface occupied by boulders A_{Bs} measured parallel to the river bed (top view) and called the "boulder surface," was determined by means of video analysis. Each calculation was performed using a single video frame. A_{Bs} was calculated either for every velocity measurement or every minute, when the entire experiment was videotaped (cf. Table 6.1). The boulder surface was scaled by the flume surface visible in the video to obtain a dimensionless boulder surface, A_{Bs}^*.

The density of the supplied sediments was 2650 kgm^{-3}, and the grain size distribution was characterized by: d_m=d$_{65}$=11.9 mm, d_{30}=7.1 mm, and d_{90}=19.0 mm, where d_m is the mean grain size, corresponding to d_{65}, and d_x is the grain size diameter for which x% of the sediments by weight have smaller diameters. Boulders were not taken into account in this calculation and were not supplied as mobile sediments; they were instead placed in the channel bed before the experiment. Boulders are relatively immobile elements, which means that they are not transported by the flow, although they may move up to several times their diameter during experiments, mainly due to the scour holes formed around them.

A plane bed of 0.2 m of thickness was prepared before the experiments and the boulders were placed in the flume half covered by mobile sediments, which corresponded to a protrusion of approximately 30% of the diameter (P^*≈0.3). The position of the boulders is randomly determined, based on the dimensionless distance between boulders λ/D and their diameter D used for a given test (cf. Table 6.1). The water and sediment supply were started at the same time.

A criterion to establish the relation between liquid and solid discharge was set, assuming the relative immobility of the boulders and imposing that the boulders always protrude after a burst in sediment transport. The test was stopped after one peak in bedload, when the average outlet sediment discharge over the previous 10 minutes was roughly the same as the sediment supply ($q_{s,out,10} \approx q_{s,in}$, values determined per unit width). In addition, we verified that the cumulative average of the outlet sediment transport was within ±15% of the sediment supply at the end of the experiment. The cumulative average of the outlet sediment transport ($q_{s,out,av}$) is computed for a given instant T as shown in Eq. (47), based on the one minute interval sediment transport.

$$q_{s,out,av}\left(T\right) = \frac{\int\limits_{0}^{T} q_{s,out}(t)\mathrm{d}t}{T} \tag{47}$$

Table 6.1 presents the configuration of the experiments used for the analysis, characterized by the slope S, the dimensionless boulder distance λ/D (a measure of boulder density based on linear parameters, where λ is the average distance between the boulders), the boulder diameter D, the number of boulders per square meter N_{Bs}, the water discharge q per unit width, and the sediment supply $q_{s,in}$ per unit width. The main bulk results are presented as well, such as the total average sediment at the outlet $q_{s,end}$ (where T in equation (47) refers to the total duration of the test) calculated at the end of the test, the bedload standard deviation σ_{qs}, the period of bedload fluctuations T_{qs} (defined later in the text), the normalized bedload amplitude $\sigma_{qs}/q_{s,end}$ (defined later in the text), the mean flow velocity $\bar{U}$, and the $\overline{P_{av}}$ the average of the average boulder protrusion (P_{av}) throughout experiment.

Table 6.1: Experiment details and main results. The symbols used to represent the experiments in Figure 6.5 to Figure 6.8 are given in the last column of the table. The filling of the symbols depends on λ/D (*inf* represents the tests without boulders, with an infinite distance), the shape on D and the contour line color on the flume slope S. The line with characteristics in bold presents the results of the test described in detail in sections 6.3.1 and 6.3.2. For tests with *, the boulder surface was measured every 15 minutes; for the others,

the boulder surface was measured every minute. For tests with x, the number of hydraulic jumps was not counted. The test numbers correspond to those given in Table 3.1 and in Appendix B.

	S (%)	λ/D (-)	D (m)	N_{Bs} (m⁻²)	q (m³s⁻¹m⁻¹)	$q_{s,in}$ x10⁻³ (m³s⁻¹m⁻¹)	$q_{s,end}$ x10⁻³ (m³s⁻¹m⁻¹)	σ_{qs} x10⁻³ (m³s⁻¹m⁻¹)	$\bar{U}$ (ms⁻¹)	$\bar{P}_{av}$ (m)	T_{qs} (min)	$\sigma_{qs}/q_{s,end}$ (-)	Symb.	Test Nr.
	6.7	inf.	-	0.0	0.0148	0.056	0.065	0.059	0.35	0.000	155	0.90	✳	16
	6.7	inf.	-	0.0	0.0159	0.094	0.100	0.080	0.58	0.000	135	0.80	✳	22
*	6.7	inf.	-	0.0	0.0162	0.134	0.119	0.046	0.49	0.000	51	0.39	✳	26
*	6.7	2	0.075	44.6	0.0209	0.029	0.024	0.011	0.56	0.022	30	0.48	◆	8
*	6.7	2	0.075	44.6	0.0391	0.134	0.146	0.028	0.77	0.027	10	0.19	◆	19
*x	6.7	2	0.100	25.1	0.0228	0.057	0.065	0.029	0.71	0.024	128	0.45	▲	4
*	6.7	2	0.100	25.1	0.0372	0.134	0.139	0.019	0.70	0.029	9	0.14	▲	5
*x	6.7	2	0.100	25.1	0.0424	0.157	0.174	0.031	0.84	0.036	13	0.18	▲	17
*x	6.7	2	0.125	16.0	0.0228	0.063	0.075	0.028	0.64	0.037	29	0.38	■	7
*	6.7	2	0.125	16.0	0.0352	0.134	0.137	0.018	0.70	0.040	14	0.13	■	18
	6.7	3	0.075	20.0	0.0188	0.056	0.053	0.035	0.52	0.023	98	0.66	◈	6
*x	6.7	3	0.075	20.0	0.0212	0.091	0.104	0.045	0.63	0.031	60	0.43	◈	13
*	6.7	3	0.075	20.0	0.0238	0.134	0.140	0.034	0.70	0.033	23	0.24	◈	24
*	6.7	3	0.100	10.9	0.0177	0.056	0.061	0.039	0.49	0.024	56	0.64	▲	15
*	6.7	3	0.100	10.9	0.0233	0.134	0.124	0.034	0.55	0.031	21	0.27	▲	20
*	6.7	3	0.125	6.9	0.0236	0.134	0.112	0.058	0.60	0.043	110	0.52	■	9
*	6.7	3	0.125	6.9	0.0235	0.101	0.119	0.036	0.60	0.054	23	0.30	■	14
	6.7	5	0.075	6.9	0.0168	0.056	0.057	0.052	0.53	0.017	160	0.91	◇	11
*	6.7	5	0.075	6.9	0.0222	0.134	0.131	0.048	0.58	0.029	34	0.36	◇	23
*	6.7	5	0.100	4.0	0.0162	0.056	0.056	0.033	0.42	0.031	65	0.58	△	10
	6.7	5	0.100	4.0	0.0183	0.094	0.088	0.051	0.55	0.028	63	0.59	△	21
*	6.7	5	0.100	4.0	0.0223	0.134	0.135	0.037	0.57	0.046	85	0.27	△	27
	6.7	5	0.125	2.3	0.0156	0.056	0.060	0.047	0.52	0.027	161	0.78	□	12
*	6.7	5	0.125	2.3	0.0208	0.134	0.150	0.056	0.63	0.061	84	0.37	□	25
	9.9	inf.	-	0.0	0.0112	0.094	0.088	0.063	0.40	0.000	193	0.72	✳	29
	9.9	3	0.100	10.9	0.0131	0.094	0.089	0.089	0.38	0.021	130	1.00	▲	28
	9.9	3	0.100	10.9	0.0146	0.136	0.143	0.053	0.53	0.035	18	0.37	▲	30
	9.9	3	0.100	10.9	0.0166	0.192	0.198	0.039	0.61	0.036	26	0.20	▲	31
	13	inf.	-	0.0	0.0106	0.192	0.216	0.101	0.28	0.000	108	0.47	✳	38
	13	2	0.100	25.1	0.0128	0.146	0.168	0.038	0.41	0.017	14	0.23	▲	35
	13	**3**	**0.075**	**20.0**	**0.0109**	**0.146**	**0.172**	**0.125**	**0.36**	**0.010**	**76**	**0.73**	◈	34
	13	3	0.100	10.9	0.0107	0.146	0.145	0.140	0.28	0.016	163	0.97	▲	32
	13	3	0.100	10.9	0.0114	0.192	0.199	0.116	0.37	0.013	53	0.58	▲	33
	13	3	0.100	10.9	0.0124	0.236	0.254	0.121	0.38	0.025	69	0.48	▲	39
	13	3	0.100	10.9	0.0118	0.236	0.261	0.113	0.37	0.021	58	0.43	▲	40
	13	3	0.125	6.9	0.0104	0.146	0.165	0.098	0.27	0.035	112	0.60	■	37
	13	4	0.075	10.9	0.0118	0.236	0.266	0.140	0.34	0.013	45	0.53	◇	41
	13	5	0.100	4.0	0.0104	0.146	0.168	0.074	0.37	0.024	36	0.44	△	36

6.3 Results and discussion

6.3.1 Data time series

Pulses in the bedload per unit width ($q_{s,out,10}$), coupled with cyclic changes in the average flow velocity (U) and the calculated morphological parameters (P^*, $A_{Bs}{}^*$, HJ^*), were observed in all of the experiments. The durations and amplitudes of these pulses varied among the tests. Both phenomena mentioned by *Iseya and Ikeda* (1987), grain sorting and bedform migration, were observed (cf. Chapter 5).

Figure 6.2 presents the time series of the bedload, mean flow velocities (U), dimensionless average boulder protrusion (P^*), dimensionless boulder surface ($A_{Bs}{}^*$), and dimensionless number of hydraulic jumps (HJ^*) for the test signaled in bold in Table 6.1. Three bursts in the sediment transport $q_{s,out,10}$ and the morphological parameters (P^*, $A_{Bs}{}^*$, HJ^*) are clearly visible, as well as coupled fluctuations in $q_{s,out,10}$ with U and the morphological parameters. The interval between occurrences of their peak values was approximately 80 minutes. Despite the low measurement resolution, two peaks were identified in the average flow velocity U for this test. These peaks always corresponded to high sediment transport values.
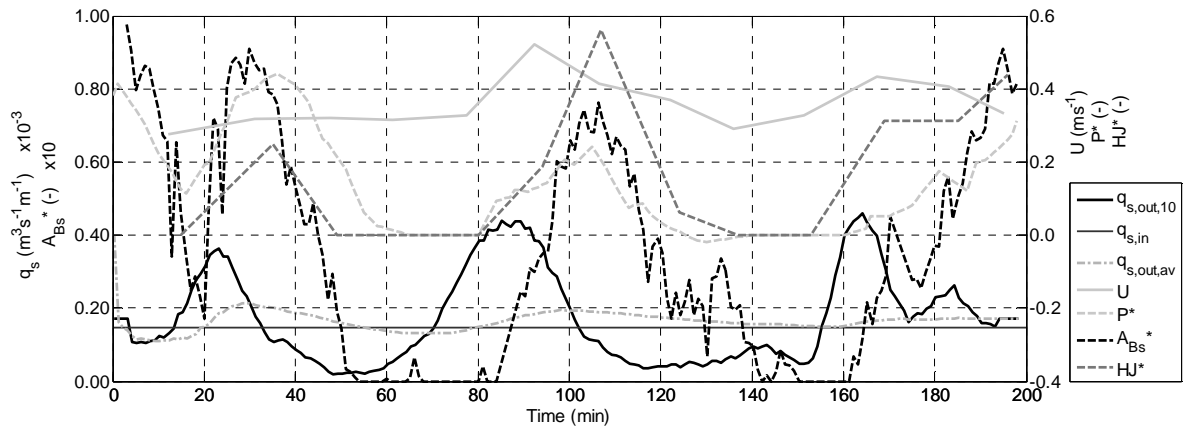
Figure 6.2 Time series of the sediment supply ($q_{s,in}$), bedload at the outlet averaged over a 10-minute window ($q_{s,out,10}$), cumulative average of the outlet bedload ($q_{s,out,av}$), and dimensionless boulder surface ($A_{Bs}{}^*$) on the left-hand axis. Time series of the mean velocity (U), dimensionless average protrusion (P^*), and dimensionless number of hydraulic jumps (HJ^*) on the right-hand axis. Test with N_{Bs}=20 m^{-2} boulders of diameter D=0.075 m, λ/D=3, $q_{s,in}$=0.146 x10^{-3} m^{3}s^{-1}m^{-1}, q=0.0109 m^{3}s^{-1}m^{-1} and S=13.0% (cf. Table 6.1, line in bold).

The bedload transport per unit width varied from a minimum of $0.018 \times 10^{-3} \ m^3 s^{-1} m^{-1}$ to a maximum of $0.460 \times 10^{-3} \ m^3 s^{-1} m^{-1}$, with an average value of $0.172 \times 10^{-3} \ m^3 s^{-1} m^{-1}$ and a standard deviation of $0.125 \times 10^{-3} \ m^3 s^{-1} m^{-1}$, corresponding to 72% of the average.

The morphological parameters also exhibited notable fluctuations. These three parameters (boulder protrusion, boulder surface, and number of hydraulic jumps) clearly fluctuated in phase. The link between P^* and $A_{Bs}{}^*$ can be easily observed by approximating the boulders as partially covered spheres: the projected surface increases as a function diameter and protrusion when the latter is smaller than 0.5, remaining however constant for higher protrusions. The link between P^* and HJ^* can also be explained by the fact that a linear relationship exists between P^* and the protrusion downstream of the boulders (*Ghilardi and Schleiss* 2012). Thus, the drop height increases with average boulder protrusion, causing the formation of more hydraulic jumps, confirming the latter as a characteristic channel morphology parameter.

Sediment transport starts to increase when the morphological parameters are at their minima, close to or equal to zero. The protrusion, boulder surface, and number of hydraulic jumps reach their maxima at the end of a sediment transport peak, when the average bedload outlet over 10 minutes ($q_{s,out,10}$) corresponds to the inlet ($q_{s,in}$), which is followed by a period during which sediment transport is below $q_{s,in}$.

The fluctuations in the flow velocities were smaller. Peaks in the flow velocity occurred at almost the same time as the peak in the sediment transport. It is likely that a peak in the average flow velocity would occur at approximately t=20 minutes, but the velocity measurement interval, which was 15 minutes, did not permit capturing this peak.

As previously noted by *Iseya and Ikeda* (1987) and *Recking et al.* (2009), bedload fluctuations are linked to different bed states. A coarse plane bed, characterized by an upstream reach with mild slopes and a steep downstream reach, form in channels during low sediment transport periods, during which aggradation of the bed occurs. When the downstream part becomes too steep, a structural failure occurs. Coarse surface sediments are entrained, inducing the mobility of the fine sediments underneath them. This contributes to sediment transport and to a clear burst in bedload transport, as observed in

Figure 6.2. Before the peak, the boulders are generally not visible. At the peak in bedload transport, the boulders start to be visible, thus enduring a part of the excess shear stress. The sediment transport begins to decrease and a minimum in the bedload is reached just after the peak in the morphological parameters. A coarse surface layer and the mentioned plane bed structures start forming again, beginning another burst cycle in the bedload. During the peak in bedload transport, fine-grained particles predominate in the bed grain size distribution. At the bedload transport corresponding to average values (before and after a peak), the surface grain size distribution corresponds to that of the supplied sediments. This process is described in detail in Chapter 5 and *Ghilardi et al.* (2013).

6.3.2   Definition of amplitude and period of bedload pulses

Bedload pulses may be characterized by two parameters, their period (T_{qs}) and their amplitude ($\sigma_{qs}/q_{s,end}$). The definition of the period of a bedload pulse is based on a correlation analysis similar to the one performed in Chapter 5.

Figure 6.3 presents the normalized auto-correlation functions of the time-varying variables presented in Figure 6.2. All of the variables, except bedload, are sub-sampled by linear interpolation at regular intervals of 1 minute, the same sampling rate as the acquisition frequency of the sediment transport. The first meaningful peak in the auto-correlation function corresponding to the sediment transport occurs at a time lag of 76 minutes. This time lag corresponds roughly to the period identified in section 6.3.1 for bedload pulses of approximately 80 minutes (cf. Figure 6.2). A second peak in the auto-correlation function for the sediment transport was observed at a time lag of approximately 142 minutes, or approximately two times the time lag of the first peak, corroborating 76 minutes as a good estimate of the duration of the fluctuations in the present case.

The shape of the auto-correlation functions of the morphological parameters and the average velocities indicates, as expected, a cyclic behavior similar to that of the sediment transport. This is the case even though these variables were measured with less time resolution, given the experimental procedure followed (cf. chapter 6.2). Due to the duration of the experiment (200 minutes) and the duration of one cycle (only three cycles were

captured in this long experimental run), only the first correlational peaks are statistically relevant. An exception occurs for P^*, for which the auto-correlation values are not significant, although the shape of the function is similar to that of all of the other variables. Nevertheless, their coincidence and clarity confer meaningfulness to the above observations. The duration of the fluctuation in the sediment transport T_{qs} is defined as the time lag of the first positive peak in the auto-correlation function of the bedload (cf. Figure 6.3).
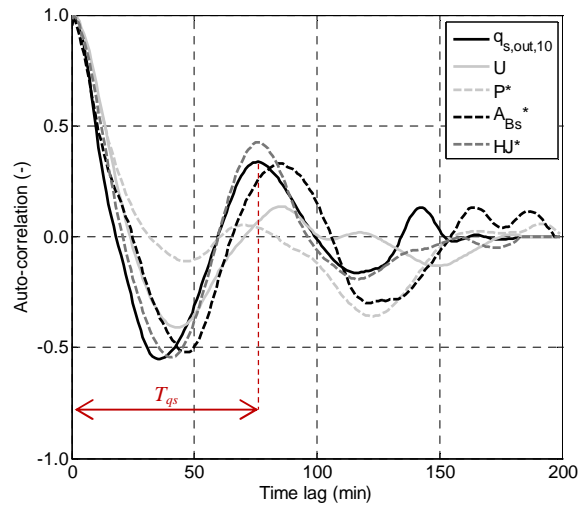
Figure 6.3: Normalized auto-correlation functions for: bedload ($q_{s,out,10}$); mean velocity (U); dimensionless average protrusion (P^*); dimensionless boulder surface (A_{Bs}^*); and dimensionless number of hydraulic jumps (HJ^*). Test with N_{Bs}=20 m^{-2} boulders of diameter D=0.075 m, λ/D=3, $q_{s,in}$=0.146 x10^{-3} m^{3}s^{-1}m^{-1}, q=0.0109 m^{3}s^{-1}m^{-1} and S=13.0% (cf. Table 6.1, line in bold).

The amplitude of the fluctuations is defined as the standard deviation of the bedload σ_{qs} divided by the cumulative average sediment transport $q_{s,end}$ calculated at the end of the test: $\sigma_{qs}/q_{s,end}$. The calculated periods and amplitudes of the bedload burst are shown in Table 6.1 for all tests, after application of the data treatment described here, together with the test characteristics (S, λ/D, D, N_{Bs}, q) and other results ($q_{s,end}$, $\bar{U}$, $\bar{P_{av}}$).

6.3.3 Analysis of amplitude and period of bedload pulses

The cyclic fluctuations described above and clearly visible in Figure 6.2 and Figure 6.3 were observed in all of the tests. A total of 38 tests were carried out for various boulder configurations (λ/D and D), flume slopes (S=6.7%, 9.9%, and 13%), and sediment supply (0.029x10^{-3} to 0.236x10^{-3} m^{3}s^{-1}m^{-1}) to further investigate bedload pulses in steep slopes in the presence of randomly distributed large-scale boulders.

The normalized amplitude of the bedload fluctuations, as defined above, ranged between 13% for the smallest slope and 97% for the largest slope, while the duration of the fluctuations varied between 9 (for S=6.7%) and 193 (for S=9.9%) minutes. The water discharge needed to transport the sediments varied between 0.0424 m^{3}s^{-1}m^{-1} for the test with a high density of boulders (λ/D=2, D=0.100 m) and the smallest slope and 0.0104 m^{3}s^{-1}m^{-1} for the smallest density of boulders and the steepest slope. The mean water depth (calculated as $h=q/U$), ranged from 0.027 m to 0.053 m.

Figure 6.4 presents the relationship between the amplitude $\sigma_{qs}/q_{s,end}$ and period T_{qs} of the bedload fluctuations (cf. Table 6.1). The pulse amplitude clearly increases with the period, which may be explained by the fact that, in longer cycles, the period during which low sediment transport occurs is extended. For similar bedload rates, the volume of accumulated gravel available to be released and to build a sediment burst is directly proportional to the period of low sediment transport. Larger amounts of accumulated gravel will induce more significant bursts in sediment transport, caused by the bed ripple destruction, explaining the trend between amplitude and period illustrated in Figure 6.4. The graph suggests that the pulse amplitude can increase up to a maximum of 100% of the average sediment transport, whereas there is no apparent limit on the duration of a pulse. No particular trend was confirmed when the data were analyzed partially channel slope, boulder density, and boulder diameter.
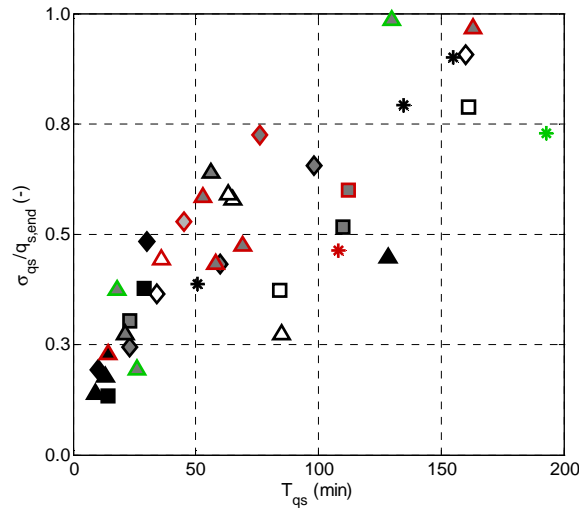
Figure 6.4: Relation between period T_{qs} and amplitude $\sigma_{qs}/q_{s,end}$ of bedload fluctuations. The symbols used are presented in Table 6.1.

When plotted against the liquid discharge, a clear link with both the period (Figure 6.5a) and amplitude (Figure 6.5b) of the bedload fluctuations is observed. For high-flow conditions (high q), the fluctuations become smaller in both period and amplitude. The data points are grouped as a function of the flume slope (distinguished by the contour color) and are aligned as a function of water discharge, both in amplitude and period. When the water discharge increases, the period and amplitude of the pulses decreases. The discharge needed for a given characteristic (period or amplitude) is smaller on steeper slopes. Furthermore, a smaller decrease in water discharge is needed to obtain the same increase in the pulse duration and amplitude on steeper slopes. This means that for steep reaches, even a small change in hydraulic conditions can induce an abrupt change in bedload transport. The effect of the boulder configuration is also perceptible in Figure 6.5. For a given bedload pulse period or amplitude, the water discharge increases as the dimensionless boulder distance (λ/D) decreases (i.e., when a higher proportion of the bed surface is occupied by boulders; the parameter is indicated by the fill color). No effect of the diameter (indicated by the symbol shape) is visible in this plot. For a similar sediment transport and a given slope, the discharge needed for equilibrium conditions is generally higher for smaller λ/D (cf. Table 6.1, *Ghilardi and Schleiss* (2012)).

Figure 6.5: (a) Period T_{qs} and (b) amplitude $\sigma_{qs}/q_{s,end}$ of bedload fluctuations as a function of water discharge q. The symbols used are presented in Table 6.1.

The data in Figure 6.5 are clearly grouped as a function of the slope and aligned with increasing liquid discharge. Both these variables enter into the calculation of the stream power ω (cf. Eq.(46)), which represents the rate of loss of energy as water flows downstream. Plots of T_{qs} and $\sigma_{qs}/q_{s,end}$ as a function of the stream power are given in Figure 6.6a and Figure 6.6b, respectively, which show that the duration and amplitude of the fluctuations clearly decrease when the stream power increases. For higher stream power, no grain sorting was observed during the tests, likely due to the higher energy available to transport all the mobile sediment diameters. The absence of vertical sorting does not permit the creation of coarse plane bed structures, the subsequent destruction of which causes bedload fluctuations (cf. section 6.3.1 and Chapter 5). The attenuation of fluctuations is rapid at first (increase in low values of stream power), but quickly reaches a lower limit for a stream power of approximately 15–20 Wm^{-2}. The stream power is especially high for tests with $\lambda/D=2$ on the 6.7% slope (the four data points in Figure 6.6 that stand apart from the rest of the data points and correspond to a stream power of approximately 25 Wm^{-2}). In these tests, the water discharge was considerably higher than in the other tests. This was the case even for similar levels of sediment discharge, due to the extra flow resistance

provided by the large density of boulders present and their protrusion from the mobile sediments.

Figure 6.6: (a) Period T_{qs} and (b) amplitude $\sigma_{qs}/q_{s,end}$ of bedload fluctuations as a function of stream power ω. The symbols used are presented in Table 6.1.

Extra resistance to momentum balance (momentum sink terms) induced by macro-rough bed has two main sources (*Nikora et al.* 2001): form-induced or dispersive stresses, due to the spatial and time intermittency of the turbulent velocity field in the heterogeneous river bed, and pressure drag caused by flow separation and recirculation around the boulders. The magnitude of the influence of the macro-roughness elements in the flow is intrinsically related to the spatial density of the individual macro-elements and in particular to the distance between the elements. Depending on λ/D, boulders can act as individual or interacting elements in the flow. For large λ/D, boulders act individually and as isolated elements in the flow, and the shear layers around them do not intersect. When λ/D is smaller, the shear layers around boulders overlap and an interference type of flow is formed, causing extra flow drag (*Canovaro et al.* 2007; *Yager et al.* 2007). For small λ/D, the flow is concentrated above the roughness elements, which are eventually submerged and work as a layer whose collective roughness decreases with λ/D. *Canovaro et al.* (2007) found that a boulder density $\lambda/D \approx 2$ (i.e., $\Gamma \approx 0.2$, according to their definition, where Γ is a parameter representing the boulder density) is the threshold value at which the most

interaction among boulders is observed, causing the drag to be maximum. According to *Canovaro et al.* (2007) and our observations, this value seems to correspond to a maximum state of interference flow, with a clear influence on the amplitude and period of the bedload bursts, as observed in Figure 6.6. The results indicate that the stream power explains the bedload fluctuation for a limited density of boulders above the threshold corresponding to wake interference flow.

In Figure 6.7, the pulse duration and amplitude are plotted against the bed shear stress, which is calculated as $\tau=\rho g R_h S$, where R_h is the hydraulic radius. Assuming a uniform flow, the flume slope S is used rather than the energy slope, which is acceptable in a reach-averaged analysis. The bed shear stress is larger on higher slopes, but no clear trend in the fluctuation period (Figure 6.7a) or amplitude (Figure 6.7b) can be discerned. Thus, the bed shear stress does not seem relevant to quantifying fluctuations in the bedload. Figure 6.6 and Figure 6.7 show that the potential energy available to the stream (ω), and not the total bed forces acting on the channel bed (τ), dictates the amplitude and duration of bedload pulses and thus morphological changes.
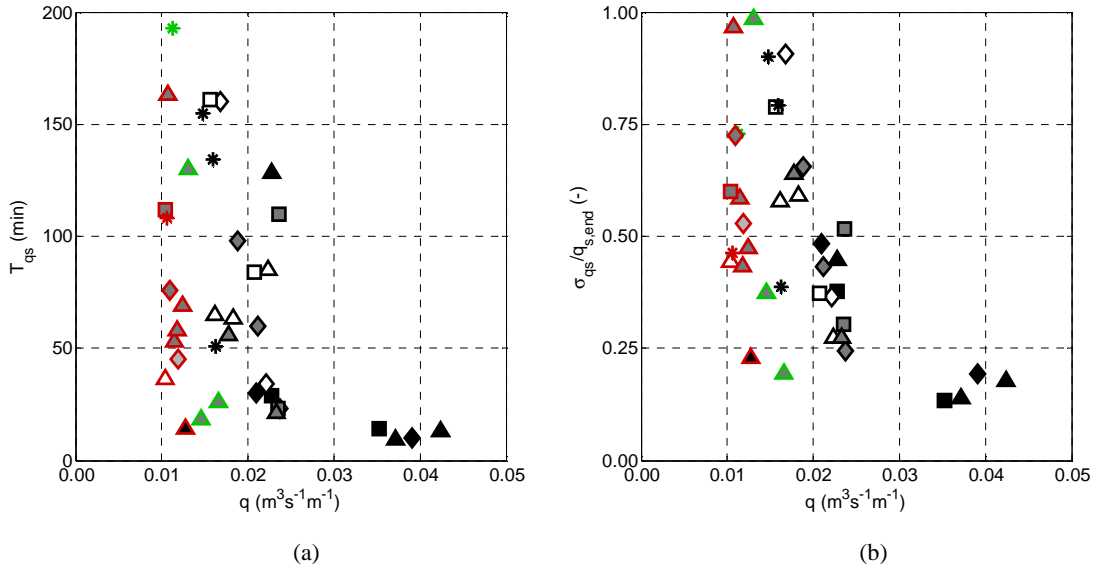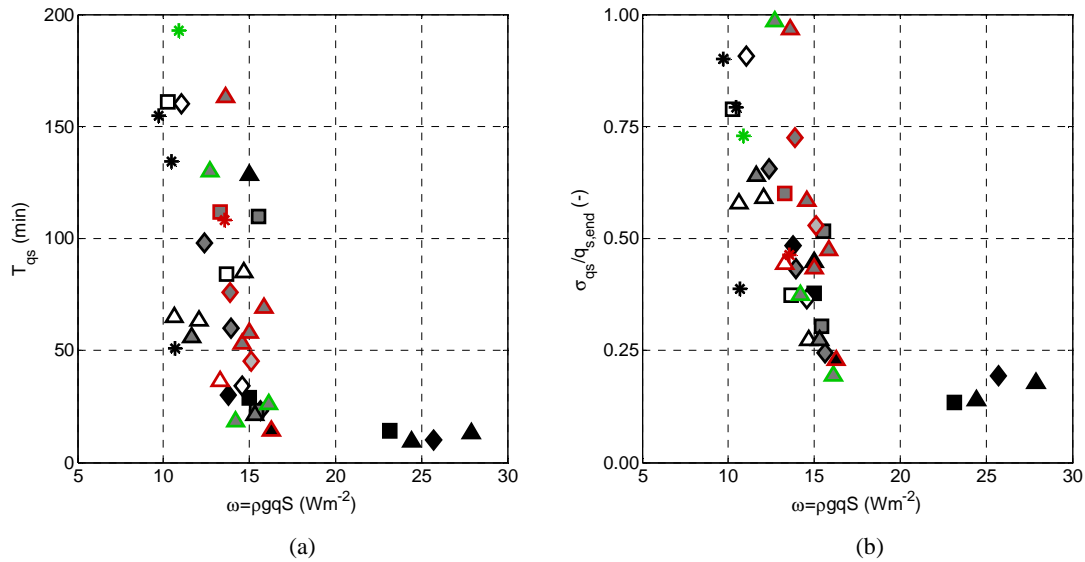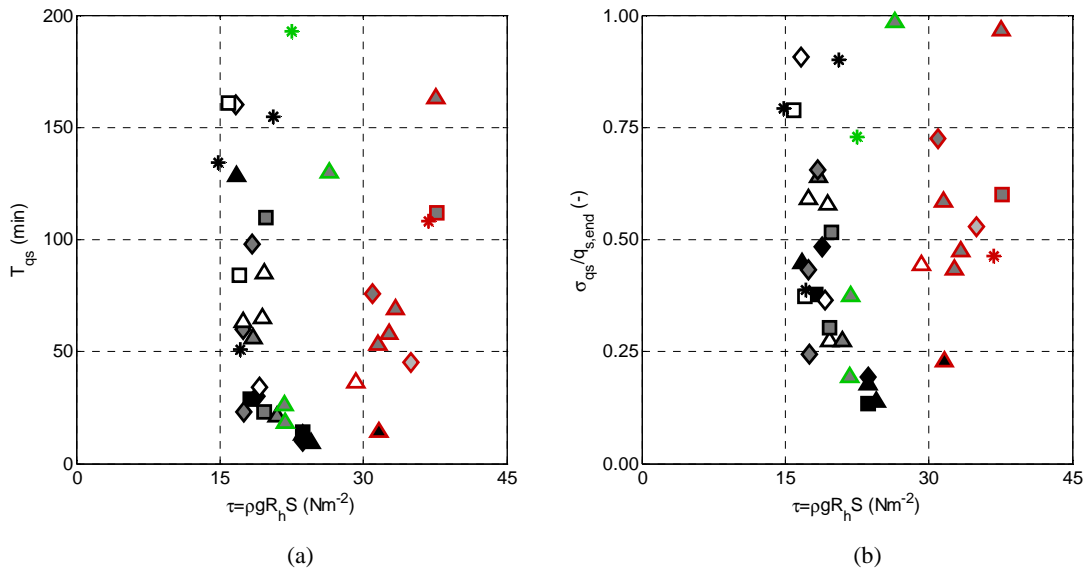

Figure 6.7: (a) Period T_{qs} and (b) amplitude $\sigma_{qs}/q_{s,end}$ of bedload fluctuations as a function of bed shear stress τ. The symbols used are presented in Table 6.1.

As suggested by several authors (*Lenzi et al.* 2006; *Yager et al.* 2007; *Yager et al.* 2012a), the presence of boulders decreases the excess stress available for sediment transport. The relevant parameters characterizing the presence of boulders are generally the bed surface occupied by them and their number and protrusion.

In Figure 6.8a, the stream power is plotted against the surface occupied by boulders, represented by $P_{av}^{-2} N_{Bs}$. A linear relation between these variables is observed. This behavior underlines the important role of the presence of boulders in flow energy losses. However, boulder protrusion alone cannot explain bedload fluctuations. The number of macro-roughness elements, represented by the number of boulders, must be taken into account to explain the rate of total energy losses ω. Figure 6.8b illustrates the relation between the bed surface not occupied by boulders and the stream power ω. Figure 6.8c illustrates the relation between the total number of hydraulic jumps in the experimental flume *HJ* and the stream power ω. The linear relationships among the morphological parameters presented in Figure 6.8 and the stream power confirm that they yield redundant information and that they all influence the sediment transport capacity and its time-varying nature. Figure 6.8 shows the clear dependence between stream power and bed morphology characteristics which, in turn, are strongly related to the period and amplitude of bedload bursts.

6.4 Conclusions

The amplitude and period of bedload fluctuations was analyzed using the results of 38 tests carried out with various flume slopes, boulder configurations (couples of λ/D and *D*), and sediment supplies. Although these fluctuations are caused by the presence of graded bed materials and not by macro-roughness elements, the presence of boulders does have an effect on the sediment transport capacity and thus on the duration and amplitude of bedload fluctuations. For high-flow conditions, sediment transport fluctuations decrease in both period and amplitude. A higher discharge is needed to transport the sediments when numerous boulders are present in the flume.
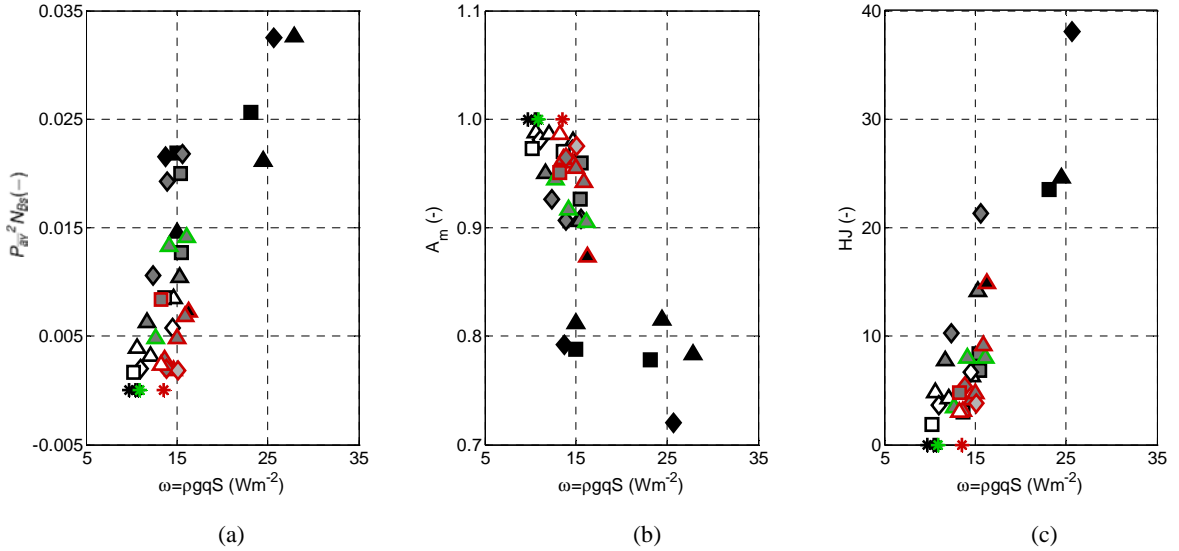
Figure 6.8: a) Squared average protrusion P_{av}^{-2} multiplied by the average number of boulders per square meter N_{Bs} ($P_{av}^{-2}N_{Bs}$), b) mobile portion of the bed surface A_m and c) total number of hydraulic jumps in the flume HJ, as a function of stream power ω. The symbols used are presented in Table 6.1.

Bedload fluctuations characteristics are influenced by both the water discharge and the slope. The amplitude and period of bedload pulses clearly decreases as the stream power increases, accounting for the effects of both of the above-mentioned parameters. A direct relation between the stream power and the presence of boulders, which can be explained in terms of any of the morphological parameters (boulder protrusion, boulder surface or number of hydraulic jumps) was found. This relation shows that the energy losses caused by the boulders have an influence on both the sediment transport capacity and the bedload pulse characteristics (period and amplitude). Decreases in the period and amplitude of bedload pulses caused by increases in energy losses decrease morphological changes over time. The results of this study show that the stream power explains the bed morphology changes and bedload fluctuations better than the bed shear stress.

Chapter 7

Sediment transport in steep channels with boulders

This chapter, written in the form of a scientific article, analyses the influence of boulders on the sediment transport capacity on a steep channel. A sediment transport formulae is proposed based on the data collected during the present research. Results are then compared to existing formulae.

Abstract: Most sediment transport equations overestimate the bedload rate by several times when applied to mountain rivers. The overestimation occurs since these formulations do not take into account the presence of macro-roughness elements, such as large relatively immobile boulders, that disrupt the flow and alter channel roughness. Sediment transport on steep channels with boulders was investigated using 41 laboratory experiments carried out on a tilting flume with several combinations of constant sediment and water discharge, for three different slopes (S=6.7%, 9.9%, and 13%). The channel bed was composed of mobile sediments and immobile boulders. Sediment transport, bulk mean flow velocities and variables describing the morphology of the channel bed were measured regularly during the experiments. The sediment transport capacity is clearly decreasing with dimensionless boulder distance (a spatial density parameter). It was observed that the critical discharge for incipient motion of mobile sediments is dependent not only on the channel slope but also on the boulder density, and a formula for critical discharge accounting for the presence of boulders was developed. The link between the excess shear stress relative to a critical value and the transport capacity is less clear than the link between the latter and the excess discharge. A sediment transport formula based on excess discharge relative to a critical value for incipient motion of mobile sediments and considering the presence of boulders is herein proposed. The critical discharge formula is used in existing sediment transport formulae, showing an improvement of bedload estimates for the present experimental data.

Key words: Bedload, Boulders, Steep channel, Sediment transport equation.

7.1 Introduction

Despite the importance of mountain rivers in the control of sediment supply to lowland mild-slope rivers (*Wohl* 2000; *Yager et al.* 2007), only a few studies were made on steep channels, mainly during the last two decades. These rivers are typically characterized by a stepped longitudinal profile (*Chin and Wohl* 2005; *Comiti et al.* 2009) and slopes ranging from 0.1% to almost 20% (*Papanicolaou et al.* 2004). The channel bed is composed of coarse mobile sediments, found generally in the pools or scouring holes downstream of steps, and by large relatively immobile boulders (*Rickenmann* 2001; *Papanicolaou et al.* 2004; *Yager et al.* 2007), that can be found in steps spanning across the whole channel section (step-pool morphology) or in a more irregular fashion (cascade morphology) (*Montgomery and Buffington* 1997).

To the authors knowledge, before the present study the impact of isolated boulders on bedload transport in steep channels was analyzed only by *Yager et al.* (2007), which used regularly spaced spheres simulating boulders and a uniform bed material. The presence of macro-roughness elements endure a significant part of the total shear stress and disrupt the flow by altering the channel roughness (*Wohl* 2000; *Yager et al.* 2007; *David et al.* 2011). The form drag caused by the boulders increases with their number, implying lower shear stress available at the bed for sediment entrainment (*Bathurst* 1978; *Lenzi et al.* 2006; *Yager et al.* 2007; *Yager et al.* 2012a). Hence, the presence of boulders decreases the sediment transport capacity of rivers (*Yager et al.* 2007; *Ghilardi and Schleiss* 2011, 2012). Boulder dimensionless distance λ/D (a measure of spatial boulder density), where λ is the average distance between boulders of diameter D, and boulder protrusion from the lower bed substratum are good proxies for sediment transport in mountain streams *Yager et al.* 2012b. A multitude of parameters may be used to take into account the presence of boulders in bed shear stress and bed resistance equations (form drag). Nevertheless, they generally resume to the number of boulders per unit area, their cross section, the bed area occupied by them, the distance between boulders (i.e., a spatial density parameter) and a drag coefficient (*Bathurst* 1978; *Canovaro et al.* 2007; *Yager et al.* 2007; *Pagliara et al.* 2008; *Yager et al.* 2012a). Along with form drag resistance caused by boulders, flow

energy is dissipated by spill resistance, which is due to flow acceleration and deceleration, usually over or downstream of steps (*Curran and Wohl* 2003; *David et al.* 2011). The energy loss by spill resistance is linked to the presence of hydraulic jumps downstream of steps or boulders and is proportional to the drop height (*Curran and Wohl* 2003; *Comiti and Lenzi* 2006).

Most sediment transport formulae have the following general form:

$$q_b = \alpha \left(X - X_{cr} \right)^{\beta} S^{\gamma} \tag{48}$$

Where q_b is the bedload transport, which may be expressed in different units depending on the equation ($m^3 s^{-1} m^{-1}$, $kg s^{-1} m^{-1}$, or dimensionless; most often either the first or the last unit are used), α, β, and γ are empirical constants, S is the bed slope, X may be the liquid discharge q per unit width (*Rickenmann* 1990), stream power ω per unit width (*Bagnold* 1980), or, more commonly used, the dimensionless shear stress τ^* (*Fernandez Luque and van Beek* 1976), being X_{cr} the corresponding critical value at which the bedload begins. The coefficient α is often expressed as a function of grain size diameters and liquid and solid densities. The exponent β is often set to 1 (*Schoklitsch* 1962; *Rickenmann* 1990), but can range up to 2 or 3 (*Fernandez Luque and van Beek* 1976; *Bagnold* 1980; *Wong and Parker* 2006). γ has been found to vary between 1.5 and 2 by *Meyer-Peter and Müller* (1948), *Schoklitsch* (1962) and *Rickenmann* (1990) and found to be zero by *Fernandez Luque and van Beek* (1976) and *Wong and Parker* (2006). Other more complex forms of sediment transport formulae exist, but they can often be reduced to the afore-mentioned form (*Smart and Jäggi* 1983).

Several authors highlighted the possible dependence of critical bed shear stress from the channel roughness and hiding effects due to the wide grain size distribution (*Buffington and Montgomery* 1997; *Lenzi et al.* 2006), the channel gradient (*Papanicolaou et al.* 2004; *Lamb et al.* 2008; *Recking et al.* 2008a) and morphology (*Church et al.* 1998). Bed shear stress calculations need a precise knowledge of the channel hydraulics, which has a high local variability in mountain rivers. On the other hand, *Bagnold* (1966) stream power (per unit width) criterion, which quantifies the rate of loss of energy as water flows downstream, and thus the power potentially available for performing geomorphic work

(*Bagnold* 1966; *Ferguson* 2005; *Petit et al.* 2005; *Parker, C et al.* 2011), can be approximated from such bulk channel properties as width and slope, combined with the river discharge. *Gomez and Church* (1989) showed that the stream power has a more significant correlation with sediment transport than any other hydraulic parameter. *Rickenmann* (1990, 1991b) used another approach needing only gross channel properties: the discharge itself, with the corresponding critical discharge, which is solely related to the sediment grain size and the channel slope through a power law. Nevertheless, most formula do not predict sediment transport consistently well (*Montgomery and Buffington* 1997; *Yager et al.* 2007).

The objective of this chapter is to analyze the influence of real boulders (and not idealized boulders, such as spheres) on sediment transport capacity. This is achieved through flume experiments where bedload, flow velocity, and bed morphology are assessed over time. Results herein presented are based on 35 experiments with boulders and 6 experiments without boulders, carried out for varying water and sediment discharges.

Following this introduction, the experimental methods are presented. Then, a general characterization of bed morphology is described and the effect of boulders on sediment transport capacity is analyzed. The steps leading to the proposal of a sediment transport formula are then presented. Finally, the results of the herein developed formula are compared with several existing bedload transport formulae and main conclusions are drawn.

7.2 Research methods

7.2.1 Experimental setup and procedure

The impact of randomly distributed relatively immobile boulders on bedload fluctuations is investigated by means of laboratory experiments, carried out on a steep (longitudinal inclination of 6.7 to 13%), 8 m long (7 m usable) and 0.25 m wide, tilting flume at the Laboratory of Hydraulic Constructions (LCH) of the Ecole Polytechnique Fédérale de Lausanne (EPFL) (Figure 7.1a). Water and poorly sorted sediments are constantly supplied

at the flume inlet. Bedload at the channel downstream section, bulk flow velocities and morphological parameters are measured regularly during the experiments.
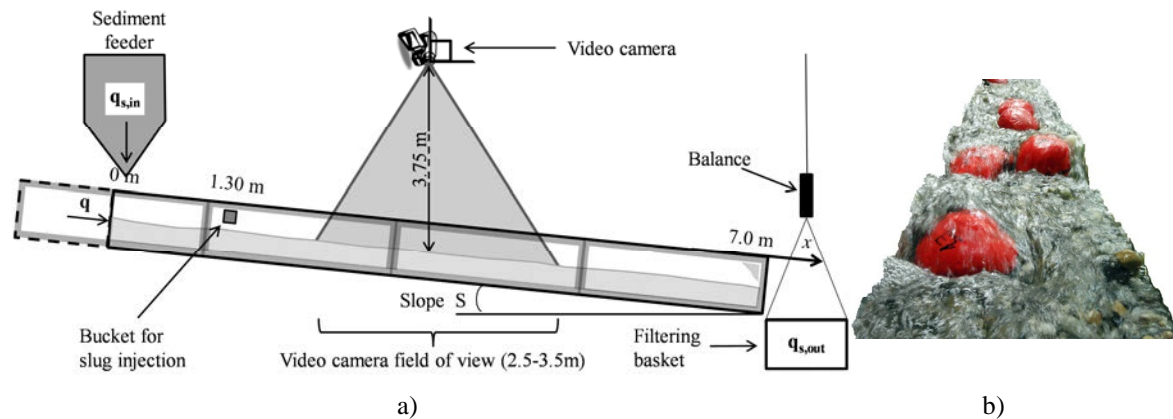
Figure 7.1: a) Sketch of the experimental setup and b) example of morphology during an experiment.

Water discharge, fed constantly by the closed general pumping system of the laboratory, is controlled by an electromagnetic flow-meter (±0.01 l/s). Sediments are constantly fed into the system by a calibrated sediment feeder situated upstream. A filtering basket suspended to a balance collects the sediments at the outlet where the weight (±1 kg) is measured every minute. An averaged value of the sediment discharge is calculated over a sliding 10 minutes window ($q_{s,out,10}$) to provide a smoothed overview of the bedload fluctuations. Sediments are recirculated between the sediment feeder and the downstream basket. During the operation of the system no sediment sorting occurred in the gravel supplied by the feeder.

Average flow velocity (U) was measured every 15 minutes by means of a technique using dye-tracer and video analysis. Similarly to salt tracer measurements, the passage of the cloud of colorant in the reach is analyzed based on the difference between images, the movement of mass center of the cloud defining the average flow velocity (*Calkins and Dunne* 1970). A velocity value is obtained by an average of five independent measures, based on five different colorant injections. A detailed description of the technique herein used is given in Chapter 4.

The protrusion (P) of four boulders is measured with a point gauge during the experiments, with a time interval of approximately 10 minutes (2 to 3 minutes per boulder, in a loop).

For every measured boulder, protrusion is sub-sampled by linear interpolation to have a value every minute. An average protrusion value between the boulders (P_{av}) is then calculated for every minute of the experiment. The definition of boulder protrusion is illustrated in Figure 7.2a.

Hydraulic jumps (*HJ*) are counted manually based on visual observation after flow velocities measurements, i.e. about every 15 minutes. This parameter is an indicator of the amount of energy dissipation and morphological variety, since hydraulic jumps generally appear downstream of the protruding boulders.

The surface occupied by boulders parallel to the river bed (A_{Bs}), called in short "boulder surface", is obtained by means of video analysis and measured with a single frame. A_{Bs} is obtained either for every velocity measurement or every minute, when the entire experiment was videotaped (cf. Table 7.1).

The frontal area of boulders (A_{if}) and the bed surface occupied by boulders (A_i) can be calculated as defined in Figure 7.2. The boulder diameter is reduced (D_x) to account for the boulder protrusion, as defined in equation (49). It corresponds to the diameter of the circle at the surface of the mobile sediments. This definition is helpful for the calculation of boulder frontal area (A_{if}, (eq. (51)), cf. Figure 7.2a) and bed parallel area (A_i, (eq. (52), cf. Figure 7.2b). A unit bed surface is defined A_t (eq. (50)), similarly to *Yager et al.* (2007), depending on the average distance λ between randomly placed boulders (Figure 7.2b). In a unit bed surface, only one boulder is present, as shown in Figure 7.2b, thus for a unit bed area A_t, the frontal surface occupied by boulders correspond to A_{if} and bed area occupied by boulders corresponds to A_i. The mobile bed surface A_m is calculated as the difference between the total and the immobile bed surface (eq. (53)).

$$D_x = 2\sqrt{P_{av}(D - P_{av})} \tag{49}$$

$$A_t = \frac{\sqrt{3}}{2}\lambda^2 \tag{50}$$

$$\begin{cases} A_{if} = \dfrac{D/2\left(D\sin^{-1}(D_x/D) - D_x\right) + D_x P_{av}}{2} & \text{if } P_{av}<0.5D \\[4mm] A_{if} = \pi\dfrac{D^2}{4} - \dfrac{D/2\left(D\sin^{-1}(D_x/D) - D_x\right) + D_x P_{av}}{2} & \text{if } P_{av}\geq0.5D \end{cases} \tag{51}$$

$$\begin{cases} A_i = \pi\dfrac{D_x{}^2}{4} & \text{if } P_{av}<0.5D \\[4mm] A_i = \pi\dfrac{D^2}{4} & \text{if } P_{av}\geq0.5D \end{cases} \tag{52}$$

$$A_m = A_t - A_i \tag{53}$$

a) b)
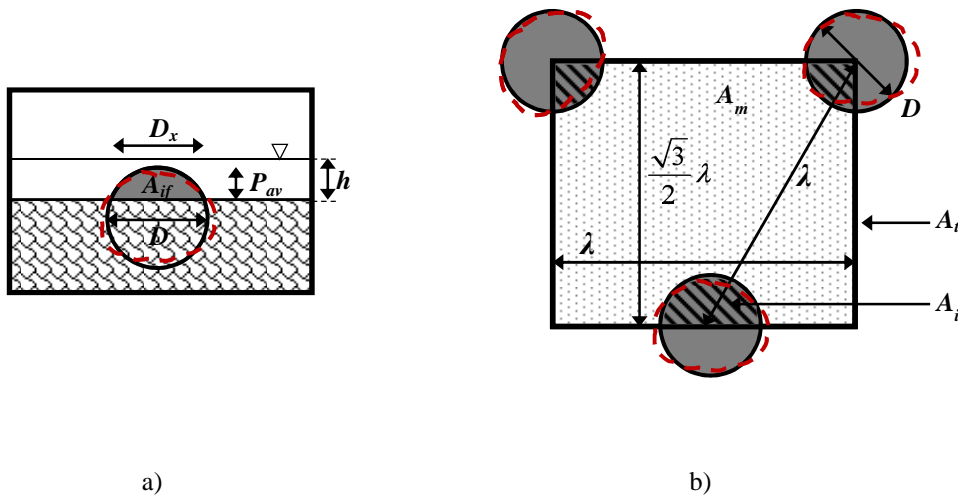
Figure 7.2: a) Schematic front view of one boulder, with the definition of the protrusion P_{av}, the reduced diameter D_x, and the frontal area A_{if}; b) plan view with the definition of the bed unit surface A_t, the immobile bed surface A_i, and the mobile surface A_m. The red dashed lines indicate the shape of real boulders.

The grain size distribution of the supplied sediments is characterized by: d_{50}=9.3 mm, $d_m=d_{65}$=11.9 mm, d_{30}=7.1 mm, d_{84}=16.6 mm, and d_{90}=19.0 mm, where d_m is the mean grain size, corresponding to d_{65} and d_x is the grain size diameter for which $x\%$ in weight of the amount of sediments have smaller diameters. Boulders are not taken into account in this calculation and are not supplied as mobile sediments; they were instead placed in the channel bed before the beginning of the experiments. Boulders are relatively immobile,

which means that they are not transported by the flow, although they may move even along a distance of a few times their diameter during experiments, mainly due to the scour hole formed around them.

An almost plane bed is prepared before the experiments and boulders are placed into the flume half buried into mobile sediments, which corresponds to a protrusion equal to approximately 30% of the equivalent sphere diameter approximately, since real stones are used in this research. Water and sediment supply are started at the same time.

The imposed equilibrium condition between liquid and solid discharge (couple q_s - q) is such that boulders are still relatively visible after a peak in sediment transport. The test is stopped immediately after a peak in bedload, when the average outlet sediment discharge over the last 10 minutes is equal to the sediment supply ($q_{s,out,10} \approx q_{s,in}$). The overall cumulative average of the outlet sediment transport has to be within ±20% of the sediment supply at the end of the experiment (q_s).

7.2.2 Experimental parameters

Table 7.1 presents the configuration of the experiments, characterized by slope S, dimensionless boulder distance λ/D, equivalent boulder diameter D, number of boulder per square meter N_{Bs}, water discharge q per unit width, and sediment supply $q_{s,in}$ per unit width. The main bulk results, averaged during the whole experiment are also presented. This includes the total average sediment outlet q_s, the mean flow velocity $\bar{U}$, the average boulder protrusion $\bar{P_{av}}$, the number of hydraulic jumps per square meter HJ, the immobile bed surface per unit surface A_i/A_t (eq. (50) and (52)), and the boulder frontal area per unit surface A_{if}/A_t (eq. (50) and (51)).

Table 7.1 (on the next page): Experimental parameters and main bulk results. The symbols used to represent the experiments in Figure 7.3 to Figure 7.10 are given in the last column of the table. The filling of the symbols depends on λ/D (*inf* represents the tests without boulders, thus with an infinite distance), the shape on boulder diameter D and the contour line color on the flume slope S. For tests with *, boulder protrusion was measured at the end of the experiment. For tests with x, the number of hydraulic jumps was not counted.

For tests with -, boulder surface was measured every 15 minutes, while for the others it was measured every minute. The test numbers correspond to those given in Table 3.1 and in Appendix B.

	S (%)	λ/D (-)	D (m)	N_{Bs} (m^{-2})	q (m^{3}s^{-1}m^{-1})	$q_{s,in}$ x10^{-3} (m^{3}s^{-1}m^{-1})	q_s x10^{-3} (m^{3}s^{-1}m^{-1})	$\bar{U}$ (ms^{-1})	$\bar{P}_{av}$ (m)	HJ (m^{-2})	A_i/A_t (-)	A_{if}/A_t (-)	Symb.	Test Nr.
x-	6.7	2	0.075	45	0.0209	0.029	0.024	0.56	0.022	-	0.19	0.048	◆	8
-	6.7	2	0.075	45	0.0391	0.134	0.146	0.77	0.027	22	0.21	0.064	◆	19
x-	6.7	2	0.100	25	0.0228	0.057	0.065	0.71	0.024	-	0.17	0.036	▲	4
-	6.7	2	0.100	25	0.0372	0.134	0.139	0.70	0.029	14	0.19	0.048	▲	5
x-	6.7	2	0.100	25	0.0424	0.157	0.174	0.84	0.036	-	0.21	0.064	▲	17
x-	6.7	2	0.125	16	0.0228	0.063	0.075	0.64	0.037	-	0.19	0.049	■	7
-	6.7	2	0.125	16	0.0352	0.134	0.137	0.70	0.040	13	0.20	0.054	■	18
	6.7	3	0.075	20	0.0188	0.056	0.053	0.52	0.023	6	0.09	0.023	◆	6
x-	6.7	3	0.075	20	0.0212	0.091	0.104	0.63	0.031	-	0.10	0.034	◆	13
-	6.7	3	0.075	20	0.0238	0.134	0.140	0.70	0.033	12	0.10	0.037	◆	24
-	6.7	3	0.100	11	0.0177	0.056	0.061	0.49	0.024	4	0.07	0.016	▲	3
-	6.7	3	0.100	11	0.0233	0.134	0.124	0.55	0.031	8	0.09	0.023	▲	15
x*-	6.7	3	0.100	11	0.0240	0.139	0.156	0.67	0.025	-	0.08	0.017	▲	20
-	6.7	3	0.125	7	0.0236	0.101	0.112	0.60	0.043	4	0.09	0.026	■	2
-	6.7	3	0.125	7	0.0235	0.134	0.119	0.60	0.054	5	0.10	0.035	■	9
x*-	6.7	3	0.125	7	0.0240	0.156	0.171	0.90	0.032	-	0.08	0.017	■	14
-	6.7	5	0.075	7	0.0168	0.056	0.057	0.53	0.017	2	0.03	0.005	◇	11
-	6.7	5	0.075	7	0.0222	0.134	0.131	0.58	0.029	4	0.03	0.011	◇	23
-	6.7	5	0.100	4	0.0162	0.056	0.056	0.42	0.031	3	0.03	0.008	△	10
	6.7	5	0.100	4	0.0183	0.094	0.088	0.55	0.028	2	0.03	0.007	△	21
-	6.7	5	0.100	4	0.0223	0.134	0.135	0.57	0.046	4	0.04	0.014	△	27
	6.7	5	0.125	2	0.0156	0.056	0.060	0.52	0.027	1	0.02	0.004	□	12
-	6.7	5	0.125	2	0.0208	0.134	0.150	0.63	0.061	2	0.04	0.014	□	25
-	6.7	inf	-	0	0.0148	0.056	0.065	0.35	0.000	0	0.00	0.000	✳	1
	6.7	inf	-	0	0.0159	0.094	0.100	0.58	0.000	0	0.00	0.000	✳	16
-	6.7	inf	-	0	0.0162	0.134	0.119	0.49	0.000	0	0.00	0.000	✳	22
x-	6.7	inf	-	0	0.0204	0.186	0.151	0.72	0.000	0	0.00	0.000	✳	26
	9.9	3	0.100	11	0.0131	0.094	0.089	0.38	0.021	2	0.07	0.013	▲	28
	9.9	3	0.100	11	0.0146	0.136	0.143	0.53	0.035	5	0.09	0.027	▲	30
	9.9	3	0.100	11	0.0166	0.192	0.198	0.61	0.036	5	0.09	0.028	▲	31
	9.9	inf	-	0	0.0112	0.094	0.088	0.40	0.000	0	0.00	0.000	✳	29
	13	2	0.100	25	0.0128	0.146	0.168	0.41	0.017	8	0.13	0.022	▲	35
	13	3	0.075	20	0.0109	0.146	0.172	0.36	0.010	3	0.05	0.007	◆	34
	13	3	0.100	11	0.0107	0.146	0.145	0.28	0.016	2	0.05	0.009	▲	32
	13	3	0.100	11	0.0114	0.192	0.199	0.37	0.013	2	0.05	0.007	▲	33
	13	3	0.100	11	0.0124	0.236	0.254	0.38	0.025	5	0.08	0.017	▲	39
	13	3	0.100	11	0.0118	0.236	0.261	0.37	0.021	3	0.07	0.013	▲	40
	13	3	0.125	7	0.0104	0.146	0.165	0.27	0.035	3	0.08	0.019	■	37
	13	4	0.075	11	0.0118	0.236	0.266	0.34	0.013	2	0.03	0.006	◆	41
	13	5	0.100	4	0.0104	0.146	0.168	0.37	0.024	2	0.03	0.006	△	36
	13	inf	-	0	0.0106	0.192	0.216	0.28	0.000	0	0.00	0.000	✳	38

7.3 Results and discussion

7.3.1 Bed morphology

The presence of boulders influences the sediment transport pulses in steep rough channels as was previously identified in *Ghilardi* (2013) and in Chapter 6. It could be shown that the period and amplitude of the bedload fluctuations decreases with increasing stream power. The latter is higher when the number and protrusion of boulders increase, which also means that there are more hydraulic jumps in the channel and that the bed surface occupied by boulders is larger. These observations indicate that the presence of boulders stabilizes the river morphology.

In the present chapter, data concerning the time averaged values of sediment transport, flow velocity, boulder protrusion, boulder surface, and number of hydraulic jumps are used to assess the influence of boulders on the sediment transport capacity.

Figure 7.3 shows the relationship among several measured morphological parameters. The number of hydraulic jumps *HJ* per square meter, dissipating energy through spill resistance, is clearly linked to the density (number per square meter) and the protrusion of boulders (Figure 7.3a), being the latter representative of the drop height (*Curran and Wohl* 2003; *Comiti and Lenzi* 2006). The bed area occupied by boulders A_{Bs}^{*} (measured by video analysis) is also, not surprisingly, correlated to the number of roughness elements, their diameter, and their protrusion (Figure 7.3b). For a given λ/D, the surface occupied by boulders A_{Bs}^{*} is similar, independent of the used diameter, when the ratio P_{av}/D is similar. Figure 7.3c indicates that the measured bed surface occupied by boulders A_{Bs}^{*} (video analysis through time) and its calculated value A_i/A_t (eq. (50) and (52)), based on boulder protrusion, diameter, and distance, are well correlated even if the value of A_i/A_t assumes a spherical form of boulders for the calculations on a unit surface, whereas A_{Bs}^{*} actually measures the real boulder surface. Figure 7.3d, presenting the frontal area A_{if}/A_t as a function of the calculated bed area A_i/A_t, reveals that data are grouped by dimensionless boulder distance. The relation is not linear and the bed surface occupied by boulders increases only up to a maximum value, and becomes constant when the protrusion is

higher than the boulder radius, while the frontal area continues to increase with protrusion. Moreover, the frontal area increases almost linearly whit boulder protrusion, while the bed surface occupied by boulders increases faster for increase in small values of protrusion.
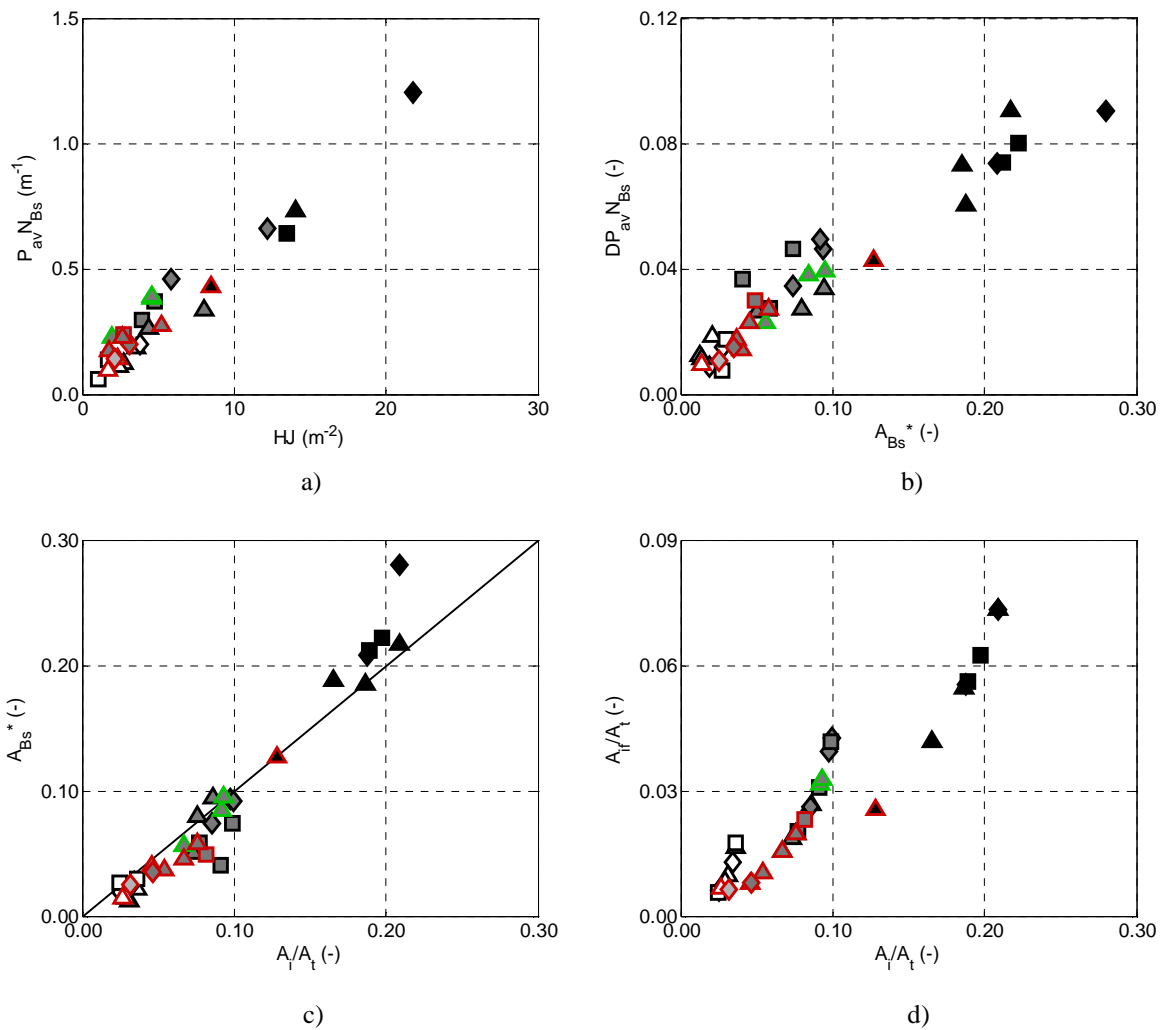

Figure 7.3: Relations between : a) the number of hydraulic jumps and the boulder protrusion and number; b) the measured bed surface occupied by boulders and the number of boulders and their protrusion and diameter; c) the measured and calculated boulder surface, where the black line indicates the unit slope curve; d) the frontal area of boulders and the bed surface occupied by these, per unit surface area. The symbols used are presented in Table 7.1.

In Figure 7.4 it can be seen that the average bulk flow velocity increases as a function of the discharge and is higher on steeper slopes for the same discharge, as expected. Data obtained with a slope of 6.7% suggest that the velocity is lower when the dimensionless

boulder distance is smaller. Figure 7.4 shows that for four tests carried out with $\lambda/D=2$ with a liquid discharge much larger than for the other experiments, flow velocities are only slightly higher. This may be a good indicator that the transport capacity is drastically reduced when boulders are closely packed ($\lambda/D=2$), confirming the observations made by *Yager et al.* (2007) and *Canovaro et al.* (2007) on flow conditions. According to *Canovaro et al.* (2007), the smallest flow velocities are observed for a roughness density equivalent to $\lambda/D=2$.
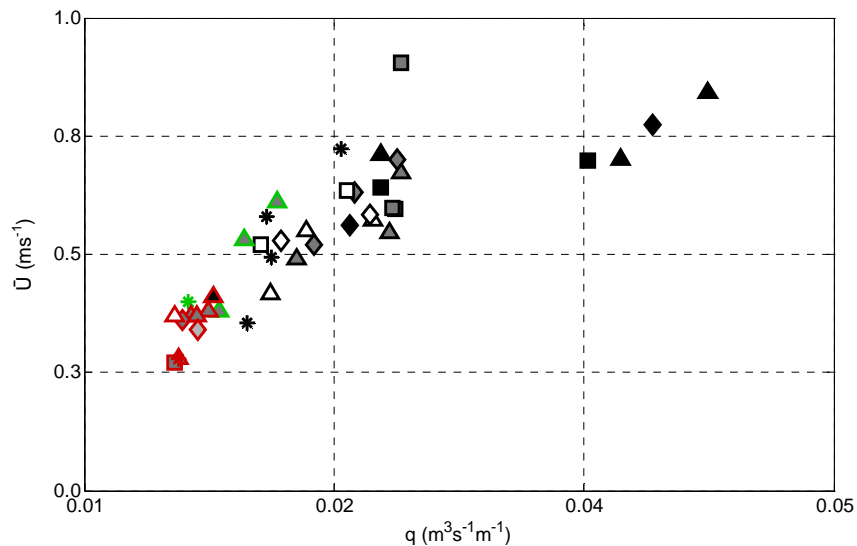

Figure 7.4: Measured bulk flow velocity $\bar{U}$ as a function of unit discharge q. The symbols used are presented in Table 7.1.

7.3.2 Sediment transport capacity and beginning of sediment motion

7.3.2.1 Relation with the liquid discharge

In Figure 7.5 the sediment transport, measured along each test and averaged over time, as a function of water discharge is presented. Reference tests without boulders as well as all the boulder configurations (combinations of several D and λ/D, except $\lambda/D=4$), were tested for several couples of solid and liquid discharge on the smallest slope ($S=6.7\%$). For the 9.9% slope, only the boulder configuration corresponding to $\lambda/D=3$ and $D=0.1$ m (three tests) and one reference test without boulders were carried out. For the steepest slope ($S=13\%$), a

reference test without boulders, all the configurations with D=0.1 m and those with λ/D=3, and an extra configuration with λ/D=4 and D=0.075 m (same boulder position as λ/D=3 and D=0.100 m) were tested, for a total of 10 tests.

As expected, the tests are clearly grouped by slope (Figure 7.5). For a given liquid discharge, higher bedload transport occurs at steeper slopes. This is highlighted by the linear trend lines obtained for each slope, that do however not include the experiments with λ/D=2 since these, with small boulder dimensionless distance, behave clearly differently from the other configurations. A trend as a function of boulder dimensionless distance (λ/D) is also visible. This is most evident on the smallest slope (S=6.7%), where the highest number of tests with different boulder densities was carried out.

Experiments without boulders show a higher sediment transport capacity, indicating that with boulders a greater liquid discharge is needed to transport the same amount of sediments. The transport capacity decreases for decreasing dimensionless distances λ/D (boulder more closely packed), as observed by *Yager et al.* (2007). Relatively small differences are observed between λ/D=5 and λ/D=3. For a dimensionless distance of 2, the transport capacity decreases abruptly, especially for higher discharges. As mentioned by *Yager et al.* (2007), the impact of boulders rapidly decreases with increasing distances, and this also confirms *Canovaro et al.* (2007) observations about the higher effect of boulder geometry on shear stress for $\lambda/D{\approx}2$ (i.e. Γ=0.2, in their spatial parameter). This may be related to the characterization of the flow around boulders changing from an isolated roughness to a wake interference flow (*Canovaro et al.* 2007). In the latter case, interference between boulders become more important and more energy can be dissipated.

By further analyzing the data for each value of λ/D on the smallest slope (S=6.7%, Figure 7.5), the influence of the diameter becomes also visible. For a given sediment discharge, slope, and λ/D, the data are aligned with increasing discharge for decreasing diameters. For example, for a sediment supply of $0.056{\times}10^{-3}$ $m^3s^{-1}m^{-1}$ on the 6.7% flume slope, the liquid discharge needs to increase from 0.0148 $m^3s^{-1}m^{-1}$ for the reference test without boulders, to 0.0156 $m^3s^{-1}m^{-1}$ for a λ/D =5 and D=0.125 m (+5.4% with respect to the reference test), to 0.0162 $m^3s^{-1}m^{-1}$ for D=0.100 m (+9.5% with respect to the reference test), and finally

0.0168 $m^3s^{-1}m^{-1}$ for D=0.075 m (+13.5% with respect to the reference test). This effect may be due to the boulder diameter itself or the number of boulders, or both of them, since for a given λ/D the number of roughness elements increases with the diameter.

Although the same trend as a function of λ/D and D is visible on the steepest slope, the impact of boulder configuration becomes almost negligible. Here again, the experiment carried out for λ/D=2 is the only one detaching from the trend line, confirming the possible change in boulder interaction and flow behavior, going from isolated roughness elements to wake interference between boulders (*Canovaro et al.* 2007).
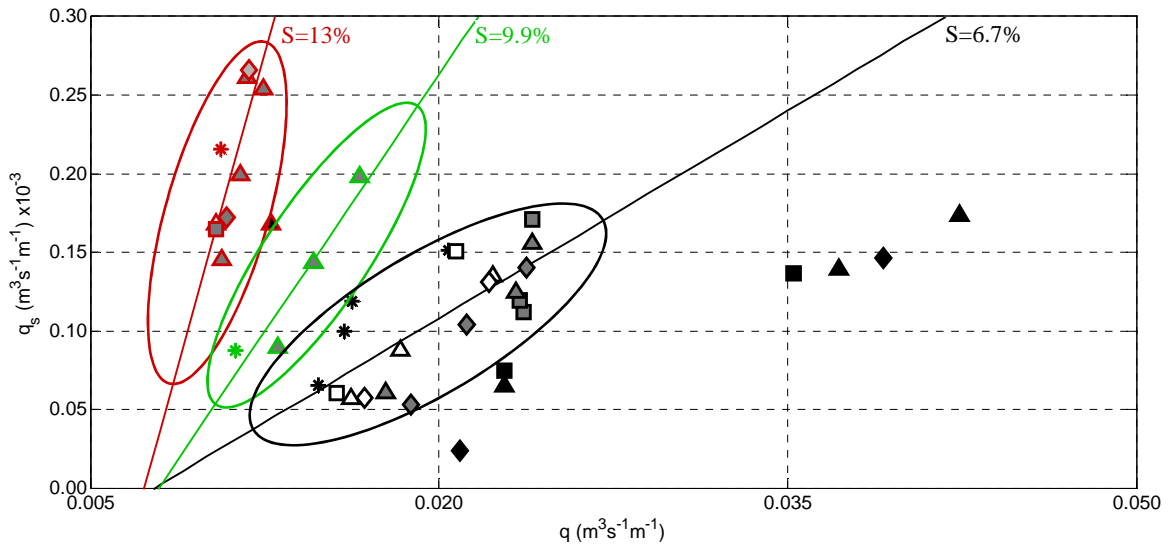

Figure 7.5: Average sediment transport capacity q_s ($m^3s^{-1}m^{-1}$) as a function of water discharge q ($m^3s^{-1}m^{-1}$). Data are grouped by channel slope and linear trend lines are given for each slope, without taking into account the experiments with λ/D=2. The symbols used are presented in Table 7.1.

In Figure 7.6 it can be seen in detail how sediment transport capacity is affected by the flume slope for a given boulder configuration (λ/D=3 and D=0.100 m, Figure 7.6a) and by the distance among boulders for a given diameter and a given flume slope (D=0.100 m and S=6.7%, Figure 7.6b).

Figure 7.6a shows a clear linear relation between the liquid and solid discharge data for the tested longitudinal inclinations of the flume. The slope of this linear trend increases with S, for λ/D=3 and D=0.100 m, which is consistent with the observation for the entire dataset presented in Figure 7.5, with the exception of experiments characterized by a

dimensionless distance of $\lambda/D=2$. In Figure 7.6, the discharge corresponding to the zero-crossing of the vertical axis is the critical discharge (q_{cr}) for the onset of bedload. Figure 7.6a indicates that it increases with slope ($q_{cr}=0.0134$, 0.011, and 0.0084 $m^3s^{-1}m^{-1}$, for slopes of 6.7%, 9.9%, and 13% respectively, for experiments with $\lambda/D=3$ and $D=0.1$ m), which is consistent with the observations made by *Rickenmann* (1990).

Figure 7.6b indicates that the influence of dimensionless distance λ/D exists, but it is secondary when compared to the slope effect. As it can be seen, q and q_s within the same boulder density (λ/D) are linearly linked. For $\lambda/D=3$ and $\lambda/D=5$ the slope of this trend is similar to that of experiments without boulders, and generally q values increase with decreasing λ/D, for the same q_s value. For the larger boulder density ($\lambda/D=2$), the slope of the linear relation between q and q_s is smaller. These results indicate that the correlation between λ/D and the values of liquid and solid discharge is probably non-linear and increases exponentially with decreasing distances between boulders. The critical discharge for beginning of motion slightly increases with decreasing dimensionless boulder distance ($q_{cr}=0.0087$, 0.0117, 0.0144, and about 0.0150 $m^3s^{-1}m^{-1}$ for experiments without boulders and with $\lambda/D=5$, 3, and 2 respectively). For small dimensionless distances ($\lambda/D=2$), the effect of boulders increases with the solid discharge (trend line slope smaller than for the experiments without boulders), going from an increase of liquid discharge of approximately 50% for the smaller solid discharge (about 0.060×10^{-3} $m^3s^{-1}m^{-1}$) with respect to the test without boulders, up to about 85-100% for the highest solid discharge. More precisely, for a sediment supply of about 0.136×10^{-3} $m^3s^{-1}m^{-1}$ the corresponding liquid discharge is increased of 10-15% for $\lambda/D=5$, 25-35% for $\lambda/D=3$, and up to 100% for $\lambda/D=2$ compared to the reference test without boulders. This clearly indicates again that the roughness elements need to be taken into account when evaluating the critical discharge for the beginning of sediment motion in a mountain river with boulders.

In Figure 7.6, the critical discharge seems to vary linearly with λ/D and as a power law with the flume slope S. A similar equation for critical discharge as a function of the channel slope was found on steep flumes by *Rickenmann* (1990), with the critical discharge dependent on the slope to the power -1.12. For a 6.7% channel slope, the very same value of 0.0087 $m^3s^{-1}m^{-1}$ is obtained from the linear regression presented in Figure 7.6b and from

Rickenmann (1990) critical discharge formula. The critical discharge, and thus the bedload transport capacity, is probably also a function of the boulder diameter or protrusion, as suggested by the data alignment (tendency to a decrease in transport capacity for an increasing diameter) in Figure 7.5.
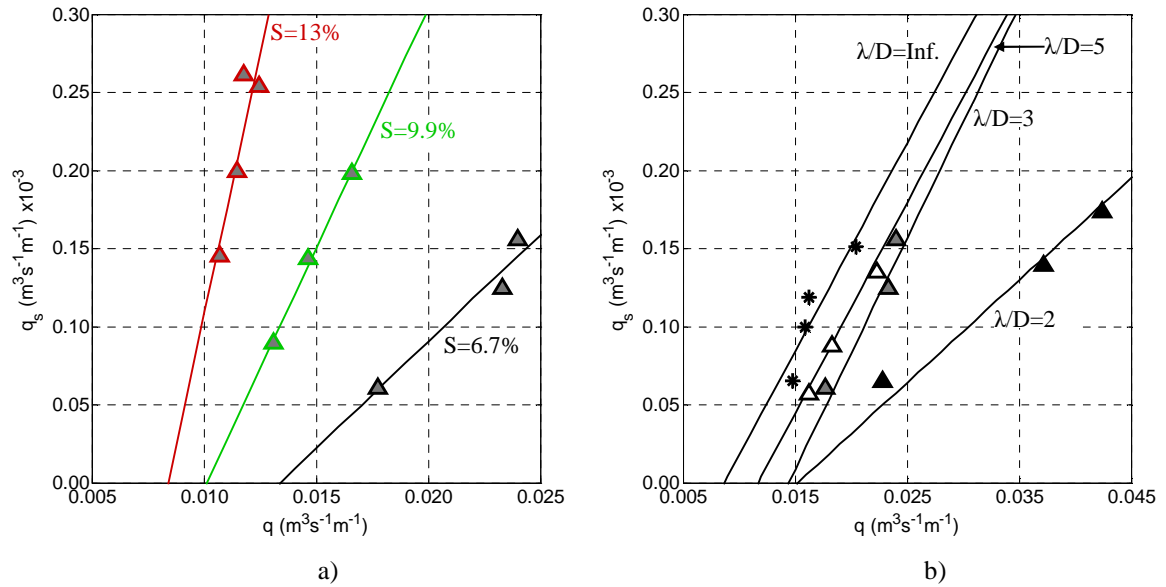

Figure 7.6: Average sediment transport capacity q_s (m^{3}s^{-1}m^{-1}) as a function of water discharge q (m^{3}s^{-1}m^{-1}). a) Effect of the flume slope for a given boulder configuration (λ/D=3 and D=0.1 m). b) Effect of dimensionless distance λ/D for a given slope (S=6.7%) and a given boulder diameter (D=0.1 m), and for experiments without boulders. The linear trend lines are shown for each data set. The symbols used are presented in Table 7.1.

With the data herein collected a formula for critical discharge (in dimensionless form following *Lenzi et al.* (2006)) is inferred, through a non-linear leas square solver, as a function of the above-mentioned parameters, namely the flume slope S and the boulder spatial density λ/D:

$$q_{cr}^* = \frac{q_{cr}}{\sqrt{g d_{50}^3}} = S^{-0.46}\left(1 - \frac{D}{\lambda}\right)^{-0.7} \tag{54}$$

where q_{cr} is a discharge per unit width (m^{3}s^{-1}m^{-1}) and q_{cr}^* its dimensionless form. The determinant coefficient of the equation is R^2=0.87. Figure 7.7 plots the values of the

calculated critical discharge according to equation (54) as a function of the values measured based on Figure 7.6.
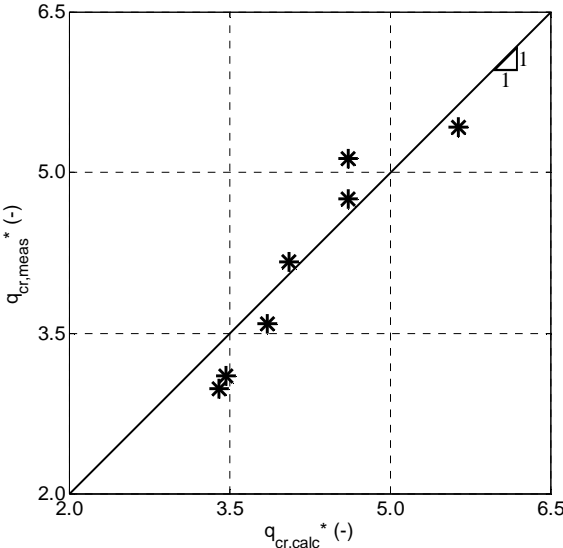

Figure 7.7: Measured critical discharge as a function of the critical discharge calculated according to equation (54). The black line indicates the unitary slope curve.

7.3.2.2 Influence of the stream power

Figure 7.5 indicates that the sediment transport capacity is clearly a function of both, liquid discharge and channel slope. These two parameters are both used in the stream power calculation, which has been shown to be a relevant indicator for period and amplitude of bedload fluctuations ((*Ghilardi* 2013) and Chapter 6), and is thus presented in Figure 7.8 against the values of measured bedload.
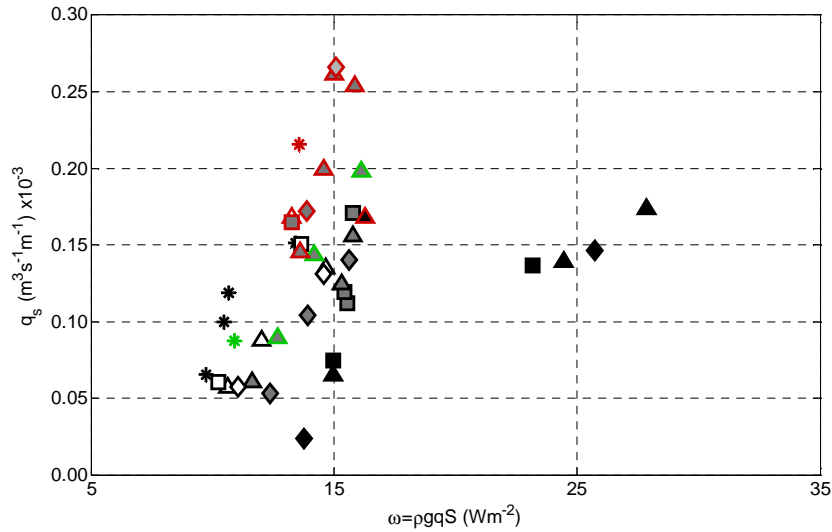
Figure 7.8: Measured sediment transport q_s (m^{3}s^{-1}m^{-1}) as a function of the stream power ω (Wm^{-2}). The symbols used are presented in Table 7.1.

As shown in Figure 7.8, the experiments are generally well aligned as a function of stream power, only the experiments with $\lambda/D=2$ being clearly separated. Moreover, experiments seem to be aligned as a function of dimensionless boulder distance λ/D, without a distinction as a function of the channel slope. This confirms that the boulder configuration is a relevant parameter to determine the sediment transport capacity as well, complementing the variables already taken into account in the definition of the stream power function.

7.3.2.3 Influence of the bed shear stress

The bed shear stress is another variable generally used as parameter to estimate bedload. Figure 7.9 presents the sediment transport as a function of the bed shear stress (Figure 7.9a) and the drag shear stress on mobile sediments (Figure 7.9b). The correlation between sediment transport and the shear stress seems weak. Nevertheless, according to Figure 7.9a, bedload capacity tends to increase with total bed shear stress τ^*, which is defined as:

$$\tau^* = \frac{\rho g R_h S}{(\rho_s - \rho) g d_{50}}$$

(55)

where ρ (1000 kgm^{-3}) and ρ_s (2650 kgm^{-3}) are the liquid and solid density respectively, and R_h (m) is the hydraulic radius.

The total bed shear stress is clearly higher on steep slopes, but no link to the presence of macro-roughness elements can be observed in the data.

The drag shear stress τ_m^* acting on mobile sediments, presented in Figure 7.9b, is estimated by the following equation:

$$\tau_m^* = \frac{0.5 \rho C_m U^2}{(\rho_s - \rho) g d_{50}} \tag{56}$$

where C_m (-) is a drag coefficient, and U (ms^{-1}) is the mean flow velocity (*Yager et al.* 2007; *Scheingross et al.* 2013). According to *Yager et al.* (2007) and *Lenzi et al.* (2006), only the part of the total shear stress acting on mobile sediments contributes to sediment transport. The drag coefficient C_m is calculated with the Variable Power Equation of *Ferguson* (2007) as suggested by *Scheingross et al.* (2013), with a relative submergence defined as R_h/d_{50}, where R_h is the hydraulic radius (cf. Chapter 5 for more details). The bed drag shear stress (Figure 7.9b) is clearly higher on smaller slopes and the transport capacity visibly tends to increase with the drag on mobile sediments. Nevertheless no trend of the drag shear stress as a function of boulder density is visible. The bed drag shear stress acting on mobile sediments is smaller than the total bed shear stress (Figure 7.9a), confirming the observations of *Yager et al.* (2007) and *Canovaro et al.* (2007).

In order to estimate a critical bed shear stress (for both the total bed shear stress and the drag shear stress acting on the mobile sediments), several formulae (*Ferro* 1999; *Papanicolaou et al.* 2004; *Lamb et al.* 2008) and several constant values were applied. These equations calculate the critical bed shear stress as a function of either the flume slope or the relative roughness. For both, the total bed shear stress and the drag bed shear stress acting on mobile sediments, a constant critical value supplied the best results ($\tau_{cr}^* = 0.091$ for the total bed shear stress and $\tau_{m,cr}^* = 0.007$ for the drag bed shear stress acting on mobile sediments).
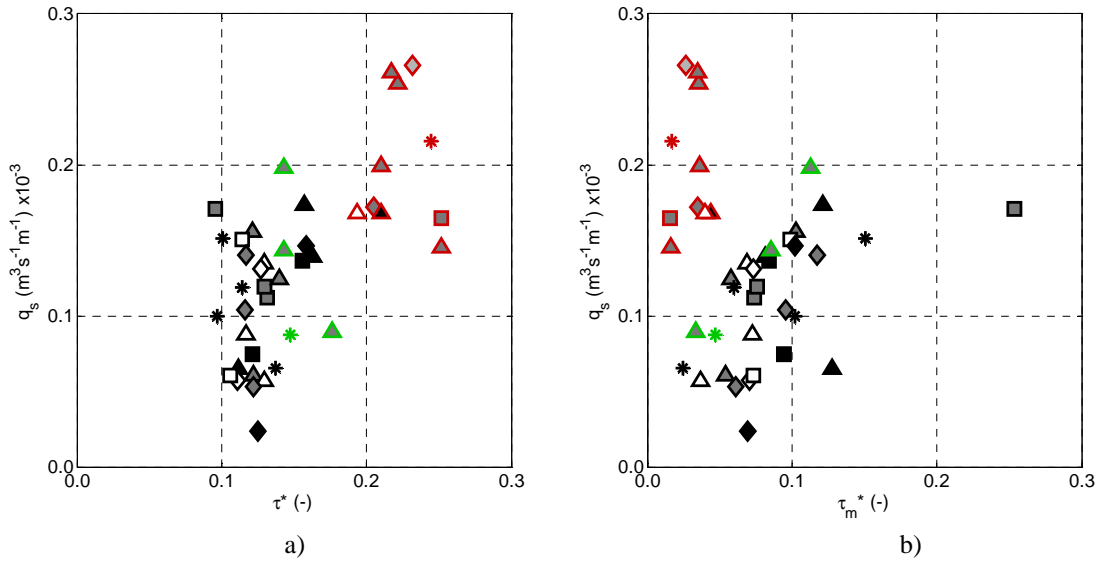
Figure 7.9: Measured sediment transport q_s (m^{3}s^{-1}m^{-1}) as a function of a) the dimensionless total bed shear stress τ^* (-) and b) the dimensionless drag shear stress acting only on the mobile sediments τ_m^* (-).The symbols used are presented in Table 7.1.

7.3.3 Development of a sediment transport equation considering boulder influence

7.3.3.1 Equation form

Hereinafter, a sediment transport formula with the form of equation (48) is developed by testing both liquid discharge and bed shear tress (total and drag reduced) as parameter identified as X in the equation. The constant coefficient α, is often dependent on sediment and fluid density, gravitational acceleration, and grain size (*Smart and Jäggi* 1983; *Rickenmann* 1990). However the variation of these parameters was not assessed in the present research and α was determined through regression analysis of the data. In order to obtain the coefficients α, β, and γ, for both cases, using liquid discharge and bed shear stress (total and drag) as main parameters, a power law regression is calculated based on the curves $q_s^* = \alpha(X^* - X_{cr}^*)^\beta S^\gamma$, where q_s^* is the dimensionless sediment transport normalized as:

$$q_s^* = \frac{q_s}{\sqrt{\left(\dfrac{\rho_s}{\rho} - 1\right) g d_{50}^3}} \tag{57}$$

The liquid discharge is adimensionalized as earlier by the gravitational acceleration and the d_{50} of the mobile sediments.

In equation (48), a critical value of parameters X (X_{cr}) represents the threshold for the beginning of movement of the mobile sediments, being the bedload directly related to the excess of X compared to this.

A total of four equations are adjusted to equation (48). As discussed above, the critical discharge (q_{cr}^{*}) for the beginning of gravel motion varies as a function of S and λ/D, according to equation (54) developed with the present dataset. However, in order to analyze the need to take into account the influence of boulders on the incipient motion, a constant value of critical discharge equal to q_{cr}^{*} =2.71 (-) is also used. For both the total bed shear stress and the drag bed shear stress acting on mobile sediments, and as indicated before, constant critical values supplied the best results and are equal to τ_{cr}^{*}=0.091 for the total bed shear stress and $\tau_{m,cr}^{*}$=0.007 for the drag bed shear stress acting on the mobile sediments.

7.3.3.2   Correction factors to account for boulders

As shown by the previous discussion of results, the sediment transport capacity is clearly linked with the presence of boulders. As suggested by *Yager et al.* (2007), a correction factor taking into account the presence of these may thus be introduced in the sediment transport formula. Several correction factors depending on the morphological parameters are hereafter tested, individually or in a combined fashion (cf. Table 7.2): A_m represents the mobile bed surface, calculated according to equation (53); A_{if} is the frontal area occupied by boulders per unit surface calculated using equation (51); $1 - \dfrac{D - 2P_{av}}{\lambda}$ represents the wetted perimeters between boulders; $(\lambda-D)\lambda^{-1}$ is an indicator of the boulder spatial density. The correction factors are introduced in equation (48) as shown in equation in (58). One or more correction factors C can be applied to the sediment transport formula to account for the presence of boulders. The dependence of the bedload to these factors may or may not be linear, thus the optimal power coefficient ε is searched for each coefficient.

$$q_{s}^{*} = \alpha(X^{*} - X_{cr}^{*})^{\beta} S^{\gamma} C_{1}^{\varepsilon_{1}} ... C_{n}^{\varepsilon_{n}} \tag{58}$$

Table 7.2, presents the bedload transport formulae herein developed, showing the constants α, β, γ, and ε_i obtained for each form of formula and the performance of each formula. A non-linear least square algorithm was applied to obtain these constants.

Table 7.2: Coefficients of the tested sediment transport formulae as a function of varying correction factors and critical parameters. The last column gives the percentage error of sediment transport estimation when compared to measured data (in bold the best results). The line is gray is further used as sediment transport equation.

critical parameter (X_{cr})	base parameters			correction factor (C_i)				Error
				A_m/A_t	$1-A_{if}/A_t$	$1-\dfrac{D-2P_{av}}{\lambda}$	$(\lambda-D)\lambda^{-1}$	
	α	β	γ	$\varepsilon1$	$\varepsilon2$	$\varepsilon3$	$\varepsilon4$	
$q_{cr}^{*} = 2.71$	3.51	0.56	2.11	-	-	-	-	25.1%
	63.62	1.40	3.49	5.69	-	-	-	14.7%
	24.19	1.25	3.06	-	15.99	-	-	19.3%
	16.45	0.75	2.74	-	-	1.62	-	20.1%
	47.06	1.13	3.24	-	-	-	1.32	16.4%
	74.07	**1.38**	**3.53**	**4.14**	**-**	**-**	**0.47**	**14.2%**
	67.39	1.32	3.45	-	7.22	-	1.02	15.4%
q_{cr} (eq. (54))	4.69	0.49	2.10	-	-	-	-	20.6%
	4.79	0.52	2.10	0.46	-	-	-	20.4%
	4.82	0.53	2.10	-	1.68	-	-	20.4%
	4.65	0.50	2.11	-	-	-0.19	-	20.5%
	4.68	0.49	2.10	-	-	-	-0.02	20.6%
	5.54	**0.70**	**2.27**	**5.96**	**-**	**-**	**-1.62**	**17.6%**
	5.30	0.65	2.20	-	10.78	-	-0.77	19.1%
$\tau_{cr}^{*}=0.091$	0.37	0.00	0.94	-	-	-	-	32.1%
	0.42	-0.03	1.05	-0.63	-	-	-	32.0%
	0.56	-0.09	1.26	-	-4.85	-	-	31.3%
	0.45	0.01	0.97	-	-	0.48	-	31.7%
	0.37	-0.01	0.96	-	-	-	-0.05	32.1%
	0.68	-0.06	1.25	-3.30	-	-	0.79	31.4%
	1.09	**-0.12**	**1.53**	**-**	**-13.45**	**-**	**0.81**	**29.9%**
$\tau_{m,cr}^{*}=0.007$	1.98	0.23	1.34	-	-	-	-	29.6%
	1.98	0.23	1.34	0.02	-	-	-	29.6%
	1.89	0.21	1.36	-	-2.02	-	-	29.4%
	3.15	0.24	1.47	-	-	0.70	-	28.7%
	2.27	0.24	1.36	-	-	-	0.13	29.5%
	3.43	0.24	1.52	-2.99	-	-	0.92	28.8%
	3.65	**0.22**	**1.58**	**-**	**-10.37**	**-**	**0.83**	**27.9%**

7.3.3.3   Performance of the equations

For all the tested excess values (X-X_{cr}), the equations obtained without the correction factors to account for the presence of roughness elements are less performing than the corrected equations with a correction factor.

Equations based on the excess of discharge perform better than equations based on the bed shear stress. This is not surprising since in Figure 7.5 and Figure 7.9 already a clearer link between the liquid discharge and the bedload was noticed, when compared to the relation between the latter and the bed shear stress.

For equations based on the total bed shear stress (τ^*- τ_{cr}^*), the excess shear stress has an almost zero value for the coefficient. Only the slope seems to be relevant and the estimation error is of 32.1%. Coefficients obtained for the correction factors often present illogical values and only slightly decrease the estimation error, meaning that using total bed shear stress may not be adequate to parameterize the sediment transport in presence of boulders, as already argued by *Yager et al.* (2007) and *Yager et al.* (2012a).

Results obtained for equations based on the drag bed shear stress are more reasonable, although the excess shear stress is considered through a low coefficient (approximately 1/4) and presents a high bedload capacity estimation error (29.6%). This means that the dependency of the bedload transport from the drag shear stress is not strong. As suggested by *Yager et al.* (2007), *Yager et al.* (2012a), and *Lenzi et al.* (2006), only the shear stress acting on mobile sediments participate to the bedload transport.

The excess discharge q-q_{cr} allows a better estimation of the sediment transport capacity, even when no correction factor is applied, both with a constant critical value of $q_{cr}^* = 2.71$ and with the critical value calculated as a function of the dimensionless boulder distance and the flume slope (eq. (54)).

When estimating the bedload transport with the excess discharge using only the base parameters (no correction factors), better results are obtained when working with a variable critical discharge (eq. (54), error of 20.6%, cf. Table 7.2) than with a constant discharge (error of 25.1%). When introducing the correction factors, the results improve drastically

for the formulae based on the constant critical discharge. The correction factor with the best improvement to the bedload estimate is $((\lambda\text{-}D)\lambda^{-1})^{0.47}(A_m/A_t)^{4.14}$, with an error of 14.2%. In the bedload formulae obtained with a critical discharge value according to eq. (54), the improvement when introducing a correction factor in limited. In this case too, the correction factor improving most the bedload estimate is $((\lambda\text{-}D)\lambda^{-1})^{-1.62}(A_m/A_t)^{5.96}$, with an error of 17.6%.

The fact that such an improvement in bedload estimation is obtained when introducing a correction factor in the formulae based on a fixed critical discharge, confirms that the presence of roughness elements needs to be taken into account.

However, as observed in Figure 7.6a and Figure 7.6b, the critical discharge is clearly a function of the channel slope and the roughness element geometry, here identified as the dimensionless boulder distance λ/D. The fact that only a small improvement of bedload estimates is obtained when introducing a correction factor considering the presence of boulders as shown in equation (58) in a bedload formula using eq. (54) suggests that the influence of boulders is observed mainly on the incipient motion of sediments, for the range of sediment and liquid discharge used in the present research.

7.3.3.4 *Proposed sediment transport formula*

Apparently, on the dataset, a constant critical discharge value performs slightly better than a variable value, although a dependency on the channel slope and λ/D exist and should be taken into account. Furthermore, the critical discharge calculated according eq. (54) can be applied in the presence of boulders in a steep channel, since it depends on local characteristics of the river. On the contrary, it seems difficult to translate the constant critical discharge value to a channel presenting characteristics differing from those used in the present dataset. Furthermore, the errors obtained for both approach are similarly low and the differences are within the uncertainty associated to the experimental measurements. Thus, we suggest using a bedload formula based on critical discharges calculated according to equation (54). The following equation is proposed for sediment transport capacity calculation on steep slopes in the presence of boulders:

$$q_s^* = 4.69 S^{2.10} \sqrt{q^* - q_{cr}^*} \qquad (59)$$

where q^* (-) is the dimensionless liquid discharge, q_{cr}^* (-) is the dimensionless critical discharge calculated according to equation (54) and depending from the flume slope and the dimensionless distance between boulders λ/D, where D (m) the boulder diameter, λ (m) the distance between boulders, and S (-) is the channel slope.

The estimation results based on equations (54) and (59) are compared to the measured data in Figure 7.10. A larger scatter in the data points is observed for the 6.7% slope. This is explained by the fact that, as observed in Figure 7.5, the influence of the boulder configuration on the sediment transport capacity plays a bigger role on the lower slopes. This observation is replicated by eq. (59), thus decreasing the scatter between the measured and the estimated sediment transport capacity for steeper slopes.
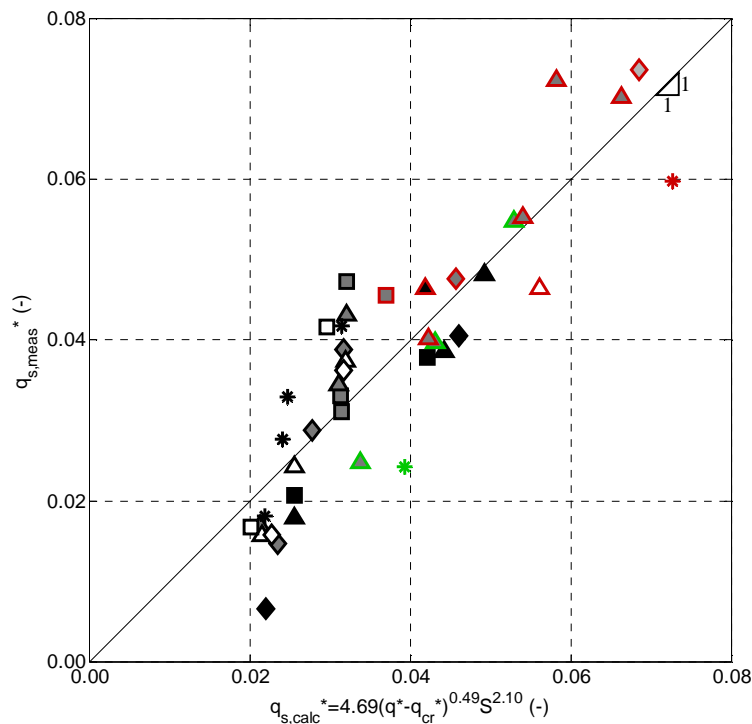
Figure 7.10: Measured sediment transport capacity against calculated sediment transport capacity, calculated as a function of the critical discharge calculated according equation (54). The black line indicates the unitary slope curve. The symbols used are presented in Table 7.1.

The constant coefficient $\alpha=4.69$, is generally dependent on sediment and fluid density, gravitational acceleration, and most importantly the grain size distribution of the mobile sediments (*Smart and Jäggi* 1983; *Rickenmann* 1990), however, as mentioned before, the variation of these parameters was not assessed in the present research. The grain size distribution used in the present study is representative of those characterizing alpines rivers. *Hersberger* (2002) showed that the grain size distribution normalized by the mean grain diameter is practically the same in most alpine rivers. Thus, assuming the gravity acceleration, and the fluid and solid density constants, the constant coefficient $\alpha=4.69$ is applicable to all alpine rivers, where typically d_{90}/d_{30} ranges between 2.5 to 6.0.

Equation (59) has been developed for slopes between 6.7% and 13% and dimensionless boulders distance $\lambda/D>2$. In case of boulders more closely packed, a change in flow conditions is expected, as exposed by *Canovaro et al.* (2007). The ratio (w/D) the channel width w to the of boulder diameter D ranges from 0.5 to 3.3, and up to infinite for tests without boulders. The relative roughness d_m/h, where h is the average water depth, ranges from approximately 0.22 to 0.45.

7.3.4   Comparison with existing sediment transport formulae

The equation herein proposed (59) is compared with the equations developed by *Rickenmann* (1990, 1991b), based on the discharge, and by *Fernandez Luque and van Beek* (1976) (FLvB), based on the bed shear stress. The FLvB formula is chosen because it was already modified by *Yager et al.* (2007) and the Rickenmann formula is chosen because it is often applied to alpine rivers. According to *Yager et al.* (2007), the FLvB equation was the most performing when modified to account for the presence of macro-roughness elements, but the Rickenmann formula was not applied in their study. *Yager et al.* (2007) suggested scaling by A_m/A_t the existing sediment transport equation, to account for the limited sediment availability. Moreover, they suggested that only the drag bed shear stress acting on mobile sediments contributes to the sediment transport. Finally, only the mobile sediments should be included in the characteristic diameters of the surface grain size distribution (*Yager et al.* 2007).

In formula based on bed shear stress calculations, *Yager et al.* (2007) do not suggest any typical value for the critical shear stress, the constant value of 0.045 being used. However, as shown in Figure 7.9b, the drag bed shear in often smaller than 0.045 and the critical value of 0.007 here estimated is used (cf. Table 7.2). Coherently, the herein determine value of critical bed shear stress (0.091) is used in the original FLvB formula.

The critical discharge formula originally proposed by *Rickenmann* (1990, 1991b) (cf. eq. (31)), dependent on the bed slope and the d_{50}, is used in the original formula. The formulae originally proposed by the author is here modified by introducing the critical discharge formula herein developed (eq. (54)) in the original bedload equation. The modification suggested by *Yager et al.* (2007) is also applied on the Rickenmann formula (scaling factor A_m/A_t) and on the FLvB formula (drag bed shear stress and scaling factor A_m/A_t). The results are given in Table 7.3 (bedload estimation errors) and in Figure 7.11.

All the modifications of the original formulae to account for the presence of macro-roughness elements ("modif. Ghilardi" and "modif. Yager") improved the results of the *Rickenmann* (1990, 1991b) and the *Fernandez Luque and van Beek* (1976) formulae. The Rickenmann formula, based on the discharge per unit width, is performing better than the FLvB equation, based on the bed shear stress. This outcome was expected, given the previous discussion on the results presented in Figure 7.5 and Figure 7.9, the Rickenmann formula being similar to eq. (59), with different coefficients. When calculating the critical discharge according to equation (54) in the Rickenmann formula instead of the critical discharge proposed by Rickenmann, the estimation error is divided two. The multiplication by the correction factor A_m/A_t proposed by *Yager et al.* (2007) only slightly improves the estimates of Rickenmann formula based on the excess of discharge. On the other hand, taking into account only the drag bed shear stress acting on mobile sediments and the correction factor A_m/A_t, in FLvB formula based on excess of bed shear stress drastically improves the bedload estimates, reducing the error by 40%. Figure 7.11 shows that the sediment transport formula herein proposed (eq. (59)), is clearly performing better with our data.

Table 7.3: Mean estimation errors for the applied original and modified formulae.

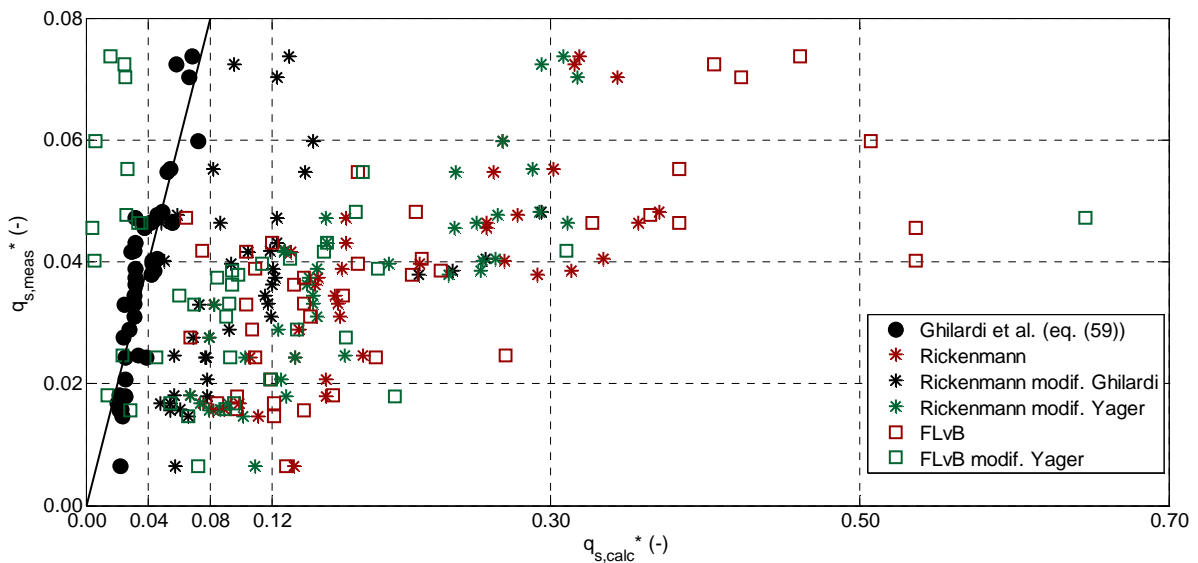|	Eq. (59)	Rickenmann	Rickenmann modif. Yager	Rickenmann modif. Ghilardi	FLvB	FLvB modif. Yager
Error	20%	481%	423%	235%	588%	345%

Figure 7.11: Measured versus calculated sediment transport for several bedload formulae. The black line indicates the unit slope curve.

7.4 Conclusions

The sediment transport capacity in a steep channel with boulders was analyzed through a dataset of 41 experiments carried out with varying flume slopes and boulder configurations (combination of boulder dimensionless distance and diameter) for several sediment supply conditions.

It is shown that the channel slope has the strongest impact on the transport capacity, namely in what concerns the critical discharge for beginning of motion. However, it is also clearly shown that the sediment transport decreases with dimensionless boulder distance λ/D. The impact of the boulder diameter D is also pointed out; for a given λ/D and a given channel slope, the transport capacity seems to decrease with boulder diameter. When the dimensionless distance corresponds to $\lambda/D=2$, the transport capacity decreases drastically,

especially for higher discharges, probably due to a change in the flow pattern, going from a flow between isolated roughness elements to a wake interference flow among boulders.

It is observed that the sediment transport in the channel is better explained by using the discharge than the bed shear stress as parameter. The critical discharge at which incipient motion occurs is shown to be related to both, the channel slope and the boulder dimensionless distance. An equation to calculate the critical discharge for incipient motion of mobile sediments on steep channels with boulders is proposed. Furthermore, an equation to predict sediment transport in steep channels taking into account the presence of boulders is proposed based on the present dataset.

Formulae based on excessive discharge (q-q_{cr}) perform better than formulae based on excessive bed shear stress, even without taking into account the presence of boulders. It is shown than when the presence of boulders is taken into account in the critical discharge value, as suggested by eq. (54), there is no need to introduce a correction factor in the bedload transport equation to account for the presence of boulders. No systematic overprediction or underprediction of sediment transport is observed as a function of boulder configuration.

The adaptation of two bedload formulae proposed by previous authors to account for the macro-roughness elements clearly shows better results when taking into account the presence of boulders. The existing formula based on excess discharge performs clearly better than the formula based on the excess of bed shear stress.

Chapter 8

Further observations on morphology and sediment transport

This chapter contains further preliminary observations ensuing from the experimental work that were not included in previous chapters.

Initially, some observations concerning the bed morphology are presented (8.1). Following, an initial analysis of the flow hydrograph experiments, described earlier in section 3.2.1d, is carried out (8.2). In section 8.3, the influence of the variation of the liquid discharge on the sediment transport capacity is analyzed based on two experiments having all other parameters constants. Finally, in section 8.4, complementary observations on the relation between bedload pulses phenomena and the grain size distribution in the channel bed are presented.

8.1 Morphological observations

The protrusion was measured for all the boulders at the end of each experiment (cf. 3.1.4 and Figure 3.11b, values given in Appendix B for each test). Figure 8.1a, presenting the relation between the protrusion downstream of boulders P_{ds} and the average boulder protrusion P_{end} measured at the end of the experiments, show that a strong correlation between these parameters exist.

Figure 8.1b gives the protrusion downstream of boulders P_{ds} as a function of the protrusion upstream P_{us} of these. As observed on steps and isolated roughness elements in mountain streams, the protrusion upstream of boulders is smaller than the downstream protrusion (*David et al.* 2011). The correlation between these values is high (R^2=0.70) the downstream protrusion representing 1.5 times the upstream protrusion. This observation is particularly useful for field applications, when deciding where to measure the protrusion around boulders or steps.

(a)   (b)
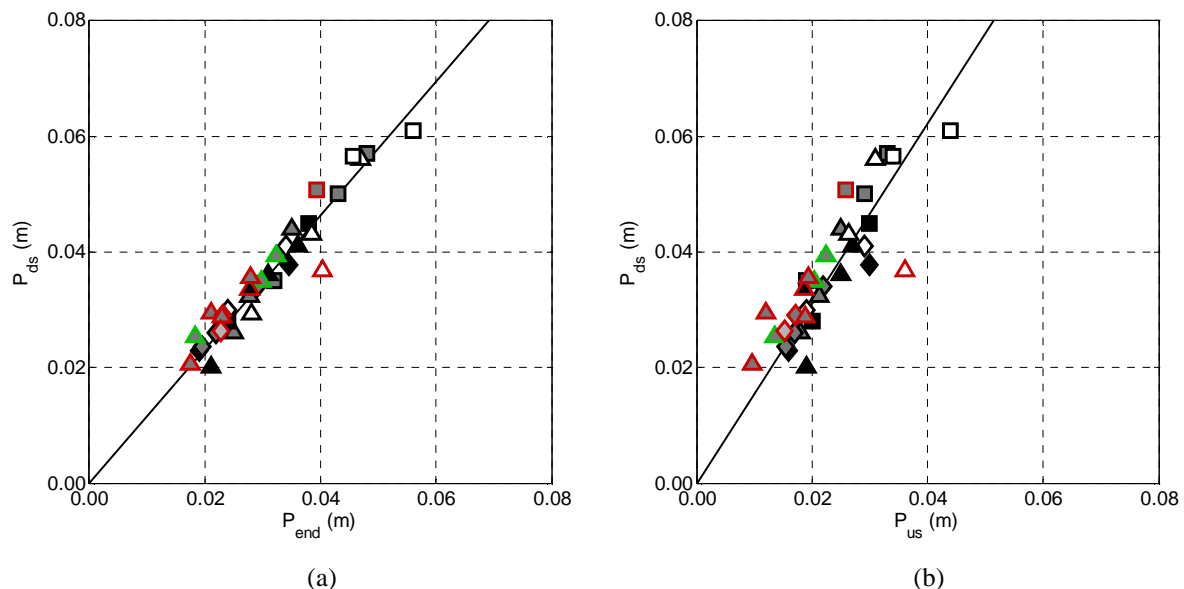
Figure 8.1: Relation between the protrusion downstream of boulders (P_{ds}) and: a) the average protrusion (P_{end}), where the trend line (black line) equation is P_{ds}=1.16P_{end}, with a coefficient of determination R^2=0.93; b) the upstream protrusion (P_{ds}), where the trend line (black line) equation is P_{ds}=1.56P_{us}, with a coefficient of determination R^2=0.70. The symbols used are presented in Table 7.1.

A correlation between the average protrusion throughout the experiments (P_{av}^-) and the average protrusion at the end of the experiment (P_{end}) is observed (Figure 8.2). Moreover, the relationship between the two values of protrusion tends to be close to the 1:1 value ($P_{end} = P_{av}^-$). This corresponds to the expectations since, as explained in section 5.3, boulders protrusions starts to increase at the peak in sediment transport and has approximately an average value at the end of the sediment transport burst, when $q_{s,in} \approx q_{s,out,10}$. The latter moment corresponds to the end of an experiment (cf. 3.2.1). Thus, the values of boulder protrusion at the end of the experiment correspond to the average values observed through time during the experiment, confirming that the morphology at the end of a bedload burst (end of the experiments) is representative of the average morphology through the experiment. P_{end} is based on the measurement of all the boulders present in the flume, while P_{av}^- is based only on 3-4 tests measured in a loop every 10 minutes during the experiment (cf. section 3.1.4).
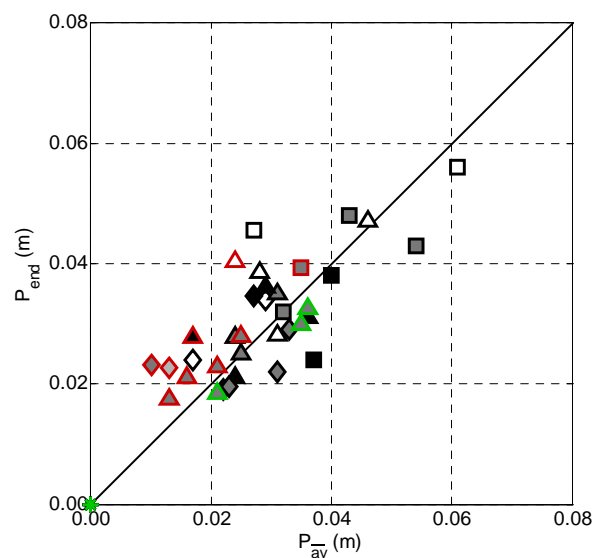
Figure 8.2: Protrusion at the end of the experiment (P_{end}) as a function of average protrusion measured during the experiment (P_{av}^-). The black line indicates the unitary slope curve. The symbols used are presented in Table 7.1.

Figure 8.3 indicates that the proportion of boulders presenting hydraulic jumps downstream of them (dimensionless number of hydraulic jumps, HJ^*) is clearly related to

their average protrusion through time P_{av}^-, which was measured continuously during the experiment. In other words, as shown in Figure 7.3a, the number of hydraulic jumps per square meter is linked to the number of boulders and their protrusion. Both morphological variables present smaller values on the steepest slope but do not present any trend as a function of the dimensionless boulder distance nor the diameter of the boulder.
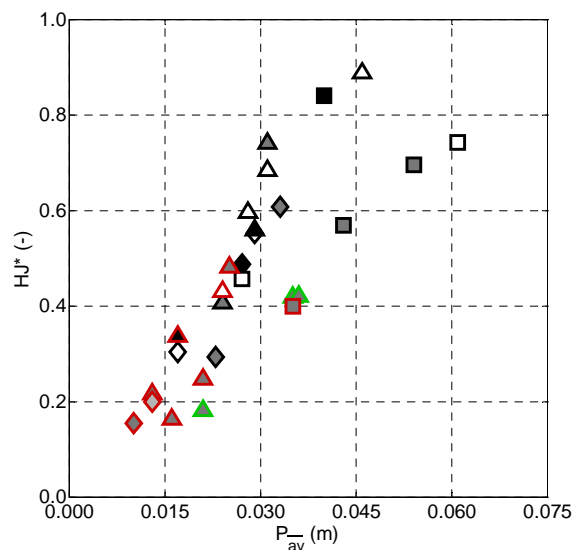

Figure 8.3: Dimensionless number of hydraulic jumps (HJ^*) as a function of the average boulder protrusion (P_{av}^-). The symbols used are presented in Table 7.1.

Figure 8.4 presents the relation between the discharge q and the number of hydraulic jumps HJ^* (Figure 8.4a) and the protrusion P_{av}^- (Figure 8.4b). The values of these two morphological variables tend to increase as a function of the specific discharge. This is especially clear for the dimensionless number of hydraulic jumps (Figure 8.4a). The trend has however a weak expression when analyzing the link between boulder protrusion and discharge (Figure 8.4b). This suggests that as the liquid discharge increases, the spill resistance and energy dissipation caused by the hydraulic jumps also increases (*Curran and Wohl* 2003; *Comiti and Lenzi* 2006).
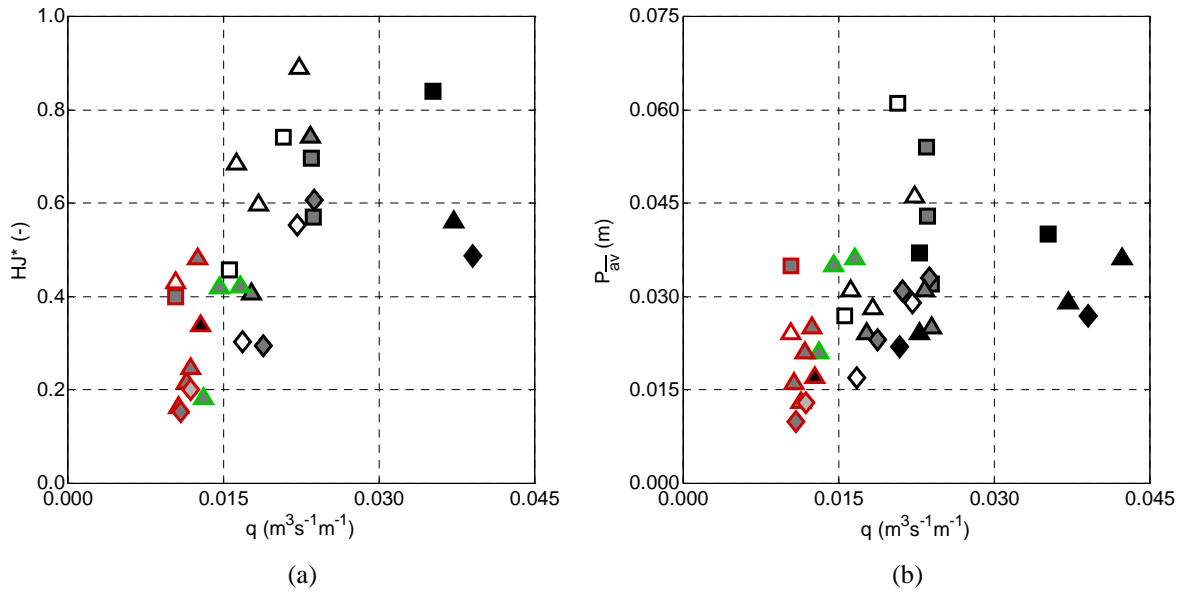
Figure 8.4: Relation between the unit discharge (q) and: a) the dimensionless number of hydraulic jumps (HJ^*); b) the average boulder protrusion ($\overline{P_{av}}$). The symbols used are presented in Table 7.1.

Figure 8.5 presents the ratio of frontal boulder area to immobile bed area (A_{if}/A_i, cf. eq. (51) and eq. (52)) as a function of the dimensionless number of hydraulic jumps ($HJ^*=HJ/N_{Bst}$, Figure 8.5a) and the dimensionless boulder protrusion ($P^*=\overline{P_{av}}/D$, Figure 8.5b).

The dimensionless number of hydraulic jumps increases with the ratio A_{if}/A_i (Figure 8.5a). Figure 8.5b shows that the ratio A_{if}/A_i depends only on the ratio between the average boulder protrusion and the boulder diameter (i.e. the dimensionless boulder protrusion P^*) with practically a 1:1 relationship (Figure 8.5b). No trend as a function of boulder configuration (λ/D and D) can be detected. This confirms that all the morphological variables are strictly dependent from each other but are not necessarily linked to the boulder configuration (λ/D and D).
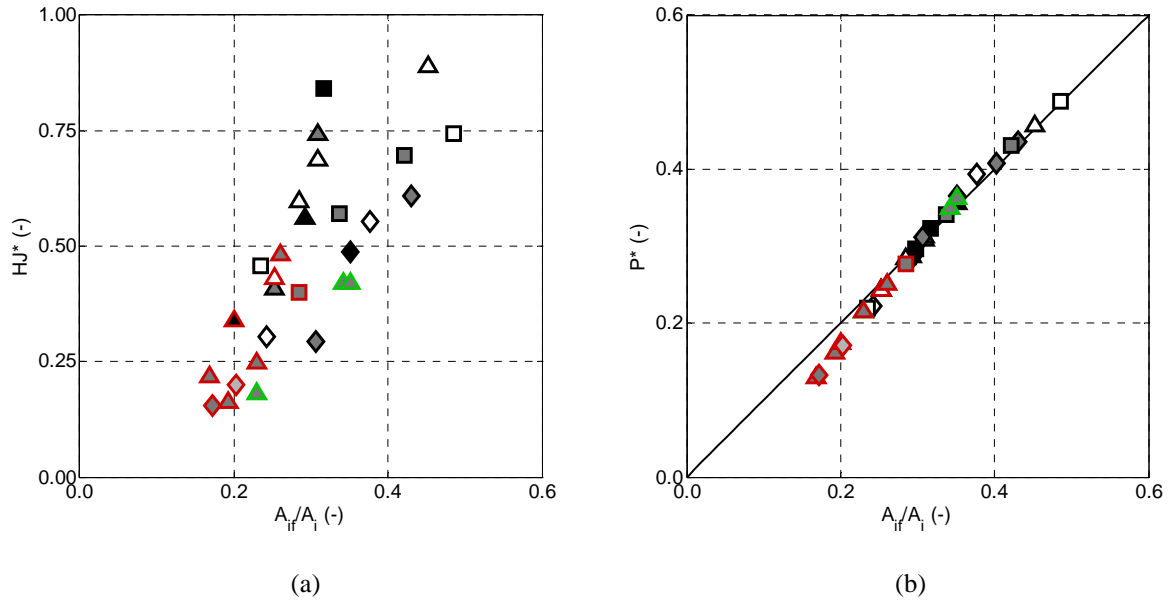
Figure 8.5: Relation between the ratio of frontal boulder area to bed perpendicular boulder area A_{if}/A_i and: a) the dimensionless number of hydraulic jumps (HJ^*); b) the dimensionless average protrusion (P^*), where the black line indicates a unitary slope curve. The symbols used are presented in Table 7.1.

8.2 Experiences with increasing discharge

Hydrograph experiments were carried out at the end of 22 experiments (cf. section 3.2.1), on the water-worked bed morphology. During these experiments, no sediments were supplied. The water discharge was increased gradually by small steps of 0.0008 to 0.0020 $m^3s^{-1}m^{-1}$. The mobilized sediments reaching the outlet were collected and their grain size distribution was analyzed individually for each discharge. The discharge was increased by small steps until, according to visual observations, grains corresponding to d_{90}=19 mm of the mobile sediments were carried to the flume outlet, or until more than 4 kg of sediments were collected over a 10 minutes period.

These experiments allow assessing the impact of a flow hydrograph on a mountain river, in situation of a water-worked bed morphology, when sediments are not supplied neither by the upstream section nor by lateral movements. Although these tests are not carried out in order to obtain incipient motion data, they give a useful insight on the topic. The obtained data allow inferring only on the grain sizes reaching the downstream section, where the

gravel are collected, and not on initiation of motion in other sections of the flume. Local grain movements were often observed even when no sediments were collected at the outlet. These movements were generally occurring in pools downstream of boulders, but sediments were not transported further downstream because the flow action was not sufficient for bedload.

As indicated by Figure 8.6, presenting the ratio of the d_{90} of the mobilized sediments ($d_{90,x}$) to the d_{90} of the total grain size distribution (bed material), the incipient motion occurs for smaller discharges on steeper slopes. This confirms observations made in Chapter 7 regarding the critical discharge, which is decreasing for higher slopes (cf. *Rickenmann* 1990). On the smaller slope (6.7%), it is observed that for $\lambda/D=3$ and 5, the discharge to mobilize a given grain size is smaller than in the absence of boulders. This is due to the mobilization of sediments in pools downstream of boulders. The behavior changes when the spatial density of boulders increases ($\lambda/D=2$). In the latter case, Figure 8.6 shows that a larger discharge is needed to mobilize a given grain size.

Figure 8.6 shows that in most cases the mobilized grain sizes are smaller than the total grain size ($d_{90,x}/d_{90}<1$), even when the discharge increases. In Figure 8.7, indicating the ratio $d_{30,x}/d_{30}$ as a function of the discharge, it can be noticed that on the 6.7% and the 9.9% slopes, as soon as there is movement the d_{30} is transported, except for the experiment with the highest number of boulders (S=6.7%, $\lambda/D=2$, and D=0.075 m, represented by black diamonds). On the steepest slope, the transport starts more gently.

Figure 8.8 presents the ratio $d_{m,x}/d_m$ as a function of the discharge. It can be noticed that for this grain size too, some experiments do not reach the transport of the d_{50} of the total grain size ($d_{m,x}/d_m<1$).

By comparing the graphs in Figure 8.6, Figure 8.7, and Figure 8.8, it is possible to notice that the mobility of sediments increases with decreasing grain sizes. In other words, there is not an equimobility of the sediments, for which the sediments would move all for the same value of dimensional bed shear stress, and thus the same value of discharge (*Lenzi et al.* 2006). Furthermore, the graphs show that, although sediments are mobilized early for small discharges, the competent liquid discharge to mobilize the entire gravel bed is

considerably higher. This leads to the need of defining competent critical values corresponding to the beginning of sediment motion, for determined grain size ranges as referred to in section 2.3.3 (*Ferreira et al.* 2007).
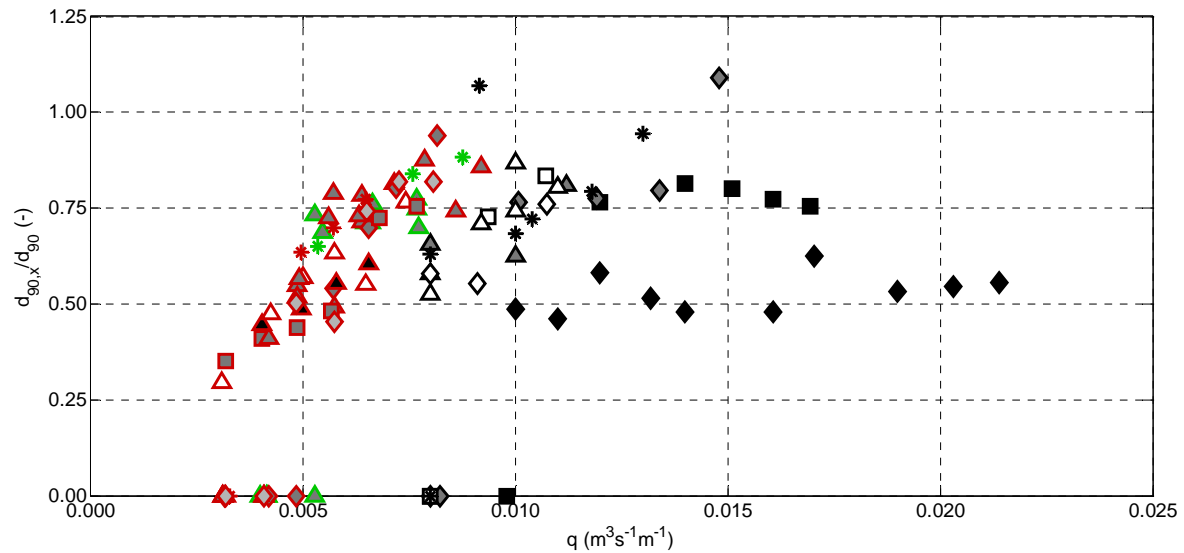

Figure 8.6: Ratio between the $d_{90,x}$ of the mobilized sediments and the d_{90} of the bed material, as a function of the discharge. The symbols used are presented in Table 7.1.
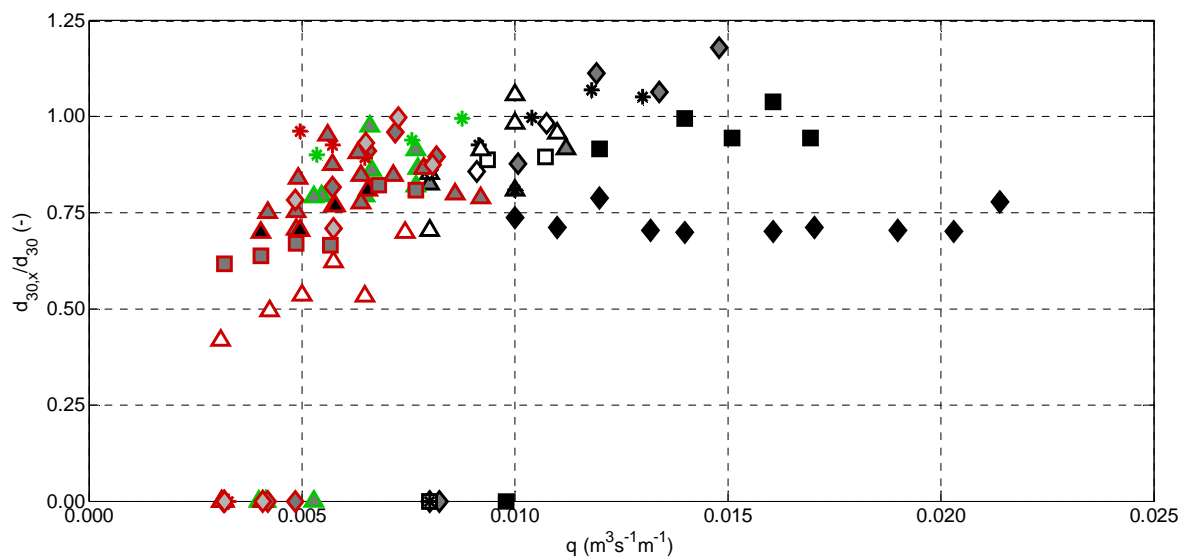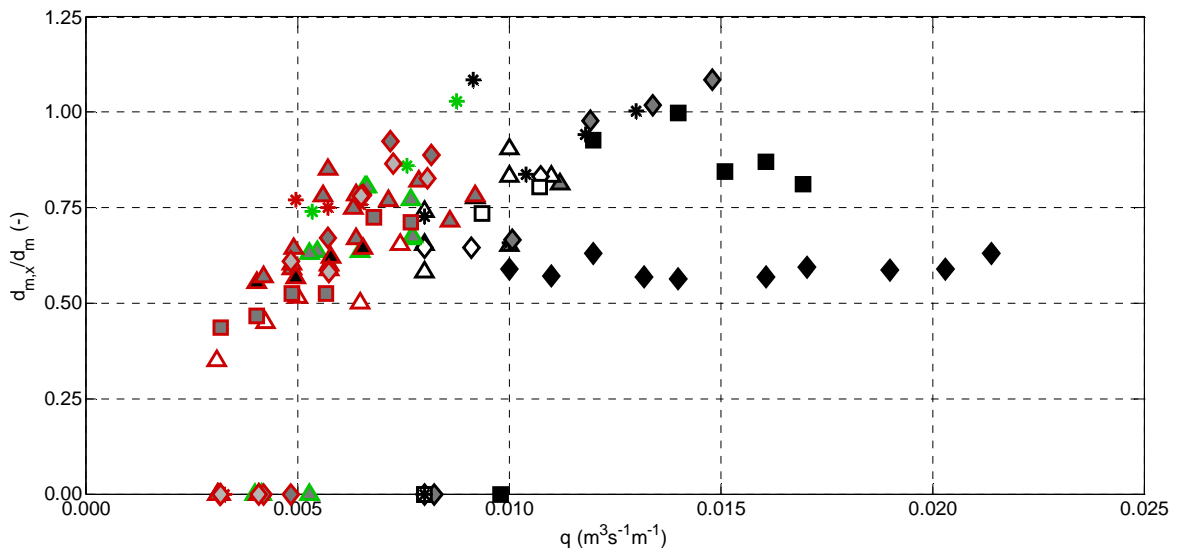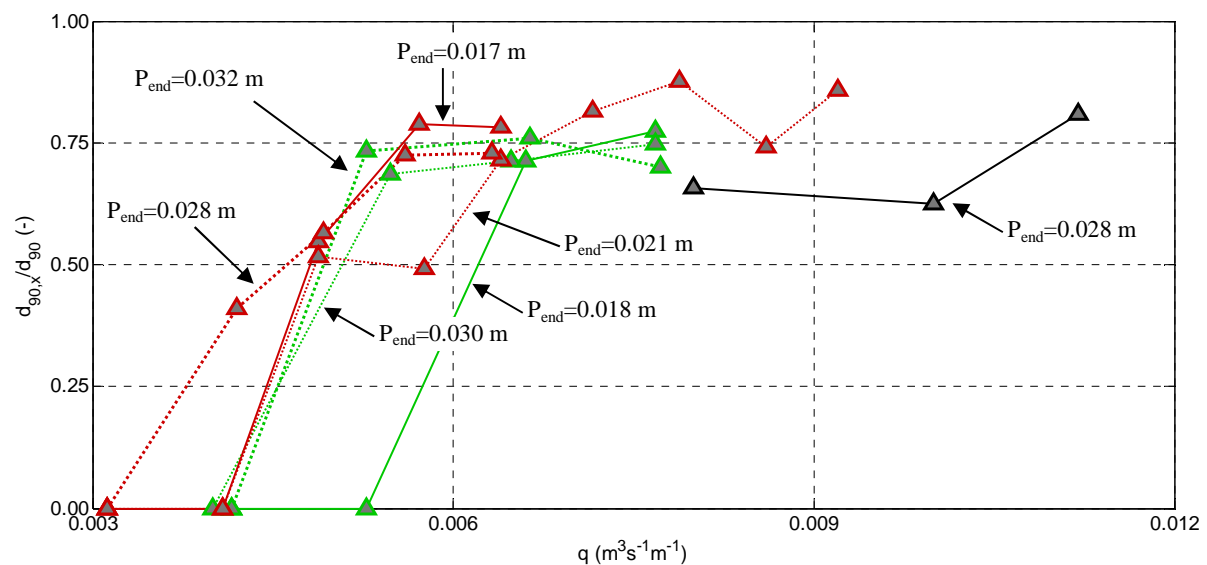

Figure 8.7: Ratio between the $d_{30,x}$ of the mobilized sediments and the d_{30} of the bed material, as a function of the discharge. The symbols used are presented in Table 7.1.

Figure 8.8: Ratio between the mean diameter $d_{m,x}$ of the mobilized sediments and the d_m of the bed material, as a function of the discharge. The symbols used are presented in Table 7.1.

Figure 8.9 reports the experiments carried out with the same configuration ($\lambda/D=3$ and $D=0.100$ m). Points coming from the same experiment are linked between them by a line, and correspond to a hydrograph applied after one sediment transport experiment. The average protrusion at the end of the sediment transport experiment is also written in the graph for every curve. As mentioned before, the experiment carried out on the 6.7% slope needs higher discharges for incipient motion, however the motion has already started for the smallest discharge used, of 0.008 $m^3s^{-1}m^{-1}$.

Tests on the 9.9% slope clearly show that the protrusion of boulders plays a role in determining the incipient motion. The movement starts earlier when the protrusion is larger. This is confirmed by the experiments carried out on the steepest slope. As mentioned above, this is due to the higher energy of impinging jets in the pools downstream of boulders. The higher the drop height downstream of boulders and the sooner the transport starts. However, as argued by *Yager et al.* (2007), at higher discharges, the sediment transport capacity decreases with increasing protrusion. In Chapter 7 it is clearly shown that the presence of protruding boulders decreases sediment transport capacity (cf. Figure 7.5). At higher discharges the transport capacity in channels without boulders is clearly higher. This is inferable by looking at the curves of Figure 8.9. When

the discharge increases, both on the 9.9 and the 13% flume slope, the moved grain size is larger when the average protrusion of boulders is smaller. The present results (cf. Figure 8.6) indicate that the beginning of movement occurs for smaller discharges, when in presence of sparse boulders (λ/D=3 and 5), confirming that the critical discharge should be a function not only of channel slope, as proposed by *Rickenmann* (1990, 1991b), but also of roughness geometry, both as a function of λ/D and boulder protrusion (cf. Chapter 7).

Figure 8.9: Ratio between the $d_{90,x}$ of the mobilized sediments and the d_{90} of the bed material, as a function of the discharge for λ/D=3 and D=0.100 m. Average protrusion P_{end} is given for every curve. The symbols used are presented in Table 7.1.

8.3 Effect of liquid discharge

Two experiments were carried out in order to analyze the influence of varying the water discharge, for a fixed sediment discharge, flume slope and boulder position. The data are presented in Table 8.1. In order to analyze the influence of a change in the couple of solid and liquid discharge, two experiments were carried out with exactly the same boulder configuration (λ/D=3 and D=0.1 m) on the steepest slope.

Table 8.1: Experimental parameters and results for two experiments carried out with the very same sediment supply and boulder configuration, but with different liquid discharge. $q_{s,in}$ =0.236x10^{-3} (m^{3}s^{-1}m^{-1}).

S (%)	λ/D (-)	D (m)	N_{Bs} (m^{-2})	q (m^{3}s^{-1}m^{-1})	$q_{s,end}$ x10^{-3} (m^{3}s^{-1}m^{-1})	$\bar{U}$ (m/s)	$\bar{P}_{av}$ (m)	P_{end} (m)	P_{us} (m)	P_{ds} (m)	HJ (m^{-2})	A_i/A_t (-)	A_{if}/A_t (-)
13	3	0.100	11	0.0124	0.254	0.38	0.025	0.028	0.019	0.036	5.2	0.08	0.020
13	3	0.100	11	0.0118	0.261	0.37	0.021	0.023	0.019	0.029	2.7	0.07	0.015

As discussed in Chapter 7, and visible in Figure 7.5, a small change in the discharge induces a high change in sediment transport capacity on the steepest slope. In order to conserve the sediment transport capacity, morphological values need to adapt to the raise in liquid discharge. *Yager et al.* (2007) findings suggest that in order to dissipate enough energy to transport an equilibrium amount of sediments, boulders need to be more exposed when the liquid discharge increases. This is confirmed by the present results, showing that when the liquid discharge is increased by 5%, the average boulder protrusion through time $\bar{P}_{av}$ increases by 19%. The number of hydraulic jumps clearly augments, as expected from the relationship observed in Figure 8.3. The frontal surface rises by 25% as well.

For both the experiments, the average boulder protrusion through time ($\bar{P}_{av}$) and the average boulder protrusion at the end of the experiments (P_{end}) are practically equal (cf. Figure 8.2). The details of the upstream (P_{us}) and downstream (P_{ds}) protrusion at the end of the experiment indicate that the upstream protrusion is the same in both tests, while the downstream protrusion is 20% higher in test 1. These results indicate that the energy losses occur mainly due to energy dissipation downstream of boulders, through spill resistance and hydraulic jumps. This suggests that even if in average the downstream protrusion is about 1.5 times the upstream protrusion (cf. section 8.1 and Figure 8.1b), it may be preferable to work with the protrusion downstream of boulders.

8.4 Surface and transported grain sizes at varying bedload transport stages

As detailed in Chapter 5, stages of sediment transport are related to different bed states. It is shown that the surface grain size distribution changes with bedload stages. In Figure 8.10 (pictures of the same long duration experiment analyzed in Chapter 5), the vertical sorting of grain sizes is shown at different bedload transport stages. Figure 5.7a indicates that at low sediment transport events, the surface grain size distribution is coarse, with the average diameter close to the d_{90} of the supplied sediments. Figure 8.10a reveals that during these events, the underlying grains have a much finer size. When the coarse riffle structures break down (cf. Chapter 5) sediment transport increases and the surface grain size becomes finer (Figure 5.7c). This is confirmed by Figure 8.10b, where no vertical sorting is visible during the peak of bedload. Finally, after a peak in sediment transport, the surface grain size distribution corresponds to the supplied curve (Figure 5.7d). The frontal picture of Figure 8.10c clearly indicates the presence of some coarser grains at this bedload stage.
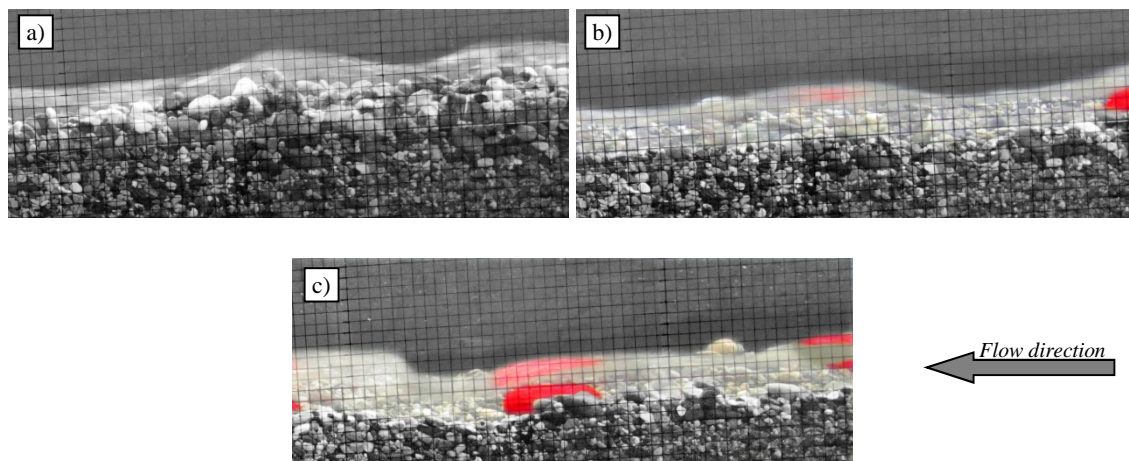
Figure 8.10: Evolution of bed morphology of the long duration experiment analyzed in Chapter 5 (cf. Figure 5.2): a) at 215 minutes, during extremely low sediment transport; b) at 256 minutes, at the peak of sediment transport; c) at 282 minutes, after the peak of bedload, when $q_{s,out,10}$ is equal to $q_{s,in}$. The pictures are taken in the central part of the flume (from *Ghilardi et al.* (2013)).

According to visual observations, at low sediment transport stages, only few coarse grains were reaching the flume outlet. On the opposite, at intense sediment transport stages, the

grain size distribution was finer, due to the mobilization of fine sediments previously trapped under the riffle structures. This phenomenon was already observed by *Frey et al.* (2003). To confirm this observation, samples of mobile sediments were taken almost simultaneously at the inlet and the outlet of the channel at varying bedload transport stages during one experiment. The results are presented in Figure 8.11. As shown in Figure 3.6, the supplied grain size distribution was constant in time. This confirms that bedload stages were not induced by the supplied grain size distribution. However, a longitudinal grain sorting occurred in the flume as shown by the variations in outlet grain size distribution (Figure 8.11). During low sediment transport events, the distribution is much coarser. On the other hand, during peaks in sediment transport, the grain size distribution is finer than that of the supplied material. Finally, when the sediment transport at the outlet corresponds to the inlet ($q_{s,in} \approx q_{s,out,10}$), after a sediment transport burst, the gradation of the outlet materials corresponds to the supplied grain size distribution. On average, the grain size distribution of the outlet equals the gradation of the inlet.
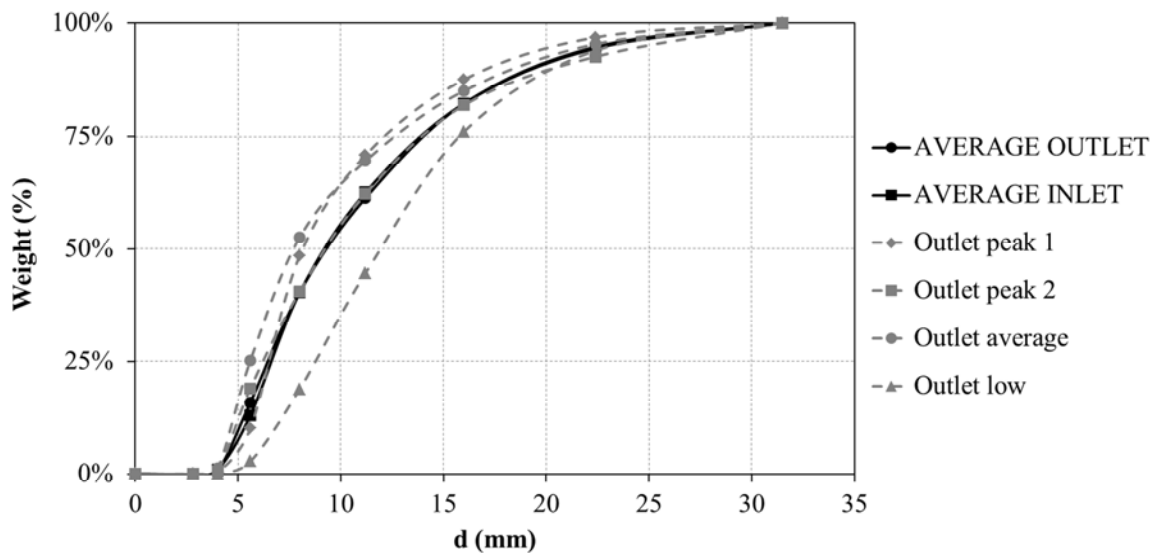
Figure 8.11: Mobile grain size distribution at the outlet at several transport stages, average grain size distribution at the outlet and at the inlet.

It was observed that a large peak in sediment transport occurs when the riffle structure breakdown starts in the upstream part of the flume. Fine sediments laying under the coarse surface are freed and enhance the destruction of coarse riffle structures in the downstream sections. Observations indicate that the sediment transport starts to gently increase when

the mobilization of fine sediments reaches the central part of the flume, but an abrupt increase in bedload transport at the flume outlet is observed only when the mobilized fine sediments reach the flume outlet.

Figure 8.12 shows the destruction process of a riffle. In Figure 8.12a, a coarse riffle is shown just before its destruction. Only approximately half of the flume width is used by the flow upstream and downstream of the riffle structure (cf. "No flow region" in Figure 8.12a). The riffle is steep and has a rapid flow. In few seconds this structure can be completely destroyed. The destruction starts from the steep riffle region. When the flow becomes too fast, some coarse grains creating the riffles are mobilized and suddenly all the bed upstream of the reach starts moving. This phenomenon occurs in only a few seconds, as can be seen in Figure 8.12b, on a picture taken approximately 20 seconds after that shown in Figure 8.12a. The movement of a large amount of fine sediments (Figure 8.12b), previously buried under the coarse surface layer, enhances the destruction of riffles in the downstream sections. After the destruction of a riffle, and in general during high sediment transport events, all the flume width is occupied by the flow. This phenomenon of structure formation and destruction is more evident in experiments carried out without boulders, but can be identified also in tests with macro-roughness elements. During experiments with a large spatial density of boulders ($\lambda/D=2$), this phenomenon becomes however marginal, because riffles can barely form, since the spacing between boulders is small.

a)   b)
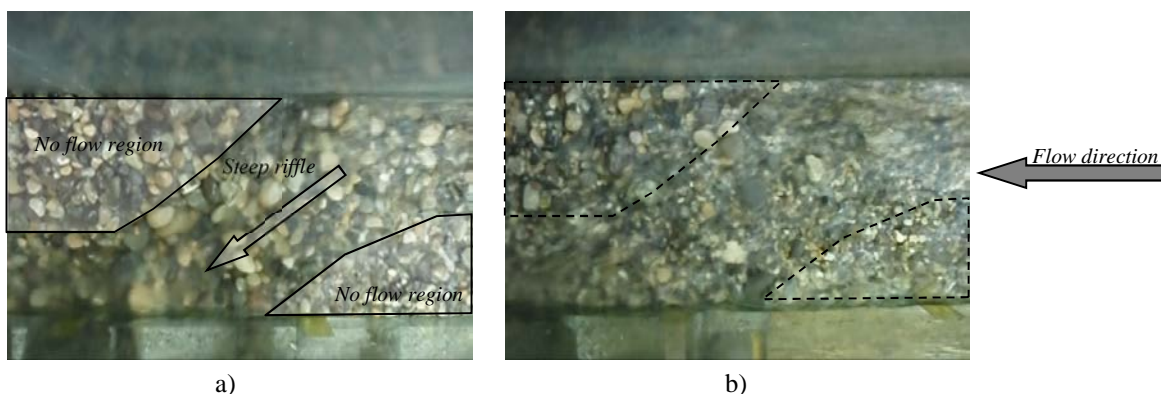
Figure 8.12: Abrupt change in surface and transported grain size distribution during a riffle destruction. a) Riffle just before the destruction; b) riffle after the destruction, about 20 seconds later. Test without boulders on the 13% slope.

Chapter 9

Conclusions and further developments

In the following, the main conclusions reached in this work are listed in the light of the motivations and objectives that were set in Chapter 1.

9.1 Conclusions

In section 1.3, three main questions synthetized the motivation of the present research. Concerning the link among bedload fluctuations, flow velocity and morphological parameters, the answer is mainly given in Chapter 5, but it is approached ubiquitously throughout the entire manuscript. This research work revealed an interaction between bedload and flow velocity fluctuations and variations in morphological parameters, such as boulder protrusion, bed surface occupied by boulders and number of hydraulic jumps. It is shown that the duration of the fluctuating cycles is the same for all the measured variables, however a delay between the variables exists, i.e. morphological parameters, influencing energy dissipation, fluctuate with a time lag with bedload transport pulses. Bedload and flow velocities fluctuate almost in phase, with the peak in velocities occurring just minutes before the peak in bedload.

Data analysis and visual observations show that when the sediment transport starts increasing, the values of morphological parameters are at a minimum, suggesting that energy dissipation is also at a minimum value. Bedload starts decreasing again when morphological variable values are at about 50% of their maximum value. When morphological parameters reach their maximum value, the bedload transport has decreased until the average transport and soon reaches a minimum value. Morphological parameters value continues to decrease until a minimum, when bedload starts increasing again for a new cycle. This phenomenon is accompanied by the continuous formation and destruction of coarse riffle structures through the channel. Moreover, it is shown that the grain size distribution of the outlet sediments evolves through time, and is coarser during small sediment transport events, fine during bedload peaks, and equal to the supplied grain size distribution after a peak in sediment transport ($q_{s,in}=q_{s,out,10}$).

The second research question referred to the influence of the presence of boulders on the duration and amplitude of bedload pulses. The analysis of 38 experiments carried out on a tilting flume treated in Chapter 6 shows that, although the bedload fluctuations are caused by the presence of graded bed materials and not by macro-roughness elements, the

presence of boulders does have an impact on sediment transport capacity, and thus on the duration and amplitude of bedload fluctuations.

The influence of boulders on bedload fluctuations occurs through two different processes. On one side, the presence of boulders obstructs the formation of the coarse riffles responsible for bedload fluctuations. Well-developed stable riffles cannot form anymore in the channel since their formation is hindered by the presence of boulders, locally perturbing the flow. According to visual observation riffles tend to become smaller for increasing spatial densities of macro-roughness elements. For the highest spatial densities of boulders used in this research work, the fluctuations had small amplitude and duration.

Another factor influencing the fluctuation characteristics is the stream power. It is proved that at higher stream powers the amplitude and period of fluctuations is decreased. A direct relation between the stream power and the presence of boulders, which could be taken into account as either of the morphological parameters (boulder protrusion, boulder surface or number of hydraulic jumps), could be found, showing that the stream power needed to transport the same average amount of sediments increases with boulder spatial density. The decrease in period and amplitude of bedload pulses, caused by the increase in energy losses, decreases morphological changes through time.

Finally, the last research question was about how boulders influence the sediment transport capacity and the initiation of motion. In Chapter 7 this research proves that, although the channel slope has the strongest impact on the transport capacity, the presence of boulders needs to be considered when estimating the bedload transport capacity. The sediment transport strongly decreases with dimensionless boulder distance λ/D and seems to decrease with boulder diameter. When $\lambda/D=2$, a change in behavior is observed: the transport capacity decreases drastically, and this especially for higher discharges, probably due to a change in wake interference between boulders.

It is observed that the sediment transport is more related to the liquid discharge than to the shear stress. The critical discharge at which incipient motion occurs is known to decrease with channel slope and the present work shows that it is also linked to boulder dimensionless distance and seemingly the boulder protrusion. However, the present dataset

is not large enough to infer a formula for critical discharge including the latter parameter. The following equation for critical discharge, based on the channel slope and the roughness geometry, is herein proposed:

$$q_{cr}^* = \frac{q_{cr}}{\sqrt{gd_{50}^3}} = S^{-0.46}\left(1 - \frac{D}{\lambda}\right)^{-0.7} \qquad \text{cf. eq. (54)}$$

A classical form of sediment transport formula is fitted to the collected data.

$$q_s^* = 4.69S^{2.10}\sqrt{q^* - q_{cr}^*} \qquad \text{cf. eq. (59)}$$

Based on the present dataset, it is suggested that formulae based on excessive discharge (q-q_{cr}), or excess stream power, perform better than those based on excessive shear stress. It is shown than when the presence of boulders is taken into account in the critical discharge value, as suggested by eq. (54), there is no need to introduce a correction factor in the bedload transport equation to account for the presence of boulders. No systematic over- or under-prediction of sediment transport is observed as a function of boulder configuration (λ/D and D).

In steep channels, water depth and morphology are rapidly varying. It is thus difficult to select representative cross-sections for measurements. For these reason, a new bulk velocity measurement technique was developed during the present research and is presented in Chapter 4. The herein developed method is based on a dye tracer measurement technique and video analysis, its main advantage that it completely avoids the problem of cross-section selection. The dye tracer method was compared to three existing velocity estimation techniques and it proved to supply good bulk velocity estimates. One of the main challenges of this technique are the light reflections on the water surface, increasing with the channel slope. However, it was shown in Chapter 4 that the misidentification of some colored pixels only slightly influences the velocity estimates.

9.2 Future work

Several answers were given concerning the effect of boulders on the sediment transport capacity and fluctuations. Nevertheless, further work is needed in order to fully understand the influence of macro-roughness elements on the flow.

In particular, in Chapter 7 it was shown that taking into account the presence of boulders in an equation for the critical discharge drastically improves the bedload estimates. The present results indicate that the critical discharge is a function of the channel slope, the boulder geometry and the roughness protrusion. The first two parameters were included in a critical discharge formula, as expressed in equation (54). However, the boulder protrusion, or another parameter varying with the latter, could not be included in the critical discharge formula. The effect of boulders on incipient motion of mobile sediments should thus be studied more into detail.

According to equations (54) and (59), the influence of boulder protrusion was not taken into account in the herein developed sediment transport formula. As observed by previous authors, the boulder protrusion should however have an effect on the sediment transport. A larger dataset is needed in order to test various hypotheses to account for boulder protrusion.

Finally, an influence on bedload transport due to the boulder diameter was observed. It was however not possible to infer whether the influence was related to the boulder diameter itself or to the number of boulders present in the channel. Further experiments with the same amount and position of boulders, using different diameters, are needed in order explain the observed behavior.

Changes in behavior, both from the sediment transport capacity (Chapter 7) and fluctuations (Chapter 6) point of view, were observed for dimensionless boulder distances of $\lambda/D=2$. This is linked to changes in flow behavior, evolving from a flow among isolated roughness elements to a wake interference flow. Further studies are needed in order to fully understand the influence of such a behavior on sediment transport capacity and fluctuations.

I believe that I have only scratched the surface in the issue of influence of boulders on flow conditions and sediment transport capacity and fluctuations, and my feelings are that this field will rapidly expand in the close future.

References

Amini, A., G. De Cesare, and A. J. Schleiss (2009), Velocity profiles and interface instability in a two-phase fluid: investigations using ultrasonic velocity profiler, *Experiments in Fluids*, *46*(4), 683-692.

Bacchi, V., A. Recking, P. Frey, and M. Naaim (2009), Experimental measurement of bedload and slope fluctuations in a channel under constant feed and water conditions, 33rd IAHR World Congress, International Association of Hydraulic Engineering & Research (IAHR), Vancouver, BC, Canada, 9-14 August 2009.

Badoux, A., N. Andres, and J. M. Turowski (2013), Damage costs due to bedload transport processes in Switzerland, *Nat. Hazards Earth Syst. Sci. Discuss.*, *1*(4), 4181-4222.

Bagnold, R. A. (1966), An approach to the sediment transport problem from general physics, *US Geol. Surv. Prof. Paper*, *422*, 231-291.

Bagnold, R. A. (1977), Bed load transport by natural rivers, *Water Resources Research*, *13*(2), 303-312.

Bagnold, R. A. (1980), An Empirical Correlation of Bedload Transport Rates in Flumes and Natural Rivers, *Proceedings of the Royal Society of London. Series A, Mathematical and Physical Sciences*, *372*(1751), 453-473.

Baiamonte, G., G. Giordano, and V. Ferro (1995), Advances on velocity profile and flow resistance law in gravel bed rivers, *Excerpta of the Italian Contributions to the Field of Hydraulic Engineering*, *9*, 41-90.

Barenblatt, G. I. (1996), *Scaling, self-similarity, and intermediate asymptotics: dimensional analysis and intermediate asymptotics*, Cambridge texts in applied mathematics, Cambridge University Press.

Bathurst, J. C. (1978), Flow resistance of large-scale roughness, *Journal of the Hydraulics Division*, *104*(HY12), 1587-1603.

Bathurst, J. C. (1987), Critical conditions for bed material movement in steep, boulder-bed streams, in *Erosion and Sedimentation in the Pacific Rim*, edited by R. L. Beschta, Blinn, T. Grant, G.E., Ice, G.G., Swanson, F.J., pp. 309-318, IAHS Press, Wallingford.

Bezzola, G. R. (2002), *Fliesswiderstand und Sohlenstabilität natürlicher Gerinne unter besonderer Berücksichtigung des Einflusses der relativen Überdeckung*, PhD thesis dissertation, Nr. 14433, 357 pp, Eidgenossischen Technischen Hochschule Zurich (ETHZ), Zürich.

Blanckaert, K., and H. De Vriend (2004), Secondary flow in sharp open-channel bends, *Journal of Fluid Mechanics*, *498*(1), 353-380.

Boillat, J.-L. (1980), *Influence de la turbulence sur le coefficient de traînée des sphères: étude expérimentale*, PhD thesis dissertation, Nr. 388, 216 pp, École polytechnique fédérale de Lausanne EPFL, Lausanne.

Buffin-Bélanger, T., and A. G. Roy (1998), Effects of a pebble cluster on the turbulent structure of a depth-limited flow in a gravel-bed river, *Geomorphology*, *25*(3–4), 249-267.

Buffington, J. M., and D. R. Montgomery (1997), A systematic analysis of eight decades of incipient motion studies, with special reference to gravel-bedded rivers, *Water Resources Research*, *33*(8), 1993-2029.

Calkins, D., and T. Dunne (1970), A salt tracing method for measuring channel velocities in small mountain streams, *J. Hydrol.*, *11*(4), 379-392.

Camenen, B., and M. Larson (2005), A general formula for non-cohesive bed load sediment transport, *Estuarine, Coastal and Shelf Science*, *63*(1-2), 249-260.

Canovaro, F., E. Paris, and L. Solari (2007), Effects of macro-scale bed roughness geometry on flow resistance, *Water Resources Research*, *43*(10).

Cao, S. (1985), *Résistance hydraulique d'un lit de gravier mobile à pente raide; étude expérimentale*, PhD thesis dissertation, Nr. 589, 318 pp, Ecole Polytechnique Fédérale de Lausanne (EPFL).

Chin, A., and E. E. Wohl (2005), Toward a theory for step pools in stream channels, *Progress in Physical Geography*, *29*(3), 275-296.

Church, M. A., and R. Kellerhals (1970), *Stream gauging techniques for remote areas using portable equipment*, Technical bulletin 90 pp., Inland Waters Branch, Department of Energy, Mines and Resources.

Church, M. A., M. A. Hassan, and J. F. Wolcott (1998), Stabilizing self-organized structures in gravel-bed stream channels: Field and experimental observations, *Water Resources Research*, *34*(11), 3169-3179.

Comiti, F., and M. A. Lenzi (2006), Dimensions of standing waves at steps in mountain rivers, *Water Resources Research*, *42*(3).

Comiti, F., D. Cadol, and E. E. Wohl (2009), Flow regimes, bed morphology, and flow resistance in self-formed step-pool channels, *Water Resources Research*, *45*(4).

Comiti, F., and L. Mao (2012), Recent Advances in the Dynamics of Steep Channels, in *Gravel-Bed Rivers*, edited, pp. 351-377, John Wiley & Sons, Ltd.

Curran, J. H., and E. E. Wohl (2003), Large woody debris and flow resistance in step-pool channels, Cascade Range, Washington, *Geomorphology*, *51*(1-3), 141-157.

References

D'Agostino, V., M. Lenzi, and L. Marchi (1994), Sediment transport and water discharge during high flows in an instrumented watershed, in *Dynamics and Geomorphology of Mountain Rivers*, edited by P. Ergenzinger and K.-H. Schmidt, Lecture Notes in Earth Sciences, pp. 67-81, Springer Berlin Heidelberg.

David, G. C. L., E. Wohl, S. E. Yochum, and B. P. Bledsoe (2011), Comparative analysis of bed resistance partitioning in high-gradient streams, *Water Resources Research*, *47*(7).

Davies, T. R. H., and M. N. R. Jäggi (1981), Precise laboratory measurement of flow resistance, XIX IAHR congress, New Delhi, India.

Day, T. J. (1976), On the precision of salt dilution gauging, *J. Hydrol.*, *31*(3–4), 293-306.

Dubois, J. (1998), *Comportement hydraulique et modélisation des écoulements de surface*, PhD thesis dissertation, Nr. 1890, 192 pp, Ecole Polytechnique Fédérale de Lausanne (EPFL), Lausanne.

Dugué, V., K. Blanckaert, Q. Chen, and A. J. Schleiss (2013), Reduction of bend scour with an air-bubble screen – morphology and flow patterns, *International Journal of Sediment Research*, *28*(1), 15-23.

Einstein, H. A. (1950), The bed-load function for sediment transportation in open channel flows, *Technical Bulletin 1026 Rep.*, 71 pp, US Department of Agriculture, Soil Conservation Service, Washington.

Einstein, H. A., and N. L. Barbarossa (1952), River channel roughness, *Transactions of the American Society of civil Engineers*, *117*(1), 1121-1132.

Endreny, T., L. Lautz, and D. I. Siegel (2011), Hyporheic flow path response to hydraulic jumps at river steps: Flume and hydrodynamic models, *Water Resources Research*, *47*(2).

Ferguson, R. I. (1994), Critical discharge for entrainment of poorly sorted gravel, *Earth Surface Processes and Landforms*, *19*(2), 179-186.

Ferguson, R. I. (2005), Estimating critical stream power for bedload transport calculations in gravel-bed rivers, *Geomorphology*, *70*(1-2), 33-41.

Ferguson, R. I. (2007), Flow resistance equations for gravel- and boulder-bed streams, *Water Resources Research*, *43*(5).

Fernandez Luque, R., and R. van Beek (1976), Erosion and transport of bed-load sediment, *Journal of Hydraulic Research*, *14*(2), 127-144.

Ferreira, R. M. L., M. J. Franca, and J. G. A. B. Leal (2007), Laboratorial and theoretical study of the mobility of gravel and sand mixtures, Proceedings of the 5th River, Coastal and Estuarine Morphodynamics, RCEM, Taylor & Francis Group, London, Enschede, The Netherlands, 17-21 September 2007.

Ferreira, R. M. L., M. J. Franca, J. G. A. B. Leal, and A. H. Cardoso (2012), Flow over rough mobile beds: Friction factor and vertical distribution of the longitudinal mean velocity, *Water Resources Research*, *48*(5), W05529.

Ferro, V. (1999), Friction factor for gravel-bed channel with high boulder concentration, *Journal of Hydraulic Engineering*, *125*(7), 771-778.

Franca, M. J., and U. Lemmin (2006), Eliminating velocity aliasing in acoustic Doppler velocity profiler data, *Measurement Science and Technology*, *17*(2), 313.

Franca, M. J., R. M. L. Ferreira, and U. Lemmin (2008), Parameterization of the logarithmic layer of double-averaged streamwise velocity profiles in gravel-bed river flows, *Advances in Water Resources*, *31*(6), 915-925.

Frey, P., C. Ducottet, and J. Jay (2003), Fluctuations of bed load solid discharge and grain size distribution on steep slopes with image analysis, *Experiments in Fluids*, *35*(6), 589-597.

Fujita, I., M. Muste, and A. Kruger (1998), Large-scale particle image velocimetry for flow analysis in hydraulic engineering applications, *Journal of Hydraulic Research*, *36*(3), 397-414.

Ghilardi, T., and A. J. Schleiss (2011), Influence of Immobile Boulders on Bedload Transport in a Steep Flume, 34th IAHR World Congress, Engineers Australia, Brisbane, Australia, 26th June-1st July 2011.

Ghilardi, T., and A. J. Schleiss (2012), Steep flume experiments with large immobile boulders and wide grain size distribution as encountered in alpine torrents, River Flow 2012, Taylor & Francis Group, San José, Costa Rica, 5-7 September 2012.

Ghilardi, T. (2013), Experimental study on bedload pulses in a steep flume with boulders, 35th IAHR World Congress, Chengdu, China, 9-13 September 2013.

Ghilardi, T., M. J. Franca, and A. J. Schleiss (2013), Temporal evolution of bedload in a steep channel over a long duration experiment, 35th IAHR World Congress, Chengdu, China, 8-13 September 2013.

Gintz, D., M. A. Hassan, and K.-H. Schmidt (1996), Frequency and magnitude of bedload transport in a mountain river, *Earth Surface Processes and Landforms*, *21*(5), 433-445.

Gomez, B., and M. A. Church (1989), An assessment of bed load sediment transport formulae for gravel bed rivers, *Water Resources Research*, *25*(6), 1161-1186.

Graf, W. H., and M. Altinakar (2008), *Hydraulique fluviale: Ecoulement et phénomènes de trasnport dans les canaux à géométrie simple*, 2nd edition ed., Traité de Génie Civil, PPUR.

Hersberger, D. S. (2002), *Wall roughness effects on flow and scouring in curved channels with gravel bed*, PhD thesis dissertation, Nr. 2632, 246 pp, École Polytechnique Fédérale de Lausanne, Lausanne.

Heyman, J., F. Mettra, H. Ma, and C. Ancey (2013), Statistics of bedload transport over steep slopes: Separation of time scales and collective motion, *Geophysical Research Letters*, *40*, 128-133.

Hinze, J. O. (1975), *Turbulence*, 2nd ed., McGraw-Hill series in mechanical engineering 790 pp., McGraw-Hill Inc., New York.

Iseya, F., and H. Ikeda (1987), Pulsations in bedload transport rates induced by a longitudinal sediment sorting: A flume study using sand and gravel mixtures, *Geografiska Annaler. Series A. Physical Geography*, *69*(1), 15-27.

Jäggi, M. N. R. (1995), Sediment transport in mountain rivers – A review, International Conference on Erosion Control. The Sabo Society of Japan, Tokyo, Japan (Keynote Address), Tokyo, Japan.

Jodeau, M., A. Hauet, A. Paquier, J. Le Coz, and G. Dramais (2008), Application and evaluation of LS-PIV technique for the monitoring of river surface velocities in high flow conditions, *Flow Measurement and Instrumentation*, *19*(2), 117-127.

Kantoush, S. A., A. J. Schleiss, T. Sumi, and M. Murasaki (2011), LSPIV implementation for environmental flow in various laboratory and field cases, *Journal of Hydro-environment Research*, *5*(4), 263-276.

Keulegan, G. H. (1938), Laws of turbulent flow in open channels, *Journal of Research of the National Bureau of Standards*, *21*(6), 35.

Kraus, N., A. Lohrmann, and R. Cabrera (1994), New Acoustic Meter for Measuring 3D Laboratory Flows, *Journal of Hydraulic Engineering*, *120*(3), 406-412.

Kuhnle, R. A., and J. B. Southard (1988), Bed load transport fluctuations in a gravel bed laboratory channel, *Water Resources Research*, *24*(2), 247-260.

Lamb, M. P., W. E. Dietrich, and J. G. Venditti (2008), Is the critical Shields stress for incipient sediment motion dependent on channel-bed slope?, *Journal of Geophysical Research*, *113*(F2).

Le Coz, J., G. Pierrefeu, and A. Paquier (2008), Evaluation of river discharges monitored by a fixed side-looking Doppler profiler, *Water Resources Research*, *44*(4), W00D09.

Le Coz, J., A. Hauet, G. Pierrefeu, G. Dramais, and B. Camenen (2010), Performance of image-based velocimetry (LSPIV) applied to flash-flood discharge measurements in Mediterranean rivers, *J. Hydrol.*, *394*(1–2), 42-52.

Leite Ribeiro, M., K. Blanckaert, A. G. Roy, and A. J. Schleiss (2012), Flow and sediment dynamics in channel confluences, *Journal of Geophysical Research*, *117*(F1).

Lenzi, M. A., V. D'Agostino, and P. Billi (1999), Bedload transport in the instrumented catchment of the Rio Cordon Part I: Analysis of bedload records, conditions and threshold of bedload entrainment, *Catena*, *36*(3), 171-190.

Lenzi, M. A. (2001), Step-pool evolution in the Rio Cordon, northeastern Italy, *Earth Surface Processes and Landforms*, *26*(9), 991-1008.

Lenzi, M. A., L. Mao, and F. Comiti (2006), When does bedload transport begin in steep boulder-bed streams?, *Hydrological Processes*, *20*(16), 3517-3533.

Lorke, A., and A. Wüest (2005), Application of Coherent ADCP for Turbulence Measurements in the Bottom Boundary Layer, *Journal of Atmospheric and Oceanic Technology*, *22*(11), 1821-1828.

MacFarlane, W. A., and E. E. Wohl (2003), Influence of step composition on step geometry and flow resistance in step-pool streams of the Washington Cascades, *Water Resources Research*, *39*(2), 1037.

MacVicar, B. J., E. Beaulieu, V. Champagne, and A. G. Roy (2007), Measuring water velocity in highly turbulent flows: field tests of an electromagnetic current meter (ECM) and an acoustic Doppler velocimeter (ADV), *Earth Surface Processes and Landforms*, *32*(9), 1412-1432.

Mao, L., G. P. Uyttendaele, A. Iroumé, and M. A. Lenzi (2008), Field based analysis of sediment entrainment in two high gradient streams located in Alpine and Andine environments, *Geomorphology*, *93*(3-4), 368-383.

Marcus, W. A., K. Roberts, L. Harvey, and G. Tackman (1992), An Evaluation of Methods for Estimating Manning's n in Small Mountain Streams, *Mountain Research and Development*, *12*(3), 227-239.

Mattioli, M., J. M. Alsina, A. Mancinelli, M. Miozzi, and M. Brocchini (2012), Experimental investigation of the nearbed dynamics around a submarine pipeline laying on different types of seabed: The interaction between turbulent structures and particles, *Advances in Water Resources*, *48*(0), 31-46.

Meyer-Peter, E., and R. Müller (1948), Formulas for bed-load transport, Proceedings of the 2nd Meeting of the International Association for Hydraulic Structures Research, Stockholm.

Montgomery, D. R., and J. M. Buffington (1997), Channel-reach morphology in mountain drainage basins, *Geological Society of America Bulletin*, *109*(5), 596-611.

Muste, M., I. Fujita, and A. Hauet (2008), Large-scale particle image velocimetry for measurements in riverine environments, *Water Resources Research*, *44*(4), W00D19.

Nelson, J. M., S. R. McLean, and S. R. Wolfe (1993), Mean flow and turbulence fields over two-dimensional bed forms, *Water Resources Research*, *29*(12), 3935-3953.

Nezu, I., and H. Nakagawa (1993), *Turbulence in open-channel flows*, IAHR Monograph Series 281 pp., A.A. Balkema, Rotterdam, Netherlands.

Nikora, V., D. Goring, I. McEwan, and G. Griffiths (2001), Spatially Averaged Open-Channel Flow over Rough Bed, *Journal of Hydraulic Engineering*, *127*(2), 123-133.

Nogueira, H. I. S., C. Adduce, E. Alves, and M. J. Franca (2013), Image analysis technique applied to lock-exchange gravity currents, *Measurement Science and Technology*, *24*(4), 047001.

Pagliara, S., and P. Chiavaccini (2006), Flow Resistance of Rock Chutes with Protruding Boulders, *Journal of Hydraulic Engineering*, *132*(6), 545-552.

Pagliara, S. (2007), Influence of Sediment Gradation on Scour Downstream of Block Ramps, *Journal of Hydraulic Engineering*, *133*(11), 1241-1248.

Pagliara, S., R. Das, and I. Carnacina (2008), Flow resistance in large-scale roughness condition, *Canadian Journal of Civil Engineering*, *35*(11), 1285-1293.

Pagliara, S., M. Palermo, and I. Carnacina (2010), Expanding pools morphology in live-bed conditions, *Acta Geophysica*, *59*(2), 296-316.

Papanicolaou, A. N., A. Bdour, and E. Wicklein (2004), One-dimensional hydrodynamic/sediment transport model applicable to steep mountain streams, *Journal of Hydraulic Research*, *42*(4), 357-375.

Parker, C., N. J. Clifford, and C. R. Thorne (2011), Understanding the influence of slope on the threshold of coarse grain motion: Revisiting critical stream power, *Geomorphology*, *126*(1-2), 51-65.

Parker, G., P. C. Klingeman, and D. G. McLean (1982), Bedload and size distribution in paved gravel-bed streams, *Journal of the Hydraulics Division*, *108*(4), 544-571.

Parker, G. (1990), Surface-based bedload transport relation for gravel rivers, *Journal of Hydraulic Research*, *28*(4), 417-436.

Petit, F., F. Gob, G. Houbrechts, and A. A. Assani (2005), Critical specific stream power in gravel-bed rivers, *Geomorphology*, *69*(1-4), 92-101.

Pokrajac, D., L. Campbell, V. Nikora, C. Manes, and I. McEwan (2007), Quadrant analysis of persistent spatial velocity perturbations over square-bar roughness, *Experiments in Fluids*, *42*(3), 413-423.

Raffel, M., C. E. Willert, and J. Kompenhans (1998), *Particle image velocimetry: a practical guide*, Springer Verlag.

Recking, A. (2006), *Etude expérimentale de l'influence du tri granulométrique sur le transport solide par charriage*, PhD thesis dissertation, Nr. 2006-ISAL-00113, 263 pp, Institut National Des Sciences Appliquées de Lyon, Lyon.

Recking, A., P. Frey, A. Paquier, P. Belleudy, and J.-Y. Champagne (2008a), Feedback between bed load transport and flow resistance in gravel and cobble bed rivers, *Water Resources Research*, *44*(5).

Recking, A., P. Frey, A. Paquier, P. Belleudy, and J.-Y. Champagne (2008b), Bed-Load Transport Flume Experiments on Steep Slopes, *Journal of Hydraulic Engineering*, *134*(9), 1302-1310.

Recking, A., P. Frey, A. Paquier, and P. Belleudy (2009), An experimental investigation of mechanisms involved in bed load sheet production and migration, *Journal of Geophysical Research*, *114*(F3).

Rickenmann, D. (1990), *Bedload transport capacity of slurry flows at steep slopes* PhD thesis dissertation, Nr. 9065, 249 pp, ETH Zürich (Swiss Federal Institute Of Technology Zurich), Zürich.

Rickenmann, D. (1991a), Bed load transport and hyperconcentrated flow at steep slopes, in *Fluvial hydraulics of mountain regions*, edited by A. Armanini and G. Di Silvio, Lecture Notes in Earth Sciences, pp. 429-441, Springer-Verlag, Berlin.

Rickenmann, D. (1991b), Hyperconcentrated Flow and Sediment Transport at Steep Slopes, *Journal of Hydraulic Engineering*, *117*(11), 1419-1439.

Rickenmann, D. (1994), Bedload transport and discharge in the Erlenbach stream, in *Dynamics and Geomorphology of Mountain Rivers*, edited by P. Ergenzinger and K.-H. Schmidt, Lecture Notes in Earth Sciences, pp. 53-66, Springer Berlin Heidelberg.

Rickenmann, D. (1997), Sediment transport in Swiss torrents, *Earth Surface Processes and Landforms*, *22*(10), 937-951.

Rickenmann, D. (2001), Comparison of bed load transport in torrents and gravel bed streams, *Water Resources Research*, *37*(12), 3295-3305.

Robert, A., A. G. Roy, and B. De Serres (1992), Changes in velocity profiles at roughness transitions in coarse grained channels, *Sedimentology*, *39*(5), 725-735.

Roy, A. G., T. Buffin-Belanger, H. Lamarre, and A. D. Kirkbride (2004), Size, shape and dynamics of large-scale turbulent flow structures in a gravel-bed river, *Journal of Fluid Mechanics*, *500*, 1-27.

Rutherford, J. (1994), *River mixing*347 pp., Wiley Chichester.

Scheingross, J. S., E. W. Winchell, M. P. Lamb, and W. E. Dietrich (2013), Influence of bed patchiness, slope, grain hiding, and form drag on gravel mobilization in very steep streams, *Journal of Geophysical Research: Earth Surface*, *118*.

Schoklitsch, A. (1962), Handbuch des wasserbaus, *Wien, Springer Verlag*.

Shields, A. (1936), *Application of similarity principles and turbulence research to bed-load movement (translation by W.P. Ott and J.C. van Uchelen)*, Berlin.

Smart, G. M., and M. N. R. Jäggi (1983), *Sediment transport on steep slopes*, Mitteilungen der Versuchanstalt für Wasserbau, Hydrologie und Glaziologie 96 pp., Zürich.

Smart, G. M. (1984), Sediment Transport Formula for Steep Channels, *Journal of Hydraulic Engineering*, *110*(3), 267-276.

Thomas, L., and B. Marino (2012), Inertial Density Currents over Porous Media Limited by Different Lower Boundary Conditions, *Journal of Hydraulic Engineering*, *138*(2), 133-142.

USBR (1980), *Hydraulic laboratory techniques*, Water resources technical publication 208 pp., U.S. Department of the Interior, Bureau of reclamation, Denver, Colorado, USA.

van Prooijen, B. C., and W. S. J. Uijttewaal (2002), A linear approach for the evolution of coherent structures in shallow mixing layers, *Physics of Fluids*, *14*(12), 4105-4114.

Voulgaris, G., and J. H. Trowbridge (1998), Evaluation of the acoustic Doppler velocimeter (ADV) for turbulence measurements, *Journal of Atmospheric and Oceanic Technology*, *15*(1), 272.

Weichert, R. B. (2005), *Bed morphology and stability in steep open channels* PhD thesis dissertation, Nr. 16316, 264 pp, Eidgenössische Technische Hochschule ETH Zürich, Zürich.

Wiberg, P. L., and J. D. Smith (1991), Velocity distribution and bed roughness in high-gradient streams, *Water Resources Research*, *27*(5), 825-838.

Wilcock, P. R., and B. W. McArdell (1993), Surface-based fractional transport rates: Mobilization thresholds and partial transport of a sand-gravel sediment, *Water Resources Research*, *29*(4), 1297-1312.

Wilcock, P. R., and B. W. McArdell (1997), Partial transport of a sand/gravel sediment, *Water Resources Research*, *33*(1), 235-245.

Wilcox, A. C., J. M. Nelson, and E. E. Wohl (2006), Flow resistance dynamics in step-pool channels: 2. Partitioning between grain, spill, and woody debris resistance, *Water Resources Research*, *42*(5).

Wilcox, A. C., and E. E. Wohl (2007), Field measurements of three-dimensional hydraulics in a step-pool channel, *Geomorphology*, *83*(3-4), 215-231.

Wohl, E. E. (2000), *Mountain Rivers*, Water Resources Monograph 14, 320 pp., America Geophysical Union (AGU), Washington, DC.

Wong, M., and G. Parker (2006), Reanalysis and Correction of Bed-Load Relation of Meyer-Peter and Müller Using Their Own Database, *Journal of Hydraulic Engineering*, *132*(11), 1159-1168.

Yager, E. M. (2006), *Prediction of sediment transport in steep, rough streams*, PhD thesis dissertation, Nr. 3228532, 231 pp, University of California, Berkeley.

Yager, E. M., J. W. Kirchner, and W. E. Dietrich (2007), Calculating bed load transport in steep boulder bed channels, *Water Resources Research*, *43*(7).

Yager, E. M., W. E. Dietrich, J. W. Kirchner, and B. W. McArdell (2012a), Prediction of sediment transport in step-pool channels, *Water Resources Research*, *48*(1).

Yager, E. M., J. M. Turowski, D. Rickenmann, and B. W. McArdell (2012b), Sediment supply, grain protrusion, and bedload transport in mountain streams, *Geophysical Research Letters*, *39*(10).

Yalin, M. S. (1977), *Mechanics of sediment transport*, Pergamon press, Oxford.

Appendixes

A. Boulder configurations

This annex presents the position of boulders for each of the tested configurations as a function λ/D and D. The flume is 7 m long and 0.25 m wide.

$\lambda/D=5$
D=0.075 m

$\lambda/D=4$
D=0.075 m

$\lambda/D=3$
D=0.075 m

$\lambda/D=2$
D=0.075 m

λ/D=5
D=0.125 m

λ/D=3
D=0.125 m

λ/D=2
D=0.125 m
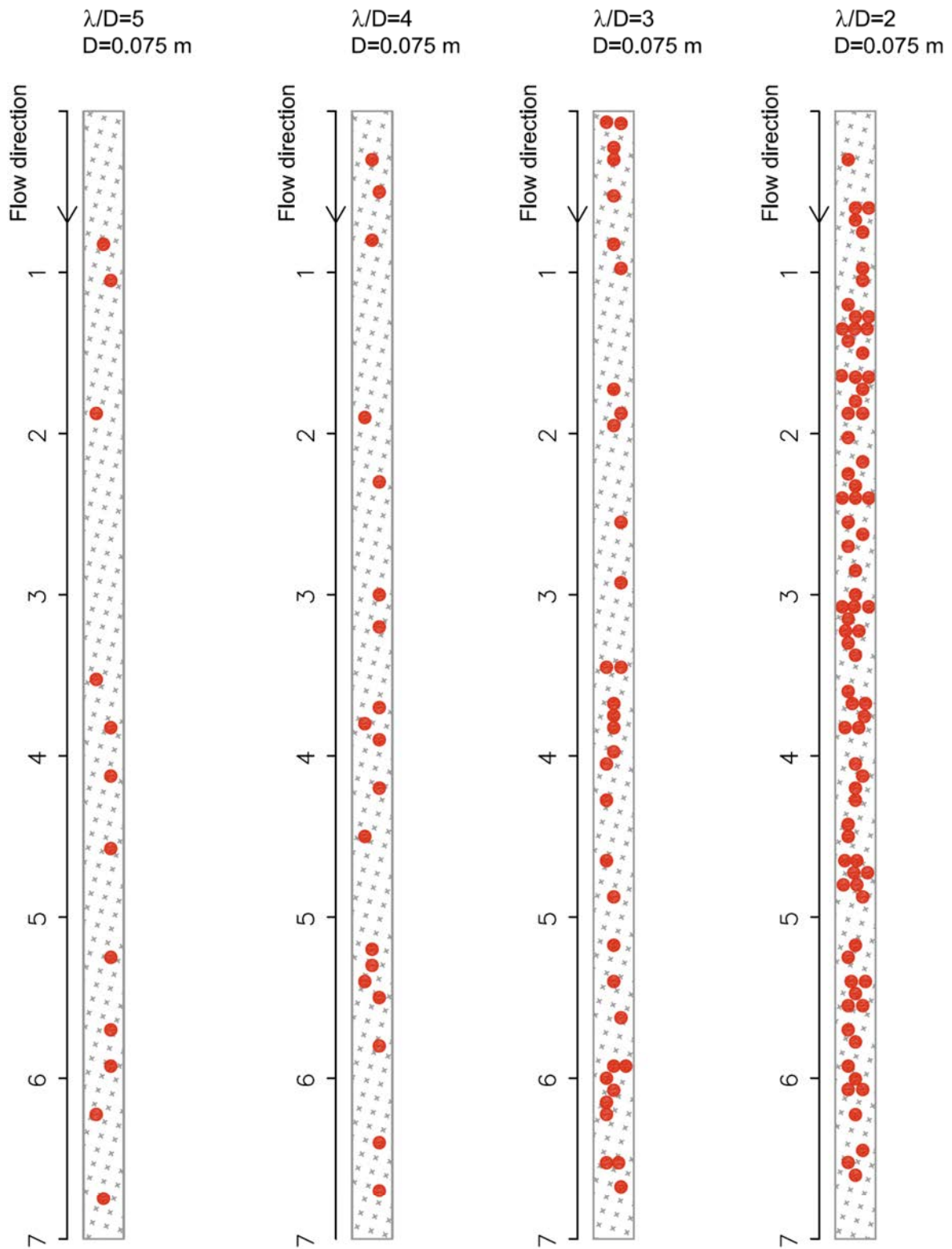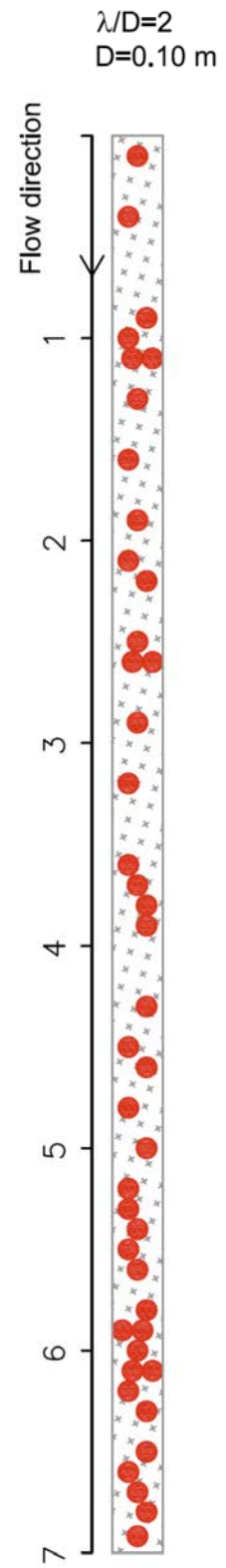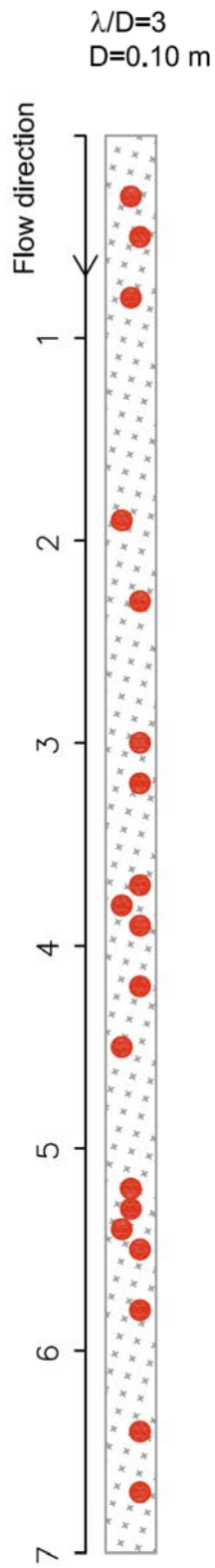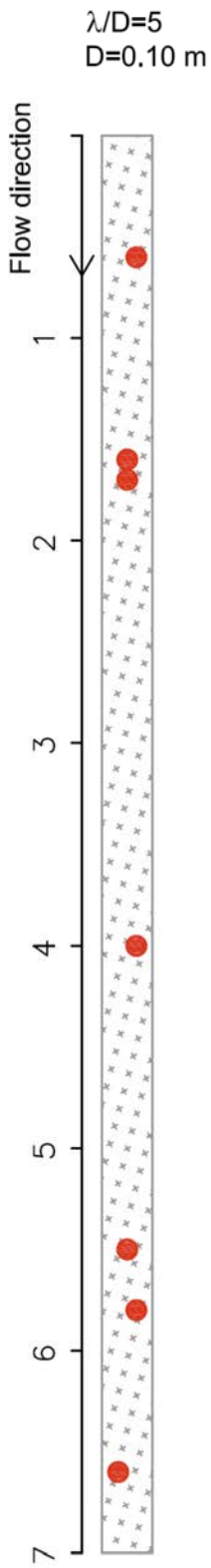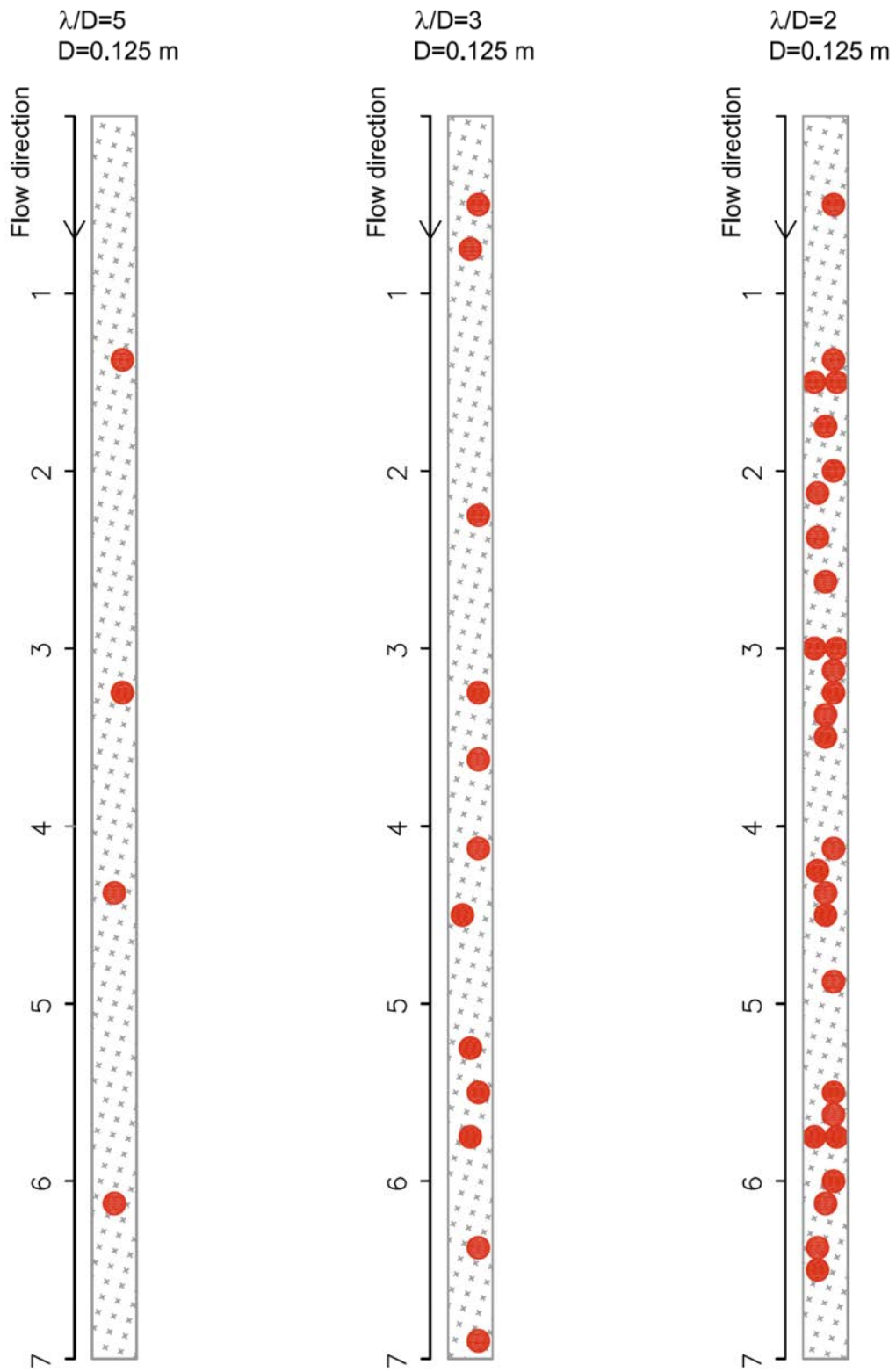
B. Experiments

In this annex, a detailed description of each experiment presented in Table 3.3 is given.

For each test the average values are presented. For tests 4 to 41, the time series of the measured values are presented, along with a correlation analysis and a phase analysis.

For tests 11 to 41 a reconstructed image presenting the central part of the flume at the end of the experiment is shown.

B.1 Test 1

Test parameters

S (%)	λ/D (-)	D (m)	N_{Bs} (m^{-2})	q (m^{3}s^{-1}m^{-1})	$q_{s,in}$ x10^{-3} (m^{3}s^{-1}m^{-1})
6.7	Inf.	0	0	0.0204	0.1857

Average results

$q_{s,end}$ x10^{-3} (m^{3}s^{-1}m^{-1})	$\bar{U}$ (ms^{-1})	$\overline{P_{av}}$ (m)	HJ (m^{-2})	A_i/A_t (-)	A_{if}/A_t (-)	P_{end} (m)	P_{us} (m)	P_{ds} (m)
0.1509	0.72	0	0	0	0	0	0	0

B.2 Test 2

Test parameters

S (%)	λ/D (-)	D (m)	N_{Bs} (m^{-2})	q (m^{3}s^{-1}m^{-1})	$q_{s,in}$ x10^{-3} (m^{3}s^{-1}m^{-1})
6.7	3	0.125	6.9	0.0240	0.1555

Average results

$q_{s,end}$ x10^{-3} (m^{3}s^{-1}m^{-1})	$\bar{U}$ (ms^{-1})	$\overline{P_{av}}$ (m)	HJ (m^{-2})	A_i/A_t (-)	A_{if}/A_t (-)	P_{end} (m)	P_{us} (m)	P_{ds} (m)
0.1706	0.90	-	-	-	-	0.032	0.019	0.035

B.3   Test 3

Test parameters

S (%)	λ/D (-)	D (m)	N_{Bs} (m^{-2})	q (m^{3}s^{-1}m^{-1})	$q_{s,in}$ x10^{-3} (m^{3}s^{-1}m^{-1})
6.7	3	0.100	10.9	0.0240	0.1389

Average results

$q_{s,end}$ x10^{-3} (m^{3}s^{-1}m^{-1})	$\bar{U}$ (ms^{-1})	$\bar{P_{av}}$ (m)	HJ (m^{-2})	A_i/A_t (-)	A_{if}/A_t (-)	P_{end} (m)	P_{us} (m)	P_{ds} (m)
0.1555	0.67	-	-	-	-	0.025	0.018	0.026

B.4   Test 4

Test parameters

S (%)	λ/D (-)	D (m)	N_{Bs} (m^{-2})	q (m^{3}s^{-1}m^{-1})	$q_{s,in}$ x10^{-3} (m^{3}s^{-1}m^{-1})
6.7	2	0.100	25.1	0.0228	0.0574

Characterization of the fluctuations (average period T=128.3 min)

	range (min ÷ max)	*mean*	*σ*	*σ/mean*
$q_{s,out,15}$	$0.0101 \div 0.1073$x10^{-3} m^{3}s^{-1}m^{-1}	0.0651x10^{-3} m^{3}s^{-1}m^{-1}	0.0225x10^{-3} m^{3}s^{-1}m^{-1}	0.35
U	$0.59 \div 0.77$ ms^{-1}	0.71 ms^{-1}	0.04 ms^{-1}	0.05
P^*	$0.19 \div 0.36$	0.24	0.04	0.15
A_{Bs}^*	$0.162 \div 0.213$	0.188	0.014	0.07
HJ^*	-	-	-	-

Average results

$q_{s,end}$ x10^{-3} (m^{3}s^{-1}m^{-1})	$\bar{U}$ (ms^{-1})	$\bar{P_{av}}$ (m)	HJ (m^{-2})	A_i/A_t (-)	A_{if}/A_t (-)	P_{end} (m)	P_{us} (m)	P_{ds} (m)
0.0646	0.71	0.024	-	0.17	0.042	0.021	0.019	0.020

Time series
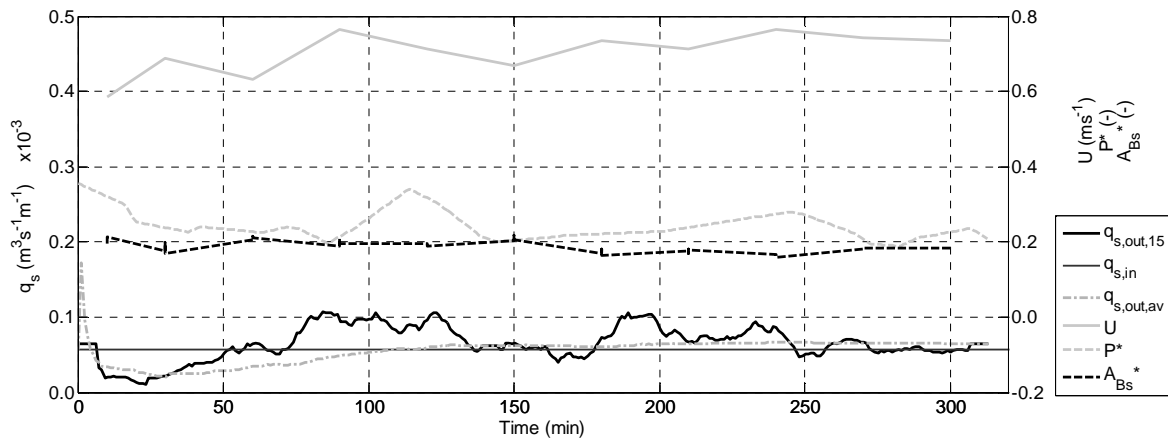
Correlation analysis
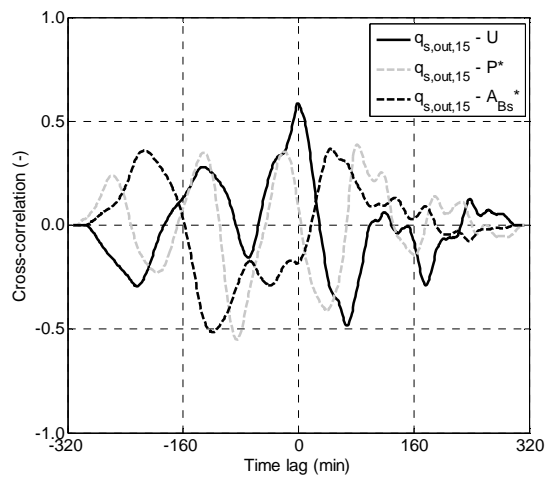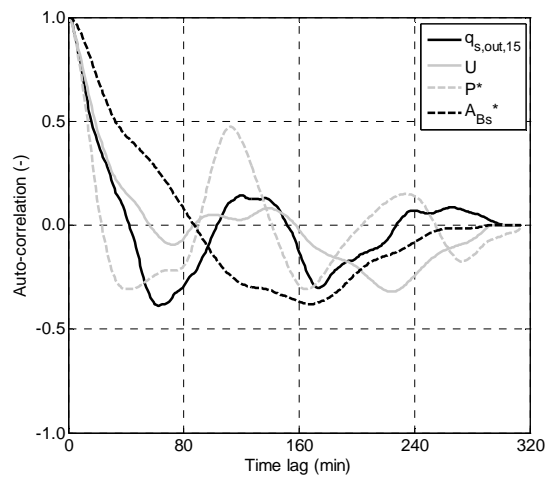
B.5   Test 5

Test parameters

S (%)	λ/D (-)	D (m)	N_{Bs} (m^{-2})	q (m^{3}s^{-1}m^{-1})	$q_{s,in}$ x10^{-3} (m^{3}s^{-1}m^{-1})
6.7	2	0.100	25.1	0.0424	0.1570

Characterization of the fluctuations (average period T=13 min)

	range (min ÷ max)	*mean*	*σ*	*σ/mean*
$q_{s,out,5}$	0.1107 ÷ 0.2616x10^{-3} m^{3}s^{-1}m^{-1}	0.1740x10^{-3} m^{3}s^{-1}m^{-1}	0.0306x10^{-3} m^{3}s^{-1}m^{-1}	0.18
U	0.78 ÷ 0.87 ms^{-1}	0.84 ms^{-1}	0.02 ms^{-1}	0.02
P^*	0.32 ÷ 0.38	0.35	0.01	0.04
$A_{Bs}{}^*$	0.181 ÷ 0.243	0.217	0.018	0.08
HJ^*	-	-	-	-

Average results

$q_{s,end}$ x10^{-3} (m^{3}s^{-1}m^{-1})	$\bar{U}$ (ms^{-1})	$\bar{P_{av}}$ (m)	HJ (m^{-2})	A_i/A_t (-)	A_{if}/A_t (-)	P_{end} (m)	P_{us} (m)	P_{ds} (m)
0.1736	0.84	0.036	-	0.21	0.074	0.031	0.025	0.036

Time series
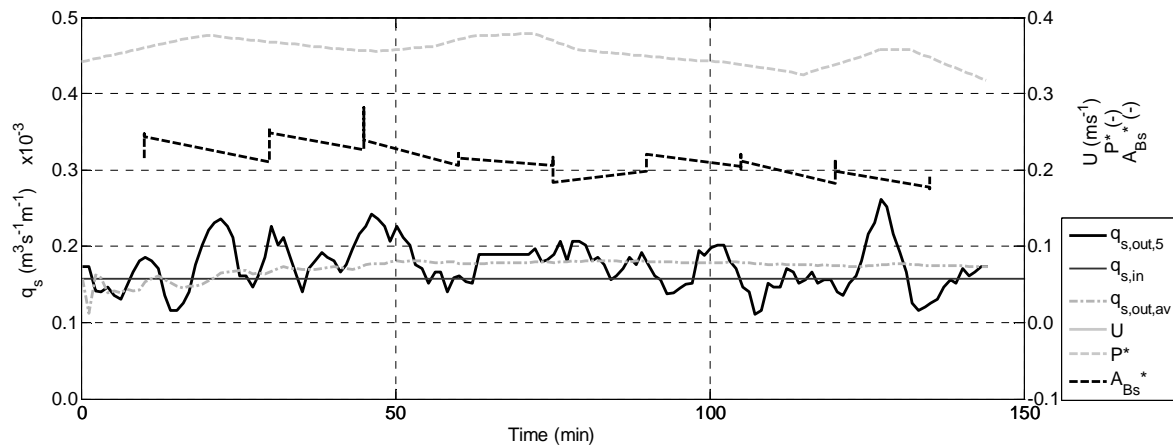
Correlation analysis
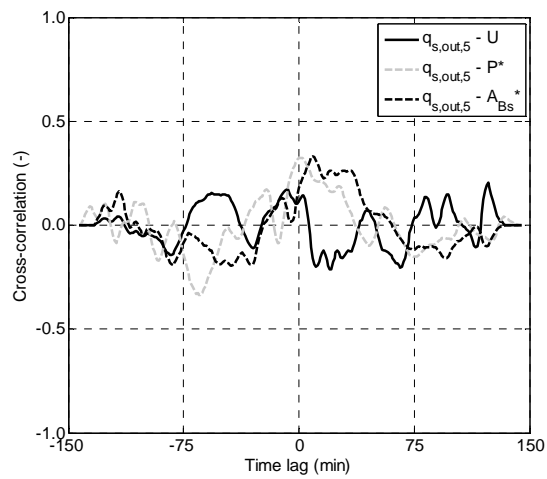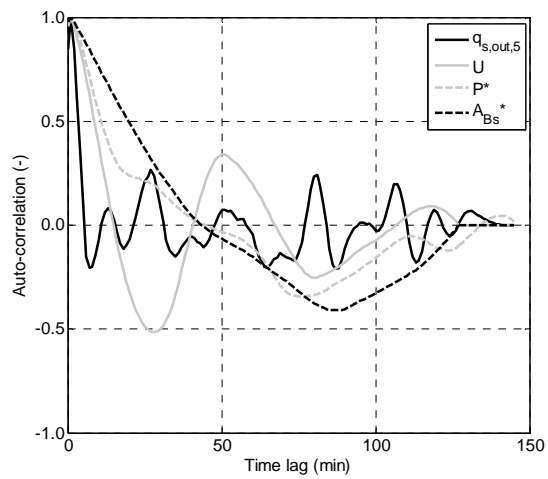
B.6 Test 6

Test parameters

S (%)	λ/D (-)	D (m)	N_{Bs} (m^{-2})	q (m^{3}s^{-1}m^{-1})	$q_{s,in}$ x10^{-3} (m^{3}s^{-1}m^{-1})
6.7	3	0.075	20.0	0.0212	0.0906

Characterization of the fluctuations (average period T=60 min)

	range (min ÷ max)	mean	σ	σ/mean
$q_{s,out,5}$	$0.0151 \div 0.2327$x10^{-3} m^{3}s^{-1}m^{-1}	0.1035x10^{-3} m^{3}s^{-1}m^{-1}	0.0514x10^{-3} m^{3}s^{-1}m^{-1}	0.50
U	$0.59 \div 0.72$ ms^{-1}	0.63 ms^{-1}	0.03 ms^{-1}	0.04
P^*	$0.27 \div 0.50$	0.41	0.06	0.14
$A_{Bs}{}^*$	$0.041 \div 0.112$	0.094	0.014	0.15
HJ^*	-	-	-	-

Average results

$q_{s,end}$ x10^{-3} (m^{3}s^{-1}m^{-1})	$\bar{U}$ (ms^{-1})	$\overline{P_{av}}$ (m)	HJ (m^{-2})	A_i/A_t (-)	A_{if}/A_t (-)	P_{end} (m)	P_{us} (m)	P_{ds} (m)
0.1040	0.63	0.031	-	0.10	0.039	0.022	0.017	0.026

Time series
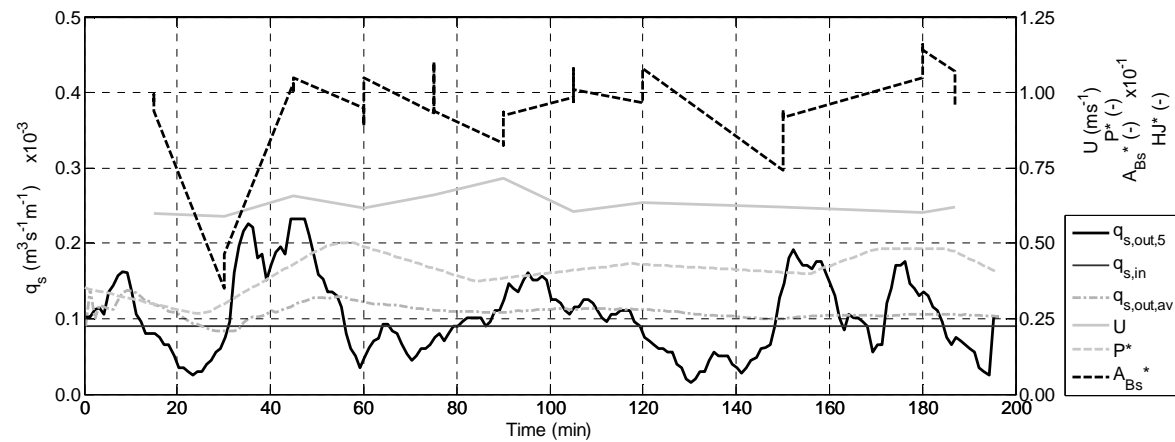
Correlation analysis
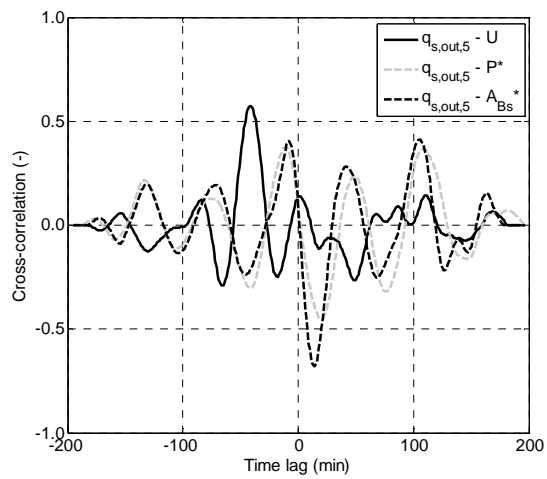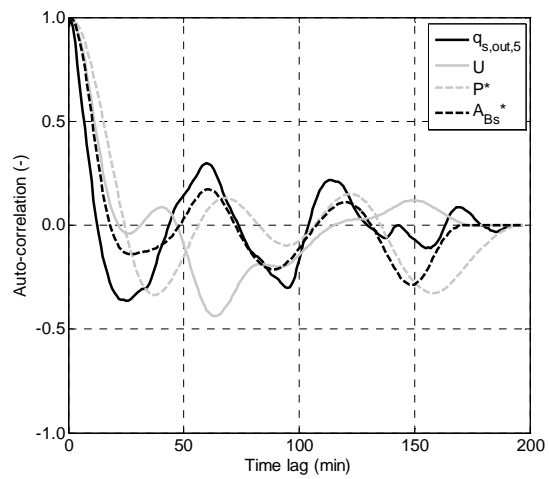
B.7 Test 7

Test parameters

S (%)	λ/D (-)	D (m)	N_{Bs} (m^{-2})	q (m^{3}s^{-1}m^{-1})	$q_{s,in}$ x10^{-3} (m^{3}s^{-1}m^{-1})
6.7	2	0.125	16.0	0.0228	0.0634

Characterization of the fluctuations (average period T=29 min)

	range (min ÷ max)	mean	σ	σ/mean
$q_{s,out,5}$	0 ÷ 0.1560x10^{-3} m^{3}s^{-1}m^{-1}	0.0745x10^{-3} m^{3}s^{-1}m^{-1}	0.0355x10^{-3} m^{3}s^{-1}m^{-1}	0.48
U	0.55 ÷ 0.70 ms^{-1}	0.64 ms^{-1}	0.03 ms^{-1}	0.04
P^*	0.25 ÷ 0.38	0.30	0.03	0.11
A_{Bs}^*	0.175 ÷ 0.249	0.212	0.014	0.06
HJ^*	-	-	-	-

Average results

$q_{s,end}$ x10^{-3} (m^{3}s^{-1}m^{-1})	$\bar{U}$ (ms^{-1})	$\bar{P_{av}}$ (m)	HJ (m^{-2})	A_i/A_t (-)	A_{if}/A_t (-)	P_{end} (m)	P_{us} (m)	P_{ds} (m)
0.0746	0.64	0.037	-	0.19	0.056	0.024	0.020	0.028

Time series
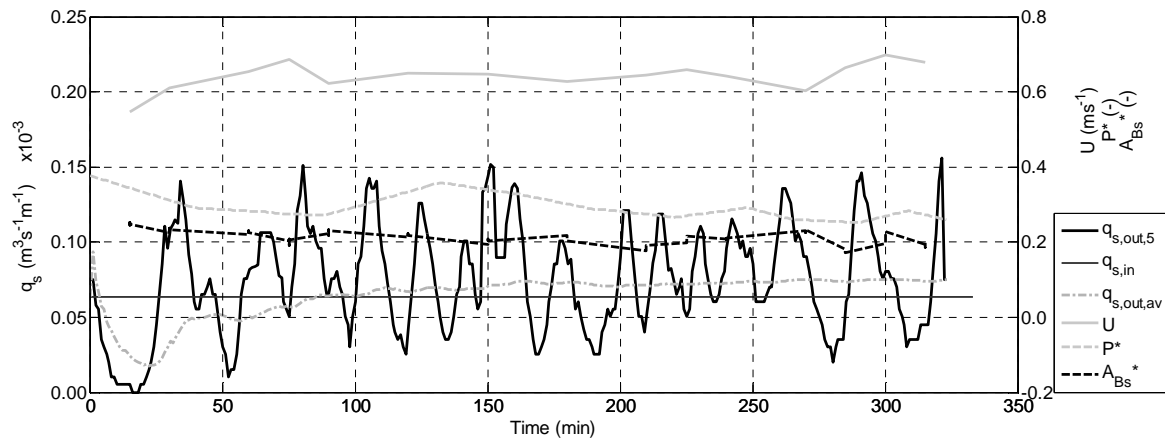
Correlation analysis
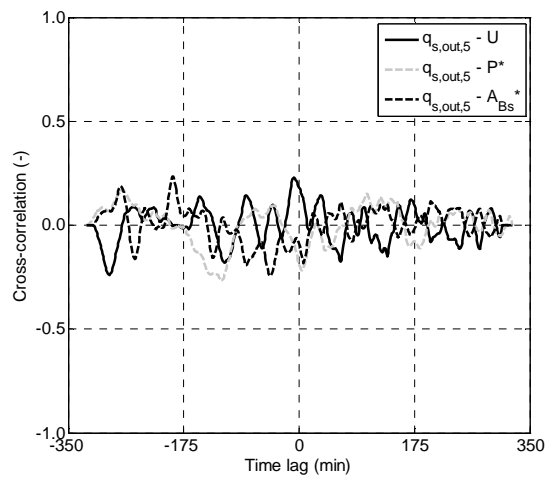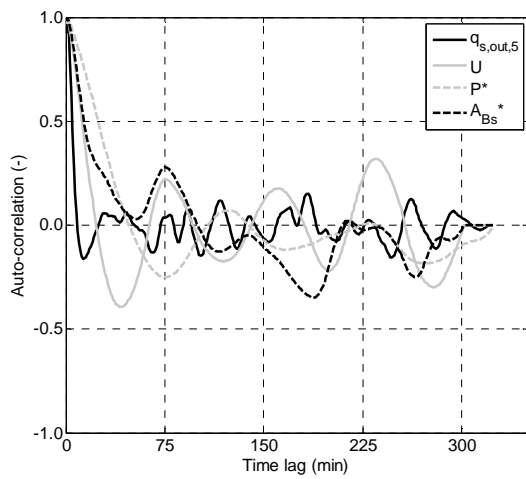
B.8   Test 8

Test parameters

S (%)	λ/D (-)	D (m)	N_{Bs} (m^{-2})	q (m^{3}s^{-1}m^{-1})	$q_{s,in}$ x10^{-3} (m^{3}s^{-1}m^{-1})
6.7	2	0.075	44.6	0.0209	0.0287

Characterization of the fluctuations (average period T=30 min)

	range (min ÷ max)	mean	σ	σ/mean
$q_{s,out,10}$	0.0025 ÷ 0.0528x10^{-3} m^{3}s^{-1}m^{-1}	0.0236x10^{-3} m^{3}s^{-1}m^{-1}	0.0114x10^{-3} m^{3}s^{-1}m^{-1}	0.48
U	0.55 ÷ 0.58 ms^{-1}	0.56 ms^{-1}	0.01 ms^{-1}	0.01
P^*	0.25 ÷ 0.32	0.29	0.02	0.09
A_{Bs}^*	0.186 ÷ 0.233	0.208	0.011	0.06
HJ^*	-	-	-	-

Average results

$q_{s,end}$ x10^{-3} (m^{3}s^{-1}m^{-1})	$\bar{U}$ (ms^{-1})	$\bar{P_{av}}$ (m)	HJ (m^{-2})	A_i/A_t (-)	A_{if}/A_t (-)	P_{end} (m)	P_{us} (m)	P_{ds} (m)
0.0236	0.56	0.022	-	0.19	0.055	0.019	0.016	0.023

Time series
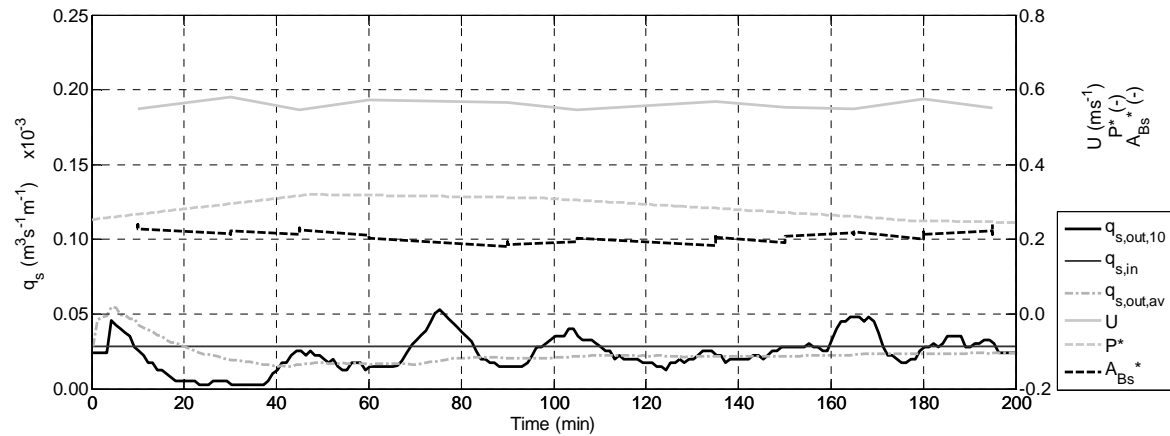
Correlation analysis
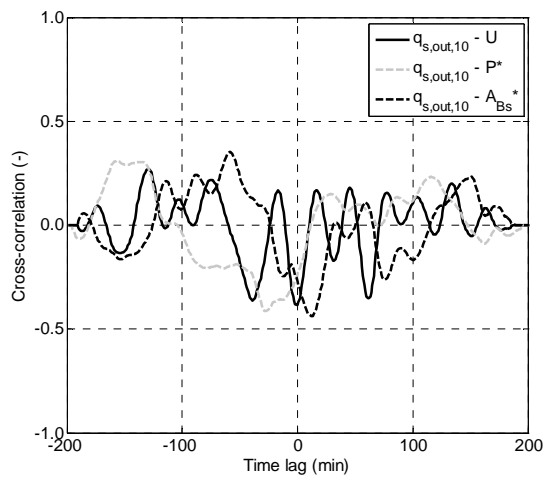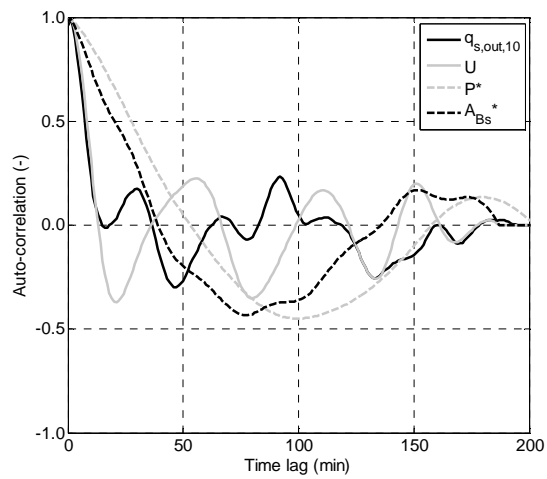
B.9 Test 9

Test parameters

S (%)	λ/D (-)	D (m)	N_{Bs} (m^{-2})	q (m^{3}s^{-1}m^{-1})	$q_{s,in}$ x10^{-3} (m^{3}s^{-1}m^{-1})
6.7	3	0.125	6.9	0.0236	0.1011

Characterization of the fluctuations (average period T=110 min)

	range (min ÷ max)	mean	σ	σ/mean
$q_{s,out,10}$	0.0101 ÷ 0.2189x10^{-3} m^{3}s^{-1}m^{-1}	0.1122x10^{-3} m^{3}s^{-1}m^{-1}	0.0580x10^{-3} m^{3}s^{-1}m^{-1}	0.52
U	0.48 ÷ 0.68 ms^{-1}	0.60 ms^{-1}	0.04 ms^{-1}	0.07
P^{*}	0.23 ÷ 0.43	0.34	0.05	0.15
A_{Bs}^{*}	0.015 ÷ 0.056	0.040	0.009	0.22
HJ^{*}	0.20 ÷ 0.80	0.57	0.16	0.29

Average results

$q_{s,end}$ x10^{-3} (m^{3}s^{-1}m^{-1})	$\bar{U}$ (ms^{-1})	$\bar{P_{av}}$ (m)	HJ (m^{-2})	A_i/A_t (-)	A_{if}/A_t (-)	P_{end} (m)	P_{us} (m)	P_{ds} (m)
0.1122	0.60	0.043	3.9	0.09	0.031	0.048	0.033	0.057

Final configuration
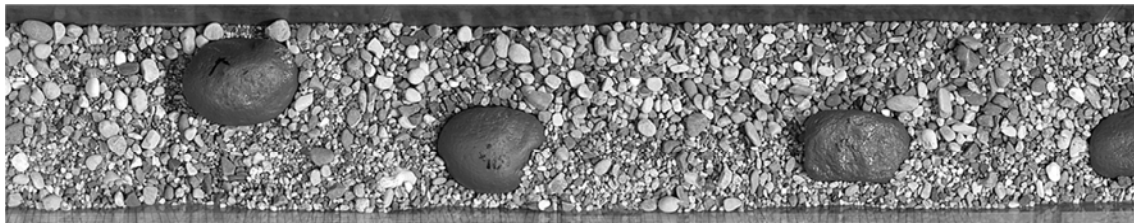
Time series
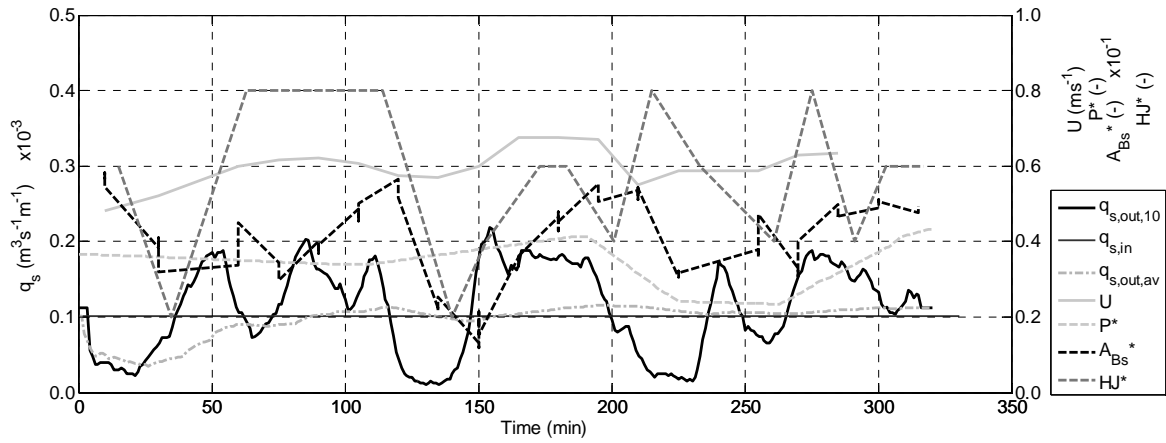
Correlation analysis
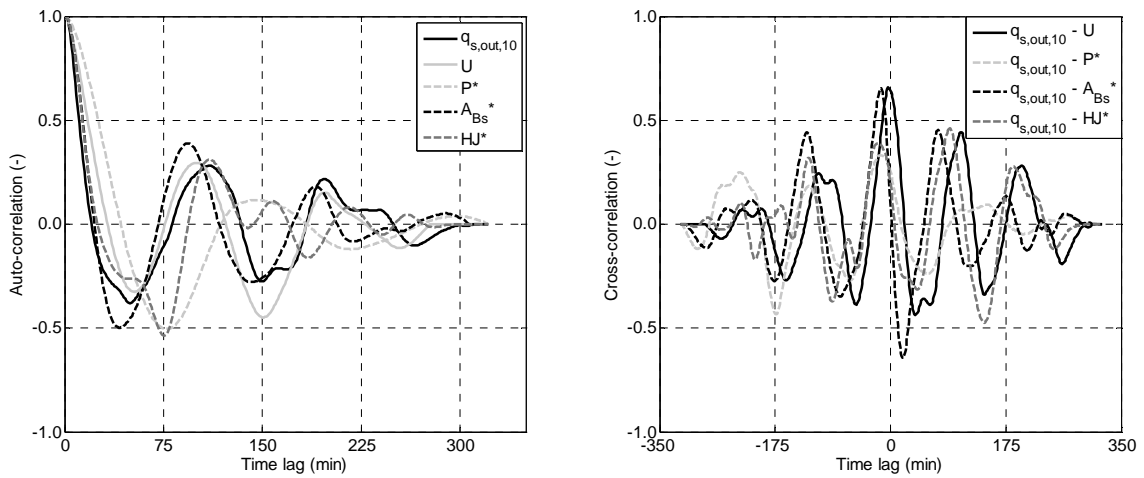
B.10 Test 10

Test parameters

S (%)	λ/D (-)	D (m)	N_{Bs} (m^{-2})	q (m^{3}s^{-1}m^{-1})	$q_{s,in}$ x10^{-3} (m^{3}s^{-1}m^{-1})
6.7	5	0.100	4.0	0.0223	0.1343

Characterization of the fluctuations (average period T=85 min)

	range (min ÷ max)	mean	σ	σ/mean
$q_{s,out,10}$	0.0654 ÷ 0.2088x10^{-3} m^{3}s^{-1}m^{-1}	0.1346x10^{-3} m^{3}s^{-1}m^{-1}	0.0369x10^{-3} m^{3}s^{-1}m^{-1}	0.27
U	0.51 ÷ 0.66 ms^{-1}	0.57 ms^{-1}	0.03 ms^{-1}	0.06
P^*	0.38 ÷ 0.61	0.46	0.06	0.13
A_{Bs}^*	0.015 ÷ 0.027	0.021	0.003	0.16
HJ^*	0.71 ÷ 1.14	0.89	0.10	0.11

Average results

$q_{s,end}$ x10^{-3} (m^{3}s^{-1}m^{-1})	$\bar{U}$ (ms^{-1})	$\bar{P_{av}}$ (m)	HJ (m^{-2})	A_i/A_t (-)	A_{if}/A_t (-)	P_{end} (m)	P_{us} (m)	P_{ds} (m)
0.1346	0.57	0.046	3.6	0.04	0.016	0.047	0.031	0.056

Final configuration

Time series
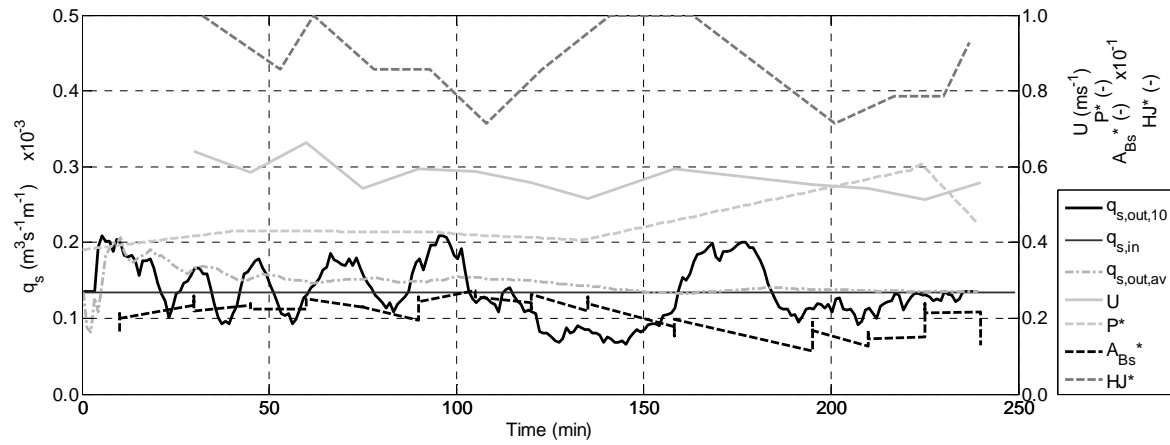
Correlation analysis
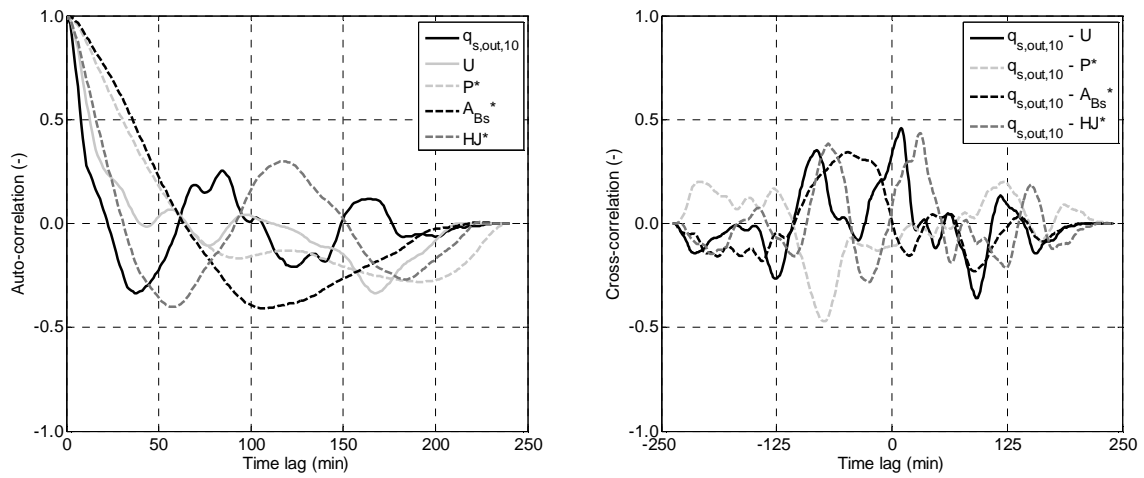
B.11 Test 11

Test parameters

S (%)	λ/D (-)	D (m)	N_{Bs} (m^{-2})	q (m^{3}s^{-1}m^{-1})	$q_{s,in}$ x10^{-3} (m^{3}s^{-1}m^{-1})
6.7	5	0.075	6.9	0.0222	0.1343

Characterization of the fluctuations (average period T=34 min)

	range (min ÷ max)	mean	σ	σ/mean
$q_{s,out,10}$	0.0277 ÷ 0.2289x10^{-3} m^{3}s^{-1}m^{-1}	0.1308x10^{-3} m^{3}s^{-1}m^{-1}	0.0477x10^{-3} m^{3}s^{-1}m^{-1}	0.36
U	0.52 ÷ 0.63 ms^{-1}	0.58 ms^{-1}	0.03 ms^{-1}	0.05
P^*	0.27 ÷ 0.60	0.39	0.06	0.16
A_{Bs}^*	0.018 ÷ 0.035	0.028	0.004	0.15
HJ^*	0.33 ÷ 0.83	0.55	0.12	0.22

Average results

$q_{s,end}$ x10^{-3} (m^{3}s^{-1}m^{-1})	$\bar{U}$ (ms^{-1})	$\bar{P_{av}}$ (m)	HJ (m^{-2})	A_i/A_t (-)	A_{if}/A_t (-)	P_{end} (m)	P_{us} (m)	P_{ds} (m)
0.1307	0.58	0.029	3.8	0.03	0.013	0.034	0.029	0.041

Final configuration

Time series
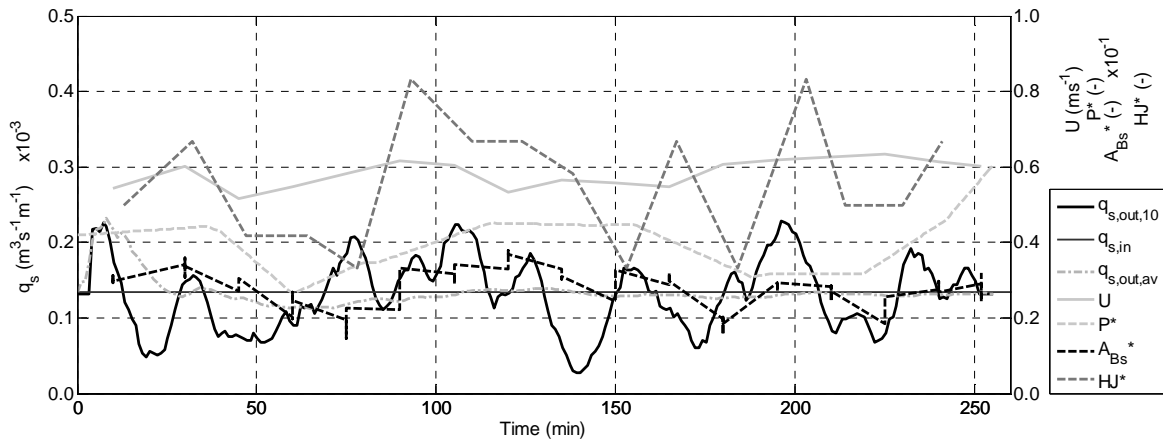
Correlation analysis
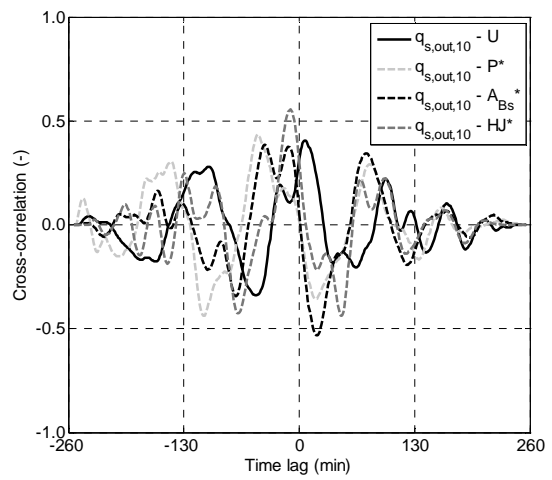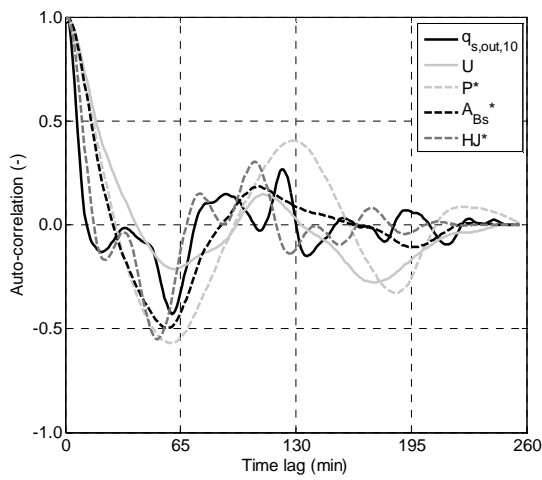
B.12 Test 12

Test parameters

S (%)	λ/D (-)	D (m)	N_{Bs} (m^{-2})	q (m^{3}s^{-1}m^{-1})	$q_{s,in}$ x10^{-3} (m^{3}s^{-1}m^{-1})
6.7	5	0.125	2.3	0.0208	0.1343

Characterization of the fluctuations (average period T=84 min)

	range (min ÷ max)	mean	σ	σ/mean
$q_{s,out,10}$	0.0201 ÷ 0.3321x10^{-3} m^{3}s^{-1}m^{-1}	0.1338x10^{-3} m^{3}s^{-1}m^{-1}	0.0642x10^{-3} m^{3}s^{-1}m^{-1}	0.48
U	0.51 ÷ 0.65 ms^{-1}	0.62 ms^{-1}	0.04 ms^{-1}	0.06
P^*	0.32 ÷ 0.55	0.47	0.06	0.14
A_{Bs}^*	0.015 ÷ 0.030	0.028	0.004	0.15
HJ^*	0.25 ÷ 1.25	0.74	0.23	0.31

Average results

$q_{s,end}$ x10^{-3} (m^{3}s^{-1}m^{-1})	$\bar{U}$ (ms^{-1})	$\bar{P_{av}}$ (m)	HJ (m^{-2})	A_i/A_t (-)	A_{if}/A_t (-)	P_{end} (m)	P_{us} (m)	P_{ds} (m)
0.1503	0.63	0.061	1.7	0.04	0.018	0.056	0.044	0.061

Final configuration

Time series
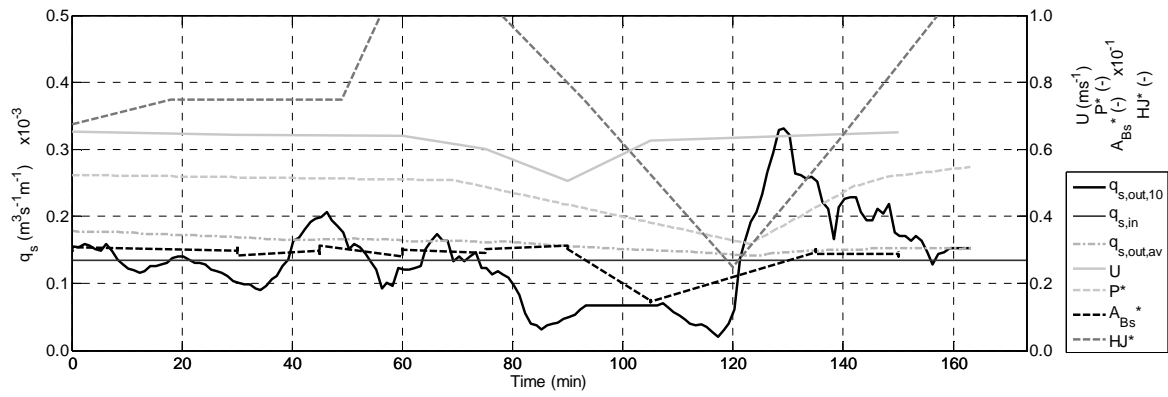
Correlation analysis
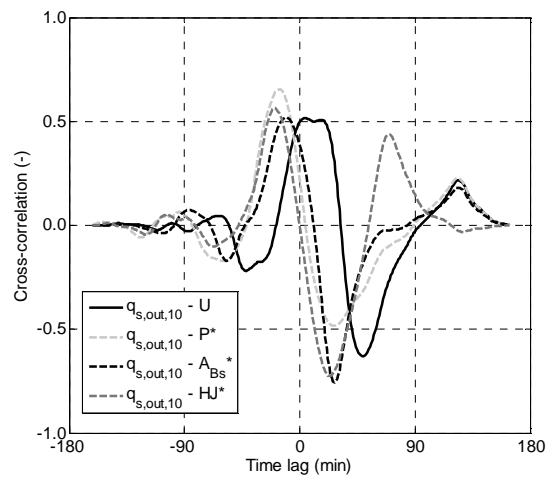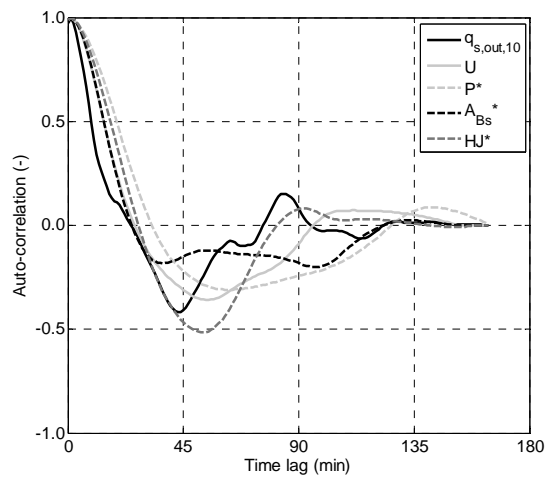
B.13 Test 13

Test parameters

S (%)	λ/D (-)	D (m)	N_{Bs} (m^{-2})	q (m^{3}s^{-1}m^{-1})	$q_{s,in}$ x10^{-3} (m^{3}s^{-1}m^{-1})
6.7	3	0.075	20.0	0.0238	0.1343

Characterization of the fluctuations (average period T=23 min)

	range (min ÷ max)	mean	σ	σ/mean
$q_{s,out,5}$	0.0503 ÷ 0.2767x10^{-3} m^{3}s^{-1}m^{-1}	0.1421x10^{-3} m^{3}s^{-1}m^{-1}	0.0447x10^{-3} m^{3}s^{-1}m^{-1}	0.31
U	0.66 ÷ 0.75 ms^{-1}	0.70 ms^{-1}	0.02 ms^{-1}	0.03
P^*	0.33 ÷ 0.52	0.44	0.05	0.11
A_{Bs}^*	0.085 ÷ 0.099	0.091	0.004	0.04
HJ^*	0.38 ÷ 0.75	0.61	0.11	0.18

Average results

$q_{s,end}$ x10^{-3} (m^{3}s^{-1}m^{-1})	$\bar{U}$ (ms^{-1})	$\overline{P_{av}}$ (m)	HJ (m^{-2})	A_i/A_t (-)	A_{if}/A_t (-)	P_{end} (m)	P_{us} (m)	P_{ds} (m)
0.1401	0.70	0.033	12.2	0.10	0.043	0.029	0.022	0.034

Final configuration

Time series
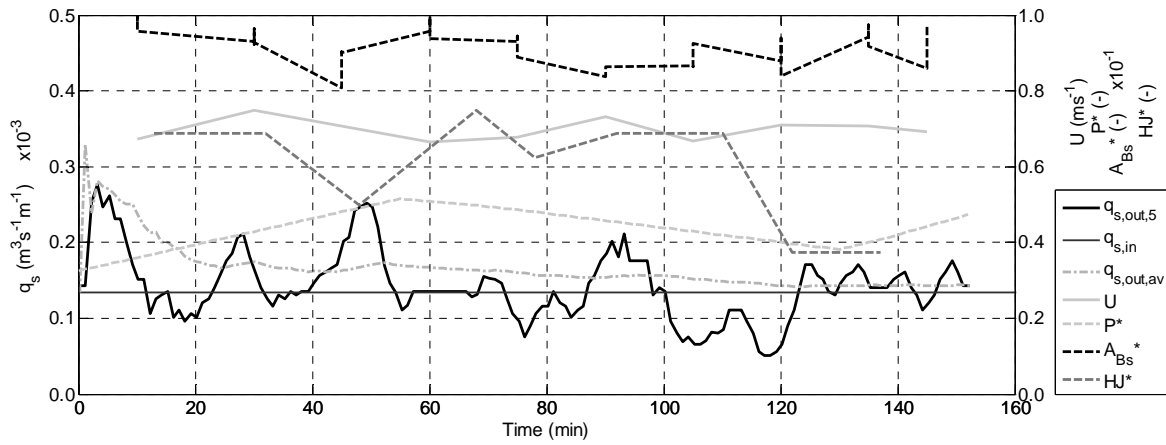
Correlation analysis
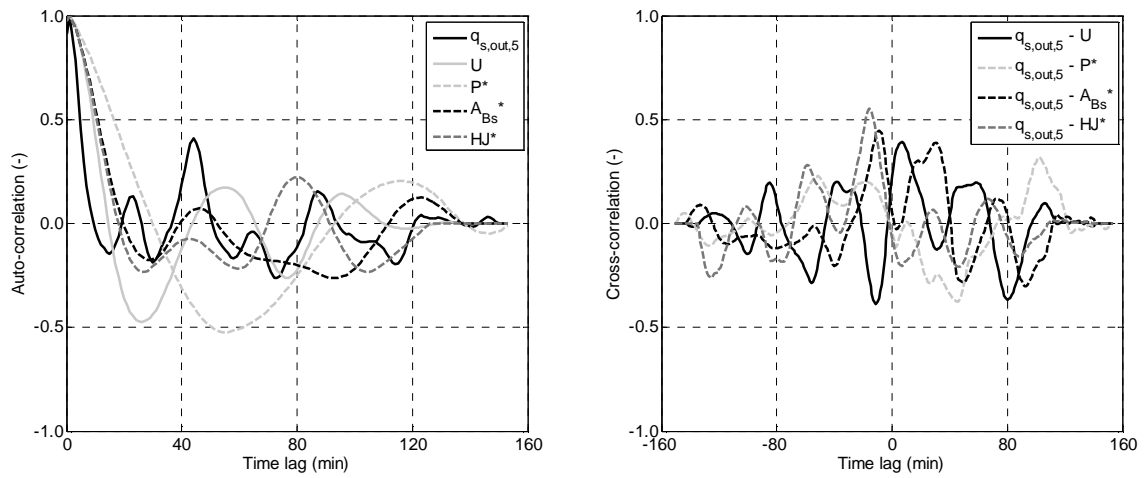
B.14 Test 14

Test parameters

S (%)	λ/D (-)	D (m)	N_{Bs} (m^{-2})	q (m^{3}s^{-1}m^{-1})	$q_{s,in}$ x10^{-3} (m^{3}s^{-1}m^{-1})
6.7	3	0.125	6.9	0.0235	0.1343

Characterization of the fluctuations (average period T=23 min)

	range (min ÷ max)	mean	σ	σ/mean
$q_{s,out,10}$	0.0327 ÷ 0.2013x10^{-3} m^{3}s^{-1}m^{-1}	0.1192x10^{-3} m^{3}s^{-1}m^{-1}	0.0361x10^{-3} m^{3}s^{-1}m^{-1}	0.30
U	0.53 ÷ 0.67 ms^{-1}	0.60 ms^{-1}	0.03 ms^{-1}	0.05
P^*	0.36 ÷ 0.52	0.43	0.04	0.09
A_{Bs}^*	0.068 ÷ 0.079	0.074	0.003	0.04
HJ^*	0.40 ÷ 1.00	0.70	0.18	0.25

Average results

$q_{s,end}$ x10^{-3} (m^{3}s^{-1}m^{-1})	$\bar{U}$ (ms^{-1})	$\bar{P_{av}}$ (m)	HJ (m^{-2})	A_i/A_t (-)	A_{if}/A_t (-)	P_{end} (m)	P_{us} (m)	P_{ds} (m)
0.1192	0.60	0.054	4.8	0.10	0.042	0.043	0.029	0.050

Final configuration

Time series
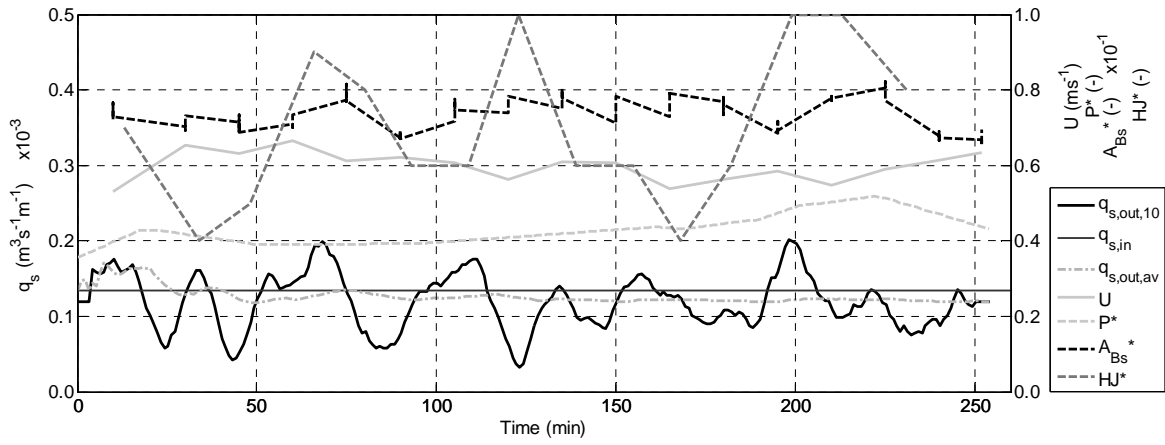
Correlation analysis
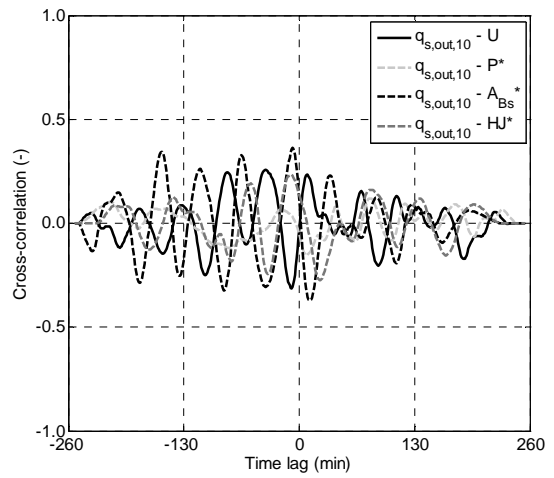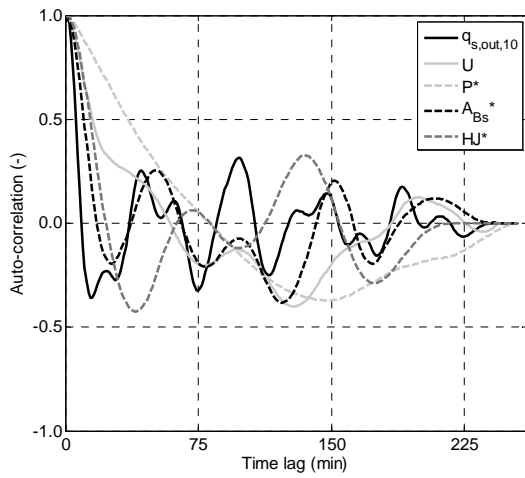
B.15 Test 15

Test parameters

S (%)	λ/D (-)	D (m)	N_{Bs} (m^{-2})	q (m^{3}s^{-1}m^{-1})	$q_{s,in}$ x10^{-3} (m^{3}s^{-1}m^{-1})
6.7	3	0.100	10.9	0.0233	0.1343

Characterization of the fluctuations (average period T=21 min)

	range (min ÷ max)	mean	σ	σ/mean
$q_{s,out,5}$	0.0151 ÷ 0.2566x10^{-3} m^{3}s^{-1}m^{-1}	0.1251x10^{-3} m^{3}s^{-1}m^{-1}	0.0455x10^{-3} m^{3}s^{-1}m^{-1}	0.36
U	0.48 ÷ 0.59 ms^{-1}	0.55 ms^{-1}	0.03 ms^{-1}	0.05
P^*	0.23 ÷ 0.40	0.31	0.05	0.17
$A_{Bs}{}^*$	0.087 ÷ 0.105	0.094	0.004	0.05
HJ^*	0.45 ÷ 0.90	0.74	0.10	0.14

Average results

$q_{s,end}$ x10^{-3} (m^{3}s^{-1}m^{-1})	$\bar{U}$ (ms^{-1})	$\bar{P_{av}}$ (m)	HJ (m^{-2})	A_i/A_t (-)	A_{if}/A_t (-)	P_{end} (m)	P_{us} (m)	P_{ds} (m)
0.1244	0.55	0.031	8.0	0.09	0.027	0.035	0.025	0.044

Final configuration

Time series
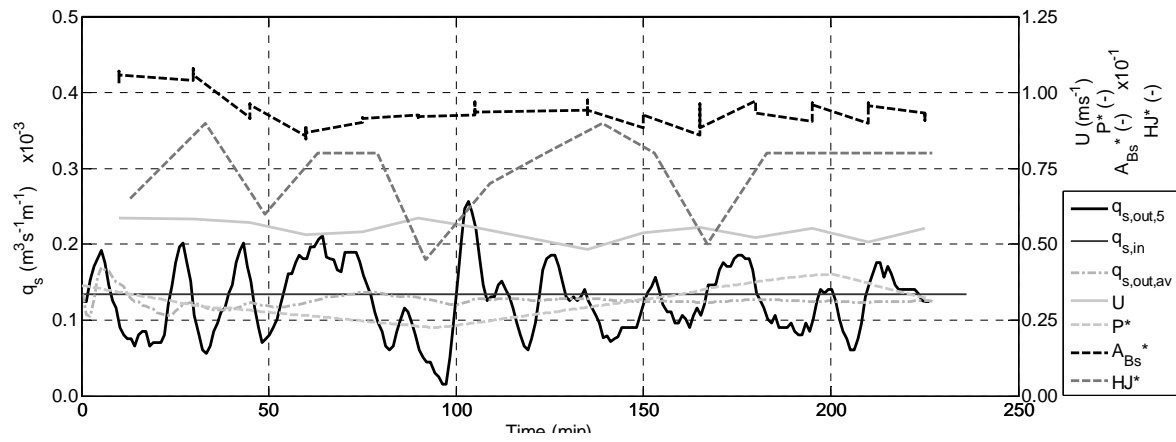
Correlation analysis
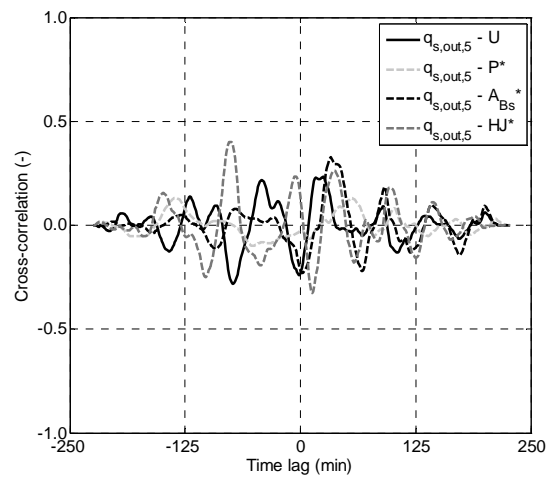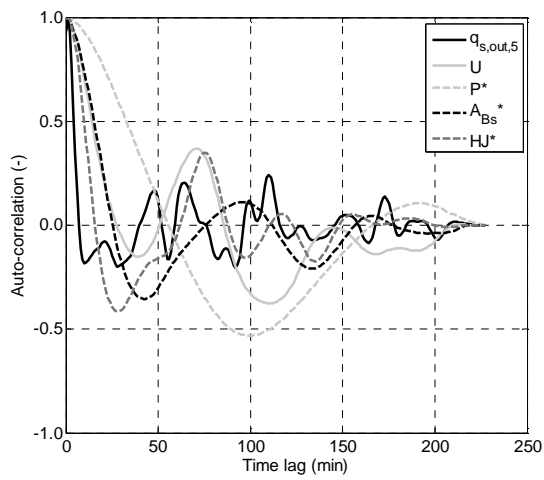
B.16 Test 16

Test parameters

S (%)	λ/D (-)	D (m)	N_{Bs} (m^{-2})	q (m^{3}s^{-1}m^{-1})	$q_{s,in}$ x10^{-3} (m^{3}s^{-1}m^{-1})
6.7	Inf.	0.000	0.0	0.0162	0.1343

Characterization of the fluctuations (average period T=50.8 min)

	range (min ÷ max)	mean	σ	σ/mean
$q_{s,out,5}$	0.0151 ÷ 0.2748x10^{-3} m^{3}s^{-1}m^{-1}	0.1187x10^{-3} m^{3}s^{-1}m^{-1}	0.0539x10^{-3} m^{3}s^{-1}m^{-1}	0.45
U	0.43 ÷ 0.55 ms^{-1}	0.49 ms^{-1}	0.02 ms^{-1}	0.05
P^*	-	-	-	-
$A_{Bs}{}^*$	-	-	-	-
HJ^*	-	-	-	-

Average results

$q_{s,end}$ x10^{-3} (m^{3}s^{-1}m^{-1})	$\bar{U}$ (ms^{-1})	$\bar{P_{av}}$ (m)	HJ (m^{-2})	A_i/A_t (-)	A_{if}/A_t (-)	P_{end} (m)	P_{us} (m)	P_{ds} (m)
0.1189	0.49	0.000	0.0	0.00	0.000	0.000	0.000	0.000

Final configuration

Time series
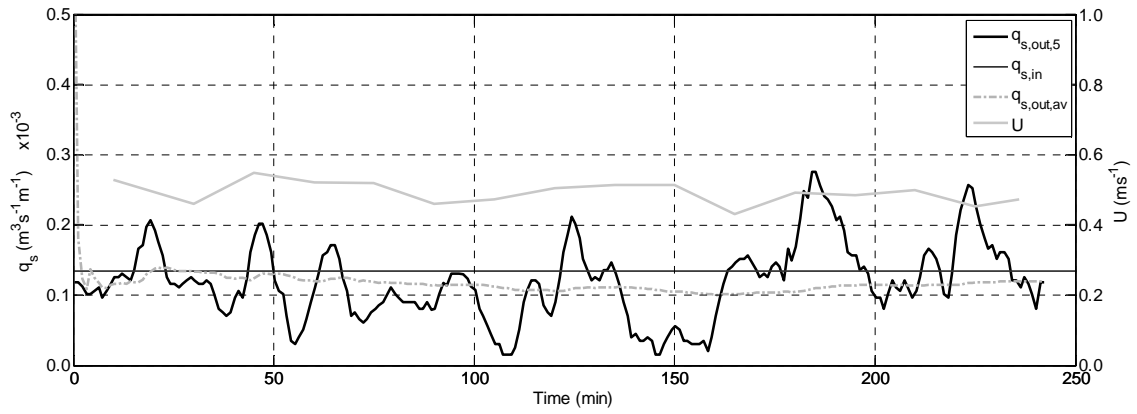
Correlation analysis
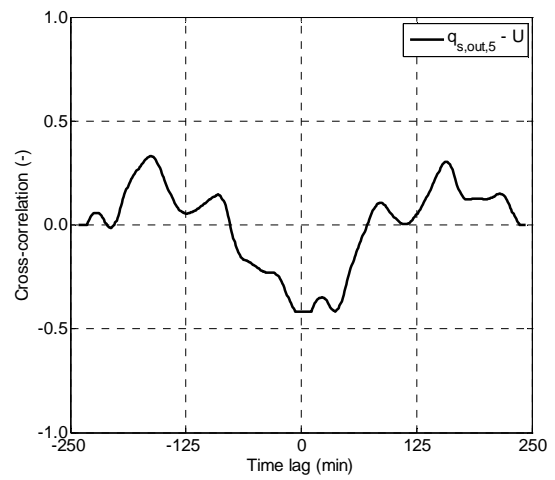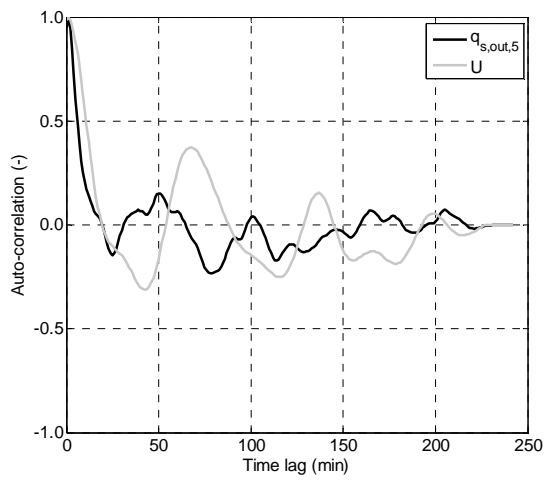
B.17 Test 17

Test parameters

S (%)	λ/D (-)	D (m)	N_{Bs} (m^{-2})	q (m^{3}s^{-1}m^{-1})	$q_{s,in}$ x10^{-3} (m^{3}s^{-1}m^{-1})
6.7	2	0.100	25.1	0.0372	0.1343

Characterization of the fluctuations (average period T=9 min)

	range (min ÷ max)	mean	σ	σ/mean
$q_{s,out,3}$	0.0587 ÷ 0.2013x10^{-3} m^{3}s^{-1}m^{-1}	0.1398 x10^{-3} m^{3}s^{-1}m^{-1}	0.0334x10^{-3} m^{3}s^{-1}m^{-1}	0.24
U	0.67 ÷ 0.75 ms^{-1}	0.70 ms^{-1}	0.02 ms^{-1}	0.02
P^*	0.23 ÷ 0.35	0.29	0.03	0.10
A_{Bs}^*	0.178 ÷ 0.193	0.185	0.003	0.02
HJ^*	0.37 ÷ 0.68	0.56	0.07	0.13

Average results

$q_{s,end}$ x10^{-3} (m^{3}s^{-1}m^{-1})	$\bar{U}$ (ms^{-1})	$\bar{P_{av}}$ (m)	HJ (m^{-2})	A_i/A_t (-)	A_{if}/A_t (-)	P_{end} (m)	P_{us} (m)	P_{ds} (m)
0.1390	0.70	0.029	14.1	0.19	0.055	0.036	0.027	0.041

Final configuration

Time series
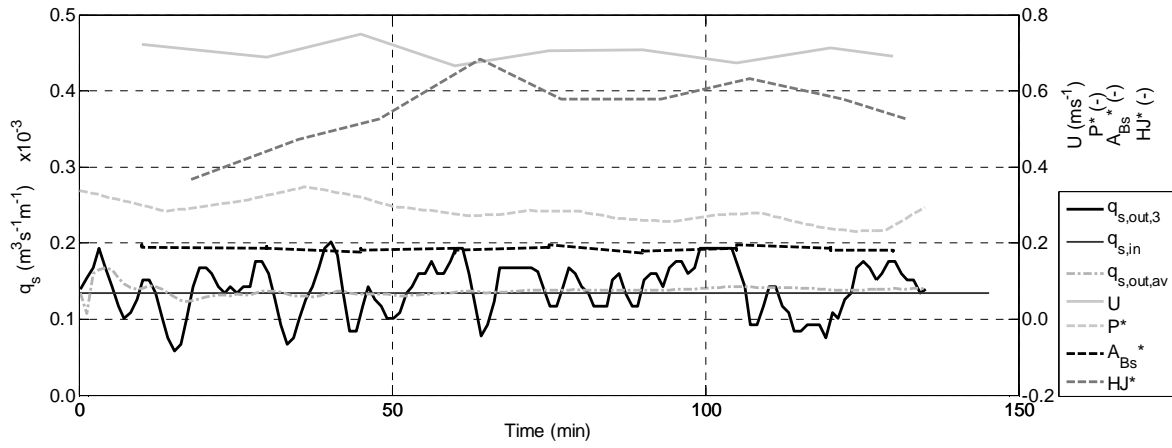
Correlation analysis
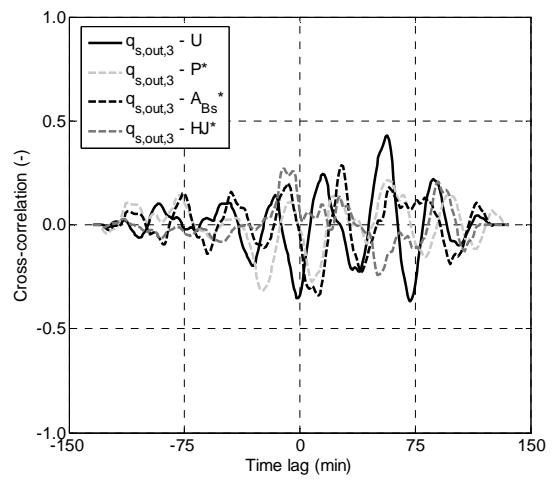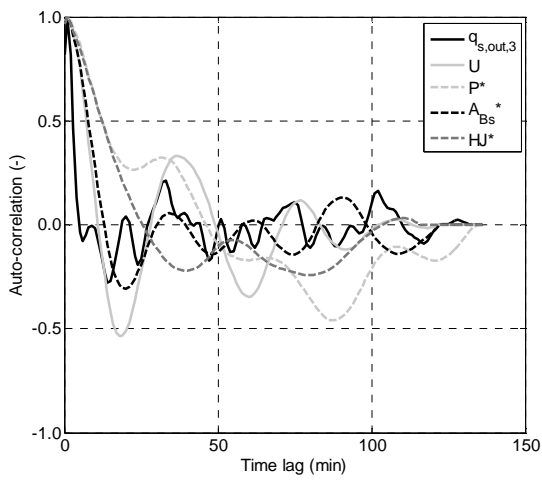
B.18 Test 18

Test parameters

S (%)	λ/D (-)	D (m)	N_{Bs} (m^{-2})	q (m^{3}s^{-1}m^{-1})	$q_{s,in}$ x10^{-3} (m^{3}s^{-1}m^{-1})
6.7	2	0.125	16.0	0.0352	0.1343

Characterization of the fluctuations (average period T=14 min)

	range (min ÷ max)	mean	σ	σ/mean
$q_{s,out,3}$	0.0587 ÷0.2117x10^{-3} m^{3}s^{-1}m^{-1}	0.1352x10^{-3} m^{3}s^{-1}m^{-1}	0.0342x10^{-3} m^{3}s^{-1}m^{-1}	0.25
U	0.63 ÷0.74 ms^{-1}	0.70 ms^{-1}	0.04 ms^{-1}	0.06
P^*	0.27 ÷0.38	0.32	0.03	0.08
A_{Bs}^*	0.212 ÷0.230	0.222	0.005	0.02
HJ^*	0.75 ÷0.91	0.84	0.04	0.04

Average results

$q_{s,end}$ x10^{-3} (m^{3}s^{-1}m^{-1})	$\bar{U}$ (ms^{-1})	$\bar{P_{av}}$ (m)	HJ (m^{-2})	A_i/A_t (-)	A_{if}/A_t (-)	P_{end} (m)	P_{us} (m)	P_{ds} (m)
0.1365	0.70	0.040	13.5	0.20	0.063	0.038	0.030	0.045

Final configuration
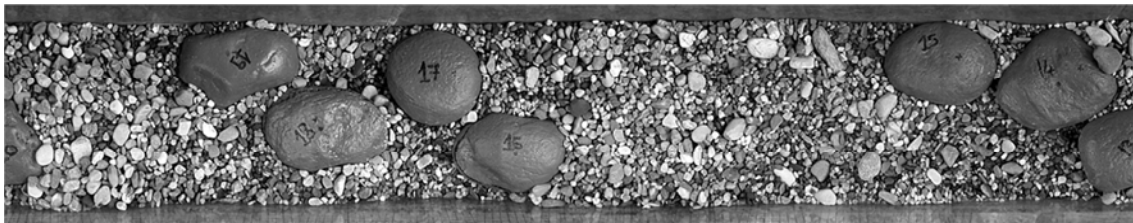
Time series
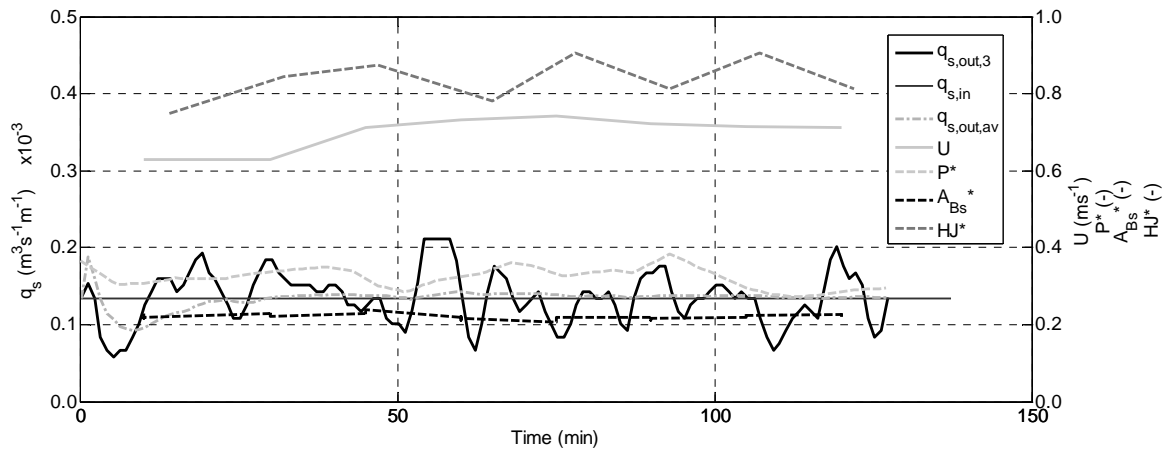
Correlation analysis
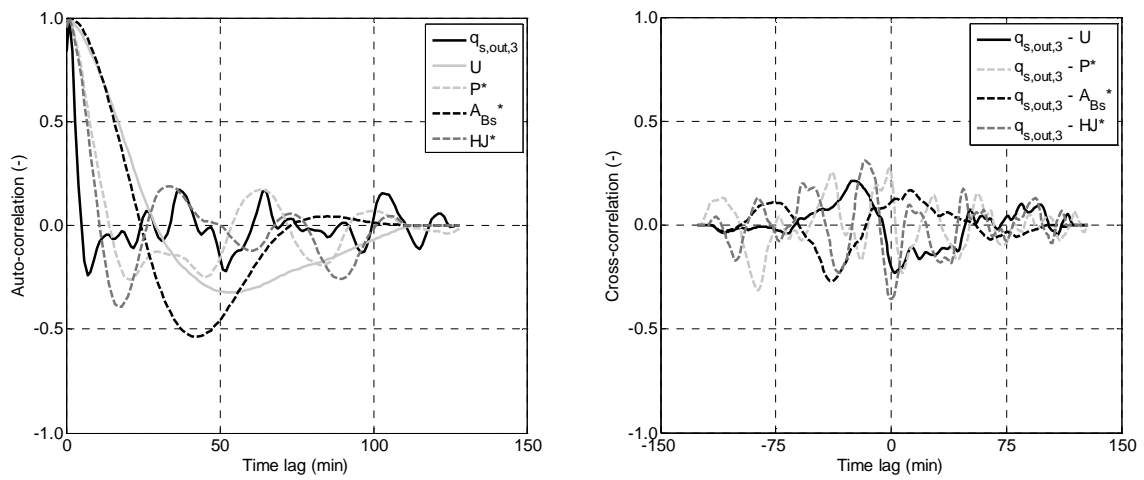
B.19 Test 19

Test parameters

S (%)	λ/D (-)	D (m)	N_{Bs} (m^{-2})	q (m^{3}s^{-1}m^{-1})	$q_{s,in}$ x10^{-3} (m^{3}s^{-1}m^{-1})
6.7	2	0.075	44.6	0.0391	0.1343

Characterization of the fluctuations (average period T=10 min)

	range (min ÷ max)	mean	σ	σ/mean
$q_{s,out,3}$	$0.0922 \div 0.2432$x10^{-3} m^{3}s$^-$	0.1470x10^{-3} m^{3}s^{-1}m^{-1}	0.0346x10^{-3} m^{3}s^{-1}m^{-1}	0.24
U	$0.74 \div 0.81$ ms^{-1}	0.77 ms^{-1}	0.02 ms^{-1}	0.03
P^*	$0.30 \div 0.40$	0.36	0.02	0.06
A_{Bs}^*	$0.251 \div 0.299$	0.280	0.011	0.04
HJ^*	$0.33 \div 0.58$	0.49	0.06	0.13

Average results

$q_{s,end}$ x10^{-3} (m^{3}s^{-1}m^{-1})	$\bar{U}$ (ms^{-1})	$\bar{P_{av}}$ (m)	HJ (m^{-2})	A_i/A_t (-)	A_{if}/A_t (-)	P_{end} (m)	P_{us} (m)	P_{ds} (m)
0.1461	0.77	0.027	21.8	0.21	0.074	0.035	0.030	0.038

Final configuration
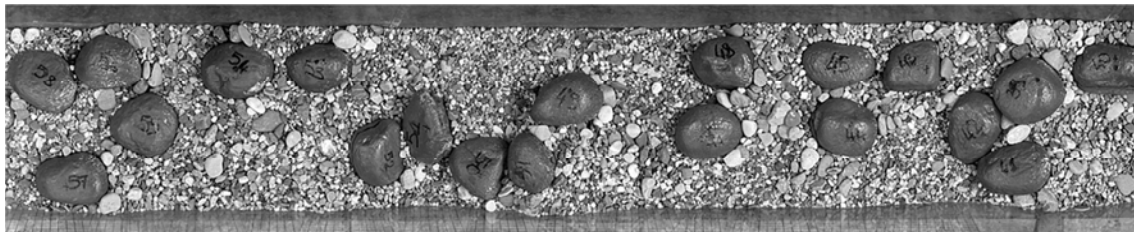
Time series
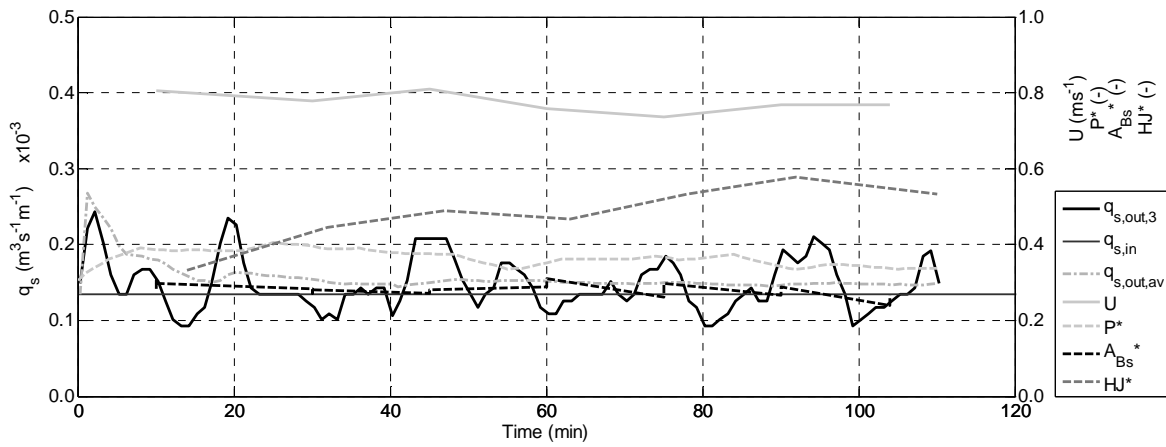
Correlation analysis
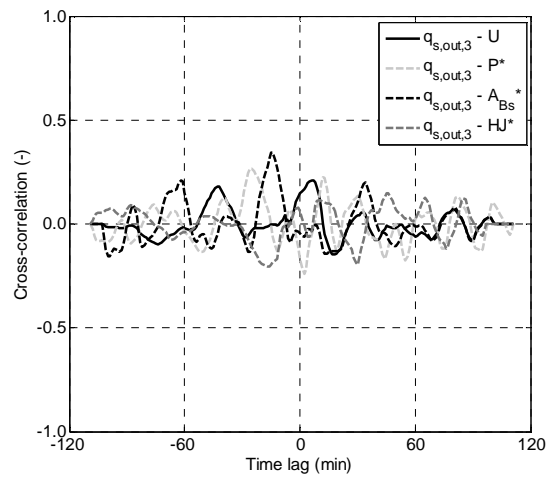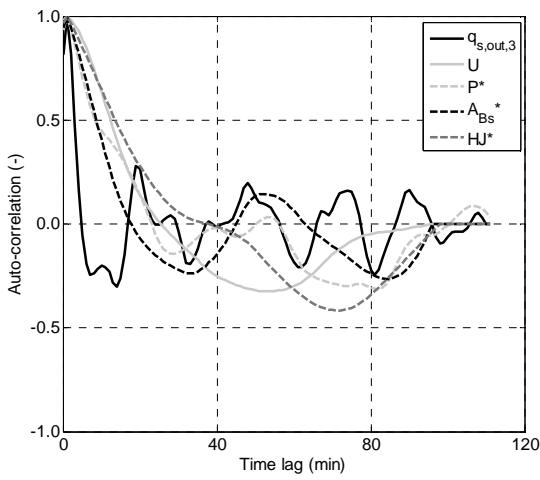
B.20 Test 20

Test parameters

S (%)	λ/D (-)	D (m)	N_{Bs} (m^{-2})	q (m^{3}s^{-1}m^{-1})	$q_{s,in}$ x10^{-3} (m^{3}s^{-1}m^{-1})
6.7	3	0.100	10.9	0.0177	0.0563

Characterization of the fluctuations (average period T=56 min)

	range (min ÷ max)	mean	σ	σ/mean
$q_{s,out,5}$	0.0050 ÷ 0.2365x10^{-3} m^{3}s$^-$	0.0608x10^{-3} m^{3}s^{-1}m^{-1}	0.0454x10^{-3} m^{3}s^{-1}m^{-1}	0.75
U	0.35 ÷ 0.59 ms^{-1}	0.49 ms^{-1}	0.05 ms^{-1}	0.10
P^*	0.01 ÷ 0.36	0.24	0.08	0.32
A_{Bs}^*	0.025 ÷ 0.074	0.050	0.014	0.28
HJ^*	0.10 ÷ 0.80	0.41	0.17	0.42

Average results

$q_{s,end}$ x10^{-3} (m^{3}s^{-1}m^{-1})	$\bar{U}$ (ms^{-1})	$\bar{P_{av}}$ (m)	HJ (m^{-2})	A_i/A_t (-)	A_{if}/A_t (-)	P_{end} (m)	P_{us} (m)	P_{ds} (m)
0.0607	0.49	0.024	4.4	0.07	0.019	0.028	0.021	0.032

Final configuration

Time series
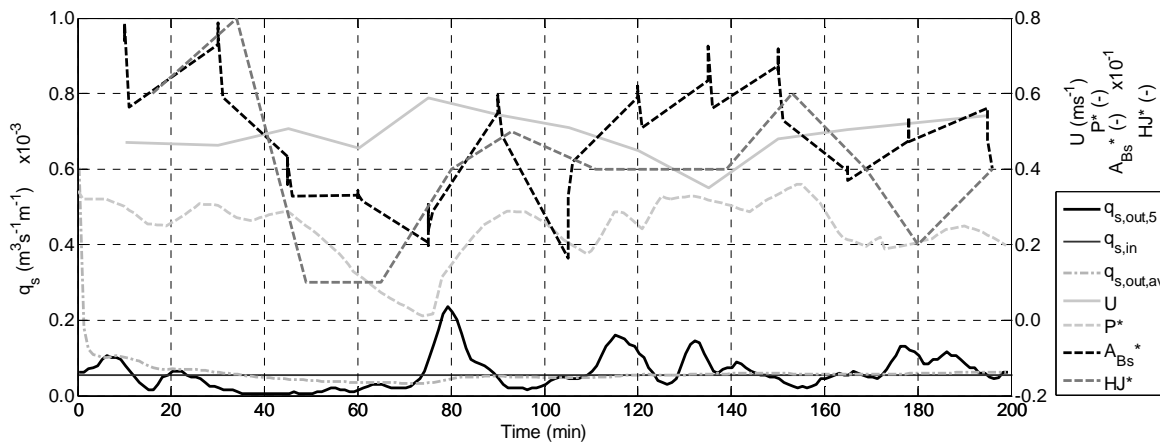
Correlation analysis
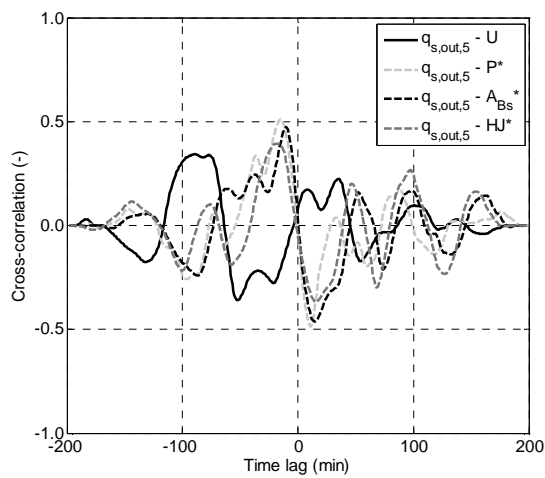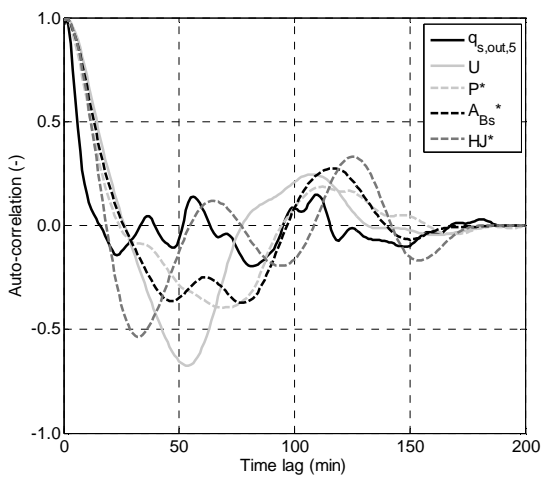
B.21 Test 21

Test parameters

S (%)	λ/D (-)	D (m)	N_{Bs} (m^{-2})	q (m^{3}s^{-1}m^{-1})	$q_{s,in}$ x10^{-3} (m^{3}s^{-1}m^{-1})
6.7	5	0.100	4.0	0.0162	0.0563

Characterization of the fluctuations (average period T=65 min)

	range (min ÷ max)	mean	σ	σ/mean
$q_{s,out,10}$	0.0050 ÷ 0.1535x10^{-3} m^{3}s^{-1}m^{-1}	0.0564x10^{-3} m^{3}s^{-1}m^{-1}	0.0325x10^{-3} m^{3}s^{-1}m^{-1}	0.58
U	0.35 ÷ 0.50 ms^{-1}	0.42 ms^{-1}	0.04 ms^{-1}	0.09
P^*	0.07 ÷ 0.52	0.31	0.12	0.40
A_{Bs}^*	0 ÷ 0.018	0.012	0.005	0.40
HJ^*	0.29 ÷ 1.00	0.69	0.18	0.27

Average results

$q_{s,end}$ x10^{-3} (m^{3}s^{-1}m^{-1})	$\bar{U}$ (ms^{-1})	$\bar{P_{av}}$ (m)	HJ (m^{-2})	A_i/A_t (-)	A_{if}/A_t (-)	P_{end} (m)	P_{us} (m)	P_{ds} (m)
0.0565	0.42	0.031	2.7	0.03	0.010	0.028	0.019	0.029

Final configuration

Time series
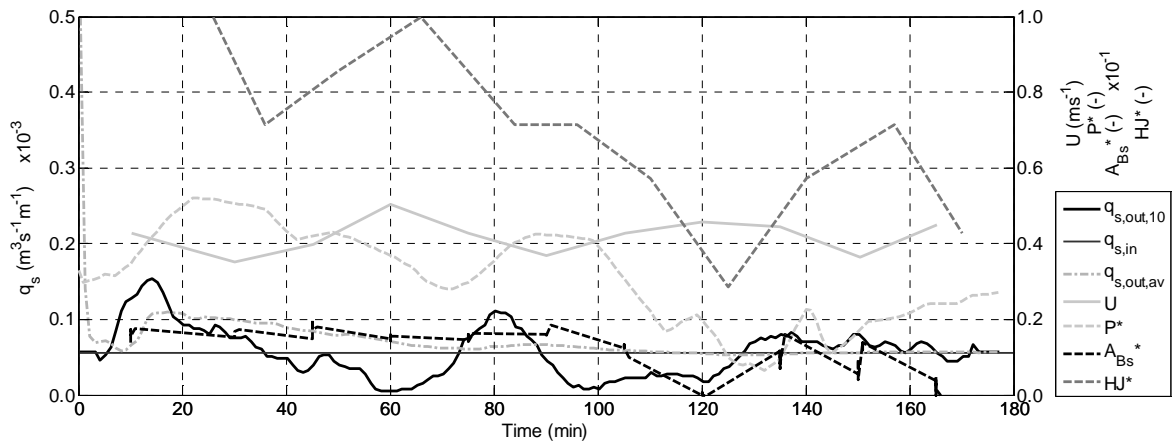
Correlation analysis
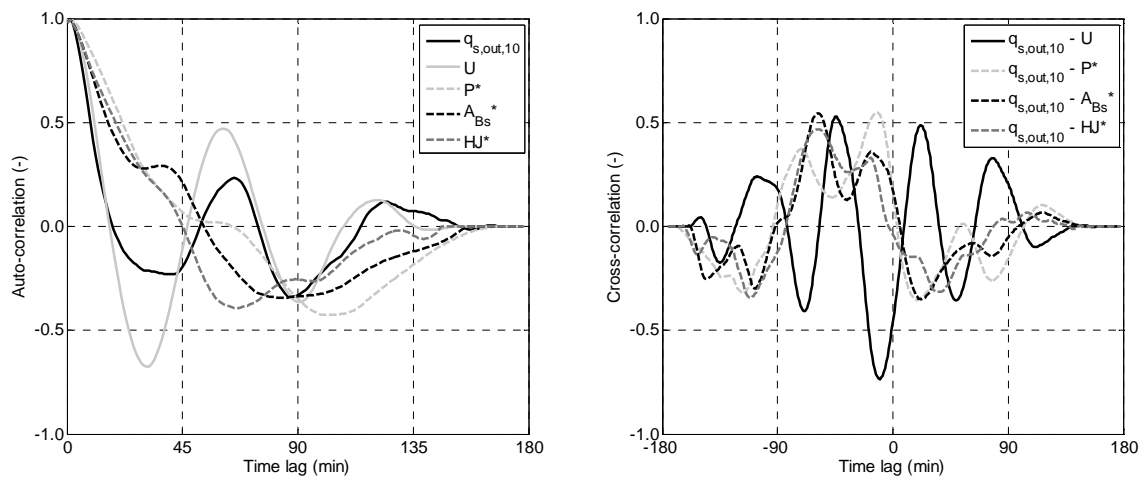
B.22 Test 22

Test parameters

S (%)	λ/D (-)	D (m)	N_{Bs} (m^{-2})	q (m^{3}s^{-1}m^{-1})	$q_{s,in}$ x10^{-3} (m^{3}s^{-1}m^{-1})
6.7	0	0.000	0.0	0.0148	0.0563

Characterization of the fluctuations (average period T=155 min)

	range (min ÷ max)	mean	σ	σ/mean
$q_{s,out,10}$	0 ÷ 0.1887x10^{-3} m^{3}s^{-1}m^{-1}	0.0654 x10^{-3} m^{3}s^{-1}m^{-1}	0.0588x10^{-3} m^{3}s^{-1}m^{-1}	0.90
U	0.22 ÷ 0.49 ms^{-1}	0.35 ms^{-1}	0.09 ms^{-1}	0.25
P^*	-	-	-	-
$A_{Bs}{}^*$	-	-	-	-
HJ^*	-	-	-	-

Average results

$q_{s,end}$ x10^{-3} (m^{3}s^{-1}m^{-1})	$\bar{U}$ (ms^{-1})	$\bar{P_{av}}$ (m)	HJ (m^{-2})	A_i/A_t (-)	A_{if}/A_t (-)	P_{end} (m)	P_{us} (m)	P_{ds} (m)
0.0654	0.35	0.000	0.0	0.00	0.000	0.000	0.000	0.000

Final configuration

Time series
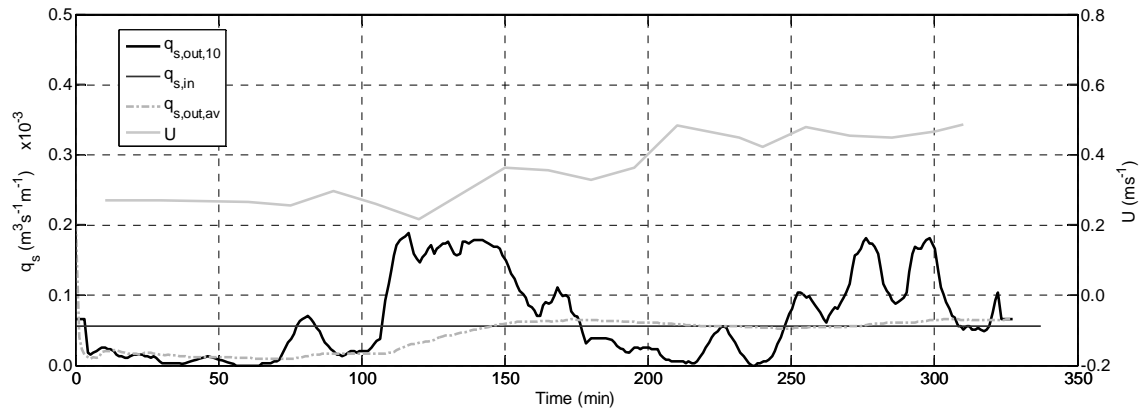
Correlation analysis
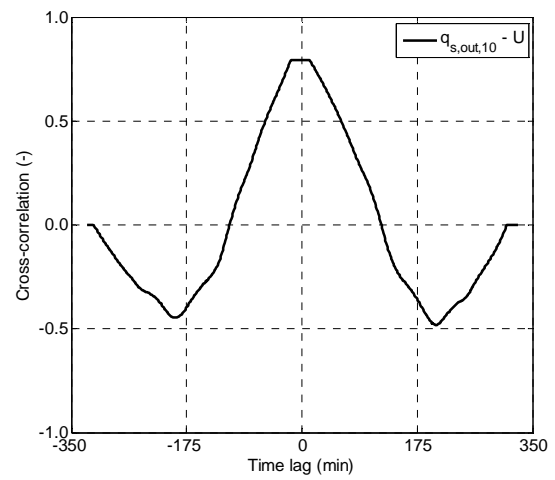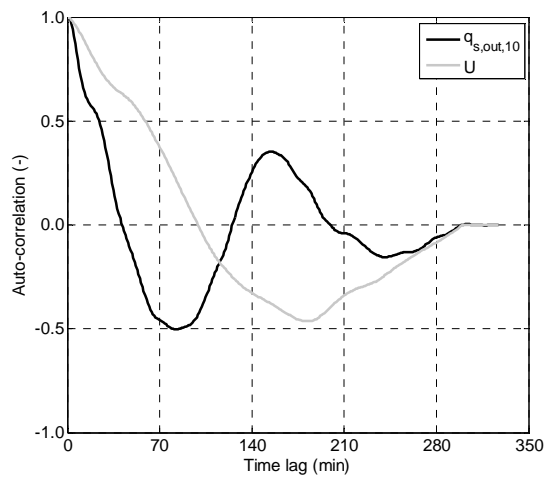
B.23 Test 23

Test parameters

S (%)	λ/D (-)	D (m)	N_{Bs} (m^{-2})	q (m^{3}s^{-1}m^{-1})	$q_{s,in}$ x10^{-3} (m^{3}s^{-1}m^{-1})
6.7	5	0.075	6.9	0.0168	0.0563

Characterization of the fluctuations (average period T=160 min)

	range (min ÷ max)	mean	σ	σ/mean
$q_{s,out,10}$	0 ÷ 0.2400x10^{-3} m^{3}s^{-1}m^{-1}	0.0570x10^{-3} m^{3}s^{-1}m^{-1}	0.0517x10^{-3} m^{3}s^{-1}m^{-1}	0.90
U	0.39 ÷ 0.69 ms^{-1}	0.53 ms^{-1}	0.06 ms^{-1}	0.11
P^*	0 ÷ 0.51	0.22	0.15	0.69
$A_{Bs}{}^*$	0 ÷ 0.047	0.016	0.012	0.75
HJ^*	0 ÷ 0.58	0.30	0.20	0.66

Average results

$q_{s,end}$ x10^{-3} (m^{3}s^{-1}m^{-1})	$\bar{U}$ (ms^{-1})	$\bar{P_{av}}$ (m)	HJ (m^{-2})	A_i/A_t (-)	A_{if}/A_t (-)	P_{end} (m)	P_{us} (m)	P_{ds} (m)
0.0571	0.53	0.017	2	0.03	0.005	0.0240	0.0190	0.0300

Final configuration

Time series
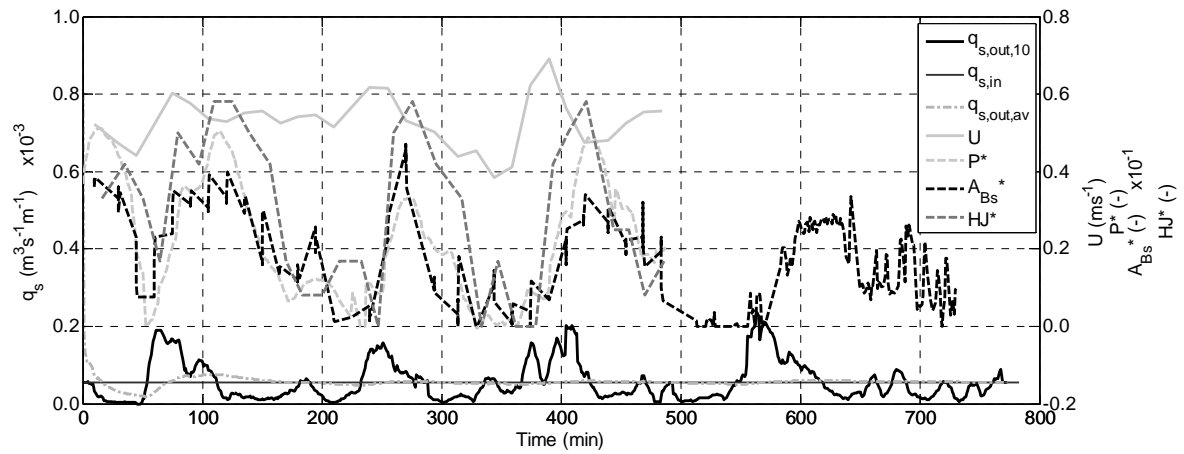
Correlation analysis
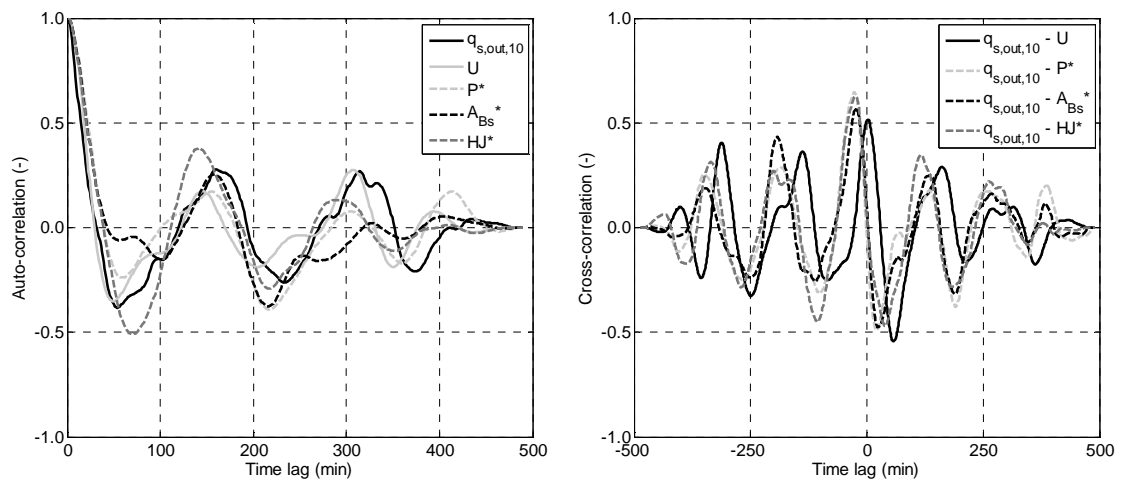
B.24 Test 24

Test parameters

S (%)	λ/D (-)	D (m)	N_{Bs} (m^{-2})	q (m^{3}s^{-1}m^{-1})	$q_{s,in}$ x10^{-3} (m^{3}s^{-1}m^{-1})
6.7	3	0.075	20.0	0.0188	0.0563

Characterization of the fluctuations (average period T=98 min)

	range (min ÷ max)	mean	σ	σ/mean
$q_{s,out,10}$	0.0050 ÷ 0.1308x10^{-3} m^{3}s^{-1}m^{-1}	0.0534x10^{-3} m^{3}s^{-1}m^{-1}	0.0351x10^{-3} m^{3}s^{-1}m^{-1}	0.66
U	0.41 ÷ 0.69 ms^{-1}	0.52 ms^{-1}	0.07 ms^{-1}	0.14
P^*	0.17 ÷ 0.47	0.31	0.07	0.22
A_{Bs}^*	0.013 ÷ 0.126	0.074	0.024	0.33
HJ^*	0.06 ÷ 0.50	0.29	0.10	0.35

Average results

$q_{s,end}$ x10^{-3} (m^{3}s^{-1}m^{-1})	$\bar{U}$ (ms^{-1})	$\bar{P_{av}}$ (m)	HJ (m^{-2})	A_i/A_t (-)	A_{if}/A_t (-)	P_{end} (m)	P_{us} (m)	P_{ds} (m)
0.0528	0.52	0.023	5.9	0.09	0.026	0.020	0.015	0.024

Final configuration

Time series
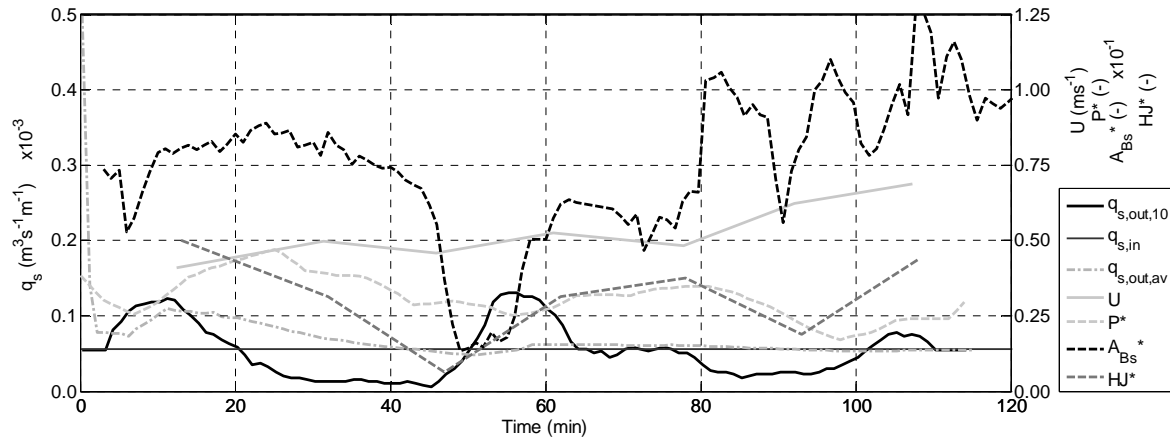
Correlation analysis
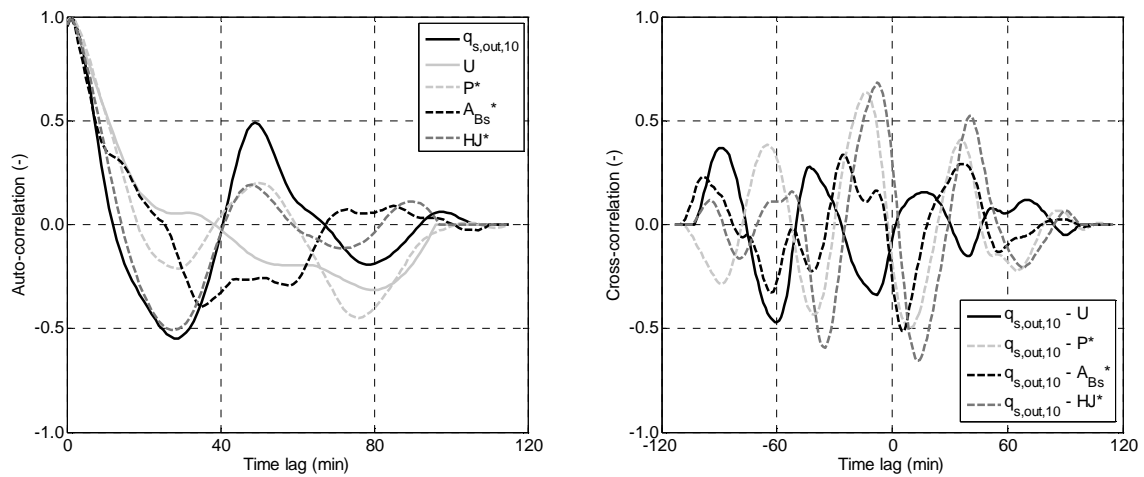
B.25 Test 25

Test parameters

S (%)	λ/D (-)	D (m)	N_{Bs} (m^{-2})	q $(m^3s^{-1}m^{-1})$	$q_{s,in}$ x10^{-3} $(m^3s^{-1}m^{-1})$
6.7	5	0.125	2.3	0.0156	0.0563

Characterization of the fluctuations (average period T=161 min)

	range (min ÷ max)	mean	σ	σ/mean
$q_{s,out,10}$	$0 \div 0.1736$x10^{-3} $m^3s^{-1}m^{-1}$	0.0599x10^{-3} $m^3s^{-1}m^{-1}$	0.0474x10^{-3} $m^3s^{-1}m^{-1}$	0.79
U	$0.44 \div 0.71$ ms^{-1}	0.52 ms^{-1}	0.07 ms^{-1}	0.13
P^*	$0.04 \div 0.43$	0.22	0.11	0.49
A_{Bs}^*	$0 \div 0.053$	0.027	0.016	0.59
HJ^*	$0 \div 1.00$	0.46	0.38	0.83

Average results

$q_{s,end}$ x10^{-3} $(m^3s^{-1}m^{-1})$	$\bar{U}$ (ms^{-1})	$\bar{P_{av}}$ (m)	HJ (m^{-2})	A_i/A_t (-)	A_{if}/A_t (-)	P_{end} (m)	P_{us} (m)	P_{ds} (m)
0.0604	0.52	0.027	1.0	0.02	0.006	0.046	0.034	0.057

Final configuration

Time series
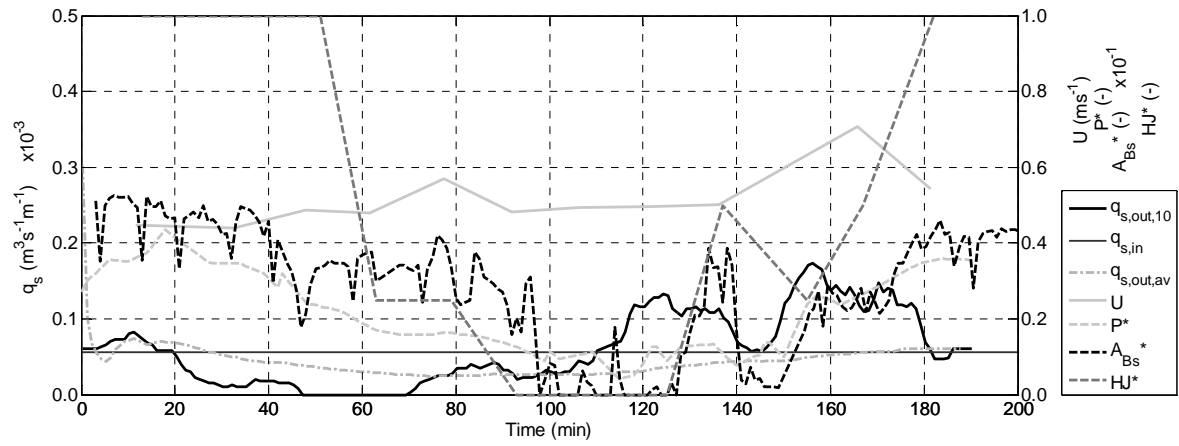
Correlation analysis
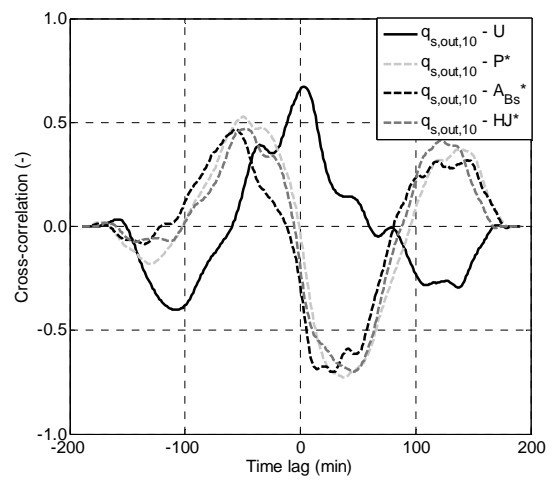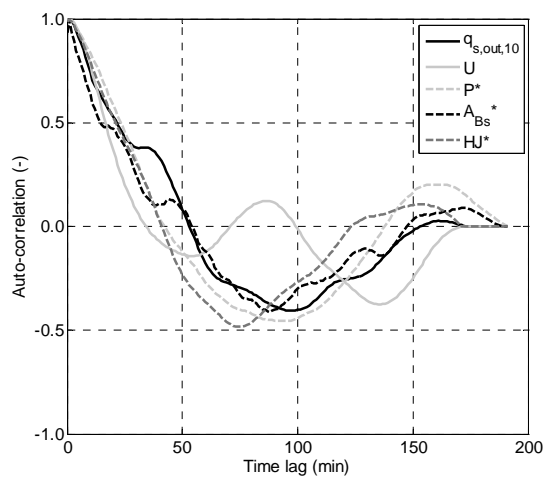
B.26 Test 26

Test parameters

S (%)	λ/D (-)	D (m)	N_{Bs} (m^{-2})	q (m^{3}s^{-1}m^{-1})	$q_{s,in}$ x10^{-3} (m^{3}s^{-1}m^{-1})
6.7	Inf.	0.000	0.0	0.0159	0.0936

Characterization of the fluctuations (average period T=134.5 min)

	range (min ÷ max)	mean	σ	σ/mean
$q_{s,out,10}$	0.0025 ÷ 0.2358x10^{-3} m^{3}s^{-1}m^{-1}	0.1002x10^{-3} m^{3}s^{-1}m^{-1}	0.0795x10^{-3} m^{3}s^{-1}m^{-1}	0.79
U	0.40 ÷ 0.72 ms^{-1}	0.58 ms^{-1}	0.12 ms^{-1}	0.21
P^*	-	-	-	-
$A_{Bs}{}^*$	-	-	-	-
HJ^*	-	-	-	-

Average results

$q_{s,end}$ x10^{-3} (m^{3}s^{-1}m^{-1})	$\bar{U}$ (ms^{-1})	$\bar{P_{av}}$ (m)	HJ (m^{-2})	A_i/A_t (-)	A_{if}/A_t (-)	P_{end} (m)	P_{us} (m)	P_{ds} (m)
0.0996	0.58	0.000	0.0	0.00	0.000	0.000	0.000	0.000

Final configuration

Time series
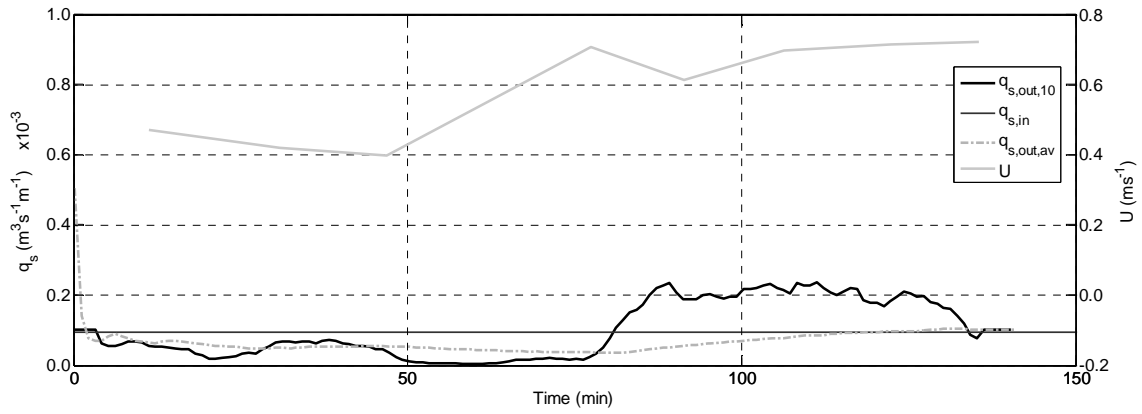
Correlation analysis
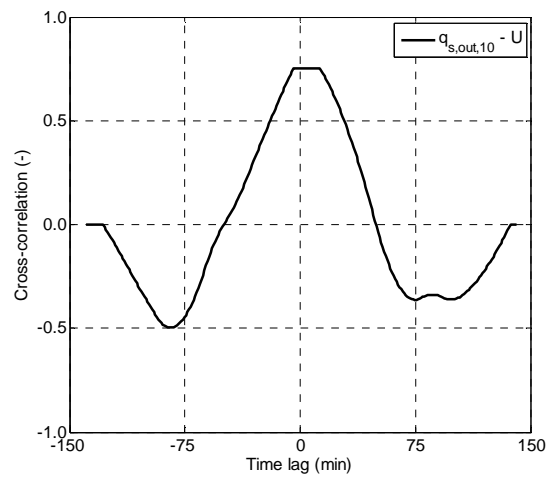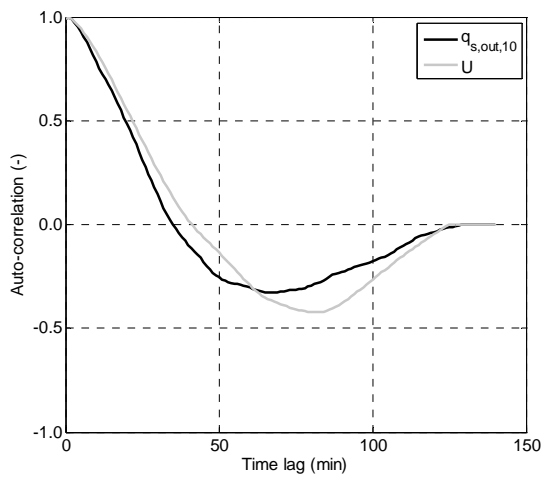
B.27 Test 27

Test parameters

S (%)	λ/D (-)	D (m)	N_{Bs} (m^{-2})	q (m^{3}s^{-1}m^{-1})	$q_{s,in}$ x10^{-3} (m^{3}s^{-1}m^{-1})
6.7	5	0.100	4.0	0.0183	0.0936

Characterization of the fluctuations (average period T=63 min)

	range (min ÷ max)	mean	σ	σ/mean
$q_{s,out,10}$	0.0126 ÷ 0.1929x10^{-3} m^{3}s^{-1}m^{-1}	0.0882x10^{-3} m^{3}s^{-1}m^{-1}	0.0520x10^{-3} m^{3}s^{-1}m^{-1}	0.59
U	0.52 ÷ 0.58 ms^{-1}	0.55 ms^{-1}	0.02 ms^{-1}	0.03
P^*	0.20 ÷ 0.37	0.28	0.05	0.16
A_{Bs}^*	0 ÷ 0.021	0.014	0.007	0.48
HJ^*	0.43 ÷ 0.86	0.60	0.09	0.16

Average results

$q_{s,end}$ x10^{-3} (m^{3}s^{-1}m^{-1})	$\bar{U}$ (ms^{-1})	$\bar{P}_{av}$ (m)	HJ (m^{-2})	A_i/A_t (-)	A_{if}/A_t (-)	P_{end} (m)	P_{us} (m)	P_{ds} (m)
0.0876	0.55	0.028	2.4	0.03	0.008	0.039	0.026	0.043

Final configuration
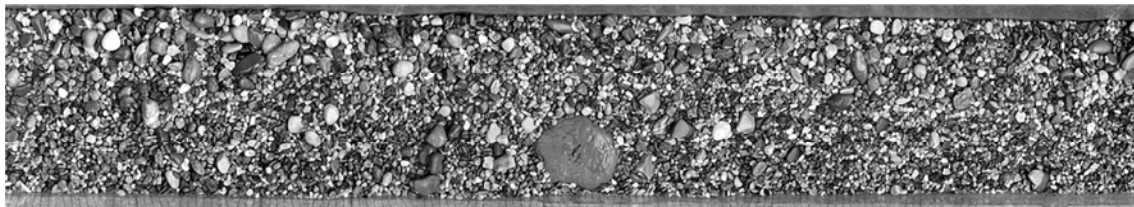
Time series
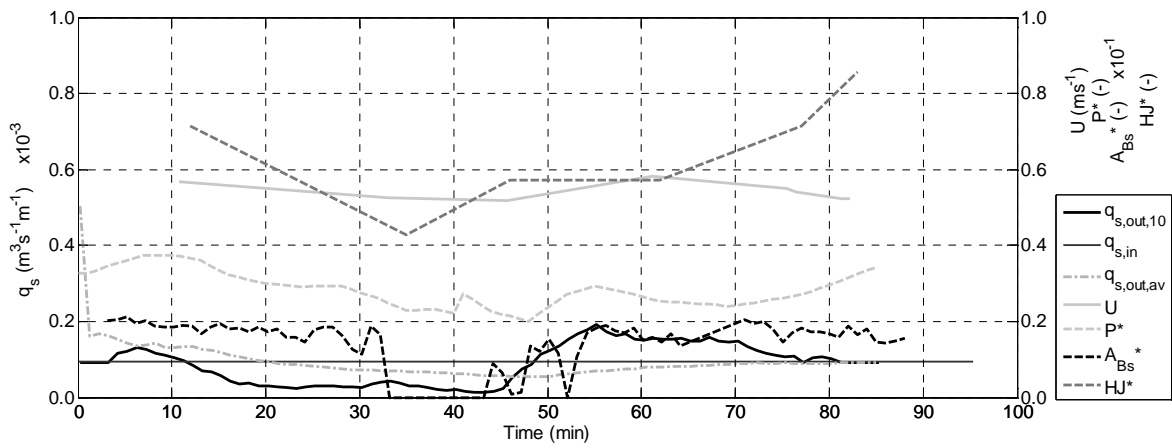
Correlation analysis
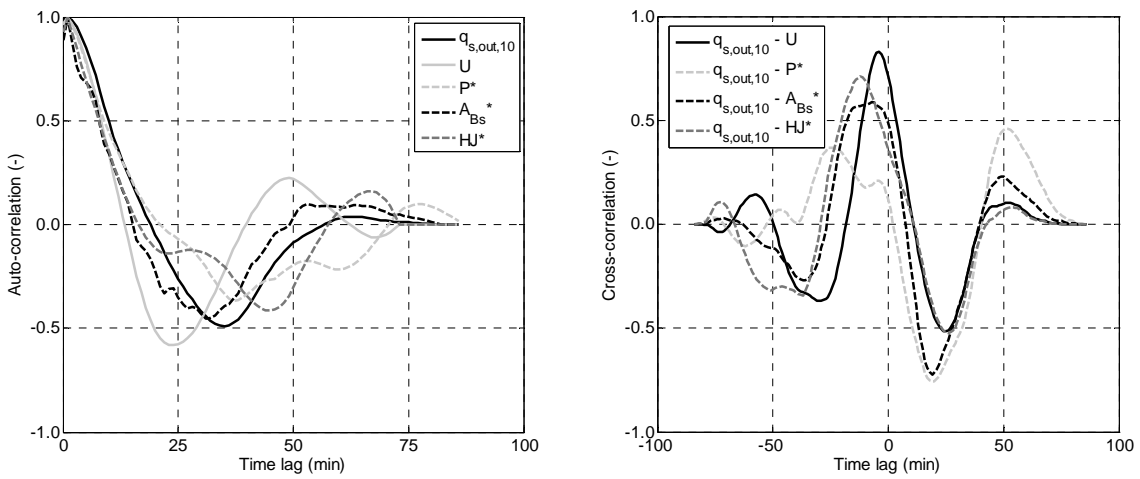
B.28 Test 28

Test parameters

S (%)	λ/D (-)	D (m)	N_{Bs} (m^{-2})	q (m^{3}s^{-1}m^{-1})	$q_{s,in}$ x10^{-3} (m^{3}s^{-1}m^{-1})
9.9	3	0.100	10.9	0.0131	0.0936

Characterization of the fluctuations (average period T=130 min)

	range (min ÷ max)	mean	σ	σ/mean
$q_{s,out,10}$	0 ÷ 0.4323x10^{-3} m^{3}s^{-1}m^{-1}	0.0898x10^{-3} m^{3}s^{-1}m^{-1}	0.0883x10^{-3} m^{3}s^{-1}m^{-1}	0.98
U	0.29 ÷ 0.55 ms^{-1}	0.38 ms^{-1}	0.06 ms^{-1}	0.16
P^*	0.02 ÷ 0.42	0.21	0.12	0.57
$A_{Bs}{}^*$	0 ÷ 0.107	0.056	0.032	0.58
HJ^*	0 ÷ 0.50	0.18	0.12	0.66

Average results

$q_{s,end}$ x10^{-3} (m^{3}s^{-1}m^{-1})	$\bar{U}$ (ms^{-1})	$\overline{P_{av}}$ (m)	HJ (m^{-2})	A_i/A_t (-)	A_{if}/A_t (-)	P_{end} (m)	P_{us} (m)	P_{ds} (m)
0.0891	0.38	0.021	2.0	0.07	0.015	0.018	0.014	0.025

Final configuration

Time series
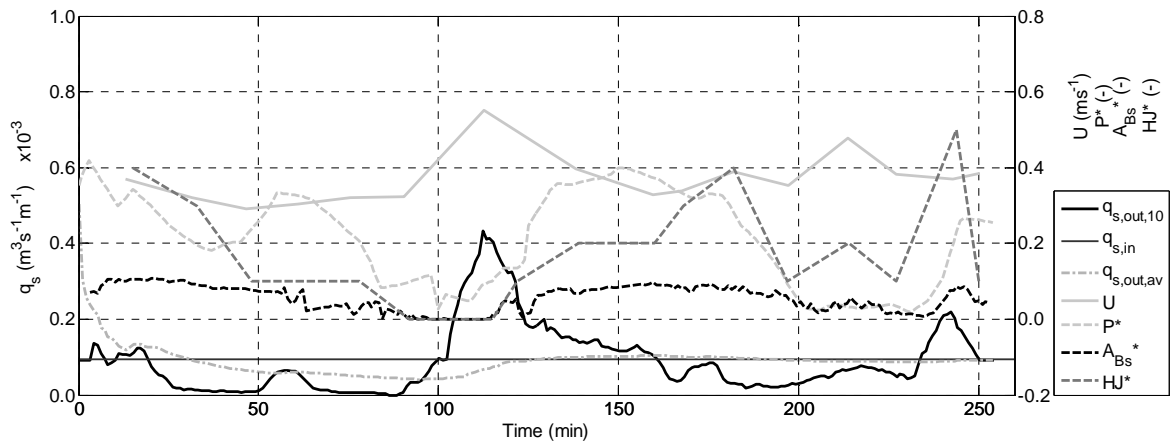
Correlation analysis
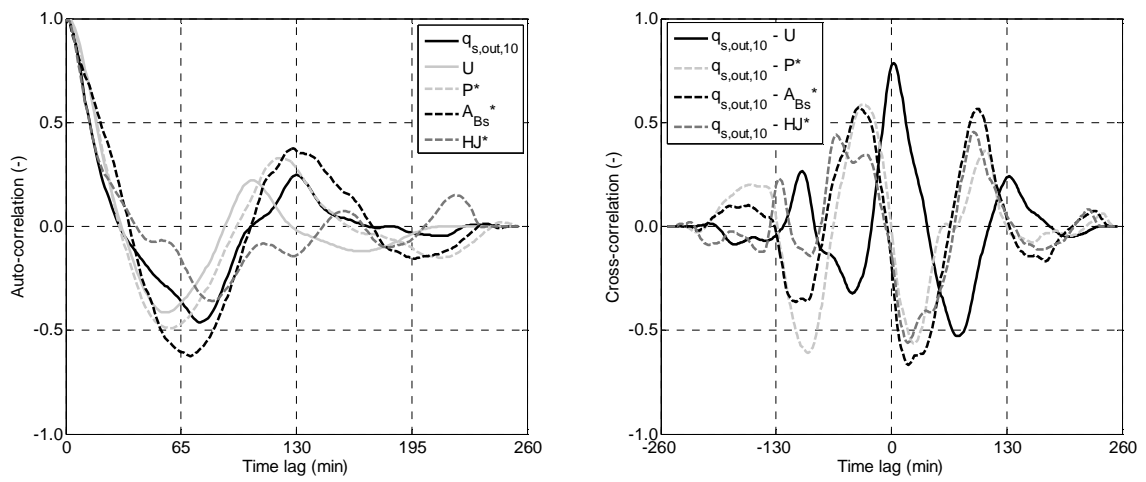
B.29 Test 29

Test parameters

S (%)	λ/D (-)	D (m)	N_{Bs} (m^{-2})	q (m^{3}s^{-1}m^{-1})	$q_{s,in}$ x10^{-3} (m^{3}s^{-1}m^{-1})
9.9	Inf.	0.000	0.0	0.0112	0.0936

Characterization of the fluctuations (average period T=193 min)

	range (min ÷ max)	mean	σ	σ/mean
$q_{s,out,10}$	0.0330 ÷ 0.3848x10^{-3} m^{3}s^{-1}m^{-1}	0.2164x10^{-3} m^{3}s^{-1}m^{-1}	0.1005x10^{-3} m^{3}s^{-1}m^{-1}	0.46
U	0.22 ÷ 0.39 ms^{-1}	0.28 ms^{-1}	0.04 ms^{-1}	0.15
P^*	-	-	-	-
$A_{Bs}{}^*$	-	-	-	-
HJ^*	-	-	-	-

Average results

$q_{s,end}$ x10^{-3} (m^{3}s^{-1}m^{-1})	$\bar{U}$ (ms^{-1})	$\bar{P_{av}}$ (m)	HJ (m^{-2})	A_i/A_t (-)	A_{if}/A_t (-)	P_{end} (m)	P_{us} (m)	P_{ds} (m)
0.0876	0.40	0.000	0.0	0.00	0.000	0.000	0.000	0.000

Final configuration

Time series
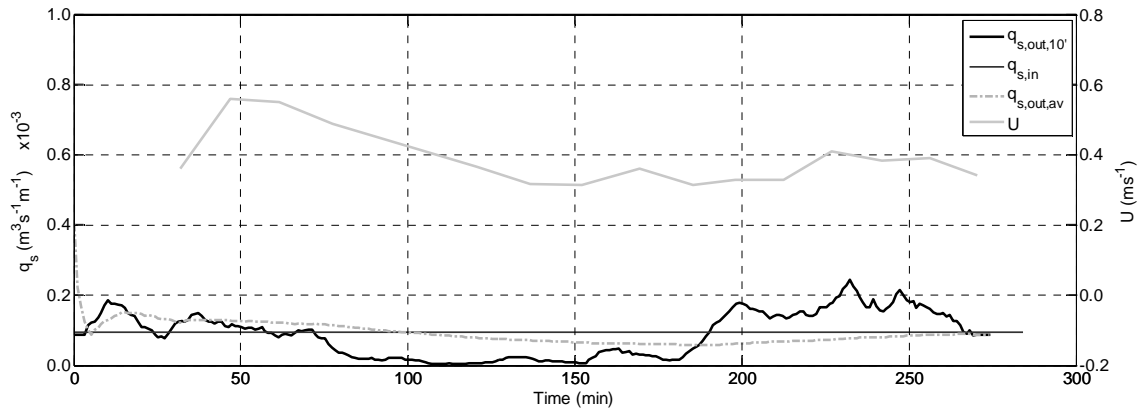
Correlation analysis
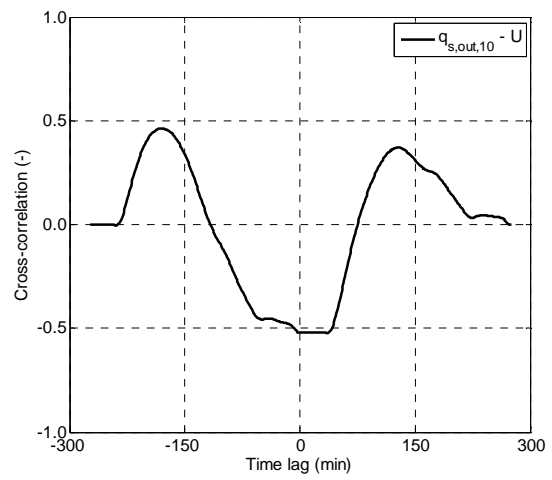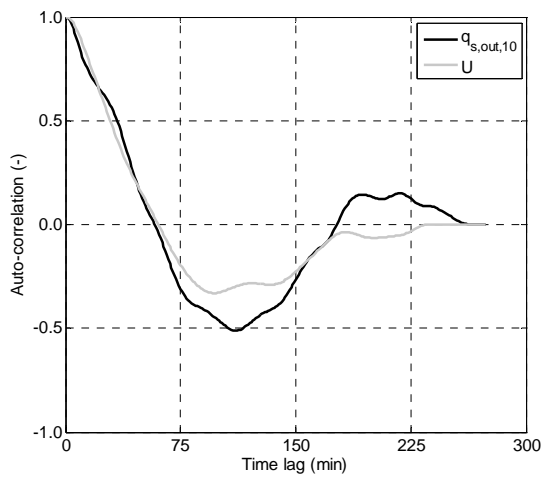
B.30 Test 30

Test parameters

S (%)	λ/D (-)	D (m)	N_{Bs} (m^{-2})	q (m^{3}s^{-1}m^{-1})	$q_{s,in}$ x10^{-3} (m^{3}s^{-1}m^{-1})
9.9	3	0.100	10.9	0.0146	0.1358

Characterization of the fluctuations (average period T=18 min)

	range (min ÷ max)	mean	σ	σ/mean
$q_{s,out,3}$	0 ÷ 0.3103x10^{-3} m^{3}s^{-1}m^{-1}	0.1426x10^{-3} m^{3}s^{-1}m^{-1}	0.0705x10^{-3} m^{3}s^{-1}m^{-1}	0.49
U	0.43 ÷ 0.59 ms^{-1}	0.53 ms^{-1}	0.04 ms^{-1}	0.08
P^*	0.18 ÷ 0.44	0.35	0.07	0.19
A_{Bs}^*	0.025 ÷ 0.104	0.084	0.015	0.18
HJ^*	0.20 ÷ 0.60	0.42	0.10	0.25

Average results

$q_{s,end}$ x10^{-3} (m^{3}s^{-1}m^{-1})	$\bar{U}$ (ms^{-1})	$\bar{P_{av}}$ (m)	HJ (m^{-2})	A_i/A_t (-)	A_{if}/A_t (-)	P_{end} (m)	P_{us} (m)	P_{ds} (m)
0.1434	0.53	0.035	4.5	0.09	0.031	0.030	0.020	0.035

Final configuration

Time series
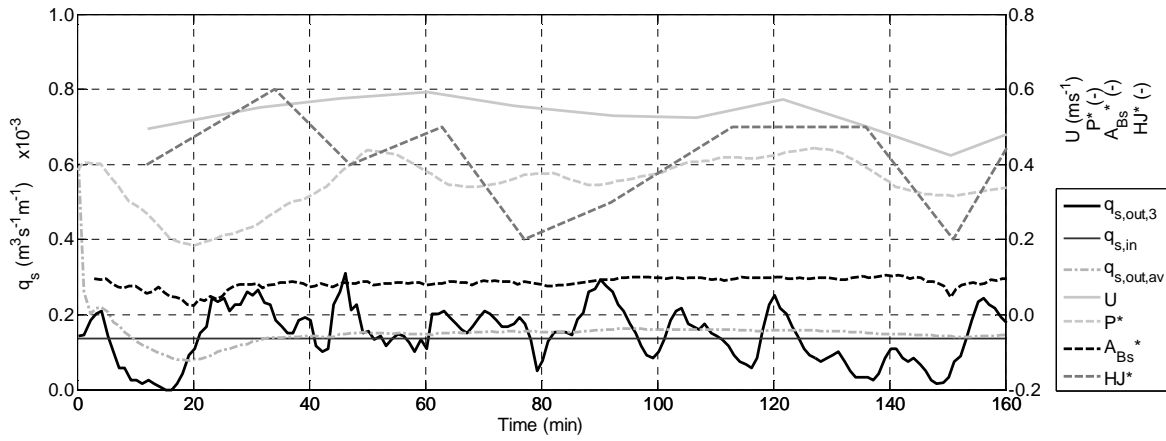
Correlation analysis
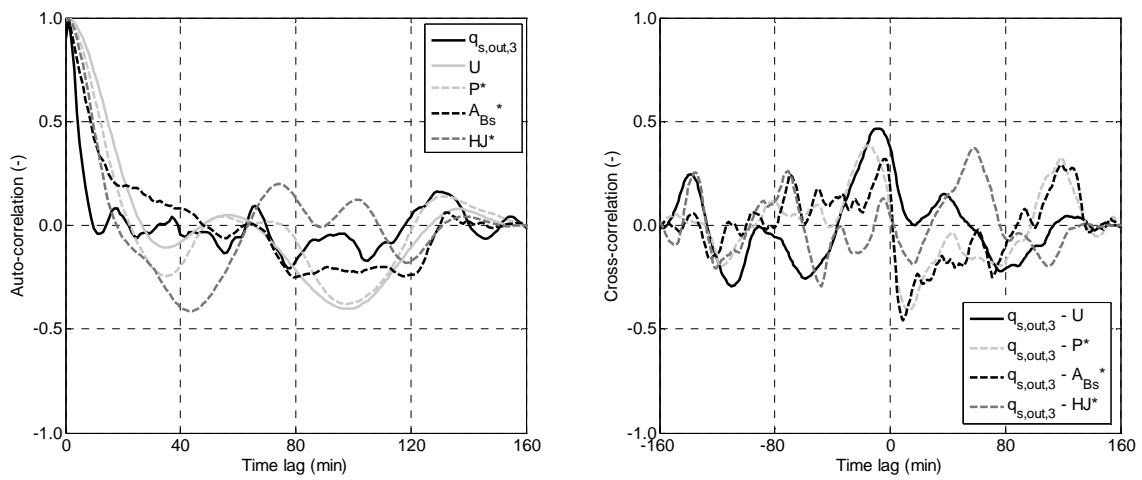
B.31 Test 31

Test parameters

S (%)	λ/D (-)	D (m)	N_{Bs} (m^{-2})	q (m^{3}s^{-1}m^{-1})	$q_{s,in}$ x10^{-3} (m^{3}s^{-1}m^{-1})
9.9	3	0.100	10.9	0.0166	0.1917

Characterization of the fluctuations (average period T=26 min)

	range (min ÷ max)	mean	σ	σ/mean
$q_{s,out,5}$	0.0909 ÷ 0.3170x10^{-3} m^{3}s^{-1}m^{-1}	0.1989x10^{-3} m^{3}s^{-1}m^{-1}	0.0492x10^{-3} m^{3}s^{-1}m^{-1}	0.25
U	0.54 ÷ 0.67 ms^{-1}	0.61 ms^{-1}	0.04 ms^{-1}	0.06
P^*	0.12 ÷ 0.46	0.36	0.07	0.19
A_{Bs}^*	0.075 ÷ 0.109	0.095	0.007	0.07
HJ^*	0.20 ÷ 0.60	0.42	0.10	0.24

Average results

$q_{s,end}$ x10^{-3} (m^{3}s^{-1}m^{-1})	$\bar{U}$ (ms^{-1})	$\bar{P_{av}}$ (m)	HJ (m^{-2})	A_i/A_t (-)	A_{if}/A_t (-)	P_{end} (m)	P_{us} (m)	P_{ds} (m)
0.1977	0.61	0.036	4.6	0.09	0.033	0.032	0.022	0.039

Final configuration

Time series
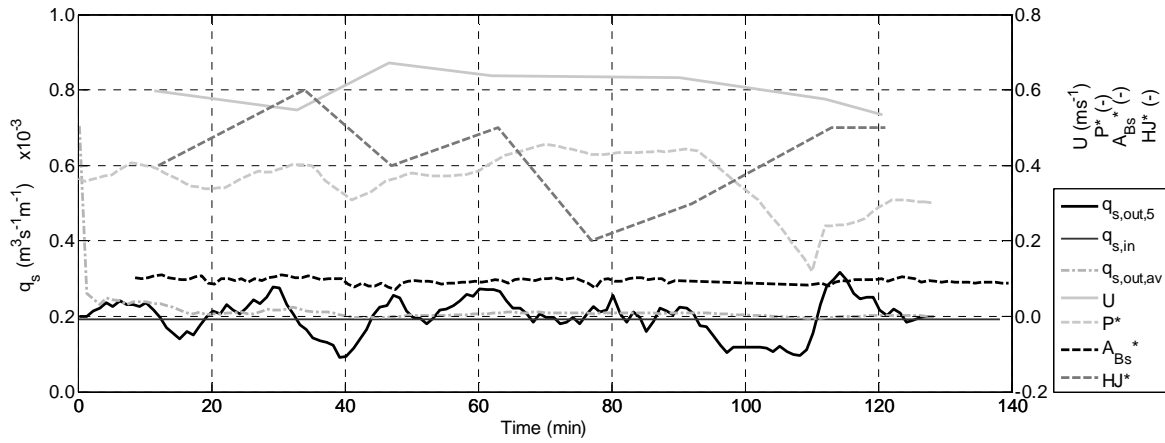
Correlation analysis
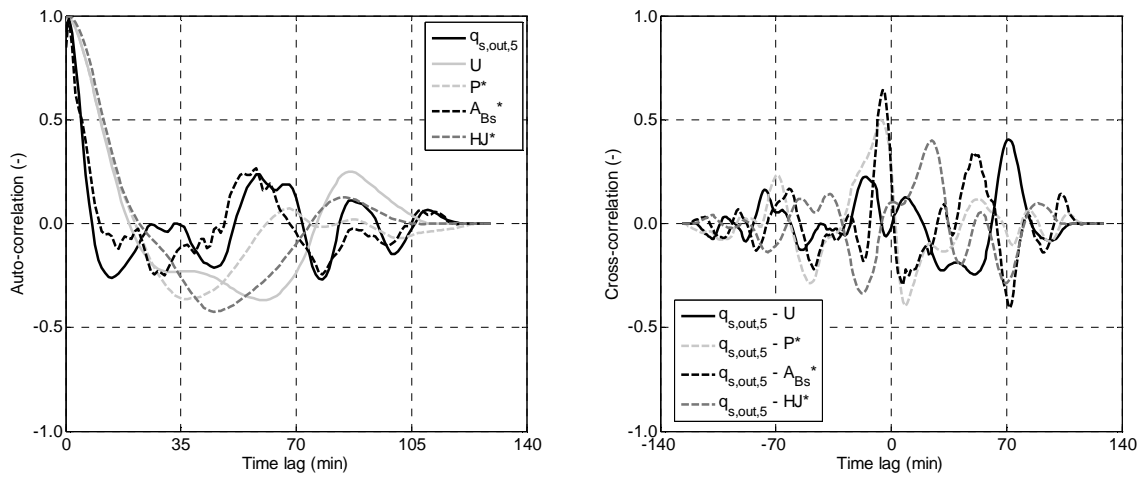
B.32 Test 32

Test parameters

S (%)	λ/D (-)	D (m)	N_{Bs} (m^{-2})	q (m^{3}s^{-1}m^{-1})	$q_{s,in}$ x10^{-3} (m^{3}s^{-1}m^{-1})
13	3	0.100	10.9	0.0114	0.1917

Characterization of the fluctuations (average period T=53 min)

	range (min ÷ max)	mean	σ	σ/mean
$q_{s,out,10}$	0.0054 ÷ 0.4235x10^{-3} m^{3}s^{-1}m^{-1}	0.1995x10^{-3} m^{3}s^{-1}m^{-1}	0.1162x10^{-3} m^{3}s^{-1}m^{-1}	0.58
U	0.28 ÷ 0.56 ms^{-1}	0.37 ms^{-1}	0.07 ms^{-1}	0.18
P^*	0 ÷ 0.41	0.13	0.11	0.85
A_{Bs}^*	0 ÷ 0.094	0.040	0.034	0.85
HJ^*	0 ÷ 0.60	0.22	0.18	0.81

Average results

$q_{s,end}$ x10^{-3} (m^{3}s^{-1}m^{-1})	$\bar{U}$ (ms^{-1})	$\bar{P_{av}}$ (m)	HJ (m^{-2})	A_i/A_t (-)	A_{if}/A_t (-)	P_{end} (m)	P_{us} (m)	P_{ds} (m)
0.1992	0.37	0.013	2.3	0.05	0.008	0.017	0.010	0.021

Final configuration

Time series
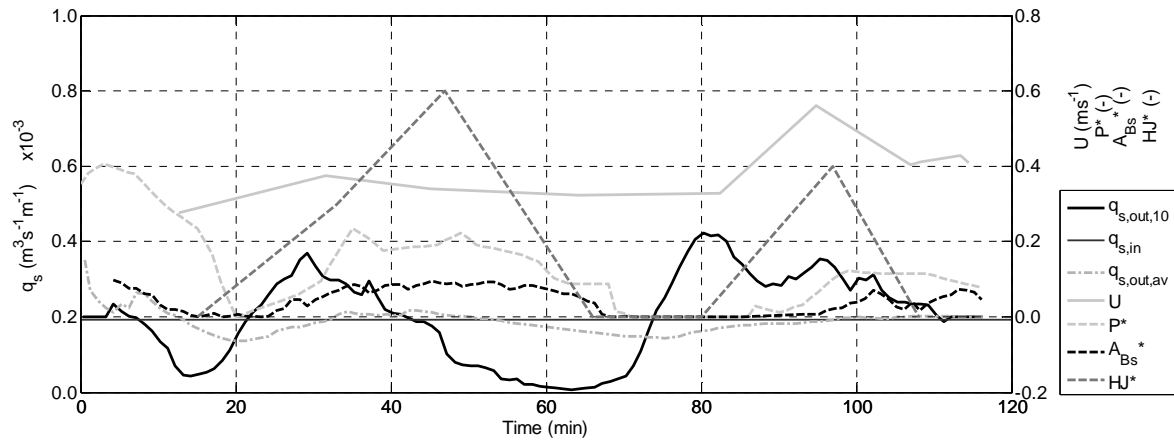
Correlation analysis
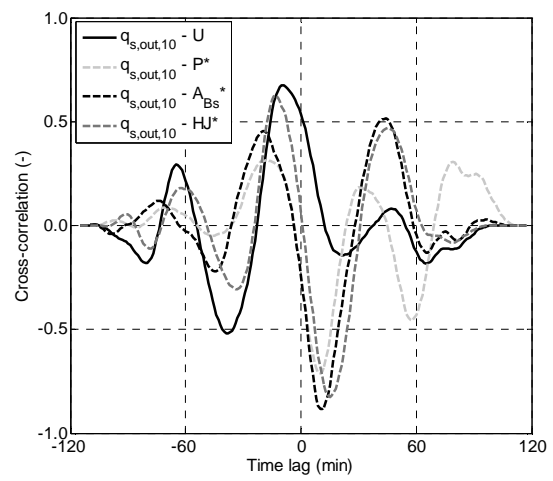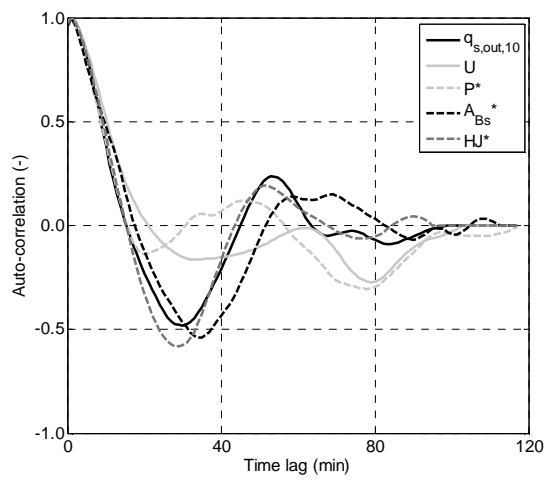
B.33 Test 33

Test parameters

S (%)	λ/D (-)	D (m)	N_{Bs} (m^{-2})	q (m^{3}s^{-1}m^{-1})	$q_{s,in}$ x10^{-3} (m^{3}s^{-1}m^{-1})
13	3	0.100	10.9	0.0107	0.1464

Characterization of the fluctuations (average period T=163 min)

	range (min ÷ max)	mean	σ	σ/mean
$q_{s,out,10}$	0.0050 ÷ 0.6060x10^{-3} m^{3}s^{-1}m^{-1}	0.1451x10^{-3} m^{3}s^{-1}m^{-1}	0.1401x10^{-3} m^{3}s^{-1}m^{-1}	0.97
U	0.22 ÷ 0.38 ms^{-1}	0.28 ms^{-1}	0.03 ms^{-1}	0.12
P^*	0 ÷ 0.39	0.16	0.13	0.80
A_{Bs}^*	0 ÷ 0.110	0.037	0.038	1.03
HJ^*	0 ÷ 0.60	0.16	0.16	1.01

Average results

$q_{s,end}$ x10^{-3} (m^{3}s^{-1}m^{-1})	$\bar{U}$ (ms^{-1})	$\bar{P_{av}}$ (m)	HJ (m^{-2})	A_i/A_t (-)	A_{if}/A_t (-)	P_{end} (m)	P_{us} (m)	P_{ds} (m)
0.1449	0.28	0.016	1.8	0.05	0.010	0.021	0.012	0.029

Final configuration

Time series
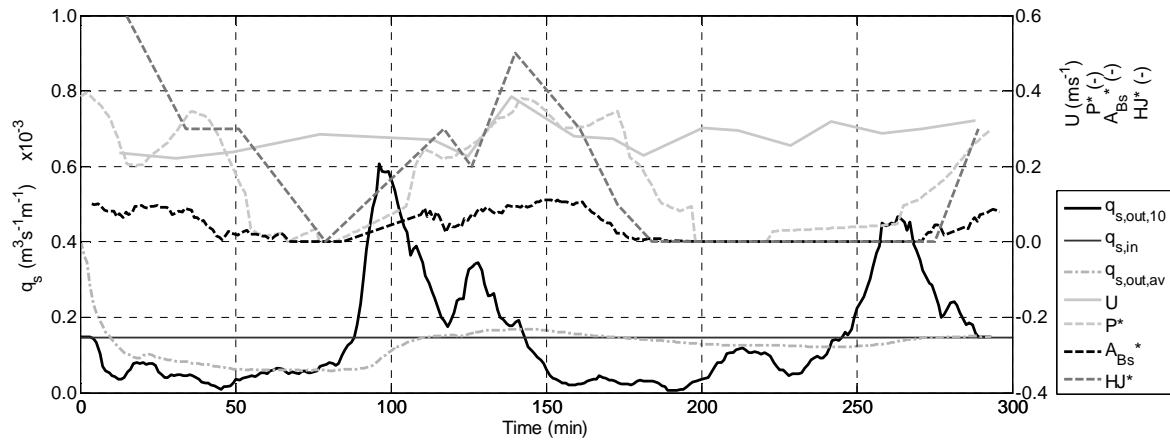
Correlation analysis
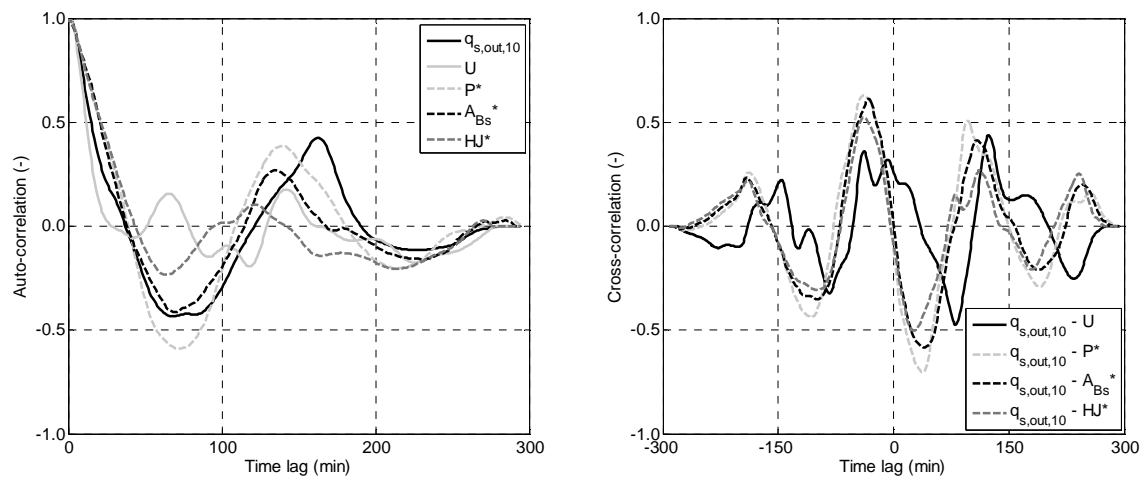
B.34 Test 34

Test parameters

S (%)	λ/D (-)	D (m)	N_{Bs} (m^{-2})	q (m^{3}s^{-1}m^{-1})	$q_{s,in}$ x10^{-3} (m^{3}s^{-1}m^{-1})
13	3	0.075	20.0	0.0109	0.1464

Characterization of the fluctuations (average period T=76 min)

	range (min ÷ max)	*mean*	*σ*	*σ/mean*
$q_{s,out,10}$	0.0176 ÷ 0.4604x10^{-3} m^{3}s^{-1}m^{-1}	0.1724x10^{-3} m^{3}s^{-1}m^{-1}	0.1249x10^{-3} m^{3}s^{-1}m^{-1}	0.72
U	0.28 ÷ 0.52 ms^{-1}	0.36 ms^{-1}	0.06 ms^{-1}	0.16
P^*	-0.02 ÷ 0.44	0.13	0.13	1.01
A_{Bs}^*	0 ÷ 0.098	0.035	0.030	0.86
HJ^*	0 ÷ 0.56	0.15	0.15	1.01

Average results

$q_{s,end}$ x10^{-3} (m^{3}s^{-1}m^{-1})	$\bar{U}$ (ms^{-1})	$\bar{P_{av}}$ (m)	HJ (m^{-2})	A_i/A_t (-)	A_{if}/A_t (-)	P_{end} (m)	P_{us} (m)	P_{ds} (m)
0.1721	0.36	0.010	3.1	0.05	0.008	0.023	0.017	0.029

Final configuration

Time series
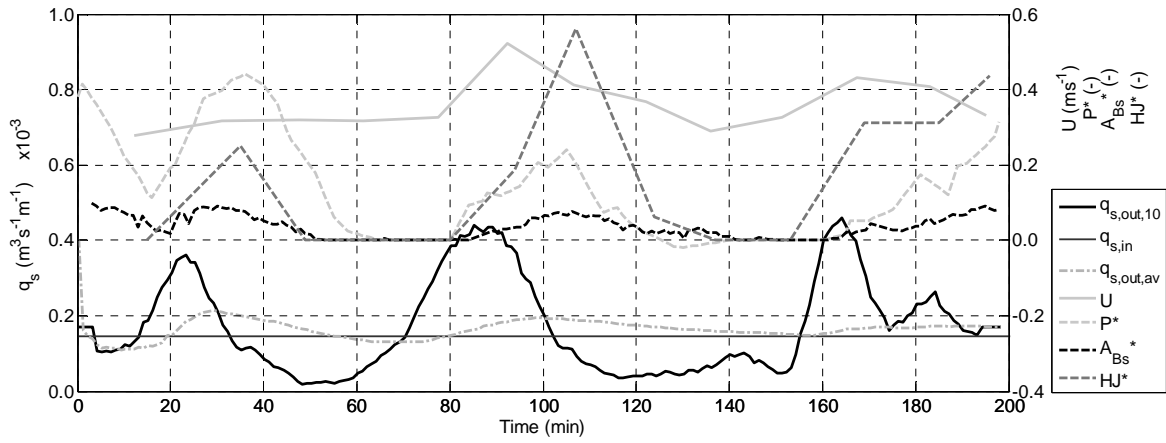
Correlation analysis
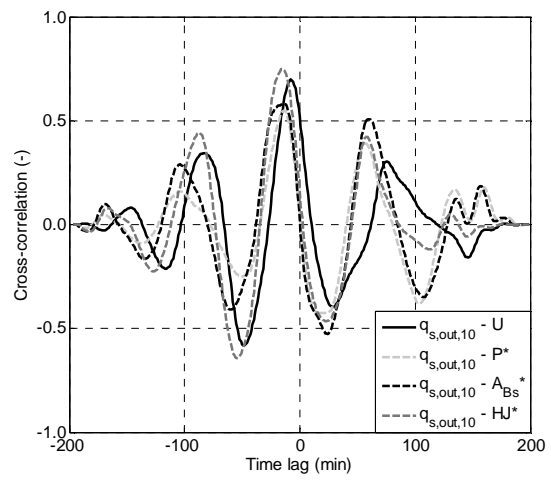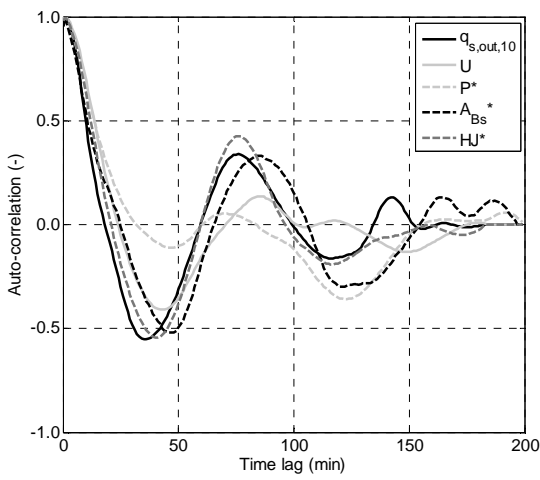
B.35 Test 35

Test parameters

S (%)	λ/D (-)	D (m)	N_{Bs} (m^{-2})	q (m^{3}s^{-1}m^{-1})	$q_{s,in}$ x10^{-3} (m^{3}s^{-1}m^{-1})
13	2	0.100	25.1	0.0128	0.1464

Characterization of the fluctuations (average period T=14 min)

	range (min ÷ max)	mean	σ	σ/mean
$q_{s,out,3}$	0.0168 ÷ 0.3774x10^{-3} m^{3}s^{-1}m^{-1}	0.1630x10^{-3} m^{3}s^{-1}m^{-1}	0.0855x10^{-3} m^{3}s^{-1}m^{-1}	0.52
U	0.38 ÷ 0.45 ms^{-1}	0.41 ms^{-1}	0.01 ms^{-1}	0.03
P^*	0.12 ÷ 0.33	0.17	0.04	0.20
A_{Bs}^*	0.053 ÷ 0.168	0.127	0.023	0.18
HJ^*	0.26 ÷ 0.47	0.34	0.04	0.12

Average results

$q_{s,end}$ x10^{-3} (m^{3}s^{-1}m^{-1})	$\bar{U}$ (ms^{-1})	$\bar{P_{av}}$ (m)	HJ (m^{-2})	A_i/A_t (-)	A_{if}/A_t (-)	P_{end} (m)	P_{us} (m)	P_{ds} (m)
0.1675	0.41	0.017	8.5	0.13	0.026	0.028	0.019	0.034

Final configuration
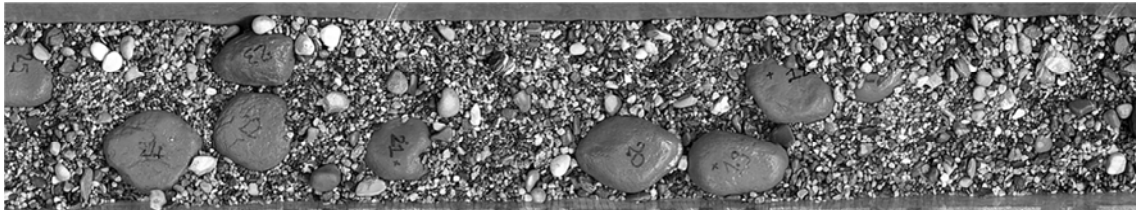
Time series
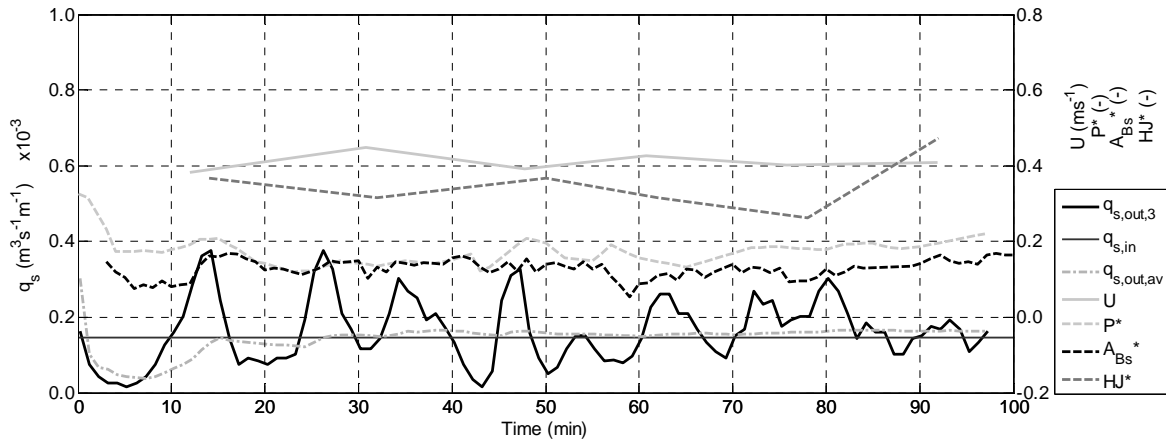
Correlation analysis
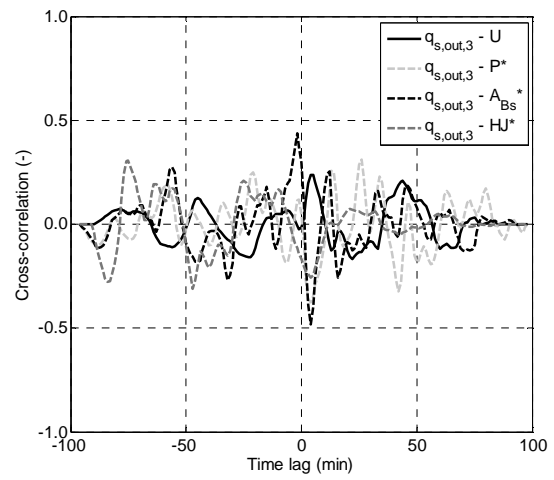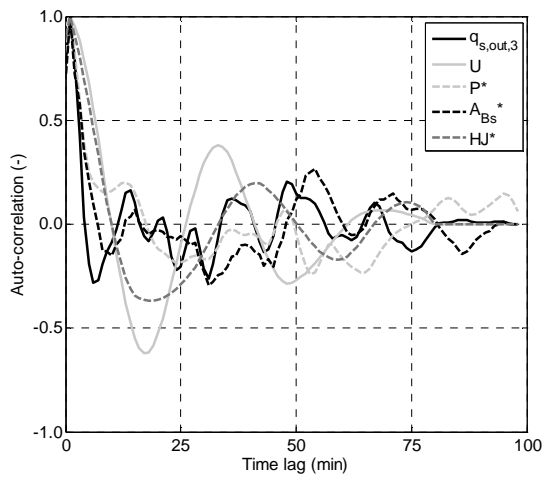
B.36 Test 36

Test parameters

S (%)	λ/D (-)	D (m)	N_{Bs} (m^{-2})	q (m^{3}s^{-1}m^{-1})	$q_{s,in}$ x10^{-3} (m^{3}s^{-1}m^{-1})
13	5	0.100	4.0	0.0104	0.1464

Characterization of the fluctuations (average period T=36 min)

	range (min ÷ max)	mean	σ	σ/mean
$q_{s,out,5}$	0.0352 ÷ 0.4126x10^{-3} m^{3}s^{-1}m^{-1}	0.1669x10^{-3} m^{3}s^{-1}m^{-1}	0.0824x10^{-3} m^{3}s^{-1}m^{-1}	0.49
U	0.31 ÷ 0.49 ms^{-1}	0.37 ms^{-1}	0.04 ms^{-1}	0.11
P^*	0.04 ÷ 0.44	0.24	0.07	0.29
A_{Bs}^*	0 ÷ 0.020	0.014	0.006	0.45
HJ^*	0.14 ÷ 0.71	0.43	0.12	0.29

Average results

$q_{s,end}$ x10^{-3} (m^{3}s^{-1}m^{-1})	$\bar{U}$ (ms^{-1})	$\bar{P_{av}}$ (m)	HJ (m^{-2})	A_i/A_t (-)	A_{if}/A_t (-)	P_{end} (m)	P_{us} (m)	P_{ds} (m)
0.1675	0.37	0.024	1.7	0.03	0.007	0.040	0.036	0.037

Final configuration

Time series
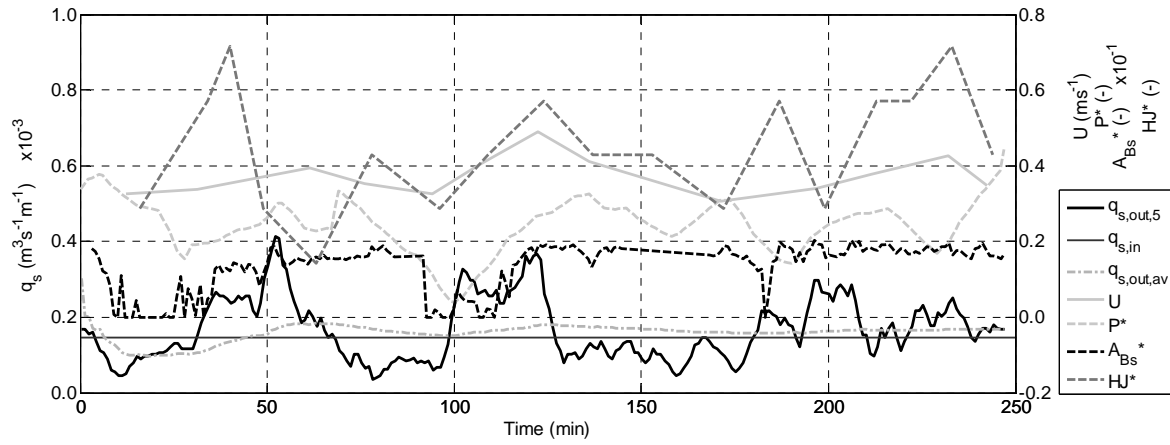
Correlation analysis
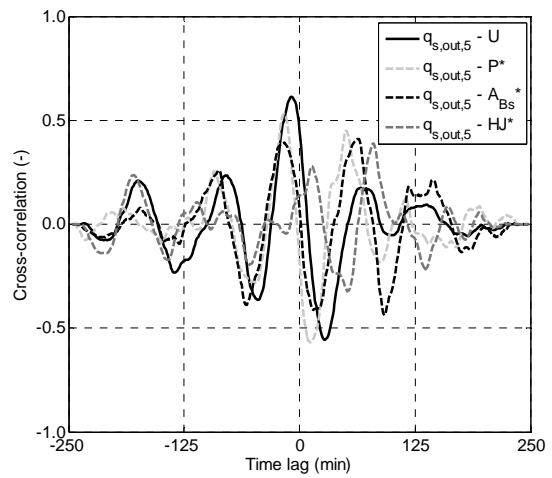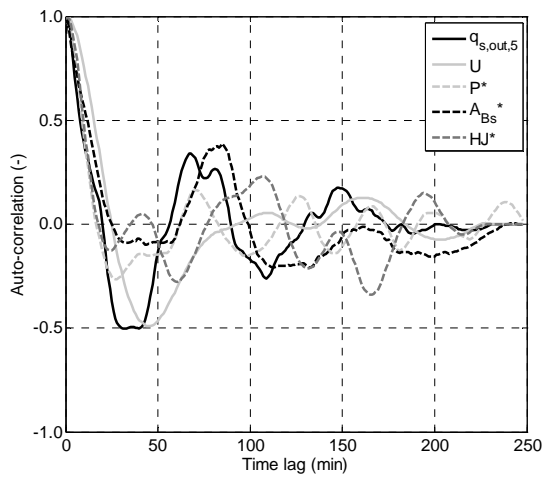
B.37 Test 37

Test parameters

S (%)	λ/D (-)	D (m)	N_{Bs} (m^{-2})	q (m^{3}s^{-1}m^{-1})	$q_{s,in}$ x10^{-3} (m^{3}s^{-1}m^{-1})
13	3	0.125	6.9	0.0104	0.1464

Characterization of the fluctuations (average period T=112 min)

	range (min ÷ max)	mean	σ	σ/mean
$q_{s,out,10}$	0.0075 ÷ 0.3522x10^{-3} m^{3}s^{-1}m^{-1}	0.1643x10^{-3} m^{3}s^{-1}m^{-1}	0.0987x10^{-3} m^{3}s^{-1}m^{-1}	0.60
U	0.23 ÷ 0.37 ms^{-1}	0.27 ms^{-1}	0.03 ms^{-1}	0.13
P^*	0.05 ÷ 0.43	0.24	0.12	0.48
$A_{Bs}{}^*$	0 ÷ 0.112	0.049	0.036	0.73
HJ^*	0.08 ÷ 0.58	0.40	0.13	0.31

Average results

$q_{s,end}$ x10^{-3} (m^{3}s^{-1}m^{-1})	$\bar{U}$ (ms^{-1})	$\bar{P_{av}}$ (m)	HJ (m^{-2})	A_i/A_t (-)	A_{if}/A_t (-)	P_{end} (m)	P_{us} (m)	P_{ds} (m)
0.1645	0.27	0.035	2.7	0.08	0.023	0.039	0.026	0.051

Final configuration

Time series
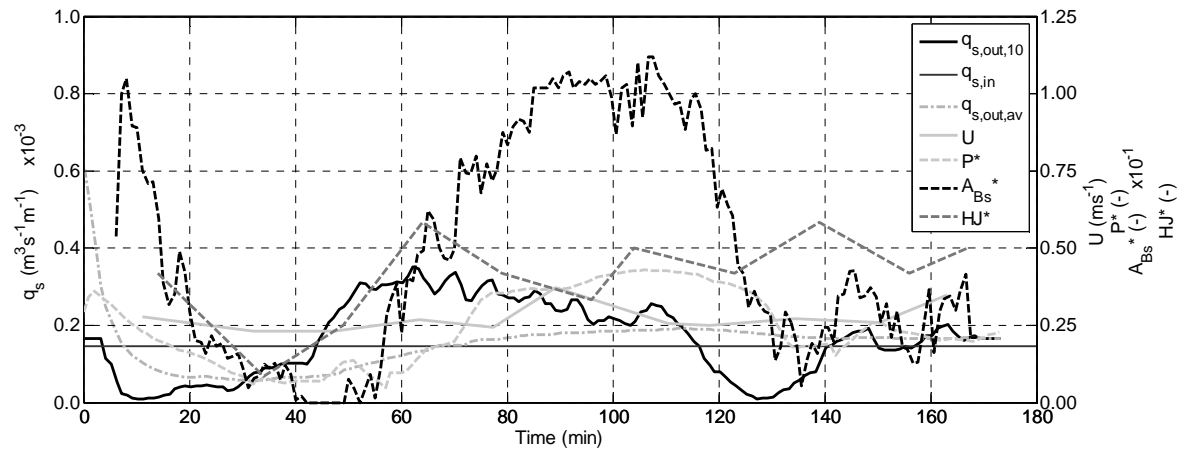
Correlation analysis
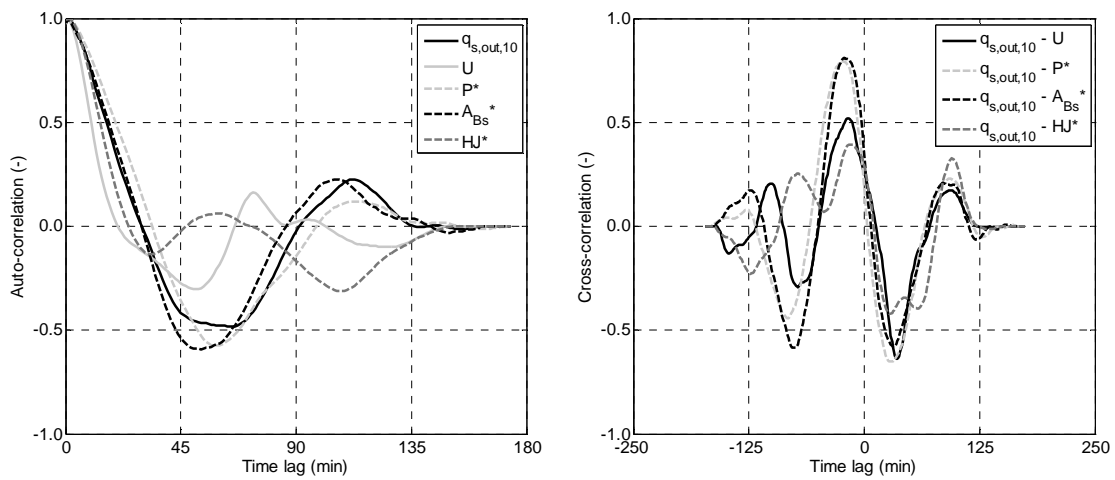
B.38 Test 38

Test parameters

S (%)	λ/D (-)	D (m)	N_{Bs} (m^{-2})	q (m^{3}s^{-1}m^{-1})	$q_{s,in}$ x10^{-3} (m^{3}s^{-1}m^{-1})
13	Inf.	0.000	0.0	0.0106	0.1917

Characterization of the fluctuations (average period T=108 min)

	range (min ÷ max)	mean	σ	σ/mean
$q_{s,out,10}$	0.0330 ÷ 0.3848x10^{-3} m^{3}s^{-1}m^{-1}	0.2164 x10^{-3}m^{3}s^{-1}m^{-1}	0.1005x10^{-3} m^{3}s^{-1}m^{-1}	0.46
U	0.22 ÷ 0.39 ms^{-1}	0.28 ms^{-1}	0.04 ms^{-1}	0.15
P^*	-	-	-	-
A_{Bs}^*	-	-	-	-
HJ^*	-	-	-	-

Average results

$q_{s,end}$ x10^{-3} (m^{3}s^{-1}m^{-1})	$\bar{U}$ (ms^{-1})	$\bar{P_{av}}$ (m)	HJ (m^{-2})	A_i/A_t (-)	A_{if}/A_t (-)	P_{end} (m)	P_{us} (m)	P_{ds} (m)
0.2158	0.28	0.000	0.0	0.00	0.000	0.000	0.000	0.000

Final configuration
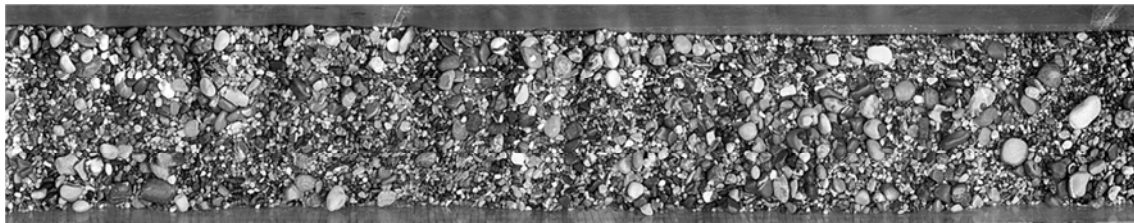
Time series
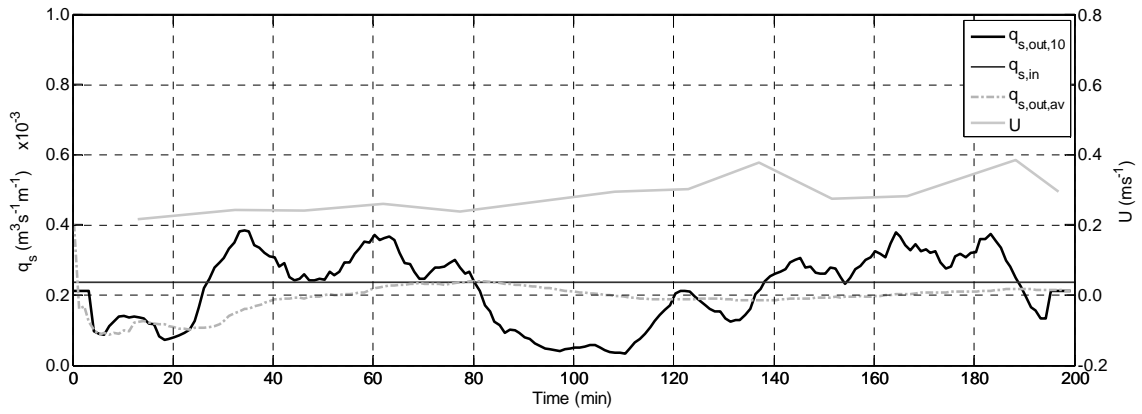
Correlation analysis
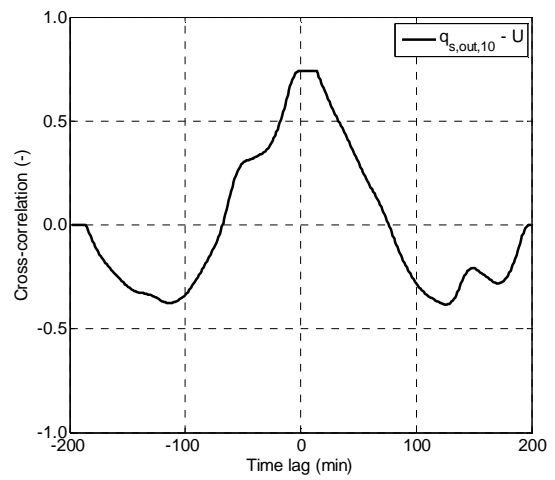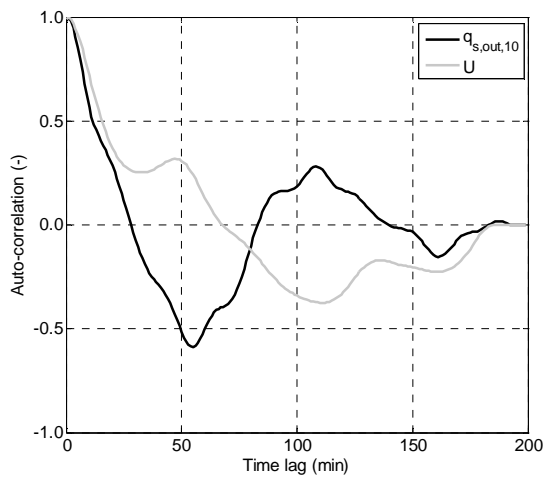
B.39 Test 39

Test parameters

S (%)	λ/D (-)	D (m)	N_{Bs} (m^{-2})	q (m^{3}s^{-1}m^{-1})	$q_{s,in}$ x10^{-3} (m^{3}s^{-1}m^{-1})
13	3	0.100	10.9	0.0124	0.2355

Characterization of the fluctuations (average period T=69 min)

	range (min ÷ max)	mean	σ	σ/mean
$q_{s,out,10}$	0.0201 ÷ 0.5333x10^{-3} m^{3}s^{-1}m^{-1}	0.2539x10^{-3} m^{3}s^{-1}m^{-1}	0.1205x10^{-3} m^{3}s^{-1}m^{-1}	0.47
U	0.31 ÷ 0.46 ms^{-1}	0.38 ms^{-1}	0.04 ms^{-1}	0.12
P^*	0.01 ÷ 0.43	0.25	0.12	0.47
A_{Bs}^*	0.003 ÷ 0.090	0.058	0.023	0.39
HJ^*	0.20 ÷ 0.70	0.48	0.10	0.22

Average results

$q_{s,end}$ x10^{-3} (m^{3}s^{-1}m^{-1})	$\bar{U}$ (ms^{-1})	$\bar{P_{av}}$ (m)	HJ (m^{-2})	A_i/A_t (-)	A_{if}/A_t (-)	P_{end} (m)	P_{us} (m)	P_{ds} (m)
0.2536	0.38	0.025	5.2	0.08	0.020	0.028	0.019	0.036

Final configuration

Time series
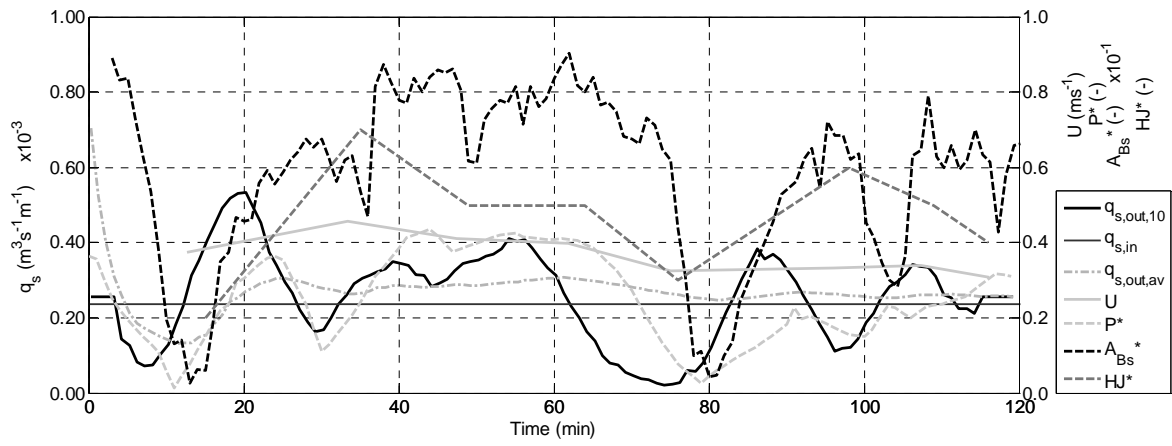
Correlation analysis
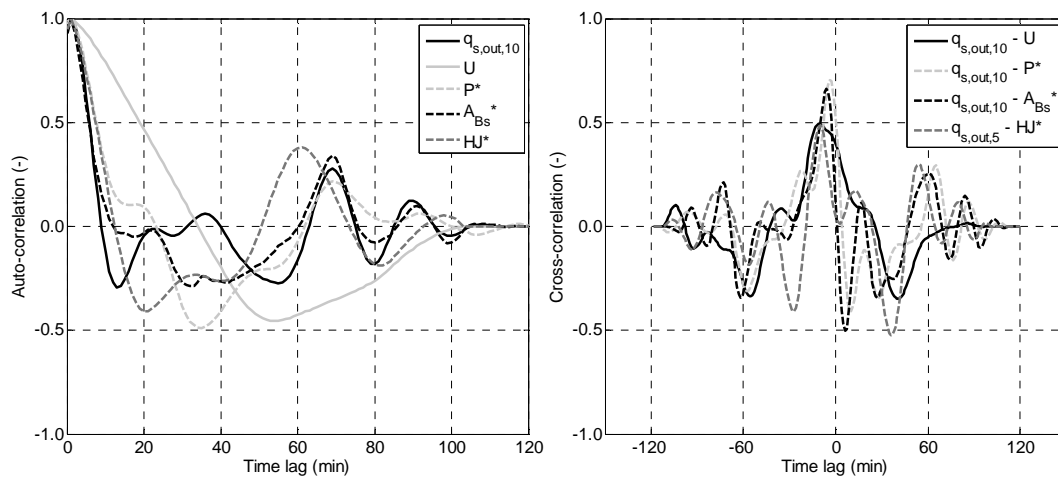
B.40 Test 40

Test parameters

S (%)	λ/D (-)	D (m)	N_{Bs} (m^{-2})	q (m^{3}s^{-1}m^{-1})	$q_{s,in}$ x10^{-3} (m^{3}s^{-1}m^{-1})
13	3	0.100	10.9	0.0118	0.2355

Characterization of the fluctuations (average period T=58 min)

	range (min ÷ max)	mean	σ	σ/mean
$q_{s,out,10}$	0.0327 ÷ 0.5333x10^{-3} m^{3}s^{-1}m^{-1}	0.2611x10^{-3} m^{3}s^{-1}m^{-1}	0.1128x10^{-3} m^{3}s^{-1}m^{-1}	0.43
U	0.24 ÷ 0.51 ms^{-1}	0.37 ms^{-1}	0.06 ms^{-1}	0.16
P^*	0 ÷ 0.42	0.21	0.13	0.60
A_{Bs}^*	0 ÷ 0.101	0.045	0.030	0.66
HJ^*	0 ÷ 0.70	0.25	0.18	0.73

Average results

$q_{s,end}$ x10^{-3} (m^{3}s^{-1}m^{-1})	$\bar{U}$ (ms^{-1})	$\bar{P_{av}}$ (m)	HJ (m^{-2})	A_i/A_t (-)	A_{if}/A_t (-)	P_{end} (m)	P_{us} (m)	P_{ds} (m)
0.2611	0.37	0.021	2.7	0.07	0.015	0.023	0.019	0.029

Final configuration

Time series
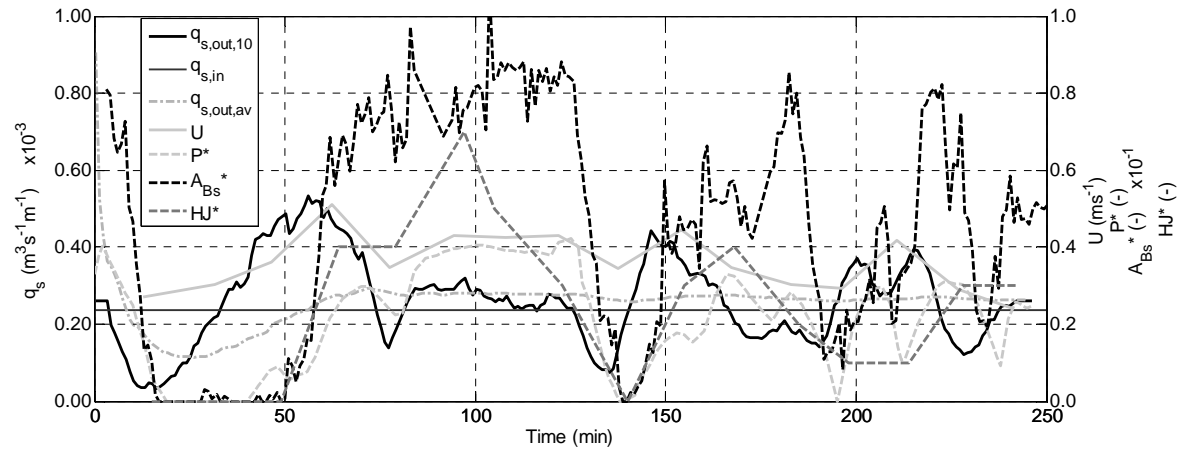
Correlation analysis
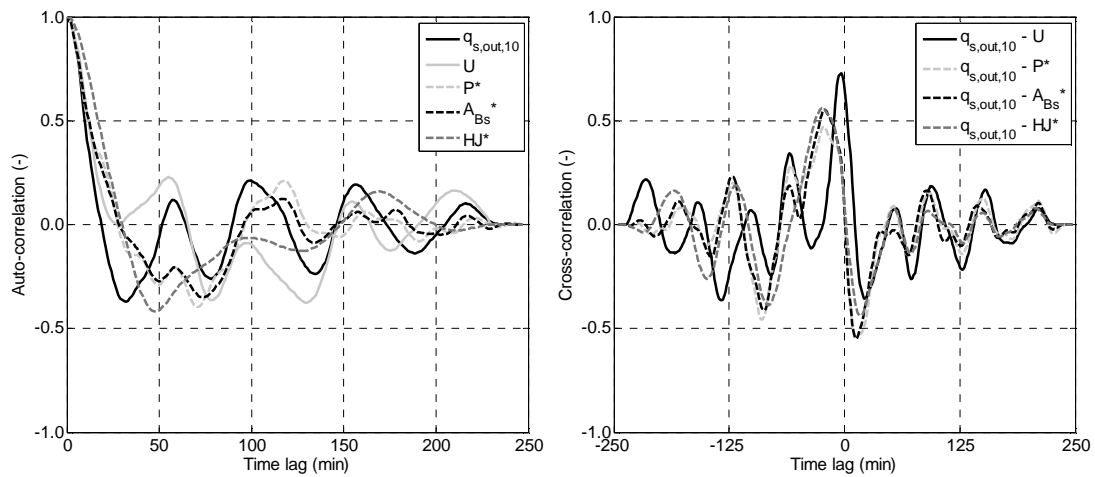
B.41 Test 41

Test parameters

S (%)	λ/D (-)	D (m)	N_{Bs} (m^{-2})	q (m^{3}s^{-1}m^{-1})	$q_{s,in}$ x10^{-3} (m^{3}s^{-1}m^{-1})
13	4	0.075	10.9	0.0118	0.2355

Characterization of the fluctuations (average period T=45 min)

	range (min ÷ max)	mean	σ	σ/mean
$q_{s,out,5}$	0 ÷ 0.5757x10^{-3} m^{3}s^{-1}m^{-1}	0.2630x10^{-3} m^{3}s^{-1}m^{-1}	0.1621x10^{-3} m^{3}s^{-1}m^{-1}	0.62
U	0.27 ÷ 0.50 ms^{-1}	0.34 ms^{-1}	0.05 ms^{-1}	0.16
P^*	0 ÷ 0.50	0.17	0.11	0.66
A_{Bs}^*	0 ÷ 0.067	0.025	0.022	0.86
HJ^*	0 ÷ 0.70	0.20	0.18	0.91

Average results

$q_{s,end}$ x10^{-3} (m^{3}s^{-1}m^{-1})	$\bar{U}$ (ms^{-1})	$\bar{P_{av}}$ (m)	HJ (m^{-2})	A_i/A_t (-)	A_{if}/A_t (-)	P_{end} (m)	P_{us} (m)	P_{ds} (m)
0.2657	0.34	0.013	2.2	0.03	0.006	0.023	0.015	0.026

Final configuration

Time series

Correlation analysis

ISSN 1661-1179